N° d'ordre NNT : 2021LYSEC16

THESE de DOCTORAT DE L'UNIVERSITE DE LYON
opérée au sein de l'Ecole centrale de Lyon

Ecole Doctorale ED 160
Electronique, Electrotechnique, Automatique

Spécialité de doctorat :
Electronique, micro et nano-électronique, optique et laser

Soutenue publiquement le 03/05/2021, par :
Gabriel Jobert

Contribution to the development and miniaturization of optical particulate matter sensors

---

Devant le jury composé de :

DI FALCO Andrea, Professor
SUPA, School of Physics and Astronomy - University of St. Andrews, Rapporteur
BONOD Nicolas, Directeur de Recherche CNRS
Institut Fresnel, Faculté des Sciences de Saint Jérôme – Aix-Marseille Université, Rapporteur
BAUDRION-BEAL Anne-Laure, Maîtresse de conférences
Institut Charles Delaunay - Université de Technologie de Troyes, Examinatrice
LECLER Sylvain, Professeur
INSA Strasbourg - Laboratoire ICube, Président
BARRITAULT Pierre, Ingénieur
Université Grenoble-Alpes, CEA-LETI, Encadrant de thèse
SEASSAL Christian, Directeur de Recherche CNRS
INL, UMR CNRS 5270, Ecole Centrale de Lyon, Directeur de thèse

Contents

Acknowledgements, Remerciements

Je tiens à tout d'abord à remercier chaleureusement tous les membres du jury : Sylvain Lecler en tant que président du jury, Anne-Laure Baudrion-Beal en tant qu'examinatrice, Andrea Di Falco et Nicolas Bonod en tant que rapporteurs. Vous avez pris le temps d'évaluer ma thèse, vous avez su la questionner en jouant le jeu de la pluri-technicité, et ce avec beaucoup bienveillance. Pour tout cela, vous avez toute ma reconnaissance.

Je remercie mon directeur de thèse Christian Seassal, et mon encadrante Cécile Jamois, de l'institut des nano-technologies de Lyon (INL), pour m'avoir suivi tout au long ma thèse et ce malgré les difficultés de la distance. Je remercie mes encadrants du CEA-Leti à Grenoble : Salim Boutami, pour avoir initié mon sujet, et pour m'avoir fait confiance dès notre entretien. Tu as toi aussi su m'encadrer à distance, mais en plus avec le décalage horaire californien ; Pierre Barritault, pour ton implication dans la thématique et pour tes qualités d'encadrement. Merci d'avoir rejoint l'équipage en cours de route, j'espère que beaucoup d'autres étudiants auront la même chance que moi de t'avoir ; Maryse Fournier, tu n'as hélas pas été mon encadrante officiellement, mais tu m'as accompagné dès le début, avec beaucoup d'implications. Je suis heureux de t'avoir rencontré, d'avoir pu discuter quasi quotidiennement avoir toi d'idées folles technologiquement ou de la vie en général, d'avoir découvert ta bienveillance, ton empathie, ton optimisme. De manière générale, à toute mon équipe d'encadrement, je voulais vous remercier à toutes et à tous pour la confiance que vous m'avez accordée. En plus de m'avoir laissé la liberté de faire épanouir ma curiosité, vous l'avez nourri, et vous étiez présents quand j'avais besoin de me refocaliser. Vous aviez en face de vous quelqu'un qui voulais n'en faire qu'à sa tête, alors félicitations !

Je souhaite aussi remercier l'équipe technique de Pyxalis : Julien Michelot, Paul Monsinjon et Pierre Lienhard, pour leur contribution dans le développement de l'imageur troué ainsi que Benoit Dupont pour son implication dans le projet. Pareillement, je souhaite remercier l'équipe technique de FEMTO-print : Pietro Bernasconi, Andrea Lovera et Daniele Braga, pour la réalisation de nos pièces optiques en verre ainsi que Giulia Bottarini pour avoir été une interlocutrice privilégiée.

Au sein de l'INL, je souhaite remercier Taha Benyattou, pour son aide sur la simulation et le design de cristaux photoniques. Au sein du CEA-Leti, je souhaite remercier l'équipe de la plateforme MEMS pour leur aide concernant le post-process de l'imageur troué ; Lara Boutafa pour son travail sur le packaging ; Sylvain Gout pour son travail sur le procédé de dépôt de miroir sur verre ; Brice Poirier de l'atelier de prototypage du YSPOT pour sa bonne humeur et son aide à l'utilisation de machines de fabrication additive et soustractive ; Arnaud Guiot de la plateforme nano-sécurité (PNS) pour son aide sur les expériences avec les aérosols calibrés ; Véronique Mourier et Dominique Lauro pour leur aide sur le moulage des pièces en verre ; Brigitte Caminiti et Aurélie Tapini pour leur aide et leur bonne volonté qu'elles ont mises à chaque démarche administrative.

Je souhaite aussi remercier l'équipe en charge des brevets avec qui j'ai eu plaisir à travailler : Hélène Loriot, Hélène Bourvon, ainsi que les rédacteur.rice.s : Nicolas Haultier et Sophie Delacour pour leurs excellents documents.

Plus spécifiquement, au sein du laboratoire des capteurs optiques (LCO), je souhaite remercier Laurent Duraffourg en tant que chef de laboratoire et Sergio Nicoletti en tant que responsable portefeuille brevets et développeur d'affaires, pour leur intérêt, leur soutien stratégique qu'ils ont apportés à la thématique, et pour l'écoute et la considération qu'ils m'ont apportés ; Olivier Lartigue pour nous avoir apporté ton aide volontaire et efficace en instrumentation et pour m'avoir inspiré dans la conception de bancs optiques ; Adrien Marchant pour ton aide sur la conception de nos structures anti lumière parasites ; Alain Glière pour aide sur la modélisation fluidique, sur les calculs électromagnétiques des diffusions de particules complexes et pour ton humour absurde sur lequel je n'ai pas réussi à rivaliser. Merci aux autres, avec qui je n'ai pas eu l'occasion de travailler, mais avec qui j'ai eu plaisir à cohabiter : Loic, Jules, Vincent, Jean-Gui, Charlotte, Christophe, Kévin, Jean-Marc et tous les autres.

Je souhaite remercier Mathieu Dupoy, pour ta personnalité, pour ta curiosité qui t'a poussé à monter un beau projet, et pour m'avoir offert la possibilité d'y participer, je te souhaite la réussite et j'espère pouvoir re-travailler avec toi à l'avenir.

Je souhaite ensuite remercier les non permanents du LCO. Merci d'avoir partagé avec moi autant de moments autours de cafés interdits, d'apéros, de randonnées de la mort, de voies d'escalade, d'escape games, de balades avec les séquoias et j'en passe. Merci à Lara, Nicolas, Boris, Jade, Joris, Jhuben, Greg, Etienne, Max et les autres, ceux partis en cours de route, et ceux arrivés récemment.

Merci à Cyrielle Monpeurt, ma deuxième bitch préférée (:p). J'ai adoré travailler en duo avec toi, à faire des designs de fous ou à pondre nos meilleurs brevets en tournant au café ... ou au vin ; mais je te remercie surtout pour avoir été aussi présente en dehors du labo, pour courir, manger, boire des Moskow mules, etc.

Je remercie également les membres de mon bureau, il faudrait vous donner à chacun et chacune une médaille pour m'avoir survécu ! Merci d'avoir été comme une famille, toujours prêts à faire des potites blagues, et surtout à partager des moments, des victoires et des difficultés. Longue vie au mur à memes, et à notre mascotte, le poti chat !

Merci à Thomas aka Dr. Lovers (ou Dr. Lolers), j'ai eu la chance de t'avoir comme frère de thèse à une semaine d'écart, tu as été littéralement à un mètre de moi pendant toute cette aventure, et tu n'as jamais failli à l'esprit du bureau, c'est pourquoi je te cède le titre de chef de bureau (et askip t'es plus responsable que moi).

Merci à Joël LeGaludec, talentueux artiste, photographe, vidéaste, écrivain, designer de memes etc., merci de m'avoir révélé une partie de ton identité.

Merci à Marine Beurrier, aka Imperatora, tu es la dernière avec qui j'ai pu transmettre la culture des potites blagues, des memes et des méthodes « à la gabi ». Tu feras heureusement le tri là-dedans, mais j'ai aucun doute que tu feras vivre l'héritage de nous autres, les vieux débiles, jusqu'à que la fin de ta propre thèse.

Merci à Valentin Le Marchand, pour être toi : dissident, ouvert, à l'écoute. Merci d'être resté dans le coin, à partager ta science des fourneaux et du shaker, cher homme au bob Krys bleu.

Merci à Marine Garcia, ma petite sœur surprise, ma compagnonne d'aventures avec qui j'irais jusqu'au Mordor. J'ai pu participer au moins un peu à ta vie remplie d'incidents, qui nous font et feront encore bien rire comme des débiles. Alors à la prochaine aventure cheftaine ! (P.S. désolé j'ai pas réussi à publier ta tête de potite blagueuse dans Nature)

Merci à Quentin Mermillod aka Mermi, l'ancêtre du bureau, pour tous tes enseignements, pour m'avoir trimballé partout dans ton camion, en bas des falaises, au bord de lacs ou le long de l'océan, et ce, en ne suivant que la météo. Merci pour les règles qu'on a enfreint ensemble, pour nos escalades urbaines nocturnes, pour les IPAs qu'on a partagé, et pour le reste.

Je ne pourrais citer tous ceux monde avec qui j'ai aimé interagir, mais je résumerais simplement mon détour au LCO, par la découverte d'une belle brochette d'êtres humains qui m'ont aidé à grandir, à débloquer des compétences, et à avoir la sagesse de rester un enfant. Certain.e.s d'entre vous sont devenus parmi mes ami.e.s les plus fidèles. J'espère avoir rendu au moins un peu de ce que j'ai reçu, et avoir eu un peu d'influence sur la culture du labo. Gardez cette identité, gardez cette fougue et soyez rebelles !

Je remercie aussi mes enseignants à Phelma : Quentin Rafhay, Jean-Emmanuel Broquin, Benoit Boulanger, etc., mes encadrants de stage et managers (Olivier Hugon, Eric Lacot, Romain Grille, Lilian Martineau, Valérie Largeau), qui m'ont accompagné jusqu'ici et pour leurs recommandations.

Je remercie le labo d'Appli de Lynred pour m'avoir accueilli dans leurs rangs, juste après ma thèse, et ce comme l'un des leurs : Xavier Brenière, Guillaume Delubac, Jessy Matias, Romain Delubac et Alexia Gorecki, à qui je souhaite une belle aventure. Et je remercie tous ceux avec qui j'ai l'habitude d'interagir pour leur accueil au sein de la R&D bolo, les opticien.ne.s, Emmanuel Bercier etc.

Je remercie tous mes autres amis qui n'ont pas de liens directs avec ma thèse, que je ne pourrais citer sans faire de jaloux. Vous avez pourtant colorés ma vie pendant cette période, parfois difficile.

Je remercie ma famille, mes parents, mes grands-parents, mes oncles et tantes, ma fratrie. Je remercie en particulier Daphnée, ma sœur, pour avoir été aussi présente à mes côtés, pour avoir emménagé dans ma ville, et même pour avoir fait un séjour au labo !

Enfin, chère lectrice ou lecteur, je te remercie d'être passé par là !

GROS BISOU

GABI

List of Acronyms

ADU Analog to Digital Unit.
AR Aspect Ratio.
ASIC Application Specific Integrated Circuit.

BC Black Carbon.
BEM Boundary Element Method.
BF33 Borofloat 33 glass.
BFL Back Focal Length.
BFP Back Focal Plane.
BOX Buried OXide.
BS Beam splitter.

CCD Charge-Coupled Device.
CMOS Complementary Metal Oxide Semiconductor.
CMP Chemical-Mechanical Planarization.
CPC Condensation Particle Counter.
CVF Charge-to-Voltage conversion Factor.

DBR Distributed Bragg Reflector.
DC Dark Current.
DRIE Deep Reactive Ion Etching.
DUV Deep Ultra-Violet.

EEA European Environment Agency.
EM Electro-Magnetic.

F-FS-S-BS-B Forward, For-Side, Side, Back-Side, Backward.
FBAR Film Bulk Acoustic Resonator.
FDFD Finite Difference Frequency-Domain.
FDTD Finite Difference Time-Domain.
FEM Finite Element Method.
FF Filling Factor.
FFL Front Focal Length.
FFP Front Focal Plane.
FFT Fast Fourier Transform.
FoV Field of View.
FP Fabry-Perot.
FSR Free Spectral Range.
FWHM Full Width Half Maximum.

GLMT Generalized Lorenz-Mie Theory.
GS Global Shutter.

HDP-CVD High Density Plasma Chemical Vapor Deposition.

IARC International Agency for Research on Cancer.
ICP Inductively Coupled Plasma.
IFoV Instantaneous Field of View.
IFP Image Focal Plane.
IoT Internet of Things.

LD Laser Diode.
LED Light Emitting Diode.
LPC Laser Particle Counter.

M & NEMS Micro and Nano Electro-Mechanical System.
MLFMM Multilevel Fast Multipole Method.
MOEMS Micro Optio-Electro-Mechanical System.
MTF Modulation Transfer Function.

NA Numerical Aperture.
NDIR Non Dispersive InfraRed.
NIR Near InfraRed wavelength range (750 nm to 1.4 μm).

OFP Object Focal Plane.
OPC Optical Particle Counter.
OSA Optical Spectrum Analyzer.
OTF Optical Transfer Function.

P-S Parallel (P) and perpendicular (S) polarization.
PBG Photonic Band Gap.
PCB Printed Circuit Board.
PCM Photonic Crystal Membrane.

PCSEL Photonic Crystal Surface Emitting Laser.
PDMS PolyDiMethylSiloxane.
PECVD Plasma-Enhanced Chemical Vapor Deposition.
PhC Photonic Crystal, or PC.
PM Particulate Matter.
PM1 Submicronic Particulate Matter subclass.
PM10 Particulate Matter subclass sized between 10 µm and 2.5 µm.
PM2.5 Particulate Matter subclass sized below 2.5 µm.
PMF Polarization-Maintaining Fiber.
PSF Point Spread Function.
PSL PolyStyrene Latex.
PTF Phase Transfer Function, also known as PhTF.

QE Quantum Efficiency.

Ra Roughness average.
RCLED Resonnant Cavity Light Emitting Diode.
RCWA Rigorous Coupled-Wave Analysis.
RGB Red Green Blue.
RIE Reactive Ion Etching.
ROI Region Of Interest.
RS Rolling Shutter.
RT Ray Tracing.

SAWR Surface Acoustic Wave Resonator.
SEM Scanning Electron Microscope.
SLA Stereo-Lithography Apparatus.
SLED Super-Luminescent Emitting Diode. Also referred as SLD.
SM Single Mode.
SMPS Scanning Mobility Particle Sizer.
SNR Signal to Noise Ratio.
SOI Silicon On Insulator.
SWG Sub-Wavelength Grating.
SWVF Spherical Wave Vector Function.

TE-TM Transverse Electric, Transverse Magnetic polarization.
TEOS TetraEthyl OrthoSilicate.
TL Tube Lens.
TMM T-Matrix Method.

UFP Ultra Fine Particles (< 100 nm). Also known as Nanoparticles, or PM0.1.
US-EPA United State Environmental Protection Agency.

VC Vertical Cavity.
VCSEL Vertical Cavity Surface Emitting Laser.
VI Virtual Impactor.
VIS Visible wavelength range (380 nm to 750 nm).

WHO World Health Organization.

List of Symbols

Symbol	*Description*	*Unit/Domain**
	General optics	
λ	Wavelength	μm
ω	Optical pulsation	$\mathrm{rad}\cdot\mathrm{s}^{-1}$
n_p	Complex refractive index of a particle p	$\mathbb{R}^+ + i\mathbb{R}$
n_m	Complex refractive index of the surrounding medium	$\mathbb{R}^+ + i\mathbb{R}$
n_i	Complex refractive index the medium i	$\mathbb{R}^+ + i\mathbb{R}$
ϵ	Dielectric function	F/m
$\overrightarrow{M}^{(k)}_{l,m,p}$, $\overrightarrow{N}^{(k)}_{l,m,p}$	SWVF, or spherical harmonics	$\mathbb{C}^3$
$\overrightarrow{E}$	Electric field	V/m
$\overrightarrow{H}$	Magnetic field	A/m
$\overrightarrow{U}$	Normalized optical vector field	$\mathbb{C}^3$
$\overrightarrow{k}$	Wave-vector	$\mu\mathrm{m}^{-1}$
P_{inc}	Incident optical power	mW
φ	Phase angle	rad
$h(x,y)$	Point spread function	$\mathscr{D}(0,1)$
ν, ν_x, ν_y	Axial, sagittal and tangential spatial frequencies	$\mu\mathrm{m}^{-1}$
$\mathscr{F}$	Optical Fourier transform	$\mathbb{C} \to \mathbb{C}$
$\mathscr{H}(\nu_x, \nu_y)$	Optical Transfer Function (OTF)	$\mathscr{D}(0,1)$
$\mathscr{M}(\nu_x, \nu_y)$	Modulation Transfer Function	$[0,1]$
$\mathscr{P}(\nu_x, \nu_y)$	Phase Transfer Function	rad
r, t	Reflectivity and transmission coefficients	$[0,1]$
$\mathscr{R}, \mathscr{T}$	Mirror OTF in reflection and transmission mode	$\mathscr{D}(0,1)$
R, T	Energy reflectance and transmittance fractions	$[0,1]$
	Scattering	
χ	Size factor	$\mathbb{R}^+$
$P_\chi(x,y)$	Sphere equivalent planar obstacle	$\mathscr{D}(0,1)$
C_{scat}, C_{bscat}, C_{ext} & C_{abs}	Scattering, back-scattering, extinction and absorption cross sections	$\mu\mathrm{m}^2$
$A_s(\chi)$	Extinction ratio	$[0,1]$
W_{scat}	Total scattered power	mW
$S(\theta)$	Scattering signature of a single particle	$\mathscr{D}(0,1)$
$S_f(\theta), S_b(\theta)$	Forward and backward scattering signature	$\mathscr{D}(0,1)$
$S_t(\theta)$	Total scattering signature of an aerosol	$\mathscr{D}(0,1)$
$\varphi_s(\theta)$	Phase scattering signature	rad

Symbol	*Description*	*Unit/Domain**
	General geometry	
θ	Scattering angle, or polar angle	rad
θ_x, θ_y	Sagittal and tangential angles	rad
ϕ	Azimuthal angle	rad
ϕ_p	Polarization angle	rad
x_p, y_p, z_p	Particle position	µm
α, β	Beam misalignment angles (pitch, yaw)	rad
γ	Vignette angle	rad
Ω	Instantaneous Field of View (IFoV)	sr
W_b	Width of a Gaussian beam	µm
Σ	Beam section	µm^2
d	Cavity length	µm
h_i	Thickness of a dielectric layer i	µm
h	Thickness of a slab	µm
P	Lattice period	µm
FF	Filling Factor	$[0, 1]$
D	Diameter of a unit cell	µm
	Aerosol science	
D_p	Particle diameter	µm
D_a	Particle aerodynamic diameter	µm
D_{pp}	Peak particle diameter of a distribution	µm
σ	Standard deviation, or log-normal deviation	$\mathbb{R}^+$
n	Particle concentration	part/cm^3; µg/cm^3
	Sensor	
p_{pix}	Pixel's pitch	µm
f_N	Nyquist frequency	cycles/mm
t_{int}	Integration time	µs
f	Detection rate	%
V_s	Sampling volume	µm^3
	Image processing	
I	Image matrix	ADU
N_{iso}	Number of iso-θ	$\mathbb{N}^+$
M	Image reduction matrix	$(N_{iso} \times 5)$
ϵ	Minimization criterion	$\mathbb{R}^+$

* Note that units are usually given when the value is scalar; the domain is given for unit-less values. The $\mathscr{D}(0,1)$ domain refers to the unit closed ball of the complex plane:
$\mathscr{D}(0,1) = \{x + iy \mid (x,y) \in \mathbb{R}^2, |x^2 + y^2| \leq 1\}$

I

Introduction

Chapter content

I.1 Introduction on Particulate Matter

I.1.1 Generalities

Particulate Matter (PM) is a distribution of objects (solids or liquids) in suspension in the air, and whose size can vary from a few nanometers to a few micrometers. PM comes in a wide variety of shapes and chemical compositions originates from a natural or anthropogenic processes. These compounds may contain toxicants and mutagenic substances in the form of fine mineral dust; organic elements such as Black-Carbon (BC) soot which are produced from the incomplete combustion of hydrocarbons, coal or fossil-fuel; bio-aerosols such as viruses, pollen or spores; acid droplets (nitric or sulfuric); heavy metals such as lead, mercury or even cadmium.

Anthropogenic PM are known to have a serious impact on health [1,2], in particular on cardiovascular, cardiac and respiratory diseases such as lung cancer and even neuro-degenerative diseases. Medical reports have shown that the finer a particle is, the deeper it penetrates the human respiratory system [3]. For this reason, a legislative classification on aerosol granulometry has been created, that classifies PM into sub-classes according to their size (see, Figure I.1).

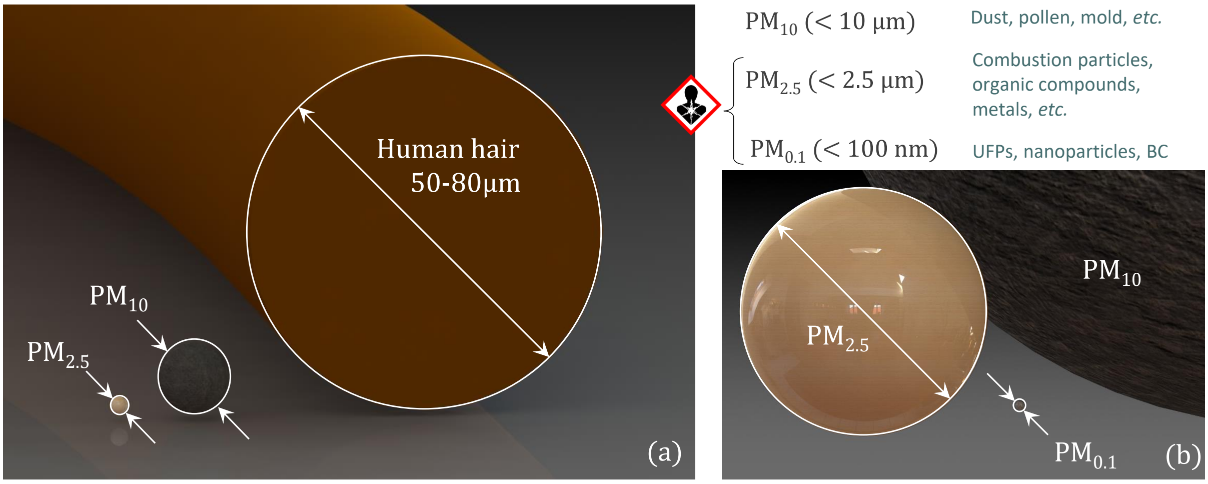

Figure I.1: *(a) Size comparison of PMs with a human hair. (b) Zoomed view of fine and ultra-fine PM.*

- ***PM10*** refers to particles with a size ranging from 10 μm to 2.5 μm: this is the less harmful subclass.
- ***PM2.5*** (particles smaller than 2.5 μm) have been classified as a known carcinogenic agent (group 1) by the International Agency for Research on Cancer (IARC) [4,5]. In addition, a meta-analysis conducted by the US-EPA concluded on the causality of premature death by PM2.5 exposure [6].
- ***PM1 and UFPs*** are unregulated subclasses that refers to submicronic particles and Ultra-Fine Particles (< 100 nm) respectively: these classes are expected to be far more harmful that PM2.5 as they can penetrate the respiratory system even deeper [7,8] (up to the alveolar duct for the UFPs).

Beyond health considerations, anthropogenic PM pollution appears to have an adverse effect on climate [9,10], especially for Black-Carbon (BC) soot. Indeed, meteorological models suggest that controlling the emissions of BC could be one of the most efficient ways to mitigate the global warming, even more than controlling carbon monoxide or methane emissions [11–14].

I.1.2 Laws and regulations

We take as a reference the regulations imposed on the member states of the European Union[1], that states the maximum legal concentration for most air pollutants (see, in Table I.1).

Polluant	*Concentration* (µg/cm^3)
PM_{10}	40
$PM_{2.5}$	25
Sulfur dioxide (SO_2)	125
Nitrogen dioxide (NO_2)	40
Carbon Monoxide (CO)	10^4

Table I.1: *European Union regulation on the concentration of some pollutants (one-year average).*

It should be noted that PM1, UFPs and BC, potentially the most dangerous for both health and climate, do not appear in the directive. On the other hand, formulating the regulation in mass concentration (µg/cm^3) is problematic in the sense that, within a same subclass, the larger particles have a considerable impact on the total mass of the subclass, even though the smaller particles are the most hazardous to health. Then, apart from direct gravimetric measurement, most PM sensors can only give concentrations in particle number, for a given range of sizes (see, Section I.2). Typically, the mass concentration is derived from the mass density of the particles using conversion tables [15]. The use of this type of tables supposes to know indirectly the composition of the particles for a given size, for example after calibration campaigns. However, the aerosol composition does vary according to the location, time of measurement and weather conditions. Note that, in this manuscript, we will consider particle number concentrations (particles/cm^3) instead of the historical (regulated) particle mass concentration (µg/cm^3), as epidemiologists consider the former as a more relevant health metric [16].

It is anticipated that regulation will be updated with new metrics in the near future [9, 17] . Indeed the scientific community, the World Health Organization (WHO) and various environmental protection agencies appear to put significant pressure toward regulatory agencies [18]. In particular, by defining metrics on the particle number concentrations for the still unregulated fractions PM1, UFPs and BC.

---

[1] 2008/50/EC Directive on Ambient Air Quality and Cleaner Air for Europe.

I.1.3 Aerosol geometry

Ambient air particles show an impressive diversity in terms of morphology: from globally spherical or polyhedral geometries to highly irregular shapes. Examples of ambient air particles are shown in electron microscopy images in Figure I.2

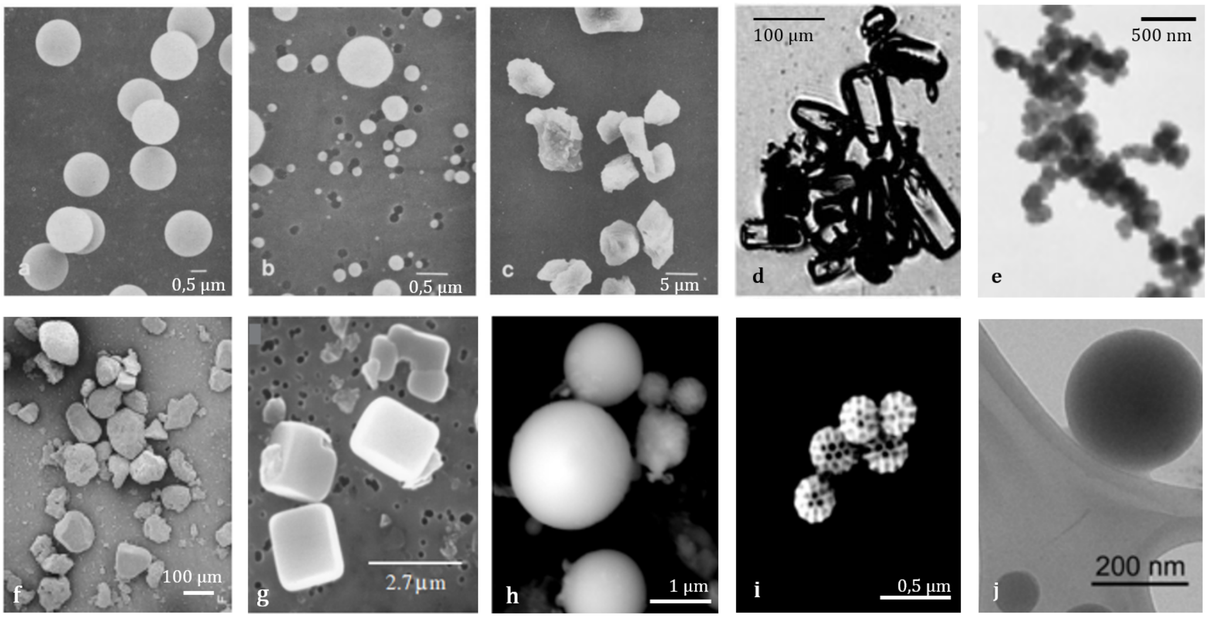

Figure I.2: Electron microscopy images of calibrated polystyrene beads (a), ammonium sulfate droplets (b), silica grains (c), Cirrus ice crystals (d), soot generated by a flaming coal combustion (e), Sahara sand grains (f), sea salt crystals (g), fly ash (h), bio-aerosol (i), a wood tarball (j) [19–22].

A large part of particles generated from incomplete combustion of carbonaceous elements forms BC soot [21, 23]. As seen in Figure I.2(e), BC exhibit a peculiar morphology, that can be modelled as fractal aggregates, *i.e.* agglomerated chains of identical particles where there is a certain repetition of patterns at different scales. True mathematical definition of such aggregates is the fractal relation discussed in reference [24].

I.1.4 *Size distribution of an aerosol*

From the previous sub-section, we showed that certain particles are very irregular, in terms of geometry. However, a particle diameter D_p can still be defined. The first reason for such a definition is that an aerosol includes particles with random orientations. This allows us to consider any particle as statistically spherical, and thus to define a diameter. Several definitions can be given, for example a geometrical definition such as the volume-equivalent diameter, where the particle is assimilated to a sphere of same volume. This is the best definition since such a diameter refers directly to the mass of the particle[2]. It is also possible to define sphere-equivalent diameters that share certain physical properties with the particle. These definitions are generally associated with measurement methods. For example, the aerodynamic diameter of a particle is the diameter of a uniform sphere that has the same aerodynamic mobility as the particle. Similarly, the optical diameter (which will be used in this manuscript) can be defined as the diameter of a sphere with the same optical index as the particle and with similar optical scattering properties (see, Section I.2).

Depending on the definition of the diameter (*i.e.* according to the characterization method), errors can be created when estimating the actual particle size. Calibration campaigns are sometimes necessary to correctly estimate the mass of the aerosol. In the case of characterization by optical scattering, errors in estimating the refractive index of a particle can lead to large errors in estimating the real particle diameter, which is an issue we will encounter and discuss in the following chapters.

An aerosol size distribution usually exhibit a log-normal law (I.1), which is a kind of normal law, when considering $\ln D_p$ as the argument.

$$n(\ln D_p) = \frac{dN}{d(\ln D_p)} = \frac{N}{\sqrt{2\pi}\ln\sigma}\exp\left(-\frac{\ln {D_p}^2 - \ln {D_{pp}}^2}{2\ln^2\sigma}\right) \tag{I.1}$$

With N the total particle number concentration[3], σ the log-normal deviation (which is usually about $\sigma \sim 2$), D_p the equivalent diameter of particles, D_{pp} the peak diameter of the distribution. This law means, notably, that there aer many more particles smaller than D_{pp} than there are larger particles.

The Whitby trimodal atmospheric model is frequently used [25]. This simplified model, based on the physical-chemical formation process of particles, characterizes the particle size distribution according to a sum of three log-normal distribution modes: the nucleation mode, the accumulation (or coalescence) mode, and the coarse particle mode. An example of such a distribution is shown in Figure I.3.

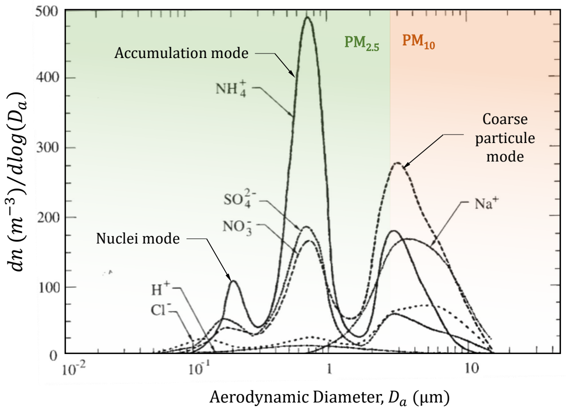

Figure I.3: *Size distribution of the most common aerosols of ionic origin (modified from [26]).*

We can mention other distribution models, depending on the aerosol considered: for example, the γ distribution is used to describe the size of water droplets within clouds, mists or fogs [27]. *A priori*, the log-normal distribution is used.

---

[2] As a reminder, the legislation imposes a mass concentration limit.

[3] The concentration integrated over the whole distribution.

I.2 Particulate Matter sensors

I.2.1 Overview of PM sensors

In this section, we aim to provide a brief overview of the PM sensing techniques [28] by giving a list that is far from exhaustive. The specific case of optical sensors will be discussed in the next subsection.

Historically, particle concentration is quantified by the gravimetric method. It consists of the direct measurement of the mass of an accumulation of particles by weighting particles captured by a filter. Modern gravimetric methods allows for the mass measurement of single particles by using Micro and Nano Electro-Mechanical Systems (M & NEMS) such as oscillating piezoelectric cantilevers [29,30], Film Bulk Acoustic Resonators (FBAR) [31] or Surface Acoustic Wave (SAW) resonators [32,33].

Other main approaches that were historically used to measure particle concentrations are the β attenuation [34,35] and the ionization method [36]. Both methods take advantage of the fact that small particles efficiently absorb the radiation from a radioactive material. The former directly measures the attenuation of a radioactive β source induced by PM. The latter measures electrostatic effects of ionized particles that have absorbed radiation from an α source[4]. For both cases, the concentration is then evaluated from the overall absorption of radiation.

These examples are some methods for detecting particles. Then, other methods allows to determine the size of particles, by evaluating a related physical behaviour. The most popular way to size particles is the inertial (or aerodynamic) sizing: it is achieved by measuring the aerodynamic mobility (inertia) of a particle that is carried by an accelerating air flow, deriving the aerodynamic diameter. This is conventionally done through cascaded impactors or cascaded aerodynamic lenses. But the preferred modern method, refereed as Aerodynamic Particle Sizing (APS) consist in generating this acceleration using a nozzle and a time-of-flight module [37]. Another widely used sizing methods, such as the diffusion size classifier [38] or the SMPS (Scanning Mobility Particle Sizer), involve measuring the deviation by an electrostatically charged particle submitted to an electric field, using an electrostatic classifier [39,40], the electrostatic charge being linked to the surface area of the particle. Most of these sizing methods are designed to expose a specific particle's physical behaviour, the detection is often done by another technique such as gravimetric or optical. These techniques can accurately determine the size of particles, but are generally bulky and expensive. In the following section, we will discuss the optical sensing techniques for both detection and sizing, and we will see why it makes sense to try to miniaturize an optical PM sensor specifically.

---

[4] This technique, which was very popular for domestic smoke detectors, is gradually being abandoned as it does not provide sufficient accuracy.

I.2.2 Optical PM sensors

Optical methods for PM sensing are particularly interesting as they are rather easy to implement and often allow real-time measurements. They are generally based on absorption and scattering of light by particles. The common methodology is to illuminate an air chamber or fluidic channel and have the particles interact with the light.

- ***Extinction (or obscuration) method:*** The principle of this method is to measure the loss of optical intensity from a single light source (visible or near infrared[5]) that passes through a plume of suspended particles (or measuring the blackening of a particle filter) using a single, on-axis photodetector [41] (illustrated in Figure I.4). In accordance with the Beer-Lambert's law of attenuation, this setup makes it possible to estimate a concentration if the particle distribution of the plume is known: meaning that such instruments requires calibration campaigns. However, this simple method is unsuitable for the measurement of fine particles in low concentrations due to a poor signal to offset ratio, resulting in a quite low sensitivity. The term aethelometer, or nethelometer is sometimes used to refer to such instruments.
- ***Light-scattering method:*** The method is somehow similar to the extinction setup except that the photodetector is placed in an off-axis configuration [42] and is able to detect only the light deviated by a particle accordingly to the principle of light scattering. The sensitivity is much better here than in the extinction setup because the signal to offset ratio is only impacted by stray light from the source. Such a setup is illustrated in Figure I.4.

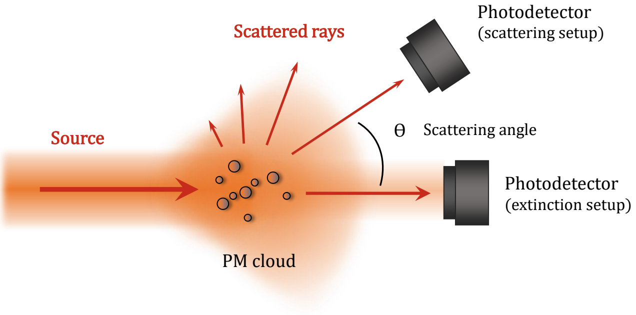

Figure I.4: *Illustration of the extinction and scattering techniques.*

Figure I.4 illustrates the simplest light-scattering setup. In the same way as the extinction setup, it is able to estimate the total concentration of PM but is insensitive to the nature and size distribution of the particles from the sampled aerosol. In most cases, a particle filtering stage can be used prior to the optical measurement unit, allowing for example the sensitivity to PM2.5, excluding PM10 [43]. Particle filtering can be efficiently achieved by taking advantage of their inertial proprieties: it is used in fluidic devices like Virtual Impactors (VI) [44] and cyclones [45] to cite only a few.

- ***Light scattering analysis:*** In an alternative light-scattering setup, retrieving and analyzing more precisely the light-scattering properties of particles (spectral, angular, polarization dependencies *etc.*) makes it possible to estimate optical parameters such as refractive index and sphere equivalent diameter. For example, by multi-wavelength illumination [46] or discrete multi-angle scattering [47, 48] measurements with a set of photo-detectors or spectral filters.

  More advanced light-scattering sensors allow for complete measurement of the angular scattering efficiency function (we call 'scattering signature') by using either a rotating detection arm or periscope [49, 50] or an array of photo detectors coupled with an optical Fourier transform optical setup using mirrors [51] or lenses [52] (see, Chapter III). Indeed, for a particle of a given size,

---

[5] This spectral range is generally used because small particles efficiently interact with short wavelengths. Moreover, source prices are generally low in this range.

morphology and optical index, we can describe the theoretical angular distribution of the scattered light (for example using the Lorenz-Mie theory which will be discussed in Section I.3). Thus, knowing an experimental signature can, again, lead to the determination of optical and geometrical parameters of particles (and subsequent classification) by performing an inverse problem. This part will be detailed in Section I.3 and II.4.

- ***Optical Particle Counters (OPC):*** This family of instruments usually function in the same way as conventional light-scattering sensors [53], the difference being that only one particle should be detected at a time. It usually requires focusing optics or particle focusing fluidics (such as nozzles) to limit the detection area [54] as well as high numerical aperture detection optics (such as an elliptical mirror) to improve the sensitivity. A schematic of a typical OPC is shown in Figure I.5. OPCs that uses a laser light-source are often called LPC (Laser Particle Counter).

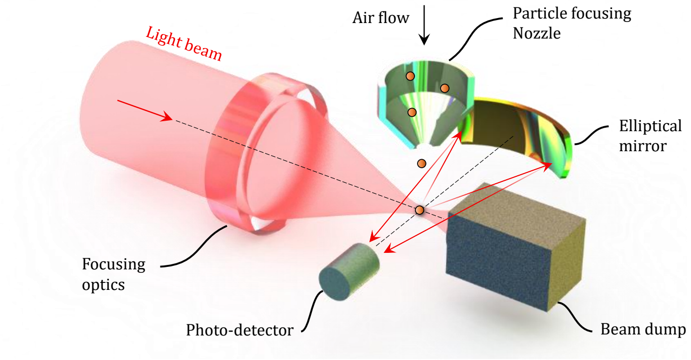

Figure I.5: *Schematic of a typical OPC.*

The size can then be estimated using the scattering intensity of a single particle although this approach isn't very accurate as the intensity does not increase monotonically with diameter (see, Section I.3). Alternatively, if the photo-detector is time-resolved, the diameter can also be estimated using the duration of the scattered pulse. These OPCs are generally calibrated and can accurately size particles within a small range of refractive indexes, however this limitation can be mitigated by evaluating an optimized line of sight and Field of View (FoV) of scattering angle [55]. OPCs can also implement light-scattering analysis modules as described above.

As a variant, the CPC (Condensation Particle Counter), artificially increases the size of small particles (*e.g.* UFPs) by solvent (or water) wetting, making scattering efficiency stronger. This allows to shift down the size range of classical OPCs.

- ***Holographic characterization:*** Another family of OPCs allows the counting and classification using a lens-less/holographic setup [56–58]. The principle of particle holographic characterization, which is illustrated in Figure I.6, is to illuminate a microfluidic channel on one side and to record the holograms created by the particles on the other side (interference between illumination and particle scattering). The holograms are recorded by an imaging system, for example a lens-less CMOS image sensor.

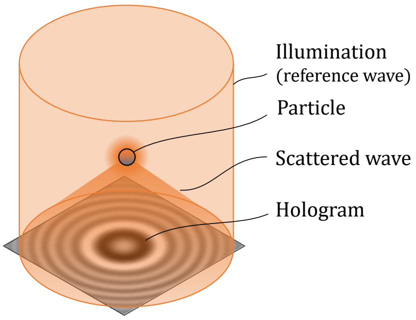

Figure I.6: *Illustration of the holography technique.*

- ***Cavity-enhanced sensing :*** This is a very sensitive detection method that puts the particle/light interaction within a resonant optical cavity, for instance a Fabry-Perot (FP) resonator constituted by two mirrors [59, 60] (see, Chapter IV). An example of a passive cavity aerosol detector is shown in Figure I.7(b). Such a structure makes it possible to exacerbate the electromagnetic field inside the cavity, where particles can circulate. The extinction or scattering is then measured with significantly improved sensitivity compared to a cavity-free arrangement (see, Figure I.7(a)).

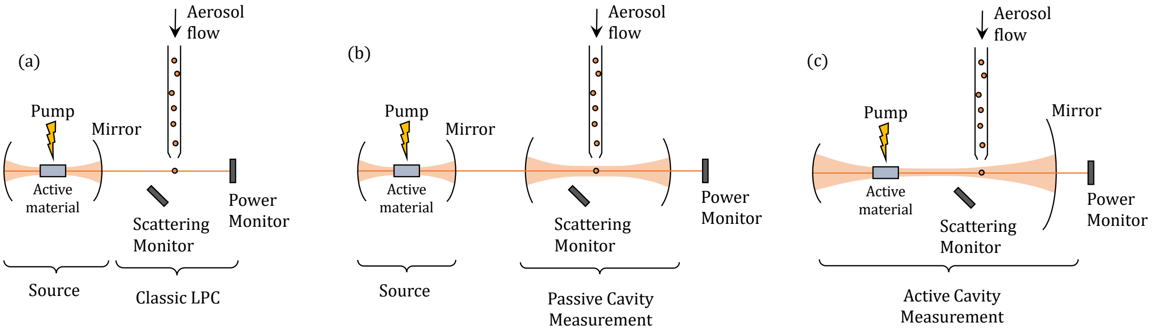

Figure I.7: *Comparative schematics of (a) a classical LPC, (b) a passive cavity and (c) an active cavity setup.*

  An alternate architecture involve using a laser cavity, or a RCLED (Resonnant Cavity Light Emitting Diode) cavity as the sensing area [61]. An illustration of such a system is given in Figure I.7(c). The cavity features an active medium and is then powered by an optical or electrical pump. The behavior of the source then depends on the presence of a particle that disturbs the cavity, resulting in an intensity drop of the emitted light associated with a degradation of the lasing threshold.

- ***Optical trapping of nano-particles:*** Nano-particles (or UFPs) have masses low enough to be sensitive to optical gradient forces (as well as radiation pressure). Thus, nano-particles can be trapped (and manipulated) using optical nano-tweezers [62]. The conventional optical trap is a focused high-power optical beam, or two counter-propagating focused beams [63]. Since the developments of optical micro-cavities [64], nano-particle sensing by optical trapping in these structures is becoming more and more popular: for instance with vertical micro-cavities [65], photonic crystal[6] defect cavities [**?**, **?**, 66, 67] or metallic meta-surfaces [**?**, **?**]. Finally, the size of a nanoparticle is derived from the trapping efficiency, or the time needed of a particle to escape the trap. This family of methods finds a notable application in the trapping and characterization of wet particles such as bio-particles [**?**, 68, 69] but one might expect further developments toward airborne UFPs characterizations.

In Table I.2, we provide a comparison of the overall properties and specifications of the main PM sensing techniques. We've selected only commercially available sensors, or laboratory sensors extensively tested on the field.

As explained earlier, we took interest in optical methods. Indeed, this family of methods allows, using relatively simple setups, to count and classify particles, with additional insights on the size the material (refractive index) and geometry (irregularities, surface roughness, volume porosity *etc.*). In order to design an optical setup that maximizes our ability to detect and classify particles, we have to understand properly the light-scattering phenomenon, for instance using scattering theories and methods that will be discussed in the following section.

---

[6] Photonic crystals are discussed in Chapter IV.

Physical family	*Technique*	*Metric measured*	*Real time*	*Portability*	*Size range*	*LoD*	*Price*	*Comment*
Gravimetric	Gravimetric filter	Concentration (cumulative mass)	No	High	> 150 nm	10 µg/m^3	Lowest	Direct mass measurement. Cheapest, simple to deploy. But sample analysis is time consuming.
	M & NEMS	Number and size distrib.	Yes	High	> 5 nm	N/A	N/A	Direct mass measurement. Only for small masses (kDa - MDa range).
Inertial	Impactors	Concentration (cumulative)	No	Variable	1 µm – 10 µm	N/A	Low	Useful when looking at size specific chemical characteristics. But sample analysis is time consuming.
	APS	Number and size distrib. (aerodynamic diameter)	Yes	Medium-Low	0.5 µm – 20 µm	10^3 part/cm^3	High	Reference technique. High sizing accuracy and resolution.
Electric	Diffusion size classifier	Size distrib. (surface area)	Yes	High	10 nm – 700 nm	10^{3-6} part/cm^3	Medium	Portable and robust. But poor accuracy for size distribution.
	SMPS	Size distrib. (surface area)	Yes	Low	2.5 nm – 1 µm	10^{1-7} part/cm^3	High	Highest resolution for size distribution.
Radiation	β attenuation	Concentration (indirect)	No	High	N/A	1 µg/m^3	Medium-High	Use of a radioactive source.
Optical	Extinction photometry	Concentration (indirect)	Yes	High	> 1 µm	600 µg/m^3	Very low	Cheap. But poor sensitivity, and mostly sensitive to large particles.
	Light scattering	Concentration (indirect)	Yes	High	300 nm – 10 µm	100 µg/m^3	Very low	Reference technique for personal PM monitors.
	Light scattering (angular photometry)	Size distrib. (optical diameter)	Yes	Variable	300 nm – 10 µm	100 µg/m^3	Low-Medium	Good sizing accuracy if calibrated. Highly dependent on refractive index.
	OPC	Particle number	Yes	High	300 nm – 10 µm (CPC, > 15 nm)	10^4 part/cm^3	Low	Cheapest counter.
	Holography	Number and size distrib. (optical diameter)	Yes	High	500 nm – 10 µm	10^4 part/mL	Low-Medium	Analysis is computationally expensive. Usually wet samples.

Table I.2: *Comparison of the overall properties and specifications of the main PM sensing techniques. Adapted from [17, 28, 35, 70]*

I.3 The optics of small particles

I.3.1 Overview of scattering theories, models and numerical methods

In this section, the main techniques that allows to model the phenomenon of elastic light scattering by particles is discussed. This knowledge would enable the design of analysis systems capable of classifying particles (particle number, size distribution, material, geometry *etc.*): for example, in order to characterize ambient air and identify environmental or sanitary hazards.

It could also allows us to create alarm systems that are less sensitive to false positives. This, in order to operate in contaminated environments (*e.g.* to discriminate fumes from kitchen water droplets or to operate in dusty areas such as mines or workshops).

There are many variants that take into account several parameters such as lighting conditions, particle morphology and orientation, size range, multiplicity of particles, *etc.* Among the vast zoology of the theories, models and numerical methods, we present some of the main ones in Table I.3.

Diameter D_p	$< \lambda/10$	$> 20\lambda$
Method	*Rayleigh's scattering*	*Ray Tracing (RT)*
	EM volume & surface methods (FEM, FDTD, FDFD, BEM)	
	Spherical Wave Vector Functions Expansion (SWVF) • Lorenz-Mie theory (spheres) • T-Matrix method (arbitrary geometries)	

Table I.3: *Main scattering description methods and their range in particle diameter. λ is the wavelength of illumination.*

Relevant light-scattering characteristic are for instance: the absorption, scattering and extinction efficiencies (or cross-sections) of a particle but also the scattering signature of a particle. The latter refers to the angular[7] scattering efficiency, meaning the angular distribution of scattered radiation. It depends on the geometry of the particle (morphology and size), its refractive index and the wavelength of the excitation light in the surrounding medium. In order to perform the inverse problem, which is to determine the nature of an aerosol (from its optical and geometrical properties), it is crucial to be able to measure this angle-dependent scattering efficiency [71,72].

Rayleigh dipolar scattering theory [73] allows to describe the scattering of a small particle ($< \lambda/10$) while the geometrical Ray-Tracing (RT) model [74] is only valid for large particles ($> 20\lambda$). These theories have the advantage of being simple but they are no longer valid when the particle size is close to the illumination wavelength. Then, we can model the scattering in the entire range of particle size by full volumetric Electro-Magnetic (EM) simulations such as the Finite Element Method (FEM) [75], the Finite Difference Time-Domain or Frequency-Domain (FDTD/FDFD) [76,77]. We can alternatively use EM surface methods such as the Boundary Element Method (BEM) [78,79], which approximate the boundary conditions with a discrete evaluation on surface points. Although these methods are theoretically applicable to model any type of structure regardless of its size and any type of lighting condition, the main limitation is the fact that the volume or surface of a particle must be discretized with elements whose size must be much smaller than the wavelength. This limits the range of size to a few tens of wavelength *de facto* for computational resource reasons, not to mention the reduced computing resources available for embedded systems.

---

[7] The 'scattering angle' is the angle between the scattered ray and the optical axis, *i.e.* the polar angle.

This is why we choose to use analytical EM theories that consists in expanding electromagnetic fields into Spherical Wave Vector Functions (SWVF) [80].

One can show that SWVFs ($\overrightarrow{M}^{(k)}_{l,m,p}$, $\overrightarrow{N}^{(k)}_{l,m,p}$), also known as *'spherical harmonics'*, forms a vector basis of the solutions of Maxwell's equations (see, Appendix B). In this method, the incident ($\overrightarrow{U}_{inc}$), internal ($\overrightarrow{U}_{int}$) and scattered ($\overrightarrow{U}_{scat}$) fields[8] are expanded into series of SWVFs. Note that internal and scattered fields are those evaluated inside and outside the particle, respectively.

Only the expansion coefficients of the incident fields are *a priori* known. The relationships between the different expansion coefficients are then determined using the boundary conditions on the particle surface [81]. These latter result from the prior definition of the particle geometry (size, morphology). Assuming there is no surface current, tangential components of the fields are continuous at those interfaces, see equation (I.2).

$$\overrightarrow{n} \times (\overrightarrow{U}_{scat} + \overrightarrow{U}_{inc}) = \overrightarrow{U}_{int} \tag{I.2}$$

$\overrightarrow{n}$ is the unit vector normal to the particle's surface. Solving this problem can be difficult for arbitrary surfaces, as solutions take integral forms (further details hereafter on Section I.3.3). However, for some simple shapes such as spheres, one can obtain analytical expressions of both the scattered and the internal fields.

I.3.2 Electro-magnetic scattering by spheres: a brief introduction to the Lorenz-Mie theory

The Lorenz-Mie theory [82, 83] is the most common description of light-scattering. It is the simplest theory within the family of SWVF expansion methods, where expansion coefficients are calculated for sphere of homogeneous complex refractive index, illuminated by a monochromatic, polarized plane wave. Assuming these hypothesis, this theory is exact and valid for any range of diameter (Figure I.8).

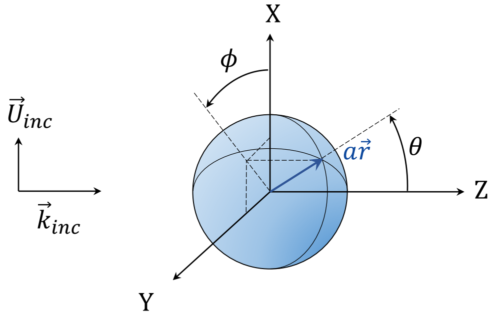

Figure I.8: *Illustration of light-particle interaction in Lorenz-Mie theory.*

Let us consider a spherical particle with a radius a, in a surrounding medium of refractive index n_m and illuminated with a wavelength λ in the vacuum. Such a spherical particle can be reduced into the adimensional size factor χ, related to the optical diameter discussed in Section I.1.4.

$$\chi = \frac{2\pi n_m a}{\lambda} \tag{I.3}$$

Note that, we agree on a convention in terms of polarization and angles. Such a convention is properly defined in Appendix A.

---

[8] We consider normalized, and unit-less waves, as explained in Appendix A.

This theory enables the calculation of the absorption, scattering and extinction cross-sections (given in µm^2) as a function of χ and the refractive index of the particle. A cross-section expresses an area associated to the portion of the incident electromagnetic wave that have interacted with the scatterer. The extinction cross-section indicates the total optical power taken from the incident wave (by absorption and scattering) over its amount of power per unit of area. For example, the theory shows that the scattering and extinction cross-sections increases non-monotonically with χ, as shown in Figure I.9.

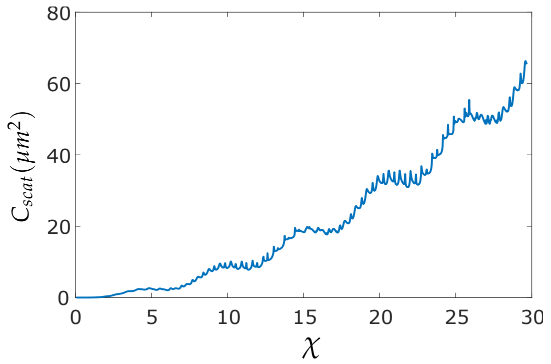

Figure I.9: *Scattering cross section $C_{scat}(\chi)$ as a function of size factor χ.*

It is also possible to evaluate the electromagnetic fields in any point of space. Finally, one can calculate the far-field radiant diagram of the scattered fields, which intensity is what we call the scattering signature (discussed above). Figure I.10 shows the scattering signatures (polar plots[9] with a logarithmic scale) of laboratory PolyStyrene Latex (PSL) spheres with three different diameters.

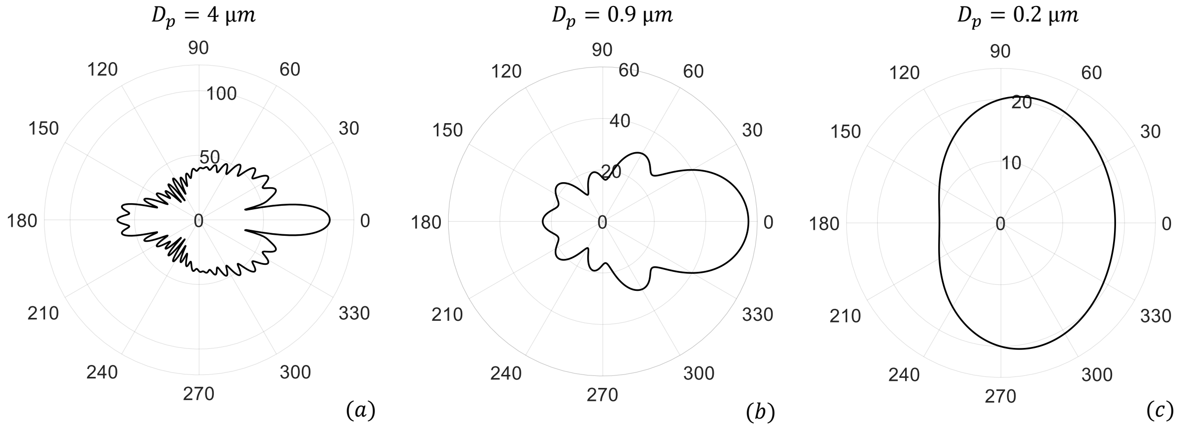

Figure I.10: *Scattering signatures of PSL spheres of three different diameters: (a)* 4 µm, *(b)* 0.9 µm *and (c)* 0.2 µm; *illuminated by an unpolarized plane wave ($\lambda = 635$ nm).*

These signatures were calculated using a Lorenz-Mie calculator developed in-house, with a non-polarized incident plane wave of wavelength $\lambda = 635$ nm onto a single PSL sphere with refractive index $n_{PSL} = 1.5875$ at this wavelength [84]. Observe that coarse particles (few wavelengths of diameter) present several scattering angular lobes of higher intensity. The number of these lobes decreases with the particle diameter and is highly dependent on the particle complex refractive index.

It should be noted that the size distribution of particles influences the scattering phenomenon and that in most cases, scattering cannot be modeled by a mono-disperse aerosol of average size [85,86].

---

[9] In such polar diagrams, the incident light comes from left to right. A scattering (polar) angle of 0° correspond to a ray that wasn't deviated.

I.3.3 Scattering by irregular particles

The Lorenz-Mie theory is only adapted to (roughly) spherical particles (such as calibrated laboratory beads, suspended droplets, wood fire smoke, some species of bio-aerosol, *etc.*), but may not be applied to describe scattering properties of particles with irregular shapes that can be found in ambient air (see, Figure I.2). Numerous theories have been developed to model non-spherical particles and clusters. Section 8 of reference [87] offers a great review of such methods. We will simply cite some of these methods in the present section.

It is always possible to apply full EM numerical methods (FEM, FDTD, FDFD, BEM) to solve such a problem, but it requires resources in terms of computing power that are not always available for most applications. Many Generalized Lorenz-Mie Theories (GLMT) [88] have been formulated in order to model different particles morphologies such as spheroidal particles [19,89] or particle clusters [90]. Then, another approach considered relevant combines the BEM with the Multilevel Fast Multipole Method (MLFMM) [91] as it can solve large scale, arbitrary scattering problems. Here, scattering is approximated by a set of dipolar sources at the vicinity of the interfaces. A fast MLFMM-BEM scattering calculator based on a scalar and vector formulation, instead of the more conventional SWVF formulations, was developed in-house prior to the preparation of this manuscript [92]. In the future, MLFMM-BEM could be applied to process the data measured by our PM sensors.

Finally, one of the most advanced scattering theories for arbitrary shapes is the T-Matrix Method (TMM[10]) [93–95]. It allows to calculate precisely the scattering by a non-spherical particle of random orientation as well as a set of n-particles[11]. TMM relies on the SWVF expansion of both the known incident field $\overrightarrow{U}_{inc}$ and the scattered field $\overrightarrow{U}_{scat}$, which has to be determined.

$$\begin{cases} \overrightarrow{U}_{inc} = \sum\limits_{n} \sum\limits_{m=-n}^{n} a_{mn} \overrightarrow{M}_{mn}^{(1)} + b_{mn} \overrightarrow{N}_{mn}^{(1)} \\ \overrightarrow{U}_{scat} = \sum\limits_{n} \sum\limits_{m=-n}^{n} f_{mn} \overrightarrow{M}_{mn}^{(3)} + g_{mn} \overrightarrow{N}_{mn}^{(3)} \end{cases} \tag{I.4}$$

Again, $\overrightarrow{M}_{mn}^{(1,3)}$ and $\overrightarrow{N}_{mn}^{(1,3)}$ are the SWVFs. The relationships between the coefficients of the expansion $(a, b, f, g)_{mn}$ are given by the T-matrix, calculated from the conditions at the interfaces of the particle (I.2).

$$\begin{pmatrix} a_{mn} \\ b_{mn} \end{pmatrix} = T \begin{pmatrix} f_{mn} \\ g_{mn} \end{pmatrix} \tag{I.5}$$

However, this rather computationally-heavy (but much faster than volume and surface EM numerical methods) method is becoming more and more used as computers become more and more powerful. A FORTRAN code developed by *Mishchenko et al.* in the public domain is available on the NASA-GISS website.

In addition, the case of clusters like Black-Carbon (BC) soot is briefly discussed. BC soot are known to be arranged in the form of fractal aggregates, that are usually generated procedurally, using aggregation models such as DLA [24], BCCA or BPCA [96][12] to cite only a few. The scattering properties of such fractal aggregates can then be computed using the arbitrary scattering calculators cited above or simplified models such as the mean field approximation of Mie's theory [97,98].

---

[10] This method is not be be confused with another TMM (extensively used in the literature), which stands for Transfer Matrix Method. The latter is refereed as the Abelès matrix method in this document (see, Appendix J).

[11] The TMM formalism can also be used to model the particle-light interaction for various illumination conditions, such as its coupling with resonant optical modes [**?**].

[12] DLA : Diffusion-limited aggregation, BCCA : Ballistic cluster-cluster aggregation, BPCA : Ballistic particle-cluster aggregation.

I.4 The stakes of miniaturized air quality sensors

I.4.1 Air quality monitoring: a new paradigm

In the classical model, air quality monitoring (PM, gaseous pollutants, relative humidity, *etc.*) is carried out by stations with expensive and bulky characterization instruments [99]. These stations are generally managed by state or city funded agencies. The data collected by these instruments allow precise characterization of the air quality where the station is located. The major disadvantage of such a model is that it does not allow the collection of pollution levels with sufficient spatial resolution (*e.g.* street-to-street air quality) and it does not allow the measurement of indoor air quality, which can be much worse than outdoors [17, 100, 101]. For example, the EEA (European Environment Agency) makes available interactive maps of the air quality index[13]. We can see for instance, that the air quality of most European middle-sized cities is monitored on the basis of only a couple stations per city. As air quality is becoming a major issue of concern, a new monitoring model is clearly needed.

With the emergence of connected on-board systems (IoT, Internet of Things) equipped with geolocalization modules, we see the possibility that a network of portable environmental sensors can measure pollution levels with high spatio-temporal resolution [102]. Such monitoring networks can also achieve great accuracy by sharing and correcting its measurements with data from weather conditions (humidity, temperature) [103] and measurements provided by climate monitoring satellites [104, 105] such as ESA's Sentinel constellation [106, 107] or NASA's EOS constellation [108]. Moreover, these data would be directly accessible to a user of such sensors, or an informed citizen. Using air quality map as in Figure I.11, the user could quantify, identify polluted areas (both indoor and outdoor) and then limit his personal exposure to pollutants.

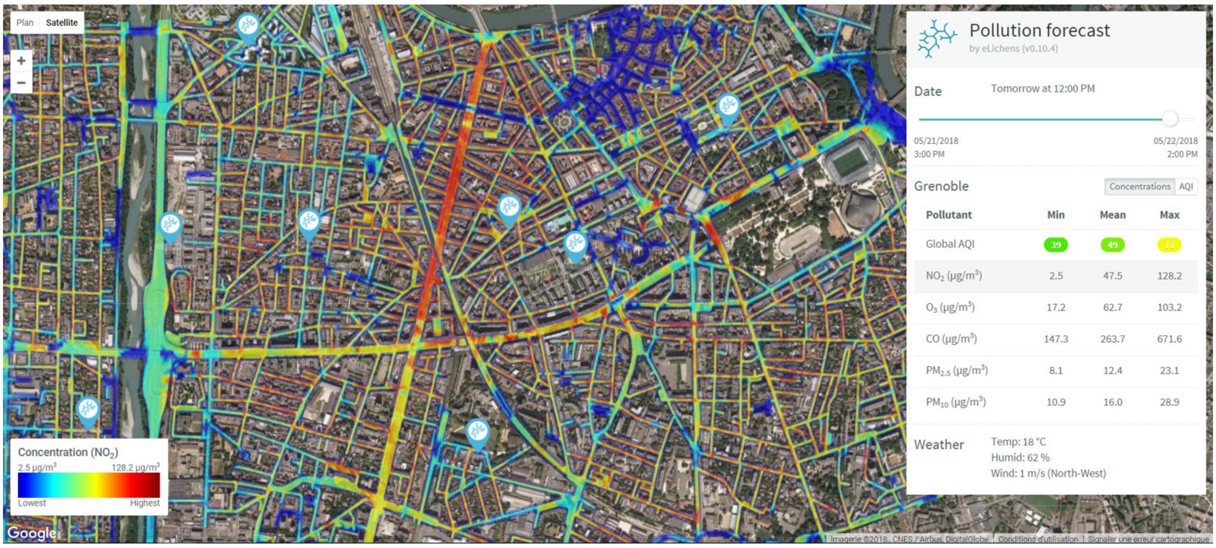

Pollution forecast
by eLichens (v0.10.4)

Date: Tomorrow at 12:00 PM
05/21/2018 3:00 PM
05/22/2018 2:00 PM

Grenoble
Concentrations | AQI

Pollutant	Min	Mean	Max
Global AQI	39	49	73
NO_2 (µg/m³)	2.5	47.5	128.2
O_3 (µg/m³)	17.2	62.7	103.2
CO (µg/m³)	147.3	263.7	671.6
$PM_{2.5}$ (µg/m³)	8.1	12.4	23.1
PM_{10} (µg/m³)	10.9	16.0	28.9

Weather
Temp: 18 °C
Humid: 62 %
Wind: 1 m/s (North-West)

Figure I.11: Air quality map of the city of Grenoble, France. Provided by eLichens.

However, an air quality monitoring model based on a broad sensor network is only possible with widely distributed sensors. Thus the clear need for low-cost, portable and personal air quality monitors [109, 110].

---

[13] Using an air quality index built upon the concentration of various pollutants.

I.4.2 A new generation of inexpensive, miniature PM sensors

We have seen previously, that optical sensors based on the light scattering phenomenon appears to be the best candidates for inexpensive systems thanks to their good sensitivity and simplicity [111]. Figure I.12 shows six low-cost PM2.5 sensors from the main manufacturers that came recently in the consumer marker. All six of those are based on the principle of light scattering.

Figure I.12: Photographs of six low-cost PM2.5 sensors from the main manufacturers with size and usual prices.

Those sensors are usually assembled from inexpensive electrical and optical components such as LEDs, photodetectors and molded optics. The circulation of air is generally generated by a fan. At the time of this manuscript preparation, such sensors suffers noticeable inaccuracies [112, 113] and soiling issues which limits their lifespan. Figure I.12 indicates the size of all six sensors, and their usual price. The main part of the manufacturing cost being assembly and packaging.

Those sensors should be seen as building blocks for low-cost and/or wearable air quality monitors and can be modified and integrated into full IoT systems [45, 105, 114]. A representative example amongst many is the Mobile Aerosol Reference Sampler (MARS), developed by Colorado State University, is a full system that comprises a commercial low-cost PM sensor (PMS5003, Plantower) disassembled and integrated along an air convection and filtering system and IoT systems such as a power unit, GPS, Bluetooth and Wi-Fi modules (see, Figure I.13).

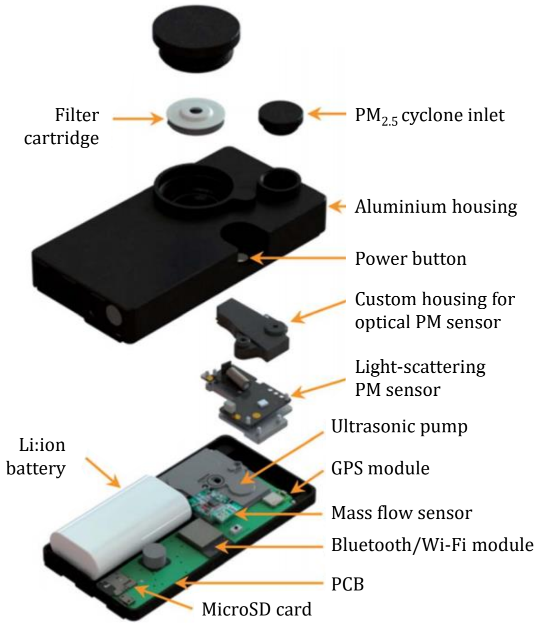

Figure I.13: Exploded view of the MARS key components (adapted from [45]).

For wearable devices, all elements should operate with a relatively small electrical consumption. In particular, this limits the optical power needed to illuminate particle to the milliwatt order of magnitude. Then, the read-out of the photo-detectors and the data processing should be kept as simple as possible.

However, the cost, reliability and energy consumption of PM2.5 and PM1 sensors could be greatly improved by taking steps toward the miniaturization and co-integration of the various elements.

I.4.3 *A future generation of integrated PM sensors*

Great efforts are being made within the scientific and technical communities to scale down optical light-scattering PM2.5 & PM1 sensors. It usually involves silicon microfabrication techniques and co-integration of optical, electro-optical elements and air micro-fluidics. The end goal being the full integration of a PM sensor *'on-a-chip'*.

However, in addition to the costs associated with the development of new clean room process flows, there are a number of challenges to be met. Indeed, it is necessary to design compact architectures (whose total footprint is of the order of a centimeter or even a millimeter), with rather planar geometries, compatible with silicon micro-fabrication methods and able to perform the same functions as the macroscopic systems implemented in current PM sensors. In particular, the geometrical dependencies of various physical functions (*e.g.* air convection, photometry, heat evacuation *etc.*), which are often not scalable, require new designs for integrated PM sensors.

For example, there have been many developments in air micro-fluidics, with the fabrication of planar circuits by deep etching of silicon, allowing for the controlled circulation of an aerosol[14]. For instance, silicon based Virtual Impactors (VI) allows to separate particles using inertial principles prior to the optical sensing unit [44]. Other works seek to sample air into channels, by the means of MEMS micro-pumps [115].

Next, optical and electro-optical elements could be co-integrated alongside fluidic parts. Those former elements are generally a light source, photodetectors and passive optics. This integration is in itself a great technical challenge (notably in terms of heterogeneous integration, thermal management, packaging and optical coupling) [116]. Then, another critical challenge is to manage stray light that may come from any scattering surface around the optical sensing area. Parasitic scattering is usually orders of magnitudes compared with the scattering from a single particle: it is the main limitation for sensitivity, causing a high signal to offset ratio. This is especially true for miniature systems with small geometries, because stray light sensitivity decrease with the inverse square of the distance between the scattering surface and the photodetector.

In Figure I.14, we provide three examples of integrated PM sensor designs found in the literature.

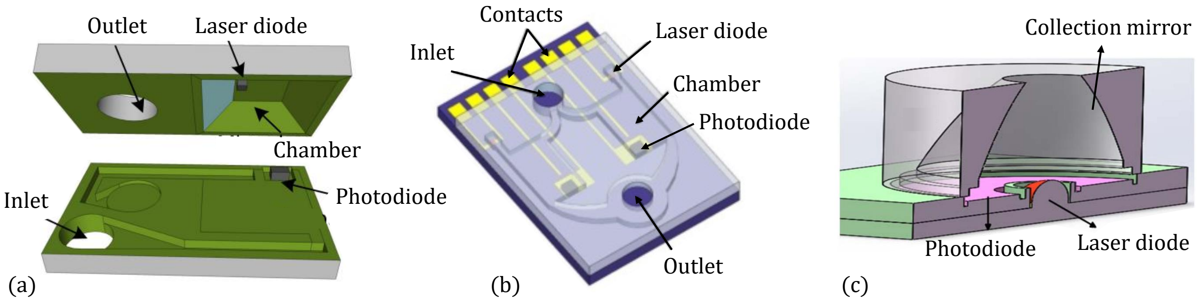

Figure I.14: *3D models of integrated PM sensors from (a) [117], (b) [118] and (c) [119].*

The design in subfigure (a), reported in reference [117], involves a silicon based fluidic system etched from two substrates. A laser diode and a photodetector are integrated separately on the two substrates before assembly. The next design shown in subfigure (c), reported in [118] involves a single electro-optic circuit, covered with a silicon air-microfluidic circuit. Finally, the third design from subfigure (c), reported in [119], features a electro-optic chip with a laser diode and a concentric ring photodetector. The scattered light for particles is collected by a concave mirror, which covers the electro-optic chip. As explained earlier, the sensitivity is mainly impacted by stray light in those PM sensors *'on-a-chip'*.

Even if the sate of the art is progressing very fast, the community has not converged yet toward an elite design, that surpasses others in terms of integration and specifications. During the preparation of this manuscript we have tried to explore other designs through various prototypes, in order to better identify difficulties and solutions.

---

[14] Note that, due to electrostatic charges usually carried by particles, channel walls should be made from a conductive material. This part forbids us to use PDMS based channels, extensively used in 'lab-on-chip' technology.

I.5 Positioning in regard to the state of the art

From the observation discussed in Section I.4, there is a clear need for the development of inexpensive and miniaturized PM2.5 and PM1 sensors targeted at the personal air quality monitoring and sensor network market applications. We will seek to take new steps in the development of tomorrow's miniaturized sensors in order to address this new need.

We rely on our background in CMOS technology and integrated photonics shared by both the CEA-Leti and the Institute of Nanotechnology of Lyon (INL). Moreover, developments on miniaturization and cost reduction of air quality sensors are the spearhead of the laboratory of optical sensors (LCO in french) [120], which already involves Non-Dispersive InfraRed gaz sensors [121], photoacoustic trace gaz sensors [122] and Volatile Organic Compounds sensors. We apply the same methodology to scale down PM sensors. In particular, our early designs involve planar chips fabricated using CMOS technology electro-optics and photonics with active components such as a light source and photodiodes, passive optics such as silicon-based waveguides and a vertical air channel drilled out of the chip. This design is described in one of our 2012 patents [123] (and redrawn in colour in Figure I.15), followed by several other patents [124–130].

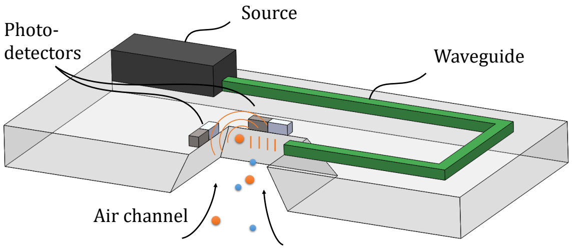

Figure I.15: Drawing of a photonic PM sensor 'on-a-chip' proposed by CEA-Leti (redrawn from [123]).

In this manuscript, we will propose three new miniature prototypes (see, Figure I.16) that aim to explore several architectures and identify both successful and unsuccessful design choices. Each prototype will be sequentially discussed in separate chapters: from Chapter II which starts by taking the firsts steps toward the miniaturization of a PM sensor through CMOS processing, with mature steps; gradually toward Chapter IV, we will explore future solutions that involve forward looking steps.

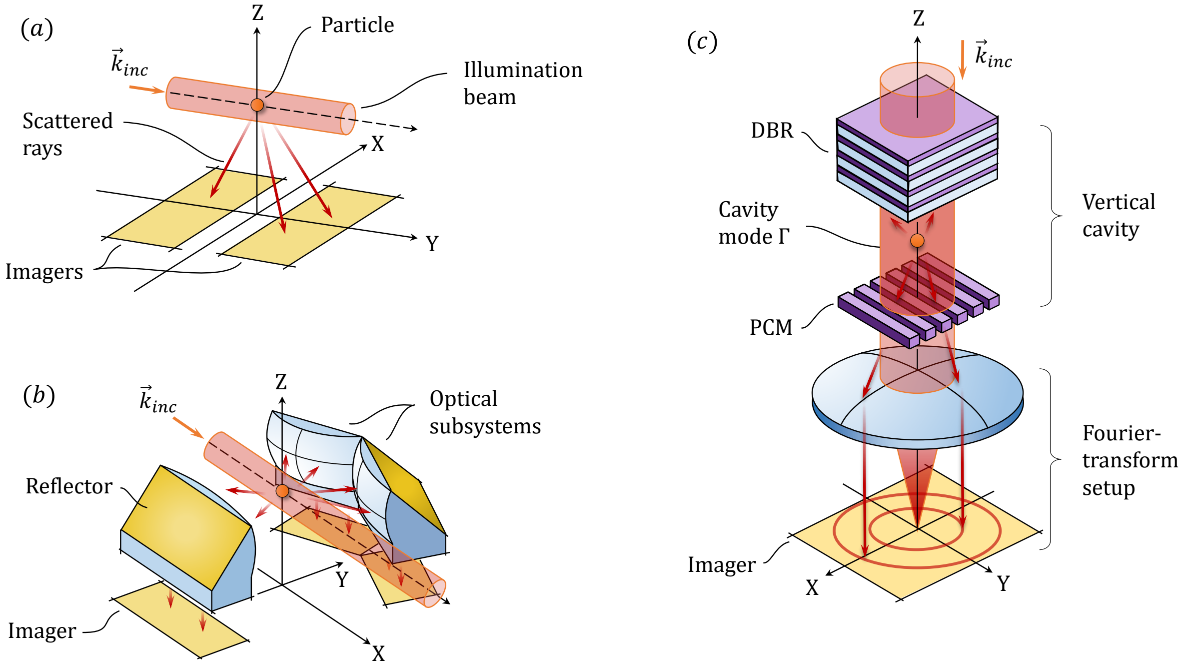

Figure I.16: Graphical presentation of the three prototypes (a,b,c) described in Chapter II, III and IV respectively.

As discussed in Section I.2, there are several possible architectures for optical PM sensors. However some appear more interesting than others and could be well suited for being implemented in miniaturized system. In particular, we want to implement in an OPC, a capability to record and analyze a scattering signature that is essential to characterize single particles. To do so, we describe in Chapter II a first prototype that can perform a lens-less imaging of a particle's scattering signature, building upon the developments on CMOS image sensors. Such a prototype is schematized in Figure I.16(a). Among the development made, we report the co-integration of a fluidic channel within the CMOS imager chip and the analysis of the recorded scattering signatures based on the Lorenz-Mie theory (see, Section I.3).

Then, we describe in Chapter III a prototype that aims to significantly improve the optical setup used to record scattering signatures. To do so, we have developed a miniature and monolithic lens assembly designed to perform an optical pre-processing of scattering signatures with a wide Field of View (FoV) of scattering angles, which is schematized in Figure I.16(b). A first improvement increase the accuracy of a particle's characterization by widening the evaluation of scattering signature. This improvement comes with an increase in sensitivity, by allowing to collect more scattered light. A second improvement reduces the computing cost used on image processing: this part was made through an optical pre-processing of the scattering signature in Fourier-domain. Indeed, energy consumption related to image processing is a critical part for on-board systems like those we target. The additional contributions associated with this second prototype are the exploration of a new approach concerning the design possibilities of miniature complex opto-fluidic assemblies with compact optical systems. We are working on making such optical systems possible by developing new manufacturing processes on glass. We hope that in the future, such optical pieces would be commonly coupled on top of CMOS optronic chips in the same fashion as photonic packaging methods.

Finally, a third prototype is described in Chapter IV: this last prototype aims to explore forward looking designs in order to pave the way toward future PM sensors. As energy consumption is a major factor for portable systems, we seek to lower the energy needed to power a light source. that is to say, we will seek to optimize the sensitivity of the sensor so that it can operate with very low optical intensities. Very good sensitivities will be sought, for example by means of optical cavities. Here we explore the cavity-enhanced PM sensors that uses vertical micro-cavities. The latter have already shown great promises in several fields such as VCSELS[15] or MOEMS[16] especially when using Photonic Crystal Membrane (PCM) reflectors. In this chapter, we will show a system that features a PCM-based Vertical Cavity (VC) that is deliberately perturbed by the presence of a particle within the cavity. Then we characterize such perturbator through transmission imaging. Such proposed method can be referred to imaging a cavity-perturbation scattering signature. It can use similar and updated image analysis procedures developed for the previous prototypes. Such a system is schematized in Figure I.16(c). Our work on this third prototype involves both a theoretical and experimental study of the optical behaviour of a PCM-based VC and especially its sensitivity to a particle-induced perturbation, as such system is poorly explored in the scientific literature.

---

[15] Vertical Cavity Surface Emitting Lasers.

[16] Micro Opto-Electro-Mechanical Systems.

I.6 Chapter conclusion

In this introduction, we hope we gave the reader an overview of the environmental and health issues posed by PM pollution (Section I.1), as well as the importance of having the capability to monitor and characterize ambient air quality. We have discussed the different sensing methods for this purpose, focusing in particular on optical PM sensors (Section I.2). The latter are particularly interesting as they can - by using reasonably simple architectures - measure PM concentrations as well as characterizing particles through the recording and analysis of scattering signatures. We have reviewed the most relevant theories used to predict those scattering signatures, such as the Lorenz-Mie theory (Section I.3), and discussed how they can be used to estimate both the size and the refractive index of a particle.

At a time when air quality degradation is becoming a major and global concern, we see that the monitoring of air quality is shifting toward the wide distribution of inexpensive, portable air quality monitors as opposed to conventional air quality stations. The need for this new generation of air quality sensors is being recently addressed by research institutions and industrial R&D research groups all over the world. The goal is to develop a miniaturized, fully integrated PM sensor (Section I.4).

In this manuscript, we propose three prototypes with different levels of maturity. Each prototype helps solving challenges encountered while scaling down PM sensors (new designs for stray-light management, integrated photonics, air micro-fluidics *etc.*) by exploring different designs, in order to identify sucessful and unsucessful setups. Chapter II aims to take step toward the miniaturization of PM counters and analyzer using CMOS technology. Chapter III proposes an implementation of a miniature optical piece using innovative designs and new manufacturing techniques. Finally, Chapter IV describes a novel architecture designed to enhance the sensitivity of the sensor compared with cavity free setups, while allowing a new way to analyze scattered light from a particle.

II

Lens-less imaging of scattering signatures with a holed retina

Chapter content

II.1 Architecture of the sensor

II.1.1 General overview of the architecture

In this chapter, we present a miniaturized PM counter and analyzer that is able to measure the 'light scattering signature' (angular scattering efficiency) of a single particle using a lens-less imaging setup [131]. The principle of lens-less projection of a scattering signature is presented in Figure II.1.

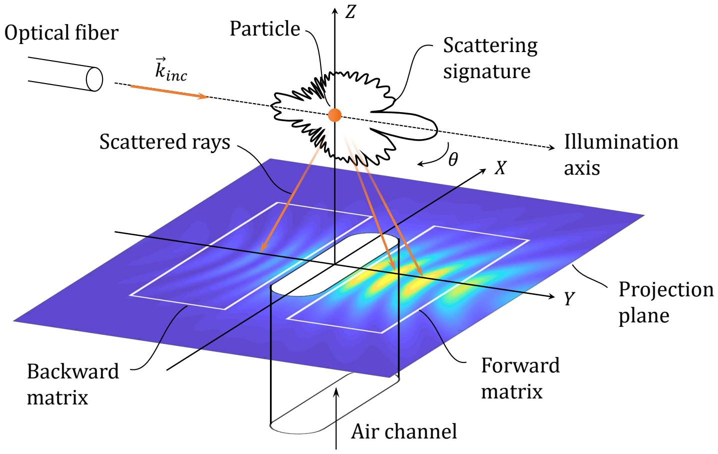

Figure II.1: *Illustration of the lens-less projection of a scattering signature.*

As previously explained in Section I.2, this technique is designed to be able to estimate the diameter and the refractive index of a particle, using light-scattering descriptions such as the Lorenz-Mie theory for spherical particles (see, Section I.3). We present in Figure II.2, a schematic rendering of the architecture of the sensor.

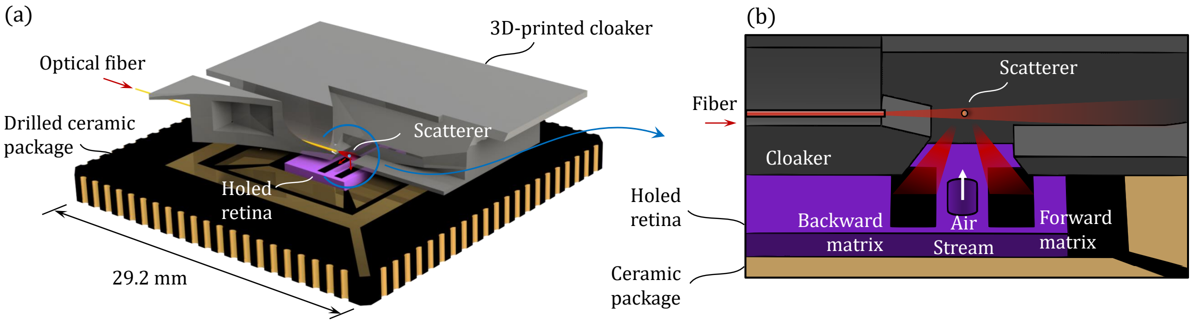

Figure II.2: *(a) Architecture of the sensor (partial cross-sectional view). (b) Close up view of the sampling region.*

The device is composed of a specifically designed CMOS imager chip (see, Section II.1.2) that is drilled at wafer level to create a vertical fluidic channel (see, Section II.1.3). This opto-fluidic chip, we call a 'holed retina' is mounted on a holed ceramic and driven by an electronic board (see, Section II.1.4). Particles are illuminated by the light beam formed by a lensed fiber placed nearby the muzzle of the channel. The fiber is mounted onto a multipurpose 3D-printed piece we call a 'cloaker', that prevents stray light from blooming the retina (see, Section II.1.5). Finally, we measure a lens-less projection of the scattered signature of a single particle on the holed retina.

II.1.2 Dual matrixes global shutter imager chip

We have developed a CMOS imager chip customized for our special requirements [132], as explained later, our unusual design will allow us to drill a hole through the chip to form the fluidic channel [124]. Our chip was modified from the CreaPYX standard platform proposed by the Pyxalis company [133]. The former is designed in a prototyping fashion: flexible and quickly modifiable with little cost and effort.

We present the layout in Figure II.3(a). The imager is composed of a classic frame part and an uncommon dual matrix core part. This core part has two detection areas ('forward' and 'backward matrix') separated by a central blind area. These matrixes are labelled according to the direction of the scattered light they assess: forward scattering and backscattering. Both matrixes are sized by 75×281 pixels, with a pitch of $p_{pix} = 10$ µm. The blind area between the two detection matrixes is sized by 2160 µm × 660 µm (rectangular profile) and is made free of pixels or metallic lines (and thus, ready to be drilled).

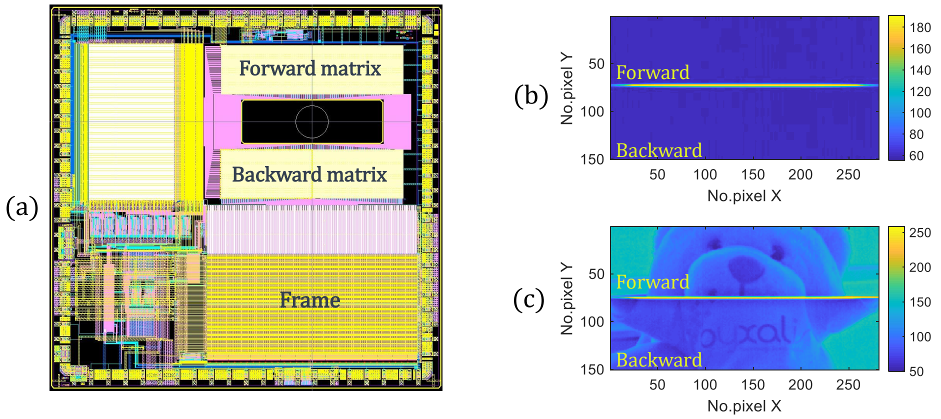

Figure II.3: (a) Imager chip layout. Image example in (b) flat-field mode and (c) focus mode.

We show examples of images obtained in flat-field and focus modes in subfigures II.3(b) and (c) respectively. X and Y labels are the pixel numbers, all the following images will be presented with this format, lines from 1 to 75 and lines from 76 to 150 correspond respectively to the forward and backward matrixes. We observe saturated hot pixels at the internal edges (central bright lines), caused by a higher Dark Current (DC). For the image processing, we simply ignore these eight defective lines.

The pixel is designed with a 2 gains high dynamic range, 5T architecture allowing a low noise Global-Shutter (GS) readout procedure [134]. Unlike the common Rolling Shutter (RS) mode where each line is captured sequentially, GS mode allows to capture the full image simultaneously. Since the particle is moving, the latter mode is essential to prevent motion blurring or distortion of the image. The Charge-to-Voltage conversion Factor (CVF) is 120 $\mu V/e^-$ in high gain mode and the gain is 45 µV/ADU (Analog to Digital Unit). In GS mode, the minimal integration time is $t_{int} = 76.8$ µs, longer integration time will be multiples of this minimal time, as it is the duration needed to read a full image[1]. The external Quantum Efficiency (QE) is 57% at 637 nm, and drops to 22% at 850 nm. Such pixel design is well suited for capturing low intensity scattering signatures with good sensitivity.

Note that the chip is a front-side imager. A back-side imager would be more interesting for our application because it has a better angular acceptance[2]. Nevertheless, we prefer to use the former as it is about three times cheaper than the latter: price reduction remains the main goal of this chapter's prototype.

---

[1] In the following, a given integration time is implicitly the closest multiple of the minimal integration time.

[2] We will discuss the angular acceptance of a front-side imager later, in Section II.2.

II.1.3 Post-process

The imager chips were fabricated on 200 mm silicon wafers that were supplied from a shuttle run (multi-project wafer) of an undisclosed, advanced CMOS manufacturing fab (see, Figure II.4). Then, we have developed a post-process in our in-house 200 mm MEMS foundry to drill the components at wafer scale [132]. The drilling post-process should use conventional micro-fabrication technologies that are widely used today in industrial micro-fabrication platforms. By doing so, such a post-process can be efficiently transferred to an industrial foundry, which can then manufacture the sensors in volume production.

The layout includes an alignment mark for our lithography steps. An external seal ring is commonly used around the chip. Here, we also added an internal seal ring around the hole area designed to protect the matrix of photodetectors during the drilling process.

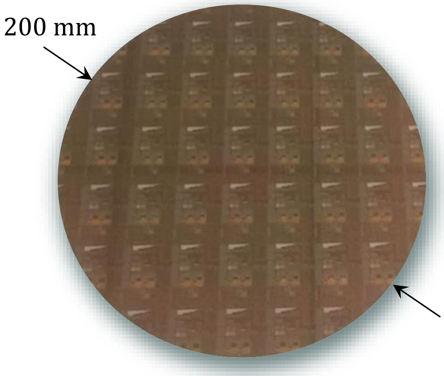

Figure II.4: *Photography of a* 200 mm *wafer containing our custom imagers.*

The first step concerns a front-side process that etches the multilayer passivation with an oblong profile (2 mm×0.5 mm). To do so, we use a C_4F_8/CO plasma process in a Reactive Ion Etching (RIE) reactor. We finalize the etching of the air channel by a backside process. We deposit a few microns of oxide hard mask by PECVD (Plasma-Enhanced Chemical Vapor Deposition) and use a contact photolithography on a positive resin to pattern the oblong profile. In order to achieve a fast, deep anisotropic etching of 725 µm, we use an Inductively Coupled Plasma-Deep Reactive Ion Etching (ICP-DRIE) [135]. The ICP reactor is widely used for anisotropic silicon etching because it maintains vertical sidewalls with high aspect ratio. In our case, a standard Bosch process (cyclic isotropic etching with SF_6 gaz followed by C_4F_8 plasma) is sufficient to obtain a straight profile as our aspect ratio $AR = 1.45$ is sufficiently small. We present the final holed retina in Figure II.5.

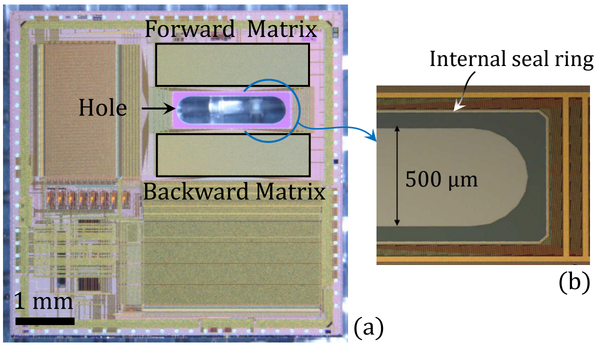

Figure II.5: *Images of the fabricated holed retina. (a) Optical view of the chip. (b) Optical view zoomed on the hole.*

We will simply use the term DRIE to refer to this etching process. Figure II.5(b) shows an optical image of the hole, suggesting the high quality of the DRIE process. Alternatively, first trials[3] have demonstrated that it is also possible to form the fluidic channel at wafer level using an ablative laser process and still get functional CMOS sensors.

Both the SEM and DC studies validates the post-process. That is to say that it allowed to form a channel, while allowing a good functioning of the retina.

---

[3] The results were obtained only on a first trial and on a few samples in this work and the process could be significantly improved if necessary.

Figure II.6 shows tilted Scanning Electron Microscope (SEM) images as well as optical images of the hole fabricated with both techniques. Comparing subfigure II.6(a) and (b) shows that the sidewalls roughness is much more important with the laser ablation technique. Note that the roughness has no impact on our application. We also observe on subfigure II.6(c) that some burned residues of the protective resin could not be removed by standard acetone solvent spraying.

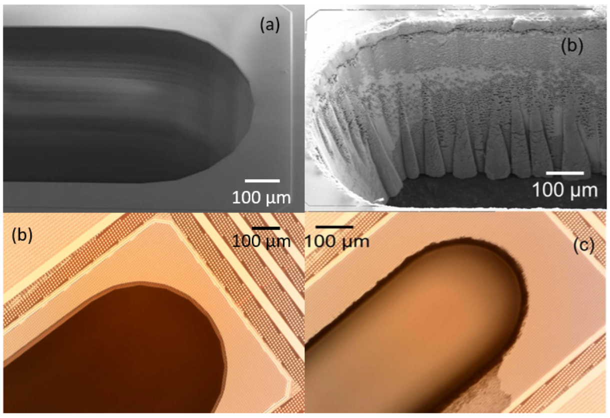

Figure II.6: Comparison of drilled hole obtained by DRIE or laser technology. (a,d) SEM and microscopy view of DRIE process. (b,c) SEM and microscopy view of Laser process.

In order to estimate the impact of the post process on the Dark Current (DC) of the image sensor, we made DC maps before (Figure II.7(a)) and after the post-process (Figure II.7(b)). We acquire dark images for increasing integration time $I_d(t_{int})$ expressed in ADU (AnalogToDigitalUnit). We can obtain a DC map by taking the slope map $DC = dI_d/dt_{int}$ expressed in ADU/ms.

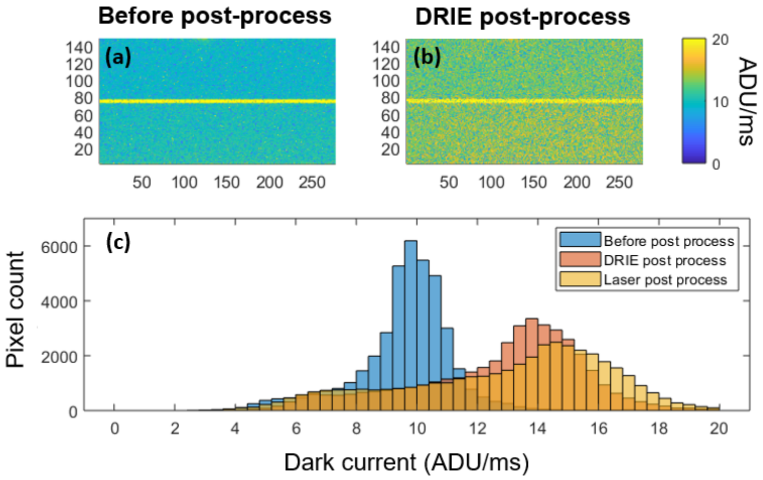

Figure II.7: Cartography of the dark current (in ADU/ms) before (a) and after (b) the drilling post-process, and associated histograms (c).

Histograms in Figure II.7(c) show that the drilling post-process have increased the DC level by about 30 % in a similar way for both drilling techniques (DRIE and laser ablation). Fortunately, there is no evidence of gradient in noise distribution: the post-process didn't increase the DC in the vicinity of the drilled area. We will see in the following that the chip is packaged on a drilled ceramic carrier, which reduces the cooling surface of the CMOS: this may be an explanation for the increase in DC. Finally, we should emphasize that the DC increase is not a critical parameter for our application because we use short integration time. Indeed, the readout noise remains predominant compared with the DC for short integrating time.

II.1.4 Packaging and fluidics

The chip was wire-bonded (ball bonding) to a ceramic carrier (see, Figure II.8(a)). The device, in the state in which it is described in this chapter, has exposed wires. In the meantime, we have developed a glob-top (insulating silicone rubber) process to protect these wires. This step makes the device more robust to external conditions, especially when it comes to detecting aqueous particles, which can wet around the wires.

We have drilled a circular hole (2 mm diameter) through the thickness of the ceramic, which is larger than the hole of the silicon chip (0.5 mm × 2 mm oblong profile). Such fluidic profile eases the convection of the air flow through the channel and creates a flow acceleration at the channel restriction (flowing from the larger ceramic hole to the smaller silicon hole) by a Venturi effect, Figure II.8(b). The ceramic is clipped, with full contact on the socket of the driving motherboard (CreaPYX test platform [133]).

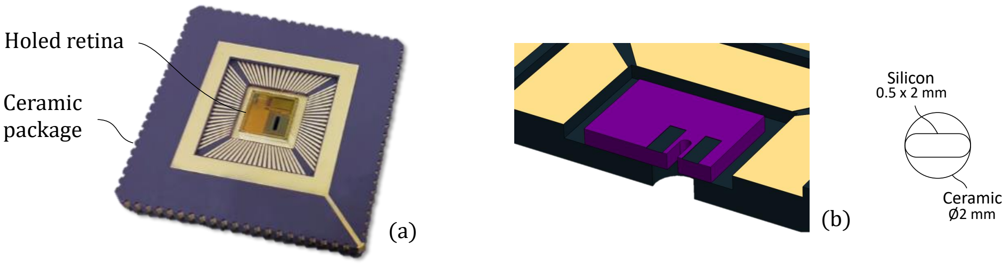

Figure II.8: (a) Photography of the holed retina bonded on the ceramic carrier. (b) Cross-sectionnal view of the channel

The footprint of the system is limited by the size of the ceramic carrier (29.2 mm, square) while the size of the silicon chip is only 6 mm × 5.9 mm. Future packaging of this sensor will include direct bonding of the CMOS chip onto PCB to reduce the footprint. The driving hardware could be performed by an ASIC (Application Specific Integrated Circuit). Compact packaging should include a compact convection system that uses a miniature fan. We can also optimize the fluidic set up by designing a nozzle-like channel profile to concentrate the beam of particles while speeding them.

II.1.5 Optical setup

We illuminate a detection volume nearby the muzzle of the channel at a good proximity of $L \simeq 1.5$ mm between the optical axis and the retina. This proximity allows for a good sensitivity to scattered light (as the scattered intensity decreases with the inverse square of the viewing distance) and a quite wide Field of View (FoV) of scattering angles. The illumination beam is shaped by a Single Mode (SM) optical fiber terminated by a GRIN lens. The beam, thus obtained has a very low numerical aperture of $NA = 0.02$. The fiber is connected to a visible light source ($\lambda = 635$ nm, SLED from EXALOS), delivering the optical power $P_{inc} = 1$ mW at the fiber output. We have selected this wavelength because it shows the best compromise between the scattering efficiency, the cost of the sources and the external Quantum Efficiency (QE) of our pixel. Figure II.9 illustrates the optical setup.

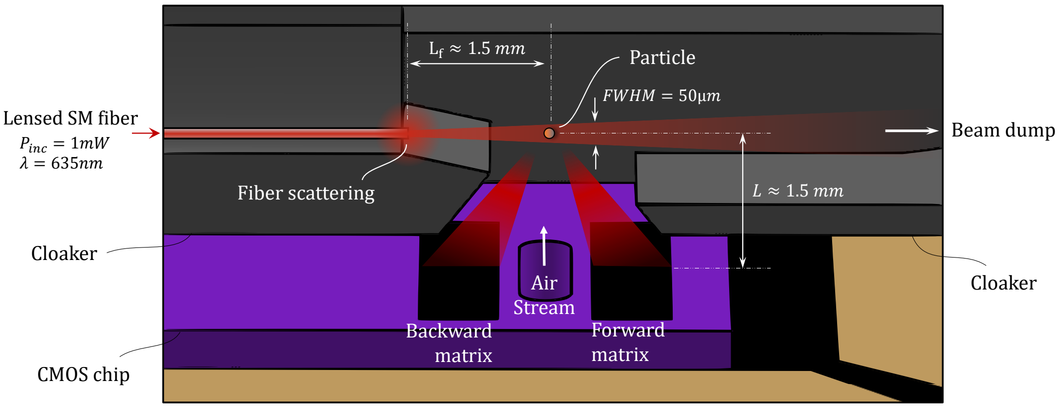

Figure II.9: Schematic of the optical setup (partial cross-sectionnal view).

The optical fiber is aligned and mounted on a multipurpose 3D-printed piece we call a 'cloaker', which primary purpose is to protect the retina from stray light as much as possible. In particular, scattered light from the output of the optical fiber can easily bloom the retina, making the sensor completely dazzled and thus blind to scattered light from particles.
The cloaker is fabricated with a high-resolution (25 µm voxel) SLA (Stereo-Lithography Apparatus) 3D printer (Form 2 printer by Formlabs), using a black photopolymer resin. Figure II.10 shows a photography of the cloaker side by side with its 3D model.

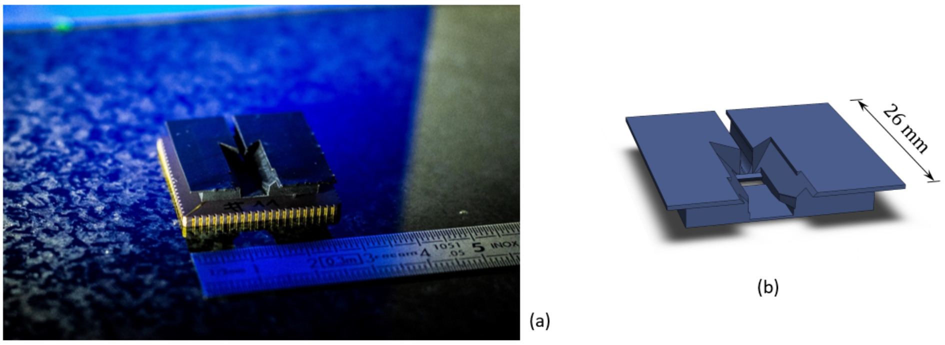

Figure II.10: (a) Photography of the chip mounted on ceramic with the cloaker. (b) 3D model of the cloaker.

II.2 Analytical modeling of the lens free projection

II.2.1 Generalities and definitions

The output of the fluidic channel (along Z axis) is illuminated by a light beam ($\overrightarrow{k}_{inc}$ wavevector) at a short distance of the retina ($L \simeq 1.5$ mm) (see, Figure II.11(a)). To calculate the scattering of the incident light by the particle, the Lorenz-Mie theory is used locally, this is an electromagnetic description where the particle is spherical and illuminated by a plane wave. Then, a near-field/far-field transformation is performed so that scattered light can be considered as rays. In alternate models, other theories can be used instead (see, Section I.3). These scattered rays are cast from the position of the particle (now considered punctual) and projected onto the retina under a scattering angle θ. The signature is carried along perpendicular trajectories[4] to what we call 'iso-θ', meaning 'the curve where all the pixels are illuminated under the same scattering angle'. In the case of a planar projection parallel to the optical axis of illumination, which corresponds to our configuration, the 'iso-θ' are hyperbolae as shown in the calculated scattering angles map in Figure II.11(b).

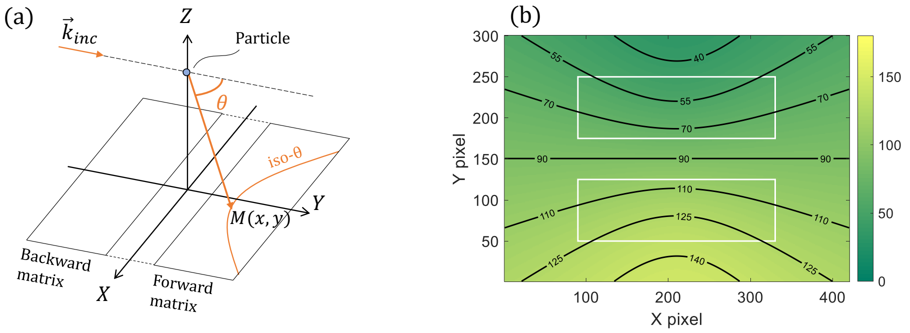

Figure II.11: (a) Schematic of the scattering projection. (b) Calculated map of projected scattering angles (in degrees).

The white rectangles correspond to the 'forward' and 'backward' detection areas where we can evaluate the scattering signatures. As a recall, each matrix is 2.81 mm × 0.75 mm. We abusively define the FoV as the range of evaluated scattering angles. In this case, each submatrix can evaluate scattering signatures within a FoV of about 25 degrees, perpendicular to the iso-θ.

II.2.2 Radiometric model

In Figure II.12, we present the calculated projection for the 4 µm, 0.9 µm and 0.2 µm PSL (PolyStyrene Latex). Those specific cases were already presented in Figure I.10.

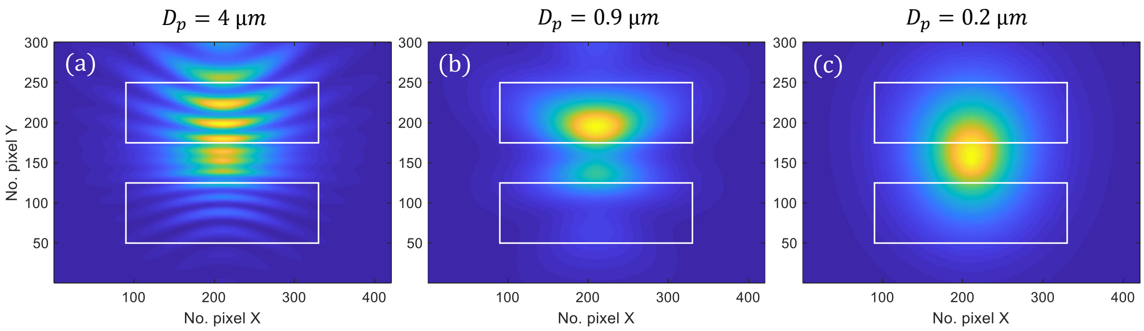

Figure II.12: Calculated planar projection of scattering signatures for particle diameters of (a) 4 µm, (b) 0.9 µm and (c) and 0.2 µm.

---

[4] A trajectory that is normal to the iso-θ is the trajectory that have the steepest gradient in terms of the scattering angle θ: meaning that those trajectories evaluates a wide range of scattering angles.

As before, white rectangles correspond to the imaging regions defined by the 'forward' and 'backward' matrixes. We observe that the lobes seen in the scattering signature are projected into luminous arcs that follow the 'iso-θ' hyperbolae. For simplicity, 'iso-θ' will now refer only to maxima and minima of theses hyperbolae. These projections well justify the relevance of the planar projection technique for scattering signature analysis as we can see a clear difference between the three images.

We describe a radiometric model where the particle is considered as a punctual source with an intensity that varies along the scattering angle, accordingly to a calculated scattering signature (see, Lorenz-Mie theory [82]).

First, we normalize such an unpolarized scattering signature $S(\theta)$ by integration over the whole sphere, such as:

$$\int_{\phi=0}^{2\pi}\int_{\theta=0}^{\pi}|S(\theta)|^2\sin\theta d\theta d\phi = 4\pi \tag{II.1}$$

The angle dependent scattered intensity (in W/sr) is given by the function $W_{scat}\cdot|S(\theta)|^2$, where W_{scat} is the total scattered power (in W). Spherical angles θ and ϕ are defined in Figure II.13.

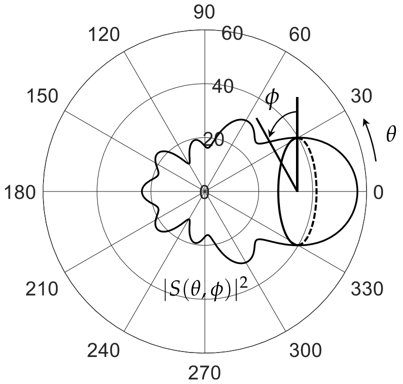

Figure II.13: *Definition of θ (polar) and ϕ (azimuthal) angles on a scattering signature.*

Second, we need to determine the intensity seen by each pixel of the retina as a function of the scattering angle. We can evaluate the scattering angle θ (and ϕ, if the signature do not exhibit an azimuthal symmetry) captured by every pixel of the retina, according to the geometry of Figure II.14.

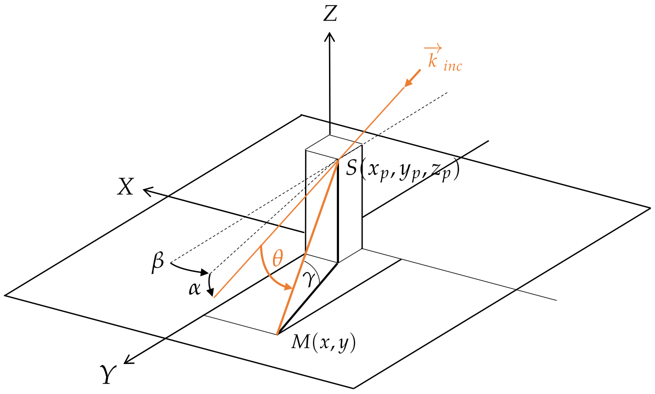

Figure II.14: *Geometry of the projection.*

In our model, the particle can have a certain position $S(x_p, y_p, z_p)$ contained within the volume of the channel and the light beam. The optical axis can be misaligned with respect to Y axis by angles (α,β)[5] delimited by the divergence of the light beam.

For a point $M(x,y)$ in the retina (centered on a pixel), we calculate the associated scattering angle θ and the vignette angle γ (and optionally, the azimuthal angle ϕ). To do so, we define a new set of coordinates (x', y') for the retina transformed with translation by (x_p, y_p) and rotation by β. If $\alpha = 0$ (parallel projection), the associated scattering angle is:

$$\theta(x,y) = \text{acos}\frac{y'}{SM} = \text{acos}\frac{(y-y_p)\cos\beta + (x-x_p)\sin\beta}{\sqrt{(x-x_p)^2+(y-y_p)^2+z_p^2}} \tag{II.2}$$

---

[5] Pitch and yaw, respectively.

Where, SM is the optical length. The case where $\alpha \neq 0$ is not discussed here, if the reader wants to solve this case, here are some hints: the optical axis can, in this case, intersect the plane (x', y') at a point F. Then, the angle θ, can be found by solving the SFM triangle using the Al-Kashi theorem.

The case where there is no azimuthal symmetry of the scattering signature[6] will not be discussed in much detail. In this case, the signature $S(\theta, \phi)$ will have to be considered and both θ and ϕ will have to be calculated for each pixel position $M(x, y)$. In the case where $\alpha = 0$ (parallel projection, only case discussed here), the azimuthal angle ϕ is written:

$$\phi(x,y) = \pi + \mathrm{atan}\frac{x'}{z_p} = \mathrm{atan}\frac{(x-x_p)\cos\beta + (y-y_p)\sin\beta}{z_p} \tag{II.3}$$

The vignette angle γ is independent of the misalignment angles of the illumination axis. It is simply written

$$\gamma(x,y) = \mathrm{atan}\frac{z_p}{\sqrt{(x-x_p)^2 + (y-y_p)^2}} \tag{II.4}$$

We define $\Omega(x, y)$ as the solid angle associated to the pixel centered on $M(x, y)$ (see, Figure II.15), explicit expression is:

$$\Omega(x,y) = \frac{FF \cdot (p_{pix} \cdot \sin(\gamma))^2}{SM^2} \tag{II.5}$$

Where p_{pix} is the pixel's pitch and FF its filling factor. This solid angle is sometimes abusively referred to as IFoV, which stands for Instantaneous Field of View.

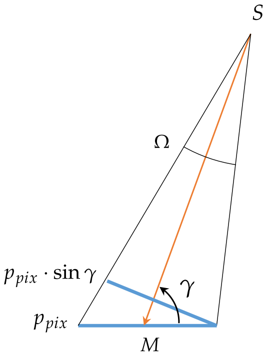

Figure II.15: Pixel's surface seen under the vignette angle γ.

Another source of vignetting is the angular response of a buried photodiode, denoted $T(\gamma)$. This function can be measured or modelled using reference [136] (see, Figure II.16(a)). This simple geometrical model, is applicable to front-illuminated pixels like the one we've developed. It can be used as a first approximation to model such a pixel. The considered pixel has a 10 µm wide photodiode, buried under a silica tunnel of refractive index $n_s = 1.45$ and thickness $h = 4.9$ µm, with a passivation layer made of silicon nitride[7] of refractive index $n_p = 1.88$. We give in Figure II.16(b) the modelled angular transmission of the considered pixel.

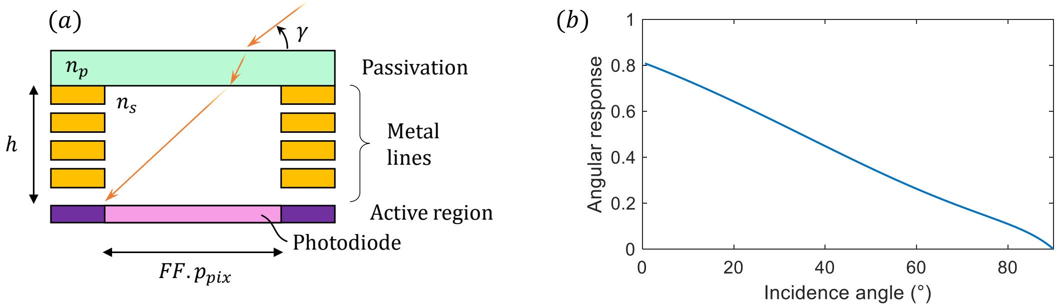

Figure II.16: (a) Cross sectional schematic of a buried pixel, redrawn from [136]. (b) Angular response model.

Note that calculating the angular response with this model is not ideal, it would be better to directly implement angular response measurements. Although this measurement requires a specialized test

---

[6] Such a scenario is to be considered when the particle is illuminated in non-polarized light and when the particle is not rotationally symmetrical along the illumination axis.

[7] The thickness of silicon nitride is not useful for this model.

bench we do not have access to at the moment. Finally, the intensity received by the pixel centered on $M(x,y)$ corrected by the pixel angular response and the solid angle is given by:

$$I(x,y) = T(\gamma(x,y)) \cdot W_{scat} \cdot \mid S(\theta) \mid^2 \cdot \Omega(x,y) \tag{II.6}$$

The projections we obtained have been compared with ray-tracing (RT) simulations (Zemax Optic Studio) coupled with the Lorenz-Mie theory (far-field). Here, we use a point source with a angle-dependent intensity imported from a computed particle scattering signature. In Figure II.17, we compare the result of the two projection methods obtained from the same computed signature (4 µm PSL).

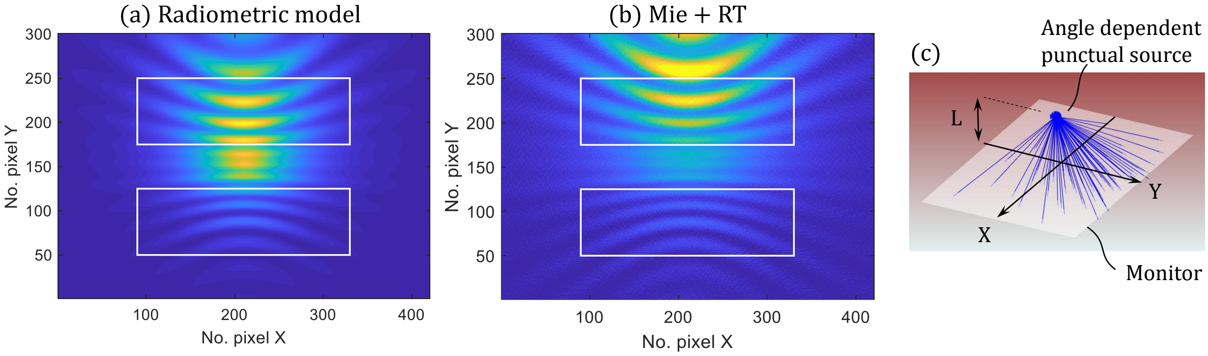

Figure II.17: Projection of a 4 µm PSL calculated with (a) the radiometric model and (b) a RT simulation. (c) 3D-view of the RT simulation window.

Those two projection methods lead to matching results. However, we must note that the vignette effects differ from the different methods: the RT method didn't take into account the angular response of pixels while our model uses an angular response calculated from a simplified geometry of the pixel, which is not ideal. Note that the radiometric model took 0.163 second to compute the image[8] while the RT simulation took 18.891 seconds using the same computer, which is 136 times faster. Indeed, the RT simulation have traced 5×10^6 rays (and still gets a noisy image) while the model only calculated the irradiance of $300 \times 420 = 126000$ pixels (one 'ray' per pixel). Thus, one can argue that such model could be well suited to be implemented in an optimization procedure where it should be called repeatedly (see, Section II.1.3).

---

[8] The model can be optimized to be even faster.

II.3 Characterization results

II.3.1 Experimental setup and protocol

We generate a controlled flow of particles using a calibrated aerosol dispenser (see, Appendix D). For the particles, we use calibrated laboratory particles (PSL from MagSphere) with monodisperse distribution of particle diameter. These particles are diluted in ultra-pure water solutions, one solution per diameter. The concentration of each solution is chosen in order to detect one particle at a time in our experimental setup (see below).

A portion of the particle flow is directed toward a reference sensor (APS Spectrometer 3321 by TSI) while the rest is sent to our sensor under test, via a silicone tube, with a flow rate of 0.8 L/min. The silicone tube is plugged onto the back of the holed ceramic so that the aerosol flow can traverse through the entire holed device toward the illumination beam (see, Figure II.18). Illuminated particles can scatter light onto the two detection matrixes.

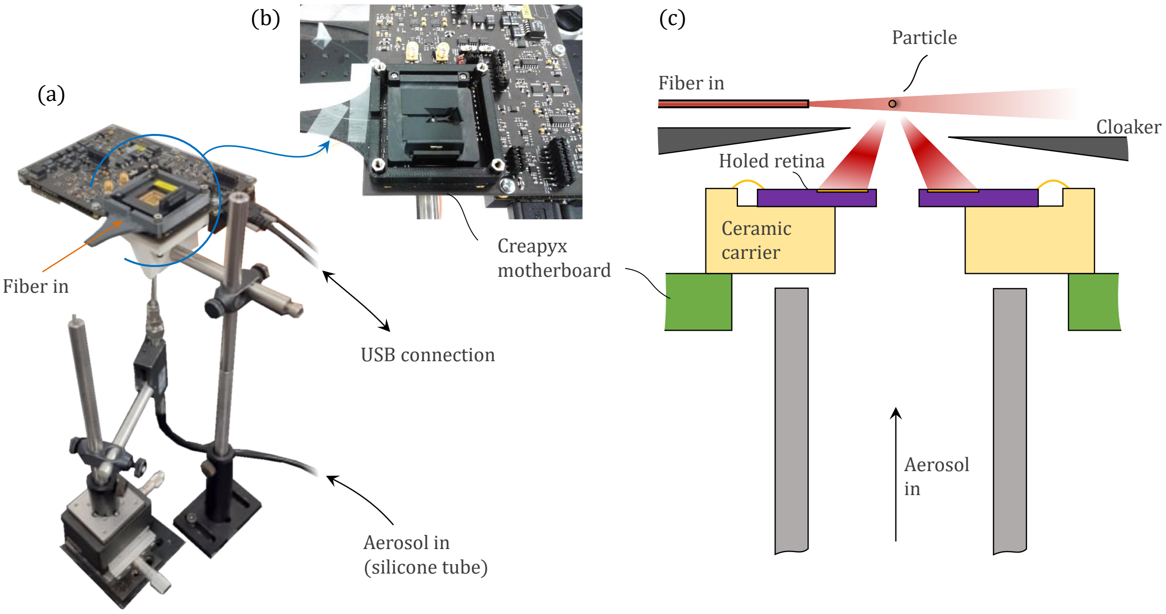

Figure II.18: (a) Photography of the experimental setup. (b) Zoomed view. (c) Schematic cross sectional view (not to scale).

We record the projected scattering signatures using the CreaPYX electronic board [133]. This driving board is interfaced with a standard PC through a USB connection and controlled with a tailored driving software. All images are integrated over time $t_{int} = 5$ ms and automatically subtracted with a background image, which was previously recorded with no particle in the illumination beam.

The electronic board allows for the collection of a pack of 32 images in burst mode (*i.e.* with maximal frame rate) before transferring this pack to the computer and collecting a new burst. Each pack is automatically analyzed with a home-made routine, which consists in a threshold detection, as illustrated in Figure II.19.

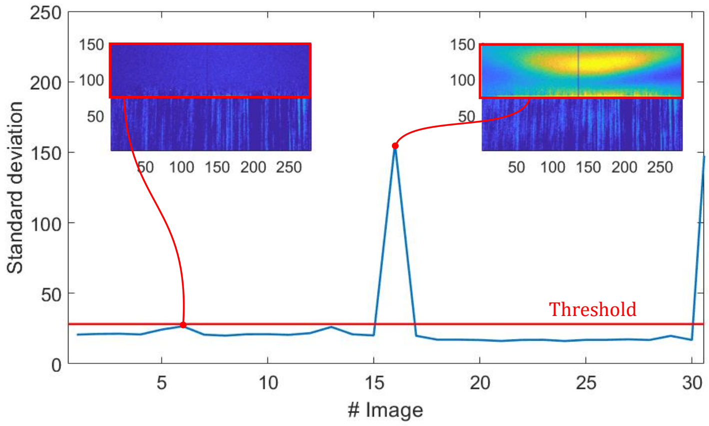

Figure II.19: *Example of threshold detection of a single particle.*

We monitor the standard deviation of the forward matrix of each image. When no particle crosses the optical beam, the standard deviation remains under the threshold value set by the user. If the threshold is reached, then it is likely that a particle was detected. The corresponding image is saved for subsequent image processing.

II.3.2 Experimental signatures

We routinely collect bursts of images for different particle concentrations and different PSL diameters. To illustrate the various signatures measured, we present in subfigures II.20(1), a set of four representative signature measurements corresponding to 4 different PSL diameters.

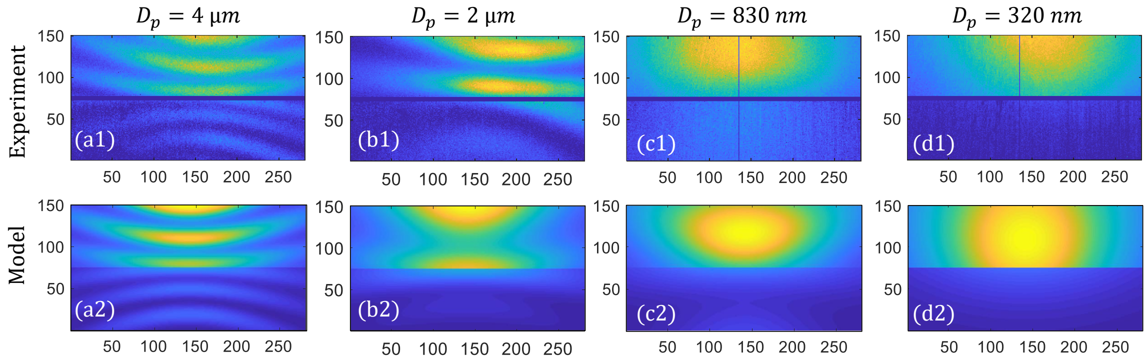

Figure II.20: *(1) Experimental signatures compared with (2) modeled signatures of four PSL diameters: (a)* 4 µm, *(b)* 2 µm, *(c)* 830 nm, *(d)* 320 nm.

We can see, in Figure II.20, important signature variations with respect to the particle diameter: for small particles (compared to the wavelength), the signature appears spherical as in subfigure (d). Then, as the PSL diameters increases, the forward projected pattern takes an elliptical shape (subfigure (c)) and divides into an increasing number of iso-θ. For particles of a few wavelengths in diameter, the backward matrix starts collecting useful information, in the form of iso-θ (subfigure (a) and (b)). These observations are consistent with our model's predictions[9]: these signatures are compared with

---

[9] The characterizations presented were performed with calibrated laboratory particles that show scattering patterns that are in great accordance with the Lorenz-Mie theory. In ambient air conditions, most particles have irregular shape and will most likely scatter light in different ways. The model will have to be modified using other theories to predict the scattering behavior of irregular particles (see, Section I.3.3).

modelled ones (subfigures II.20(2)), with default parameters (no diameter or refractive index fit, centered scatterers). Fitting modelled signatures with experimental images will be discussed in Section II.4.

It is noteworthy that the detection of a single submicronic particle down to $D_p = 320$ nm is possible. To go further, it is very likely that smaller PSL could be detected, nevertheless their signature would be very similar to the one of PSL 320 nm. Indeed, for small particles, the iso-θ can't be seen anymore (however we can still evaluate the ratio of the forward/backward intensity).

The use of a shorter illumination wavelength could be a way to bring back iso-θ to smaller diameters in addition to allowing greater sensitivity. For small particles, in the approximation of Rayleigh's dipolar scattering [73], the scattering efficiency varies in D_p^6/λ^4. We understand that scattering effects drops rapidly with particle's diameter, and that we could compensate this effect by using a shorter wavelength, with more important ratios.

II.3.3 Overall scattered intensity

All images were normalized. Indeed, one of the main experimental difficulties we encountered is the important variability of the signatures obtained for each diameter of PSL. In our experimental setup, the position and velocity of a particle when it crosses the optical beam can vary. This results in a translation of the signature along the optical axis (see, Appendix II.4) or a variation of the overall scattering intensity.

A similar sensor (described in Appendix C.2) shows a slightly better repeatability thanks to a longer fluidic channel. We were able to plot statistical data of scattered intensity versus the PSL diameter (see, Figure II.21).

Figure II.21 shows the overall intensity of images obtained with three monodisperse samples of PSL with different diameters. Vertical error bars express the experimental standard deviation (showing the variability of intensity), horizontal error bars express the diameter dispersion of our PSL samples. As a comparison, we plot in the same graph, for each particle diameter, the intensity of computed images[a]. Noteworthy, peaks that appear in the modelled curve must not be interpreted as noise: these are Mie's resonances.

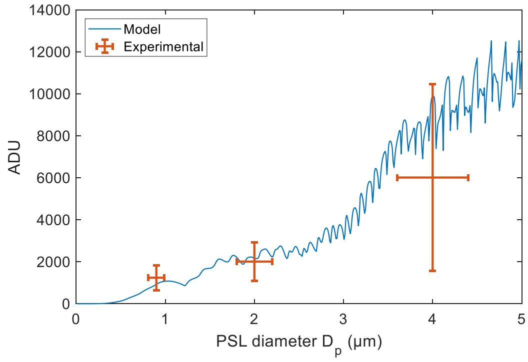

Figure II.21: Intensity vs. PSL Diameter from model and experimental data.

For this alternative sensor, an increase in intensity is observed with the size of the particle, even if the error bars are very large. For this chapter's prototype, the intensity variations are such that no graph could even be drawn. A way to improve this part is to implement better particle guiding channels, with possibly particle focusing features such as nozzles: this will reduce the range of positions accessible by the particle.

---

[a] Obtained with our radiometric model, modified to account for refraction and occultation (see, Section C.2).

II.3.4 Partial occultation of projected signatures

Some images show distinctive patterns as for instance in Figure II.22. Theses patterns are shadows created from the partial occultation of the projected signatures. This effect can happen when a particle is at the limit of the detection area: under certain conditions of position, part of the signature is occulted by the cloaker.

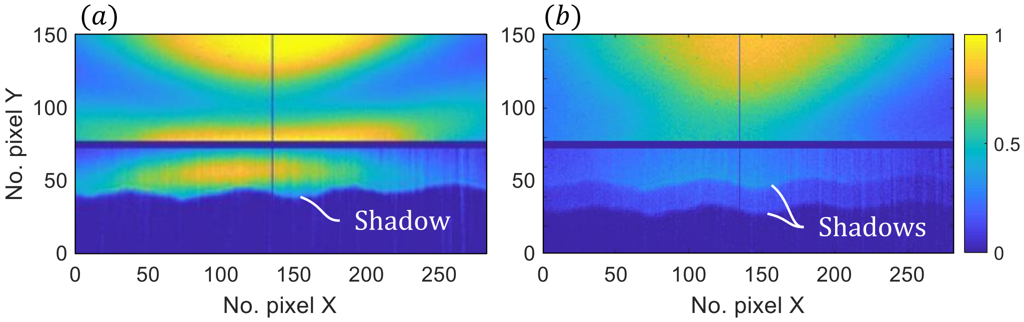

Figure II.22: *Examples of experimental images showing shadows. (a) Signature with one shadow. (b) Two superimposed signatures showing two shadows.*

Shadows can contain precious information: the position of the particle that can, for instance, be retrieved through the analysis of the position and magnification of the edge of the shadow. For high concentration aerosols, the presence of several shadows can reveal images with a multiple detection as in Figure II.22(b). More details are discussed in Appendix C.1, in which we explain the origin of these shadows, and a processing tool to detect and count them. Counting shadows can be a way to address a classic issue encountered by many OPCs, which is discriminating coincidence events [137]. We can take advantage of the phenomenon of partial occultation by designing specific occultors called ’reticles’, more details will be discussed in Appendix C.

II.3.5 Discussion about estimating particle concentration

For a given particles' diameter, we measure the detection rate f_p which is the fraction of images that passed the detection threshold over the total of images recorded. For example, we obtained a detection rate of $f_{PSL3} = 0.074$ for 3 µm PSL particles. As explained before, the particle's concentration is chosen so that we obtain a detection rate much lower than one, thus avoiding coincidence events[10]. This detection rate is the statistical metric that allows us to estimate particle concentration in the sampling volume, as these two quantities are presumably linearly equivalent.

The sampling volume V_s is the volume in which particles can cross the optical beam during the integration time of an image. To calculate such volume, one must accurately determine the optical surface crossed by particles as well as trajectories and velocities of particles. This last part would require us to perform FEM simulations of particle tracing in a turbulent air flow. Early simulations were performed to calculate the velocity map of particles, using the COMSOL Multiphysics software. However, 2D and 3D simulations of the turbulent air flow were made with both the $k - \omega$ and the SST model (suggested in a COMSOL blog post for jet flows, like in our case) but we couldn't obtain reasonable results. Further air flow studies could be performed in the future, if necessary.

Another way to find V_s is to measure the detection rate f as a function of known concentrations, and then evaluate the slope of the curve. Using a similar holed sensor (detailed in Appendix C.2), we have performed opacity measurements on a paraffin generator tunnel (by Lorenz Messgerätebau GmbH & Co. KG). This tunnel delivers paraffin particles and the concentration is set to create a plume of given opacity (unit: dB/m), circulating at a velocity of 0.2 m/s. Figure II.23 shows the distribution of the paraffin particles: mass and particle number as a function of particle diameter. We fit mass distribution with a log-normal law: best mass median diameter is $D_{pp} = 0.77$ µm and best geometric standard deviation is $\sigma = 2.03$ (see, Section I.1.4).

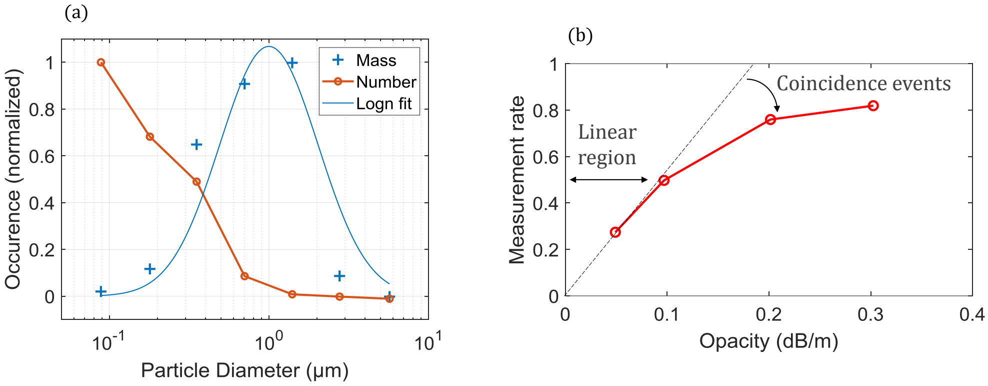

Figure II.23: *(a) Paraffin plume distribution. (b) Measurement rate vs. opacity of the paraffin plume.*

Several measurements were made for different opacity of plume, which is correlated to particle concentration: the denser the plume is, the stronger is the total light extinction. Figure II.23(b) shows f_p as a monotonic function of the plume opacity. We have shown that opacity is linearly equivalent with mass concentration. Calculations of the proportionality coefficient can be found in our reference [138]: in which we used reference [85], Beer-Lambert's law of attenuation and Lorenz-Mie's theory for an aerosol with the previously fitted log-normal mass distribution. As earlier, we count the measurement rate f_p. This rate is directly correlated to the probability that a particle, large enough to be measured, appears in the detection volume. The relation $f_p(O)$ should be linear for low opacities, the measurement rate drops for higher opacities, because the sensor measures more coincidence events. Futures studies would allow us to correct the measurement rate, taking into account coincidence events (see, Appendix C) so that we could extend the linear region to higher particle concentrations. Again, in such linear region, the sampling volume V_s could be evaluated by taking the graph's slope. Nevertheless, even without correction, one can argue that the measurement rate gives an estimation of the particle concentration as $f_p(O)$ is monotonic.

---

[10] These experimental conditions are close to what can be found in outdoor air.

II.4 Image processing

II.4.1 Strategies for diameter and refractive index retrieval

We explore the ways modelled images can be fitted to experimental signatures using our radiometric model for given particle diameter D_p and refractive index n. These target particles' parameters are variables among other geometric parameters $(x_p, y_p, z_p, \alpha, \beta)$ defined in Section II.2, that we need to fit as well. Within our experimental setup where we use a collimated fiber for illumination, we have found that some parameters have negligible effects (x_p, z_p, α). The effect of a small β can be easily retrieved by evaluating the rotation of the image. The only geometrical parameter we have to fit is the position of the particle along the optical axis (y_p). Noteworthy, another research group also working on scaled-down PM sensors, reported severe errors induced by the position of the particle [139]. Here, we propose to correct these errors within our image analysis procedure.

Our strategy consists in focusing only on the iso-θ (ridge and valleys only) and define a reduced image contained in a small matrix (see, Appendix E.1). In this step, we extract parameters from the iso-θ we consider relevant, such as coefficients of a polynomial fit, the with of the iso-θ and weather or not it is a ridge or a valley. The intensity along the iso-θ is ignored, because it cannot be well modelled given our lack of knowledge of the true vignette effects. Although this information could be analyzed in the future, to extract information on z_p, if needed. Then, we define a minimization criterion based on the comparison between reduced images of experimental and modelled signatures (see, Appendix E.2). Minimizing this criterion allows us to estimate particle parameters such as its diameter.

It should be stated that, with our current setup, we encounter experimental variability in the overall scattered intensity mainly due to particle position and spatio-temporal illumination non-uniformities. Thus, we are not able to use the overall intensity in our data processing method, at least with our current set-up.

II.4.2 Experimental versus modelled comparison of reduced images: diameter fit

The diameter of the particle is the metric we want to measure. In our laboratory measurements, we used PSL spheres of refractive index $n_{PSL} = 1.5875$ at our working wavelength [84]. Using our minimization criterion $\epsilon(D_p)$, we found $D_p = 3.81$ µm. In Figure II.24, we present the comparison of the experimental image used in the example and the fitted modeled image.

This test case is presented only to illustrate the principles of the image processing. Note that the expected diameter was $D_p = 3$ µm (error is 27%). The diameter we have found with our procedure is slightly beyond the scope of the dispersion guaranteed by the supplier of PSL spheres (10%).

This error might be due to an unknown combination of the errors from the procedure (and the model) but also the dispersion of the refractive index of PSL. Indeed, it has been found that the refractive index of commercially available polystyrene beads can vary from a sphere to another as shown in reference [140]. Moreover, other research groups performing a similar inverse problem as ours also measure a certain distribution in the refractive index [141].

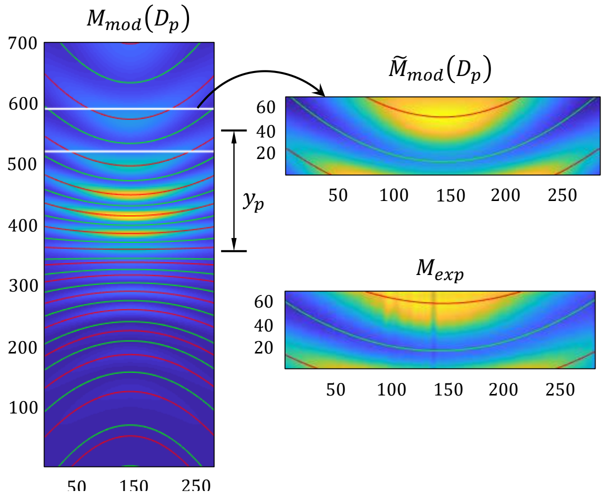

Figure II.24: *Example of diameter fit using iso-θ curves.*

II.4.3 *Sensitivity to refractive index*

In Figure II.25, we evaluate our minimization criterion $\epsilon(D_p, n)$ for a reasonable range of diameters and refractive indices[a]. The experimental image used for the comparison is the same as the one presented before in Figure II.24.

We observe that the reasonable diameter and refractive index we expect from our experimental image are within a local minimum circled in white in the $\epsilon(D_p, n)$ map shown in Figure II.25. However, other local minima may introduce large errors in the estimation of our parameters.

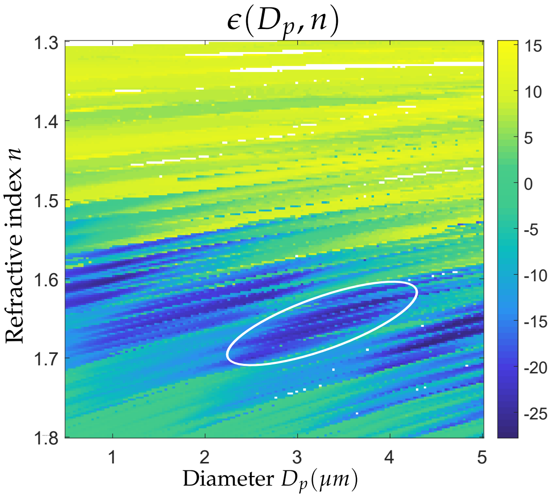

Figure II.25: *Map of our minimization criterion against particle diameter and refractive index in logarithmic scale.*

We don't know yet if solving such inverse problem is rigorous, meaning that if two different particles with different diameter and refractive index can exhibit the same projected signature (with the same iso-θ). Suppose we have a perfect setup were particles are not displaced, we still don't know how critical are local minima (when two different projected signatures look alike). From the literature, it appears that solving such a problem is possible [140,141]. In future developments, we hope to erase these unwanted local minima by a number of improvements. For example, we could investigate better definitions for $\epsilon(D_p, n)$; identify relevant parameters to be integrated into our image reduction matrix; the overall intensity of an image should be almost monotonous and could help us with the issue of local minima by pre-estimating the diameter and refractive index (to be used as a starting point for our optimization); implement the simultaneous analysis of both forward and backward matrixes etc. Optimizations within our fluidic set-up could also reduce the range of accessible particle position, improving the accuracy of the procedure. The latter will also have to be tested with a large number of test cases to conclude on its accuracy.

We also notice that the region with refractive index below 1.55 has a very high $\epsilon(D_p, n)$. This suggests that our procedure could differentiate organic media of high refractive index (such as polymers) from inorganic media with a lower refractive index (such as silicates or aqueous droplets).

It should be stated that the method presented in this section is designed to work with spheres. Particles present in ambient air can show irregularities in shape that attenuates the effects of the Mie's oscillations [142]. The method is based on the analysis of ridges and valleys found in experimental signatures obtained with spherical laboratory particles, and could not be used in its current state with ambient air particles. Future improvements of this method should include more advanced scattering calculators (see, Section I.3.3) or machine learning methods [141,143].

---

[a] The imaginary part of the refractive index was not considered here, as PSL is not absorbing at the working wavelength. For absorbing particles, the imaginary part should be added to the list of unknowns of this inverse problem.

II.5 Chapter conclusion

In this chapter, we have presented a prototype that made significant advances toward the miniaturization of PM sensors. To make such sensor, we have developed an unconventional design of a CMOS image sensor allowing for a hole drilling post process at wafer level. The hole drilling post-process (200 mm CMOS platform) and the packaging are engineered to create a vertical through fluidic channel so that an air stream carrying particles can traverse the sensor. A compact optical set-up featuring a multi-purpose 3D-printed piece (we refer to as cloaker) enables the alignment of a collimating fiber and protects the retina from stray-light. Such an optical set-up allows for the lens-free projection of a single particle's scattering signature on the image sensor. The full sensor architecture is described in Section II.1.

We have developed an analytical model that describes the lens-free projection of scattering signatures that combines the Lorenz-Mie theory and classic radiometric calculations (see, Section II.2). Experimental images were taken with calibrated laboratory particles (PSL spheres) and show great accordance with our predictions. We have successfully recorded scattering signature of single particles down to a diameter of 320 nm (see, Section II.3). Finally, we present how we can characterize single particles through image processing, by using a recorded signature and our model (see, Section II.4). This image analysis procedure is a first step toward the retrieval of a particle diameter and refractive index. However, there are still significant inaccuracies in the procedure.

Further developments will include improvements on the packaging: we aim to reduce the footprint of the system by bonding the CMOS chip directly on a compact PCB and driving it with an ASIC. The fluidic design with an optimized channel profile and a fan-induced convection would improve both the sensitivity and the image processing accuracy. The sensitivity and richness of the signatures could be improved by using shorter wavelength and optimized pixels. Once these modifications applied, we plan to test our sensor with particles more representative of what can be found in ambient air: non spherical particles, metallic, dielectric or organic aggregates. To do so, we will definitively have to adapt our image analyses procedure to cope with these morphological variations. The next generation optical set up could feature miniature optics as it will be discussed in Chapter III.

As a side note, it would be interesting to slightly modify this prototype to implement reticles in order to partially occult the scattering signature. As explained in Appendix C, such designs could improve the image processing and take advantage of coincidence events[11].

---

[11] We encourage the reader to take a look at this appendix.

III

Fourier domain imaging of scattering signatures

Chapter content

III.1 Designing the optical system

III.1.1 Generalities

In Chapter II, we have described a first prototype for an optical PM sensor, that is the base frame for the second prototype that will be discussed in this chapter. The former is able to count particles and record scattering signatures that are projected onto an opto-fluidic CMOS chip we call a 'holed retina'. The recorded signature is optically transformed through a planar, lens-free projection with a short working distance (see, Section II.2). The geometry is optimized to maximize both the sensitivity of low intensity scattered light as well as the Field of View (FoV) of scattering angles. With this first prototype, the FoV is limited by the geometry as we can evaluate scattering signatures within a FoV of only a few tens of degrees (see, Figure II.11(b)). There is little margin of improvement that can be made using the lens-free planar projection. Moreover, the uncertain position of the particle within the illumination beam can result in an affine transformation of the image as well as a blurring effect, with a shifted FoV. This last part is taken into account by our image analysis procedure (see, Section II.4) but one may want to simplify the computing part as much as possible for future portable applications.

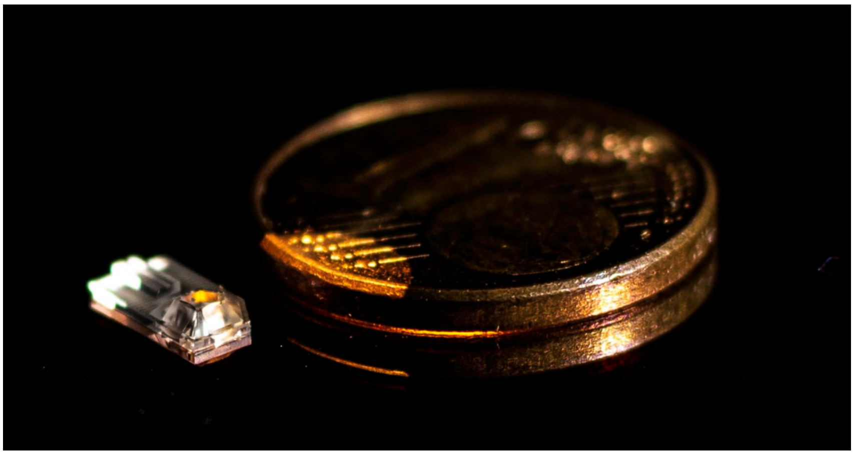

Figure III.1: *Photography of the miniature lens system next to a one euro cent coin.*

Some of these identified problems (the narrow FoV and the influence of the position of the scattering particle) concerning the lens-free projection method can be addressed. The suggested solutions resulted in the design and fabrication of our miniature optical system [144], shown in Figure III.1[1]. This piece was made from a single fused silica glass substrate and contains several optical surfaces, alignments and fluidics. All those elements are included inside a small volume of about 3 mm × 6 mm × 1 mm. More information can be found in the patent [126].

---

[1] Note that a one euro cent coin is sized by 16.25 mm in diameter.

III.1.2 Achieving position insensitivity

In most non-miniaturized light-scattering photometers, the position of the particle has no impact on the measurements. Indeed, the range of positions accessible by the particle is very small as compared to the optical path of scattered rays. In our case, the impacts of the particle position include translation, magnification and rotation of the recorded image (see, Section II.4); a superposition of shifted signatures can be generated by a distribution of particles, resulting in a position blur; as a corollary, the detection of a moving particle (with respect to the image integration time) results in a motion blur.

We will propose a way to achieve position insensitivity. A setup equivalent to a far-field setup is the common d-f lens system, where the retina is placed at the Image Focal Plane (IFP) of a thin lens (simplified model) so that the object can be seen at infinity [145]. Consequently, the retina can record an angular image by refocusing parallel rays. Indeed, let us consider the object (a particle or a distribution of particles) as a punctual source (or several punctual sources), at unspecified positions and casting rays which intensity vary according to the scattering angle. The retina will then directly record the scattering signature. The recorded image is not modified by displacing the particle because the same scattered rays are always seen under the same angles (see, Figure III.2).

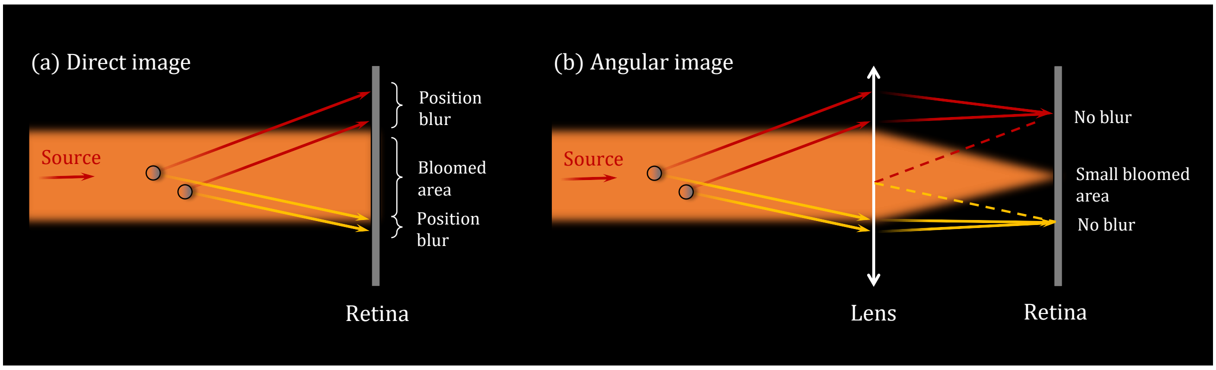

Figure III.2: *Illustration of the d-f setup that performs angular imaging by refocusing parallel scattered rays.*

In the classic d-f setup, the retina is placed on the IFP of the lens[2]. Using Fourier's harmonic description[3] of the d-f setup [146], one can show that the angular image (*i.e.* the scattering signature) is carried by the amplitude of the wave at the lens' IFP while the information on the position of the particle is only carried by the phase of the wave at this plane. Justification will be provided in Appendix F.3. A simple photo-detector array is only sensitive to the amplitude: under these considerations, the recorded image is purely an image of the scattering signature, in the Fourier domain. We will show that this optical pre-treatment of the scattering signature dramatically simplifies the analysis of the image taken by the retina, removing the need for energy-costly image processing.

Such a setup can achieve position insensitivity if we consider a thin lens with infinite lateral extension. For a real lens with a finite pupil, the scattering signature is contained within the projection of the lens' pupil on the retina. However, one must keep in mind that the projection of the lens' pupil depends on the particle's position, which will be discussed later in this chapter.

---

[2] The d-f setup is not to be confused with the more specific f-f setup, where the particle is placed on the Object Focal Plane (OFP) of the lens.

[3] For further details on Fourier's harmonic description of optical systems and optical Fourier transform (see, Appendix F).

III.1.3 Asymmetric crown assembly

Let us consider a lens system coupled to a detector array. A major factor that limits the FoV is the pupil of the system. Our idea behind improving the FoV for light scattering analysis is to merge several of these subsystems around a perpendicular air channel in a crown shape, as illustrated in Figure III.3(a). The edges of each subsystem may contain aberrations or unwanted artifacts that we call 'blind fields', especially at the limit of two merged ones where we may observe cross-talk effects[4] between the subsystems.

By taking advantage of the symmetry of the scattering signature around the optical axis, one can sacrifice a bit of redundancy by facing half of the lenses toward the blind fields of the other halves. The resulting design is an asymmetric crown shape with an uneven number of optical subsystems arranged around a perpendicular air channel. An example is shown in Figure III.3, with five subsystems (modeled as thin lenses).

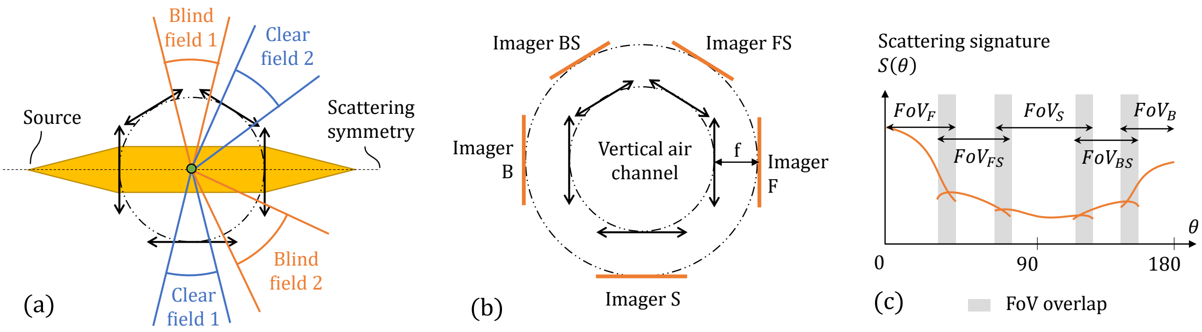

Figure III.3: *(a) Principle of blind fields asymmetrically coupled to clear fields. (b) Lenses coupled with imagers in Fourier planes. (c) Principle of overlapping sub-FoV for signature reconstruction.*

In the IFP of each subsystem, one can reconstruct a scattering signature (because there is an injunctive law linking a position on IFP and the scattering angle) along each associated sub-FoV. Subfigure (c) shows the signature seen through all five subsystems (F, FS, S, BS, B standing for Forward, For-Side, Side, Back-Side, Backward). As explained earlier, we design the sub-FoVs with an overlapping region (grey areas), in order to mitigate the defects at the edge of each sub-FoV, by taking advantage of the asymmetric design.

In this design, the total FoV can be - in theory - as wide as 180°. The limiting factor is the surface bloomed by the illumination beam (which is orders of magnitude more intense than the scattered intensity). For a collimated beam (as in Figure III.3), the bloomed area is at best, the size of the diffraction spot of our optics plus the Point Spread Function (PSF) of our retina. For a diverging (or converging) beam, the bloomed area is convoluted with associated angles within the beam divergence. In the case of a spatially extended source (*e.g.* a LED) that is difficult to collimate, the lens will at least have the effect of reducing the bloomed area.

Note that, such an sampling geometry allows for collecting the most of the scattered flux, especially around low scattering and backscattering angles where the scattering efficiency high usually high. This increases the sensitivity of the sensor to small particles.

---

[4] We call cross-talk effects the case where a scattered ray enter a sub-system through its front diopter, and exit through the adjacent subsystem's back diopter.

III.1.4 Compact optical subsystems with coincidental Fourier planes

Each optical subsystem must meet a certain set of specifications: it must be as compact as possible; it must also fold its Fourier plane (*i.e.* IFP) onto a plane perpendicular to the fluidic channel so that all subsystems' Fourier planes are coincidental. This set-up enables the use of a single holed retina (in a fashion similar to our first-generation PM sensor) to image all Fourier planes on separate Regions Of Interest (ROIs).

In Figure III.4, we present the design of an optical subsystem composed of two spherical diopters and a 45° spherical internal reflector that folds the image focal plane. The surface can be coated with a metallic reflective layer such as aluminum or gold. Alternatively, no reflective layer is used as the internal reflections within the material can be efficient enough.

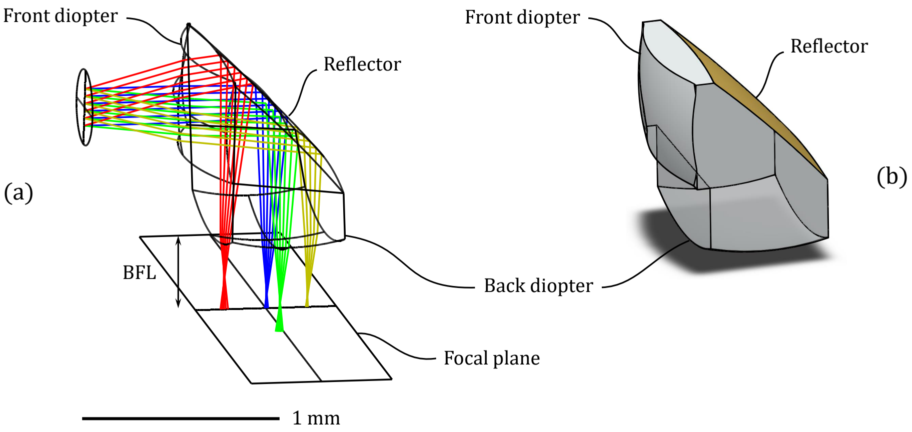

Figure III.4: *Design of the refracto-reflective optical subsystem. (a) Ray tracing view from Zemax Optic Studio. (b) 3D view of the truncated subsystem.*

Every surface participates to the focusing of rays so that we can obtain a good optical system with a wide sub-FoV (50°), with acceptable aberration which will be discussed hereafter, and a short Back Focal Length (BFL = 0.37 mm). The subsystem takes advantage of three surfaces out of a same volume, thus can be manufactured out of a unitary piece. For this prototype, the material used for the design is fused silica glass, but it can also work with most optical polymers. This refracto-reflective subsystem was designed using the optimization tools of Zemax Optic Studio software in sequential mode (see, Figure III.4(a)). Compactness is then improved by truncating such optical surfaces (see, Figure III.4(b)).

To analyze the performances of an optical system, we commonly plot the Modulation Transfer Function (MTF), which is the Fourier transform of the Point Spread Function (PSF), see Appendix F. A system's MTF describes the loss of contrast created by the optical system as a function of the spatial frequency (usually given in cycles/mm), that quantifies the finesse of a detail. The PSF is the response of the optical system illuminated by a point source: it represents the blur induced by the system. The concepts of image quality analysis, used here, are defined in more detail in the references [145, 147].

Here, we compute the PSF using Huygens' wavelet direct integration algorithm[5]. Then, the MTF is obtained by taking the amplitude of the Fast Fourier Transform (FFT) of Huygens' PSF. We present in Figure III.5 the Huygens' MTF of the optical system.

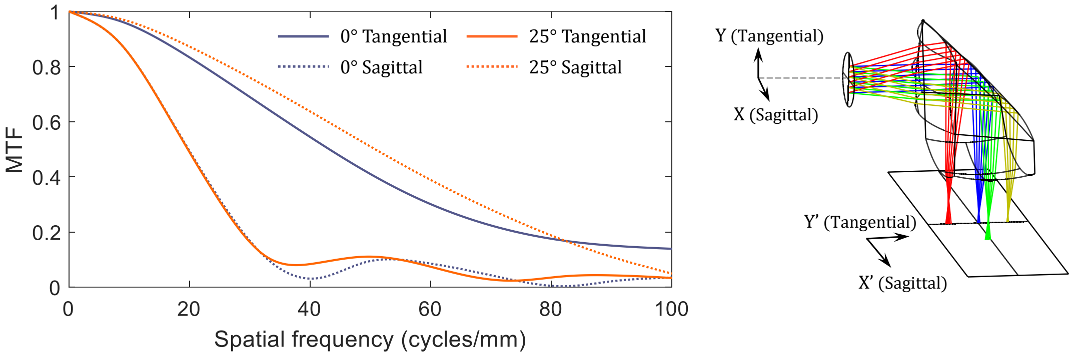

Figure III.5: Tangential and Sagittal MTF of the optical subsystem at 0° *and* 25°*.*

Our system uses a folded focusing mirror and a short BFL, these specifications do induce imperfections. First, such system has astigmatism: meaning the tangential and sagittal[6] focal planes are disjointed. It means that we can't be in focus for both vertical and horizontal rays. A second imperfection is that both tangential and sagittal focal planes are highly curved. In the same manner, we can't be in focus in both the center and the edge of the retina. This imperfection is known as field curvature aberration.

In the center of the retina (0° inclined rays), we privilege the vertical resolution (tangential MTF) rather than the horizontal resolution (sagittal MTF), see purple curves in Figure III.5. This is equivalent to say that the blur spot is elliptical and extended in the X' direction[7]. However, in the edge of the retina (25° inclined rays), the horizontal resolution is privileged instead. We choose this compromise because our subsystem is elongated in the X direction and is designed to focus scattered rays that are higly inclined in the X-direction. This part is shown in Figure III.5, where orange curves shows that the sagittal MTF is much better than the tangential MTF.

The resolution of the subsystem has to be compared with the resolution of the retina. To do so, we introduce the Nyquist frequency $f_N = 1/2p_{pix}$, which quantifies the geometrical sampling of the image plane, through the pixel's pitch, denoted p_{pix}. For a 10 µm pixel, like the one we used in Chapter II, $f_N = 50$ cycles/mm. The resolution of our subsystem appears quite good, even comparable with the resolution of the image sensor itself. Indeed, for privileged directions, the MTF is more than 50 % at the Nyquist frequency. One might argue that the subsystem is over-engineered for such pixel's pitch.

It should be noted that the MTF of our optical subsystem will not be measured. Indeed, conventional MTF characterization methods [147] require the use of a blade as an object, that can't fit within the fluidic channel. If one really wants to measure such MTF, we suggest to fabricate a subsystem alone, or cut a full subsystem assembly (described in the next section).

---

[5] According to Zemax Optic Studio's user manual, Huygens' PSF is more accurate than a PSF computed by geometric ray-tracing.

[6] The tangential focal plane is the surface were vertically aligned rays are focused by the system. In the same way, sagittal refers to horizontally aligned rays, *mutatis mutandis*.

[7] Note that the X, Y coordinate system is used only in this section, and is specific to a subsystem alone. A new coordinate system will be used later when each sybsystem will ba arranged around the air channel.

While the MTF plot is very useful to quantify the resolution of an optical system, it may be difficult for a non specialist to visualize the effects of the optical system on an image. Thus, it might be interesting to perform an image simulation obtained from an object at infinity (angular object). Image simulations are shown in Figure III.6.

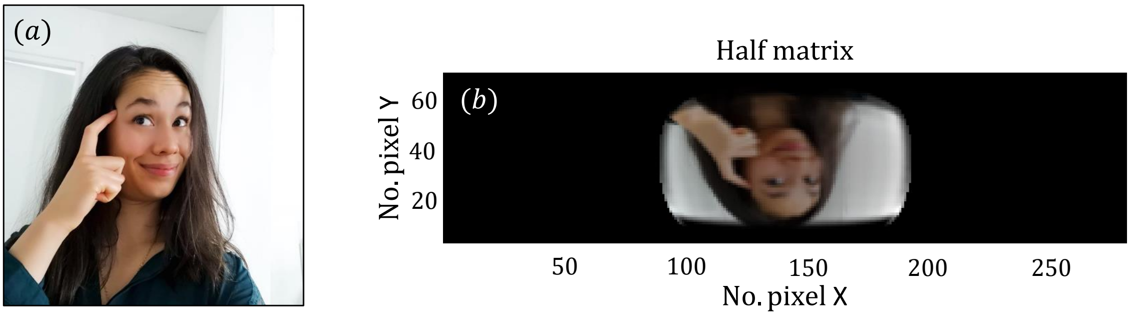

Source object at infinity
($60° \times 60°$)

Figure III.6: *(a) Picture of Marine as a source object at infinity and (b) simulated image obtained with the subsystem.*

The object is a square angular image of Marine sized by $60^\circ \times 60^\circ$ (see, subfigure (a)). Later, examples of images that we would obtain with Mie's scattering signatures will be presented in Figure III.11 with the full assembled optical system. The simulation tool (Zemax Optic Studio, Sequential Mode) computes the spatially variant Point Spread Function[8] PSF(x, y, x', y') of the optical subsystem. This PSF takes into account only geometrical aberrations, diffraction effects are ignored here[9]. Chromatic aberrations are also taken into account as the PSF is calculated with RGB colors, this information can be useful if one wants to scatter light with different wavelengths. The simulation image is finally obtained by convoluting the object and the PSF (see, Appendix F).

Subfigure (b) shows the image simulation obtained with the optical subsystem. The image sensor used for the simulation is one of the two submatrix of our holed retina presented in the previous chapter (see, Section II.1.2). One must keep in mind that this optical system was not originally intended to work with this specific retina as it was designed prior to it, with only a general idea of a holed image sensor. For instance, the magnification is not properly adapted to cover a large portion of the retina. We observe that the system shows fisheye effects as well as field curvature aberrations, especially in the Y direction. The latter is mainly caused by the fact that we have a folded optical system. The image looks pixelated, and not blurred that much: the resolution appears to be limited by the retina, as discussed earlier.

---

[8] With given set of sampling positions (x', y').

[9] These are the simulation settings we's selected because it speeds up significantly the image simulation. Indeed, we have seen that diffraction effects are negligible compared to geometric aberrations: our system is far from being limited by diffraction.

III.1.5 Subsystem merging and fiber alignment

Five identical optical subsystems are merged into a unitary piece. Front surfaces are at an equal distance (Front Focal Length, FFL) from the center of the channel. The channel is designed to have a section similar to that of the holed retina channel[10] (see, Chapter II), which is about 1 mm^2. The subsystems are assembled so that the 'radius' of the channel is FFL $=$ 0.5 mm. The resulting 3D model is rendered in Figure III.7. It contains the merged subsystems around a vertical fluidic channel. Note that the front surfaces (first diopters) are part of the inside walls of the channel.

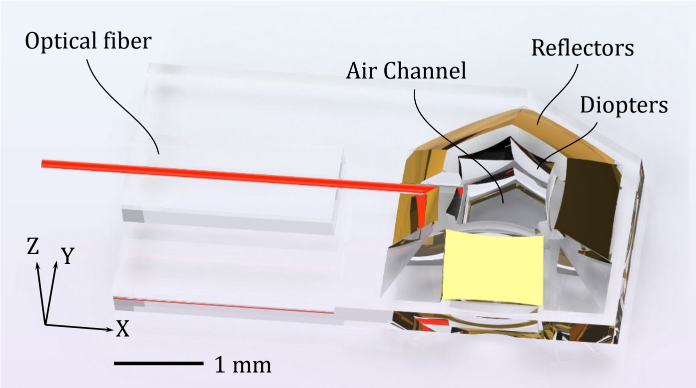

Figure III.7: Rendering of the miniature optical system.

We also design a V-groove that continues through the back subsystem and stops at the edge of the channel. This V-groove allows an easy alignment of a standard pigtailed optical fiber (125 µm of diameter). The fiber can illuminate the channel forming a beam with a divergence defined by the numerical aperture (NA) of the fiber. This piece is designed to be manufactured from a single, 1 mm thick, fused silica substrate.

In Figure III.8, we show a schematic of the device showing the path of both the illumination beam and the scattered rays. Here, only the F and B subsystems are present in the cross sectional view, the FS, S and BS subsystems are arranged around the air channel.

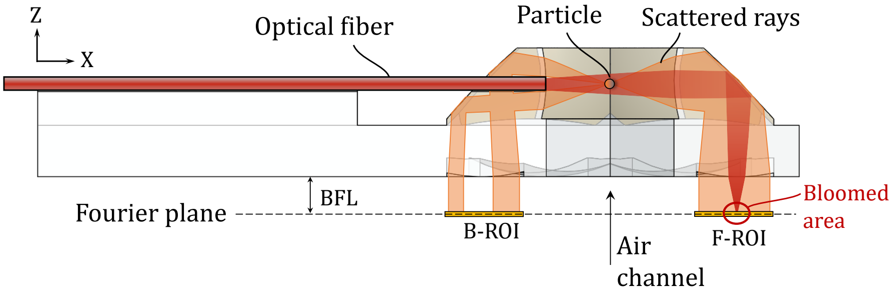

Figure III.8: Schematic cross sectionnal view showing the path of the illumination beam (red) and the scattered rays (orange).

---

[10] In order to have similar fluidic performances.

III.1.6 *Angular response at the Fourier plane*

We will now evaluate the angular response of the merged system: we present a RT (Ray Tracing) simulation of the silica glass piece in Figure III.9. For a better comprehension, we have simplified the scattering particle down to a simple conical source point, which has a given irradiance angle and is axially symmetrical around the beam axis. An image monitor is placed at the coincidental Fourier plane, and can record the irradiance pattern induced by the scatterer.

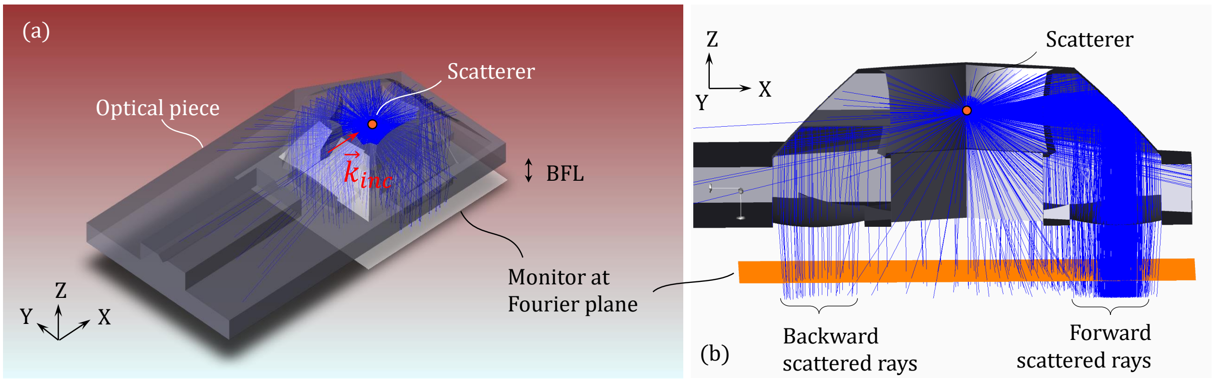

Figure III.9: *(a) 3D view of the RT simulation of the optical system. (b) Close up cross sectional view.*

By sweeping the angle of the conical source from 1° to 180°, one can obtain the intensity map in the coincidental Fourier plane for each scattering angle, and then, associate a scattering angle (and intensity) to each pixel of the monitor. In Figure III.10(a), we plot the angular response of the optical system that evaluates a centered scatterer $S(0,0,0)$. The angle map is plotted using a colored scale, and the associated intensity is plotted using a transparent-black (bright-dark) overlay.

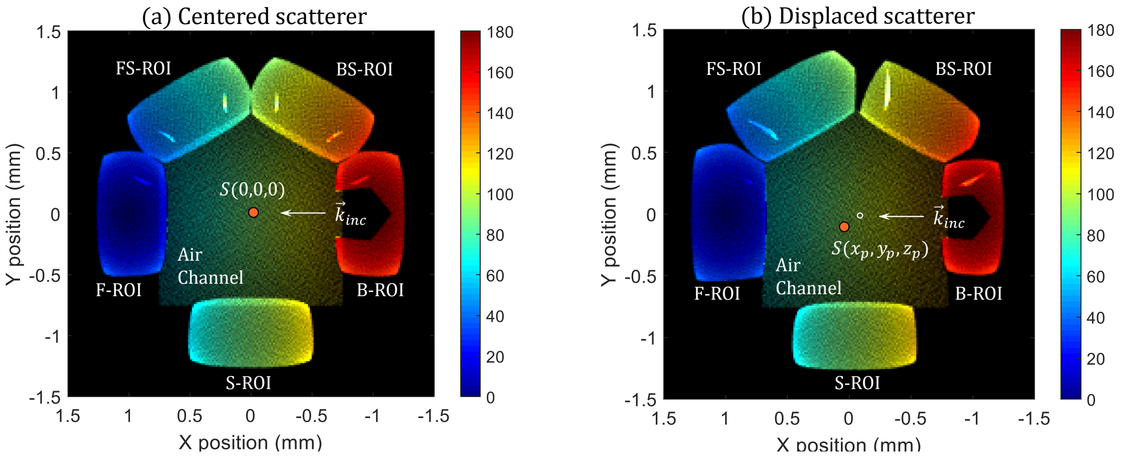

Figure III.10: *Angular response (in degrees) of the optical system that evaluates (a) a centered scatterer and (b) a displaced scatterer.*

We recognize the five Regions Of Interest (ROIs) associated with the five optical subsystems (F, FS, S, BS, B standing for Forward, For-Side, Side, Back-Side, Backward). We verify that a point within a ROI, is associated to a single scattering angle. These ROIs allow us to evaluate the scattering signature thanks to the associated overlapping FoVs. Note that we observe luminous 'claw marks' at the edge of two adjacent subsystems (at blind fields). These artifacts are cross talk effects between the systems, meaning that rays can enter through a first diopter and exit through a last diopter of the adjacent system.

In order to evaluate the impact of the position of the scatterer, we perform the same RT simulation but the scatterer is displaced at $S(x_p, y_p, z_p)$, using reasonable positions when compared with the incident beam: $(x_p = 100\ \mu\text{m}, y_p = 15\ \mu\text{m}, z_p = 10\ \mu\text{m})$. Note that the range of accessible positions is highly elongated along the axis of the illumination beam (X-axis). The result of such a simulation is presented in Figure III.10(b). We verify that every pixel is still associated with the same scattering angle. This gives us confidence that our strategy to measure a scattering signatures with position insensitivity is relevant.

The main difference between the two images is that the images of the pupils of each subsystem are slightly transformed due to the displacement of the scatterer, which was to be expected. This part should not bother us too much as it takes effect at the edge of every subsystem (blind fields), which can be easily corrected thanks to our asymmetric assembly of subsystems. Another impact of the particle's displacement is that 'claw marks' induced by cross talk effects are very dependent on the particle's position. This can be more problematic as one has to write a software that can detect such marks so that impacted pixels are excluded during the reconstruction of the scattering signature. Although, such marks could be analyzed to evaluate the position of the particle, if necessary.

For illustration purpose, we perform a simulation to predict the scattering signature of a sphere, by using the Lorenz-Mie theory (far-field) and a RT simulation. The simulation is identical to what was made in Figure II.17 for the lens-less setup. Results are shown in Figure III.11 with our usual examples of three PSL spheres (refractive index $n_{PSL} = 1.5875$ [84]) with different diameters. We can clearly see Mie's oscillations within the differents ROIs.

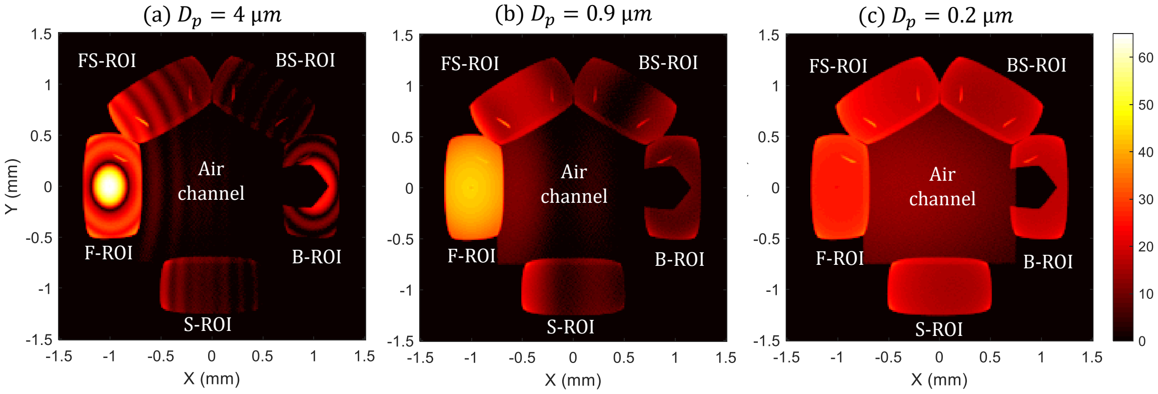

Figure III.11: Lorenz-Mie and RT simulation of scattering signature in Fourier domain for three PSL spheres diameters: (a) 4 µm, *(b)* 0.9 µm *and (c)* 0.2 µm.

The images are given with an arbitrary unit of irradiance (in logarithmic scale). The scale bar is shared by all three images so that one could compare the relative brightness of scattering signatures obtained with different diameters.

III.2 Fabrication Process

III.2.1 Micro-machining on glass

The prototype of the monolithic optical piece is a challenging piece to manufacture. It has small dimensions and the surfaces of the diopters must have optical grade surface qualities. Precision micro-tooling of molds [148] is still very expensive but can be cost-efficient if optical pieces are molded at volume fabrication (using for instance micro-injection molding [149]). Direct laser 3D printing by two-photon polymerization shows great promise printing miniature optics [150,151] but is not yet suited for printing millimeter-sized optical pieces: the lateral dimensions are limited to a few hundred micrometers.

For our prototype, we have selected a manufacturing process based on an innovative laser micro-machining of glass [152, 153], developed by FEMTOprint, which relies upon three main steps: laser exposure, wet/chemical etching and polishing.

Starting from a 1 mm thick fused silica glass wafer, the 3D shape of the device is generated by sweeping a tightly focused (20x microscope objective, $NA = 0.4$) femtosecond laser beam at a wavelength of 1030 nm, on a f200a head machine. We generate the object within the substrate by moving the sample and the beam in the fashion of a 3D printer. The exposure to femtosecond laser pulses triggers a non-linear absorption process that causes a glass densification within the laser voxel[11] that eventually induces a drastic change in selectivity (up to 1000 times) when immersed in an etching solution [154]. The excess material is then removed by a KOH solution (45 %) at 80 °C for 10h; and the unexposed volume of the device is released from the wafer. At the end, the device is cleaned with water and dried before the quality control. Since the etching process has a finite selectivity and is quite long, the original design is pre-compensated in order to achieve the desired dimensions.

The machined surfaces showed a typical roughness Ra[12] around 80 nm on the vertical sidewalls (channel-facing front diopters) and $150 - 300$ nm (Ra) on the planar or 3D surfaces (reflecting surfaces and back diopters), *i.e.* not low enough for optical elements. For this reason, a proprietary polishing process has been applied to selectively reduce the roughness of the optical elements by locally reflowing the material surfaces at the vicinity of the optical surfaces using a proximity tool, while minimizing the deformation. To this goal, a reduction of Ra to values below 30 nm has been achieved, which is much better that the roughness we've initially targeted ($\lambda/10$), and allows for minimal surface scattering. An optical image showing a top view of the fabricated glass piece is shown in Figure III.12.

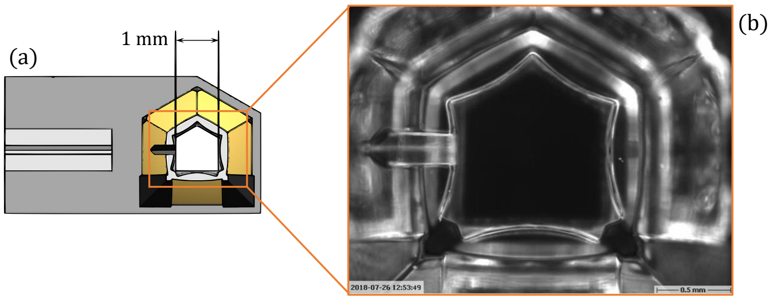

Figure III.12: (a) Original drawing. (b) Optical image of the fabricated optical system.

---

[11] The laser voxel is the volume at the vincinity of the focusing point where the optical power density has reached a certain value, allowing for the non-linear densification effect.

[12] Ra stands for Rouhness average, and is the average value of the profile heigh deviations.

III.2.2 Molding & replication

In this section, we explore the replication process that would be critical if one wants to manufacture such optical piece at a reasonable cost. We show preliminary tests with a discarded glass prototype (polishing-induced deformation test sample) that we will call 'mother' in this section. We use PDMS (silicone rubber) as the molding material. For complex 3D pieces like this one, the mold is made of two parts: the bottom part is molded and dried first so that the upper part can be molded in turn [155]. A picture of the glass prototype inside its mold is shown in Figure III.13 (a).

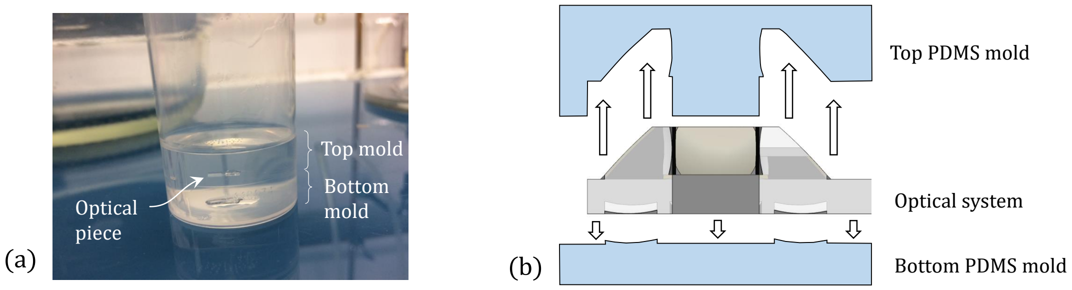

Figure III.13: (a) Photography of the mother molded in PDMS. (b) Cross sectional view of the unmolding step.

Despite the delicate surfaces of the channel inner walls (see, Figure III.13 (b)), the unmolding step went smoothly. We observe no degradation of the mother after being molded and unmolded. The low roughness of the original glass piece appears to be well transferred into the mold. Previous in-house studies have shown that this method is well suited for the molding of optical grade surfaces. This PDMS mold is then used to shape a replica (call 'daughter' hereafter) with an optical polymer. Here, we use a commercial transparent clear epoxy resin.

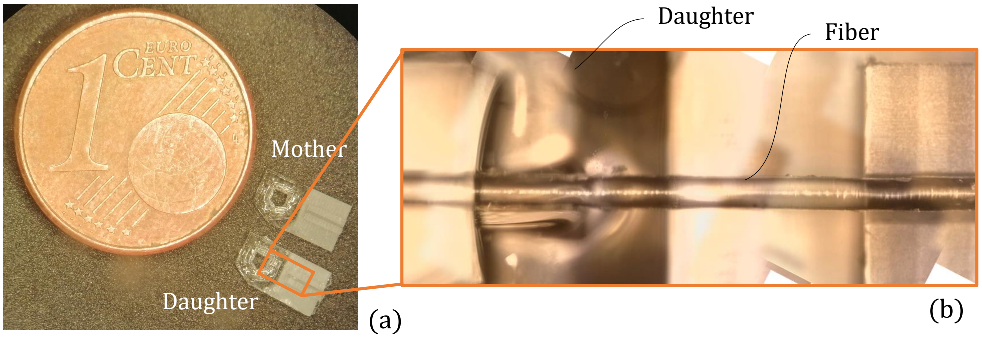

Figure III.14: Glass prototype ('mother') next to its epoxy resin replica ('daughter') (a). Optical image of the daughter with a fiber installed (b).

A photography of the resulted replica is shown in Figure III.14(a) next to the original glass prototype. Apart from the different refractive indices of the materials, the surface quality of the lenses appears very similar (although we did not perform precise measurements of the replica's roughness). The shapes are also reproduced with a great fidelity even inside the channel and with the V-groove that can hold an optical fiber with great accuracy (as shown in Figure III.14(b)).

III.2.3 Mirror deposition

In this section, we describe how the mirror deposition step is performed. A metallic layer has to coat at least the 45° slanted optical surfaces, while avoiding the first diopters facing the fluidic channel to be metallized.

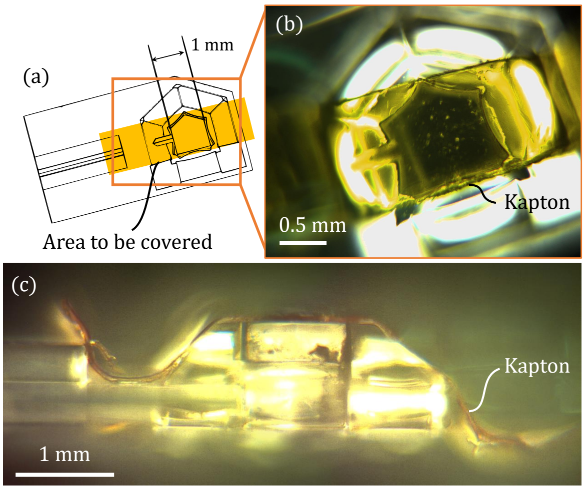

Figure III.15: *(a) Drawing of the optical piece showing the area to be covered. Optical view of the optical piece covered with a Kapton stripe, seen from the top (b) and from the side (c).*

Thus, specific areas must be covered prior to any metal deposition step. Those areas include the fluidic channel, and the surfaces that belongs to the F and S subsystems[a]. The remaining surfaces that do not have optical functionality can be metallized without affecting the operation of the system. We cover those surfaces using a stencil made from a 1 mm wide stripe of Kapton (polyimide adhesive film) which overlays the area drawn in Figure III.15(a).
In a preliminary process, we cut the said Kapton stripe manually with a blade and a pair of binoculars. We position, again manually, the stripe on the optical piece using a pair of tweezers. The result of such step is shown in subfigures (b) and (c).

---

[a] We will see hereafter, that the F and S subsystems are not functional due the stray light dazzling from the source. Thus, those systems should not have mirrors that can redirect stray light toward the retina.

In a future process, the fabrication of such stencil should be computer-assisted: for instance CNC cutting, laser ablation or lithography.

The metallic layer is deposed by PVD: first with a 10 nm titanium layer, followed by a 100 nm gold layer. The roughness on the top surface is far from ideal. Fortunately, preliminary studies have shown that the silica/metal interface is well preserved, in terms of surface quality, which justifies the use of such process to manufacture internal reflectors. The thin layer of titanium has the function of ensuring the adhesion of the gold onto the fused silica. Indeed, we have observed phenomena of detachment in the absence of such a layer. The use of gold as the coating material is motivated by its reflectivity on a range from red to NIR, which is weakly impacted by the titanium layer.
In order to prevent any movement of the sample during vacuuming of the PVD chamber, the covered piece is attached to the sample holder by means of a Kapton tape on a non-critical area. After this step, the parts that were not to be metallized are revealed, by simply removing the Kapton stencil with tweezers (see, Figure III.16(a, b)). The final optical piece, with its selectively deposited mirrors is presented in Figure III.16(c).

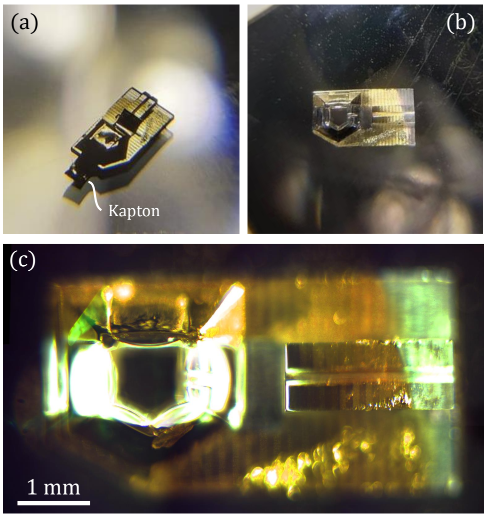

Figure III.16: *(a) Photography of the optical piece after the metallization step. (b) Photography of the optical after the removal of the Kapton stencil. (c) Optical top view of final optical piece with its selectively deposited mirrors.*

In the future, a specific mirror deposition process will have to be developed in order to be compatible with our polymer pieces.

III.3 Characterization of the optical system alone

III.3.1 Experimental setup

Preliminary tests were performed with the optical system only (without the holed retina). To do so, we packaged our optical system with an upper and a lower shell (see, Figure III.17) that were fabricated using the same high resolution (25 µm voxel) SLA-3D-printer that made the cloaker in Chapter II (Form 2 printer by Formlabs).

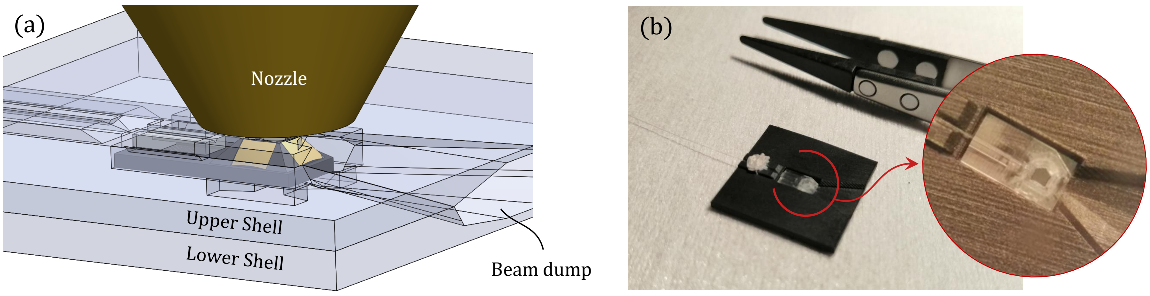

Figure III.17: (a) Assembled 3D models of the shells. (b) Photography of the lower shell holding the lenses aligned with a fiber.

The shells contain a housing with precise dimensions for the optical system, an upper 1 mm circular air channel aligned with a metallic nozzle, an opening aligned with the back diopters, an additional V-groove and beam-dump for stray light evacuation. The air stream is injected into the upper part through the nozzle so that the optical path is not obstructed by fluidic parts. In a future set-up, the air-stream will be injected from the back, trough the holed retina, as it would prevents particle soiling.

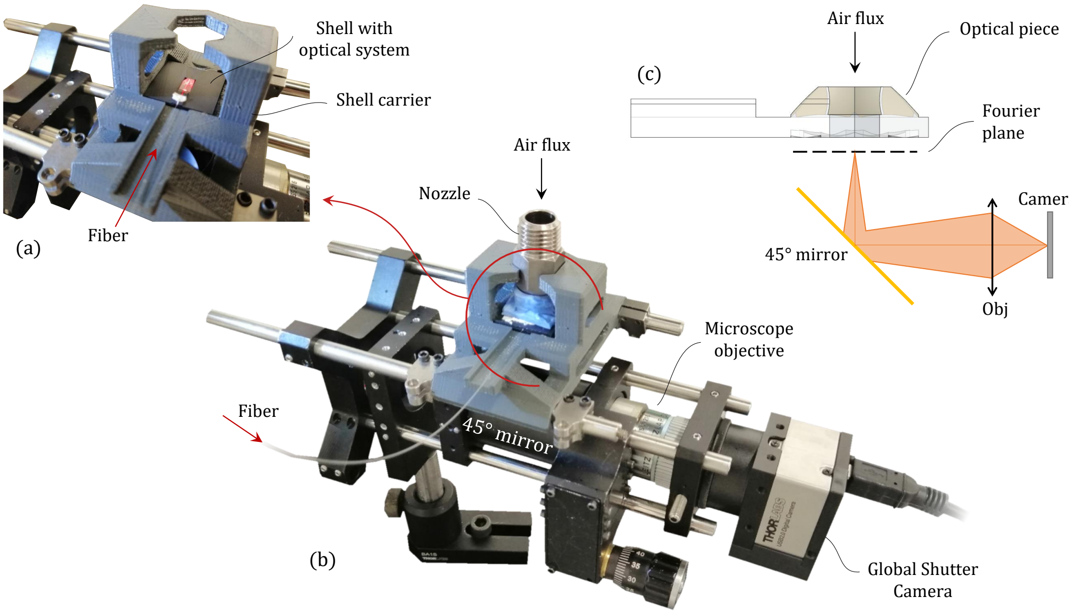

Figure III.18: (a) Close up view of the optical system under test. (b) Photography of the optical characterization setup. (c) Schematic of the bench's optical relay setup (not to scale).

We use a multimode pigtailed fiber (MMF 105/125) with low divergence (NA = 0.1) illuminated by an AlGaInP laser diode (LD) operating at a wavelength of 637 nm and with an optical power of 5 mW (HL63102MG by Oclaro). The Fourier plane is not accessible in this set-up but we can relay it using a microscope objective (NPL 10x/0.2 NA objective by Leitz Wetzlar) in reverse orientation onto a bared Global Shutter CMOS monochromatic image sensor (Thorlabs USB2.0 CMOS Global Shutter camera). The optical characterization setup is illustrated in Figure III.18.

III.3.2 Scattering signature of a smoke canister

We take a reference image (see, Figure III.19) with light on, and no air stream. The sensing area was previously cleaned up with dry air. Every image of scattering signatures will have this reference subtracted.

We observe that the Forward Region Of Interest (F-ROI) is completely bloomed by the illumination beam, the Backward ROI (B-ROI) is partially bloomed by the scattering at the end of the fiber. These white surfaces are blind areas beyond the dynamics of the pixels. However, the BS, S and FS ROIs receive very few stray light. Therefore, we will evaluate only these three ROIs to reconstruct scattering signatures with total FoV as wide as 90°.

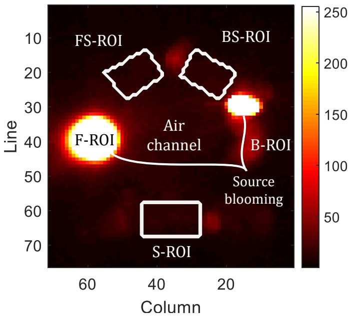

Figure III.19: Reference image.

An example of a measured scattering signature is shown in Figure III.20. It was obtained by spraying particles from an aerosol canister (Smoke Check HIS Canned Smoke by InspectUSA) in the nozzle. Subfigure (a) is the image obtained (reference subtracted) in the presence of the aerosol.

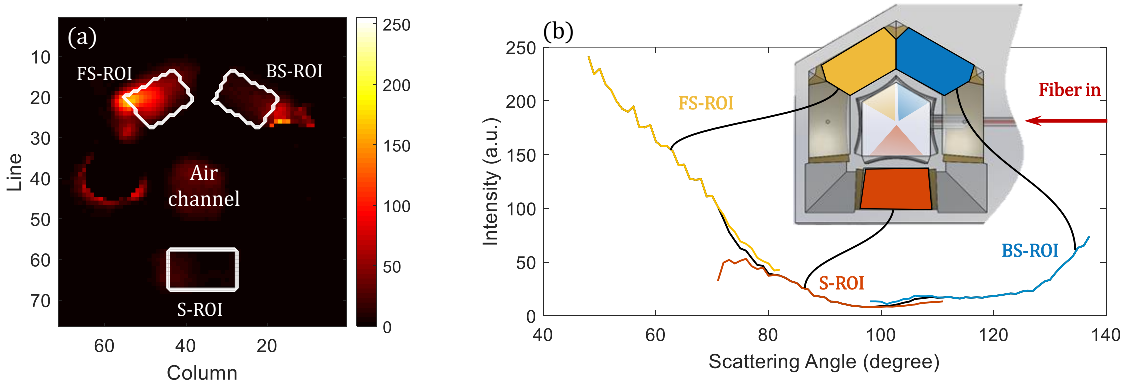

Figure III.20: (a) Example of experimental image. (b) Reconstructed signature.

The procedure to reconstruct a signature is pretty simple: let us first consider one of the three ROI separately (white contours). First, every pixel in the ROI is normalized using the simulated intensity map calculated previously using a RT simulation (intensity map in Figure III.10(a)). This step allows to compensate the intensity drop observed at the edge of the ROI. Then, for every scattering angle, we locate every pixel within the ROI associated with this very angle, by using our angle map, also calculated by RT simulation (see, Figure III.10(a)). The intensity associated to this scattering angle is the average value of these corrected pixels. With the FS, S and BS ROIs, we can draw three curves and reconstruct a scattering signature (subfigure III.20(b)).

One notices that noise due to stray light is quite important for low-scattering angles ($50 - 60°$). Also note that the curves are not perfectly overlapping: the edges of the individual curves correspond to blind field and should not be over-trusted. This overlapping mismatch will not bother us much as it appears to be very repeatable. It is most likely linked to the optical piece itself and thus, easy to correct in post-process, for example with a single calibration. To connect the curves, we make averages on the overlapping regions. The averaging weight varies linearly from 1 to 0, dropping at the edge of each curve. With this step, one can have a continuous merged curve (drawn in black), which is more representative of real scattering signatures. The reconstruction of the signature was extremely simple compared to the planar projection set-up (see, Section II.4), which gives us confidence that procedure is compatible with low energy portable applications.

In Figure III.21(b), we plot three signatures obtained with images that were recorded at different spraying events. These signatures have been normalized for comparison: we can see that the system allows to obtain signatures with a good repeatability, where the overall brightness provides us with information on the particle concentration.

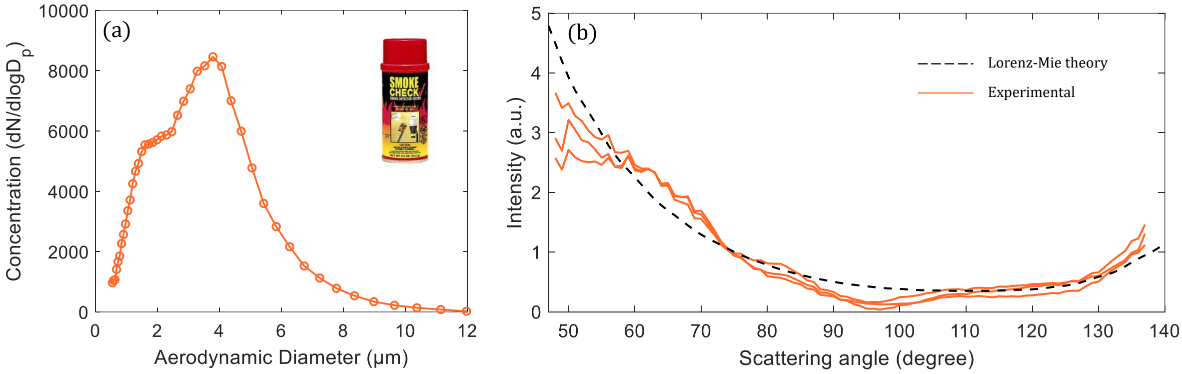

Figure III.21: *(a) Distribution of the aerosol canister (Smoke Check HIS Canned Smoke by InspectUSA). (b) Reconstructed signatures compared with Lorenz-Mie theory.*

It is noteworthy to precise that in this setup, with a nozzle above the system, the piece is highly subjected to particle soiling. Thus, we can't spray too much particles from the canister to the nozzle. If so, the optical piece has to be dismounted and cleaned. Cleaning such piece can be tricky, usual methods like pulsed ultrasound baths with solvents didn't show any results. An efficient method we have tried is a mechanical cleaning using polyurethane foam precision swabs (Texwipe TX750E).

Particles from the aerosol canister were not calibrated in size. However, we can still compare these signatures with modelled ones. Let's consider the distribution of the aerosol sprayed by the canister: this distribution is presented in Figure III.21(a) and was measured with the Aerodynamic Particle Sizer APS Spectrometer 3321 by TSI. It shows two log-normal modes with a main mode peaked around 4 µm and a smaller mode around 2 µm. Assuming that particles are spherical (which is reasonable considering that this aerosol is made of droplets), we model the signature using the Lorenz-Mie theory (see, Appendix B). The signature of the total aerosol $S_t(\theta)$ is computed with signatures $S(\theta, D_a)$ of spheres integrated over the aerodynamic diameter's distribution $n(D_a)$ measured by the APS:

$$S_t(\theta) \propto \int n(D_a) \cdot C_{scat}(D_a) \cdot S(\theta, D_a) dD_a \tag{III.1}$$

Were θ is the scattering angle, D_a the aerodynamic diameter and C_{scat} the scattering cross-section. The refractive index used is that of butane[13] ($n = 1.3326$ [156]). The signature computed is then compared with experimental ones in subfigure III.21(b), with a good accordance. Note that the model is based on a continuous integration over the diameter, resulting in a strong smoothing of Mie's oscillations. In a real aerosol with a reasonable concentration (*i.e.* with a finite number of particles), the distribution should be drawn at random, which would possibly allow us to resolve slight oscillations. The experimental signatures appear to exhibit those slight oscillations, but tests on a wider variety of aerosols will be required to conclude on this point. In the future, new versions of the device and the experimental setup should be tested with our calibrated aerosol test bench (see, Appendix D). This will allow us to conclude whether or not we can resolve Mie's oscillations on single particles, or multiple particles.

---

[13] In reality, the aerosol is a mixture of butane, isobutane, n-octanol and water, as disclosed in the the product's safety data sheet. Considering butane as the sole media does not appear to induce noticeable errors. Moreover, the refractive index of all four of these liquids is very similar.

III.4 Optical system coupled with a holed retina

III.4.1 Experimental setup

In this section, we design the assembly of the optical piece mated with the holed retina. To do so we have to design new shells in order to bring the optical piece at close proximity with the retina, at a distance BFL $=$ 0.37 mm. It is noteworthy to precise this first iteration of the optical system was designed prior to the final design of the holed retina: we will have to make slight re-purposes of this retina. In Figure III.22(c), we can see a top view of the optical system aligned with the holed retina. For this part we have to discard the denomination 'forward' and 'backward' previously used as it doesn't make anymore sense in this setup: the matrixes will simply be referred as half-matrixes. Here, we find that we can align the S subsystem with a first half matrix; the FS and BS subsystems will share the second half matrix. Bloomed subsystems F and S fortunately fall partially over the blind areas of the retina. We can see that the matrixes are not perfectly aligned with the different ROIs of the coincidental Fourier plane. Moreover, the channel changes dimensions from the silicon chip (0.5 mm × 2 mm oblong profile) to the optical piece (1 mm, pentagonal profile). A second iteration of the optical piece will have to be designed fully compatible with this specific retina.

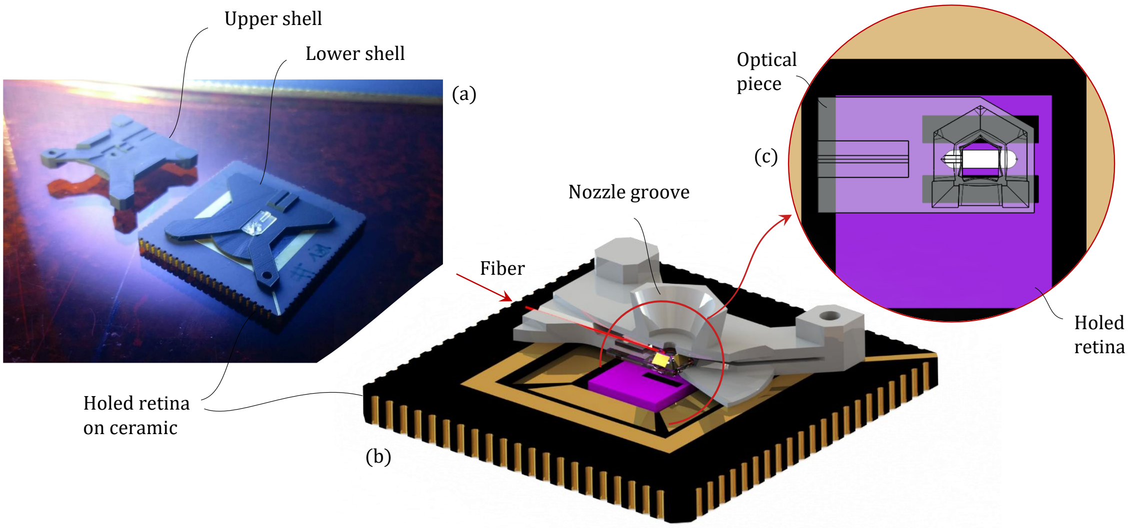

Figure III.22: (a) Photography of the shells partially assembled with the optical piece and the holed retina. (b) Schematic of the assembly (partial cross sectional view). (c) Top view of the optical system aligned with the retina.

The new shells were designed and fabricated in the same fashion as the previous ones. Figure III.22(a,b) shows the shells mounted on the holed retina. The lower shells is sized to fit within the socket of the Creapyx motherboard [133] as in Chapter II. It contains housing for the optical piece and shows apertures in front of the three functional subsystems (S, FS and BS subsystems). The bloomed subsystems (F and S) are intentionally cloaked by baffles within the lower shell to protect the retina from stray light. However, the lower shell has some issues due to fabrication limitations: the SLA-3D-printer (Forms 2 by Formlabs) is not able to print thin polymer sheets as small as BFL $=$ 0.37 mm. We had to print thicker lower shells: the optical piece is then defocused by almost 0.1 mm. An other issue is that, even with a thicker shell, cloaking baffles are still thin enough to transmit (and scatter) light from the source: partially failing at their purpose. The upper shell has no particular features apart from a conical groove that can align a metallic nozzle that would capture the air flow that comes from the back of the ceramic.

III.4.2 Unsolvable blooming issues

First tests have shown that the use of such shells to assemble the whole system successfully aligns the optical piece with the retinal horizontally. However, in this setup, the retina is completely dazzled by stray light from the source, which results in a full image of saturated pixels when using reasonable integration time and optical power. Such setup cannot be used for particle detection (see, Figure III.23).

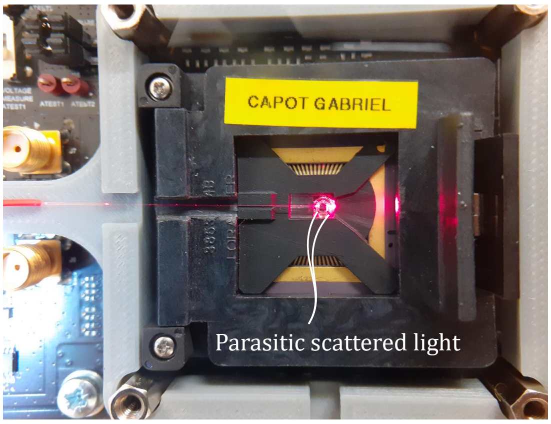

Figure III.23: *Photography of the system showing a large amount of parasitic scattered light.*

In preliminary tests described in the previous section, the microscope objective and the long optical path (see, Figure III.18) could easily filter stray light, making possible the recording of images. In this case, we are especially sensitive to scattered light from the end of the fiber as well as from the illumination beam that crosses diopters (ghost reflections and scattering, even with our optical grade polishing). In this design, the fiber is in contact with the optical piece, and the illumination beam crosses several diopters, making the system unable to operate.

III.5 *Advanced design: a second iteration*

The first iteration failed at delivering images with the full set-up (optical piece mated with the holed retina). It however, succeeded at pointing some of these 'glaring' weaknesses. From this return of experience, we have identified several improvements and modifications to make. We have mostly in mind stray-light management:

i The illumination path must be completely free of optical elements (removal of F and S subsystems), so that the system is not sensitive to scattering by diopters.
ii The illumination system must be separated from the optical piece (no V-groove).
iii The subsystems must have greater BFL so that a cloaking device with efficient stray light protection could fit between the optical piece and the retina.
iv The assembly should feature anti-cross-talk geometries.
v The systems must be designed with maximal compatibility with the holed retina.
vi The geometry should facilitates the positioning of a stencil for the mirror deposition.

III.5.1 *Design of the advanced subsystems*

The design of the second iteration of the optical system [157] comes with the knowledge of two main things. Identified weaknesses of the first iteration of the optical subsystem and a better understanding of the design tools (Zemax Optic Studio, Sequential mode). Then, three subsystems should be made: a first 90° centered system called S ('Side') subsystem and two symmetrical $90 \pm 30°$ called FS and BS ('Front-Side' & 'Back-Side'). Let's focus first on the S subsystem illustrated in Figure III.24(a).

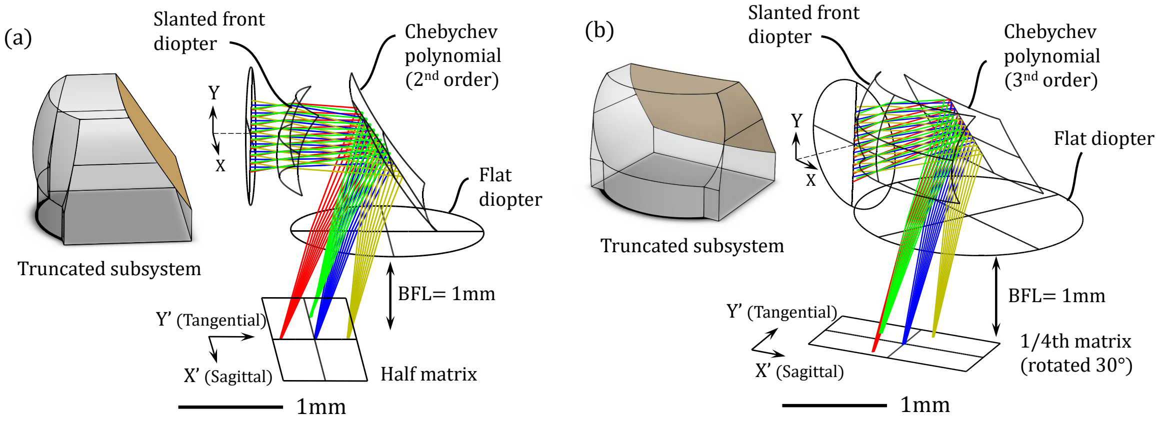

Figure III.24: *(a) Design of the S subsystem alongside its truncated model. (b) Design of the FS/BS subsystem alongside its truncated model.*

The system is designed with full compatibility with a half matrix and has a longer BFL = 1 mm. This allows us to fit an efficient cloaking device within the BFL (see, hereafter), it also allows us to use a single focusing surface instead of three, simplifying the fabrication step. Only the front surface is curved, the back surface being a simple flat surface unprocessed from the substrate[14], thus removing the need for a backside process. The front diopter is slanted by 10° in order to facilitate an eventual unmolding process. Then we can improve the uniformity of the PSF: we do so by engineering an internal reflective surface that corrects the aberrations. This reflector is a freeform surface defined by an optimized Chebychev 2D-polynomial [158]. We used third order polynomials for Y (tangential) but only second order polynomials for X (sagittal) as it creates symmetrical surfaces with respect to X, satisfying the symmetry of the setup. Due to the relative position of the front surface and the half matrix, the reflector is not slanted at 45° like before but at 33.5° so that the optical axis is rightfully aimed at the center of the half matrix. The sub-FoV is even wider than previously: up to 60°.

---

[14] The surface facing parallel (scattered) rays is the one that should be curved for lesser aberrations

Now let us focus on the FS (or BS) subsystem. The same rules were applied, however the image plane (a quarter matrix[a]) is rotated by 30° with respect to the front surface because a different viewing angle of scattering signatures is evaluated: Figure III.25 presents a top-view of the geometry, showing the relative position and tilt of the subsystems with respect to the half-matrixes. For readability reasons, only the front surfaces, internal reflectors and retinae are drawn. The main difference compared to the S subsystem is that the X symmetry is broken. Thus, the freeform reflective surface cannot be X-symmetrical: that's why we also use a third order Chebychev polynomial for X. The FS and BS subsystems are symmetrical with respect to the separation plane of the two halves of the second half matrix, as seen in Figure III.25.

---

[a] The second half matrix is shared by the FS and BS subsystems.

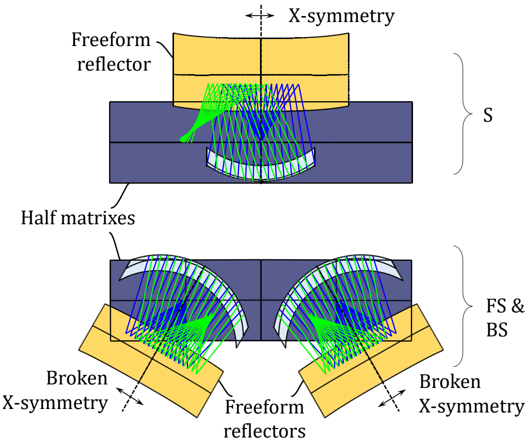

Figure III.25: *Schematic top-view of the three subsystems aligned with the two half-matrixes.*

As for the first iteration, we plot in Figure III.26 the Huygens' MTF of the advanced design in order to evaluate its performances. In particular, we want to know if the freeform surface did correct our previous issues, which are field curvature and astigmatism.

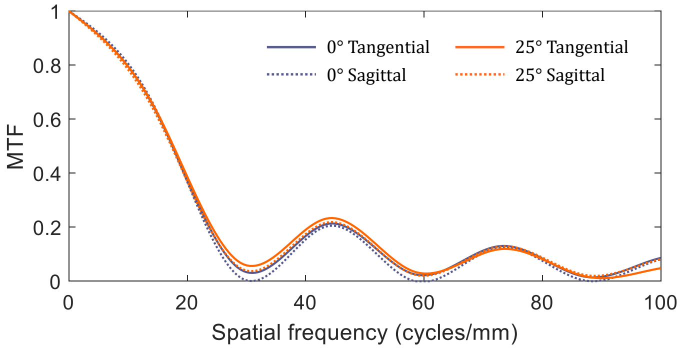

Figure III.26: *Tangential and Sagittal MTF of the second iteration subsystem at 0° and 25°.*

The likeness of the sagittal and tangential MTF curves suggests that we have a nice circular blur. This is maintained both with an on-axis and with a 25° inclination, which testifies for a uniform blur spot throughout the surface of the retina. The resolution is, however, a bit worse than for the first iteration (see, Figure III.5) which was over-engineered compared to the resolution of the holed retina. As a recall, the Nyquist frequency of our retina is $f_N = 50$ cycles/mm. Here, the contrast is completely lost at about 30 cycles/mm, which could be interpreted as low, at least compared with f_N. It means that our blur spot is a bit larger than a pixel, which is quite advantageous for our application. Indeed, we don't need to record scattering signatures with a pixel's resolution, we even blur the image in post-process (Gaussian blur, $\sigma = 2$ pixels) to attenuate noise and other artefacts.

Again, to visualize the effects of the second iteration subsystems on the recorded image, we perform image simulations on the three subsystems (see, Figure III.27)

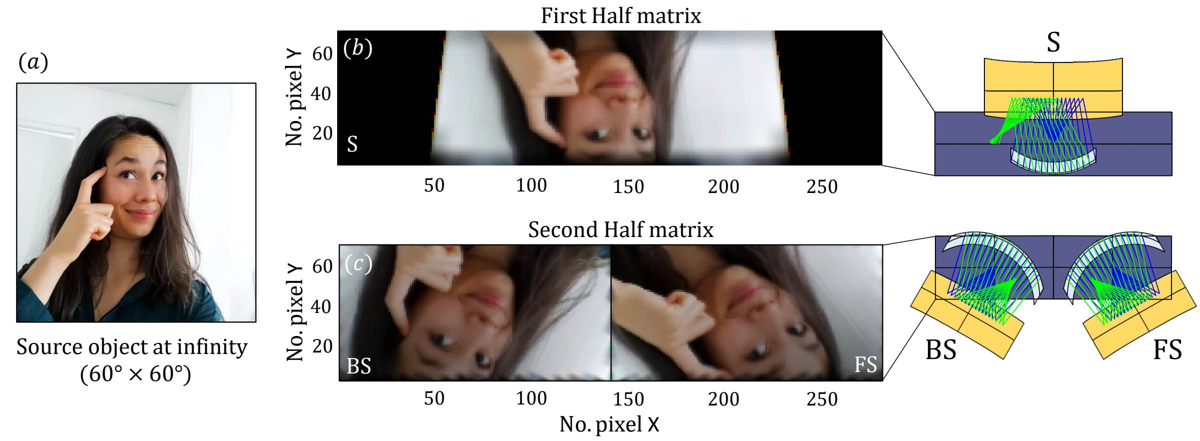

Source object at infinity
(60° × 60°)

Figure III.27: (a) Picture of Marine as a source object at infinity. (b) Simulated images obtained with the S subsystem on a first half matrix and (c) with the FS and BS subsystems sharing the second half matrix.

The advanced design (second iteration) shows great improvements compared to the first iteration (see, Figure III.6) as shown in the image simulation. As expected, the FS and BS images are shared on one half matrix, and rotated by ±30°. The magnification is rightfully adapted to a half matrix of our holed retina and the PSF appears good enough for scattering signature imaging, with a nice circular blur (and a very slight sagittal coma aberration).

Note that the beam axis is aligned with the elongated directions of the matrixes, and not perpendicular such as in Chapter II. Such modification was made because the subsystems have a wider sub-FoV in the elongated direction of detection.

III.5.2 Fabrication of the monolithic glass optical system

In the same fashion as the first iteration, all subsystems (S, FS and BS) are merged into a unitary piece as shown in Figure III.28. In this system, the fiber alignment V-groove have been removed so that the beam can be formed externally with minimal stray light. The beam path is free from any optical elements. We've kept a flat, unprocessed, surface on top of the optical piece, so that the positioning of a stencil is facilitated, in order to robustify the process of depositing mirrors.

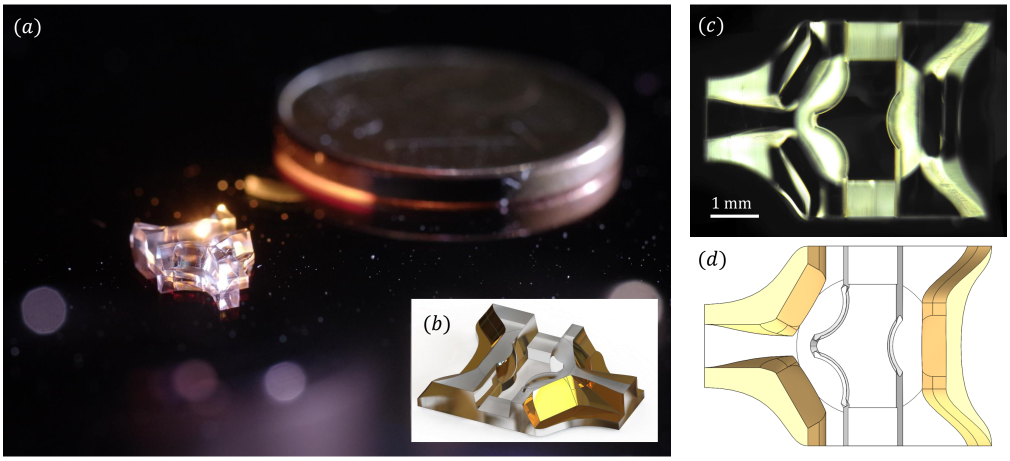

Figure III.28: (a) Photography of the fabricated optical system next to a one euro cent coin. (b) 3D view of the optical system. (c) Optical view of the fabricated glass piece. (d) Associated view of the original drawing.

This second iteration optical system was fabricated once again by the FEMTOprint company, by laser micro-machining on fused silica and selective polishing. Details on the fabrication process were already discussed on Section III.2.1. Here, the polishing process was optimized compared with the one used for the first iteration. Moreover, the slanted freeform surfaces were designed easily accessible by the polishing tool, this enables us to polish those surfaces and reach roughness values between 5 nm and 15 nm (Ra). The flat unprocessed surfaces on the top, as well as the flat back-face, have a pristine surface quality, unmodified from the original glass substrate. Figure III.28(c) shows an optical view of the polished glass piece[15]. As a comparison, subfigure (d) is a tow-view of the original drawing, which shows the great fidelity of the fabricated piece compared with the parent model.

Using the same process as described in Section III.2.3, we selectively deposit the mirrors on the freeform surfaces, using a Kapton stencil (see, Figure III.29(a)) and a PVD metal deposition (subfigures (b, c)).

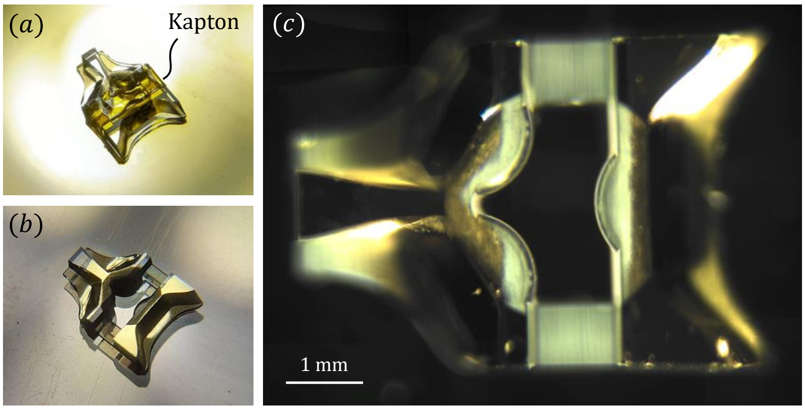

Figure III.29: (a) Photography of the optical piece with the Kapton stencil. (b) Optical piece after the metallization process and stencil removal. (c) Optical top-view of the final optical piece.

---

[15] Note that the rough surfaces (machined surfaces without polishing) appear bright because they scatter light, whereas the polished and pristine surfaces (*e.g.* the slanted freeform surfaces) appears dark, which testifies to an excellent surface quality.

III.5.3 Optical system assembly with a cloaker and a holed retina

In Figure III.30, we show the arrangement of the optical piece in relation to the holed retina. Such a figure is useful to visualize the space constraints, and to verify the alignment of the optical sub-systems with respect to the half matrixes and the fluidic channel.

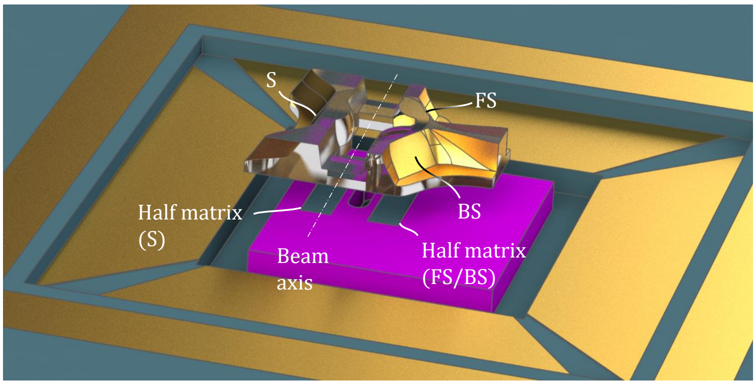

Figure III.30: *3D view of the monolithic advanced optical system aligned with the holed retina.*

We have designed a specific lower shell (or cloaker) also optimized for stray-light management. In particular, the lower shell is built with cloaking features than can fit within the BFL of the optical piece. Such a cloaker, which is presented in Figure III.31, is printed with a SLA-3D-printer (Form3 by Formlabs) using adaptive voxel resolution (down to 25 μm) using a black photopolymer resin.

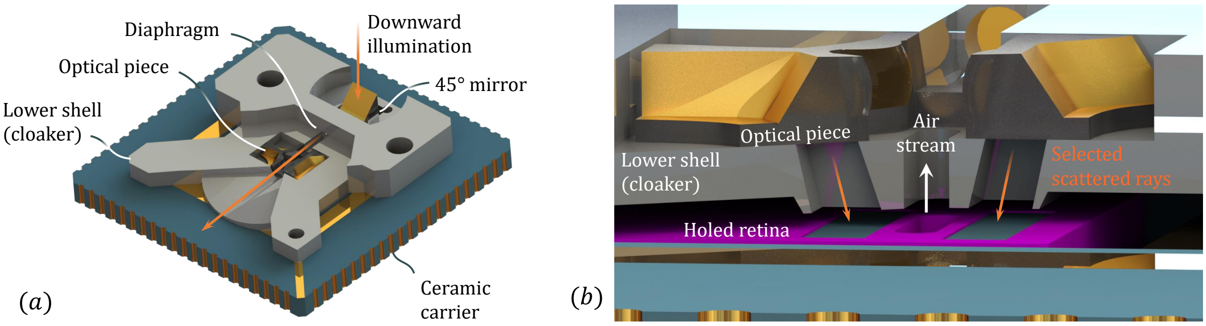

Figure III.31: *(a) 3D view of the second iteration optical piece with the lower shell (cloaker) and the holed retina mounted on ceramic. (b) Cross-sectional view of the optical setup, showing the optimized apertures.*

Unlike with the first iteration, the illumination system isn't directly integrated with the optical setup. This choice is motivated by the fact that such an optical piece can be studied separately from the illumination system. And that consequently, the latter can be interchanged easily, within the framework of an iterative approach to development. Moreover, separating the illumination system from the optical piece allows to implement elements that can protect the detectors from stray light coming from the source. Thus, we chose to implement a 45° mirror (3 mm wide), which sits on the cloaker, and separated from the optical piece by a diaphragm printed with the cloaker (see, Figure III.31(a)). By doing so, one can insert an interchangeable illumination module, as long as it provides a downward beam that recovers the pupil of the mirror. Preferably, such an illumination system would be designed in a similar way to the miniature refractive-refractive optics present in the optical piece itself, and would allow to form a beam over the fluidic channel from a bare laser diode (LD). In our case, for reasons of supply, we use a system consisting of a commercially available bare LD (637 nm, 5 mW), and aspherical lenses contained in a standard 0.5 inch optical tube. Further details on the illumination module will be provided in Appendix G.

Below the optical piece, the shell has optimized apertures that can select the scattered rays that were transformed by the optical system, as shown in subfigure (b). These apertures are slanted with the angle defined by the folding mirror (see, Figure III.24).

As for the first iteration of the optical piece, we compute its angular response, when associated with the lower shell and its optimized apertures, using a RT simulation (see, Figure III.32)

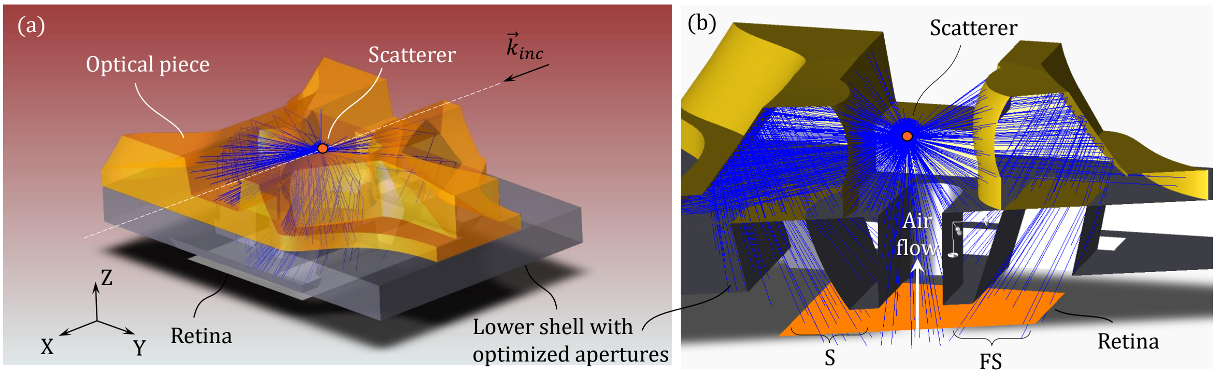

Figure III.32: (a) 3D view of the RT simulation of the second iteration optical system. (b) Close up cross sectional view.

In the same manner as for the simulation presented in Figure III.10 for the first iteration, we compute the angular response for both a centered and a displaced scatterer. The position of the displaced scattered with respect to the center of the channel is the same as for the simulation made for the first iteration: $(x_p = 100\ \mu\mathrm{m}, y_p = 15\ \mu\mathrm{m}, z_p = 10\ \mu\mathrm{m})$. Results are shown in Figure III.33.

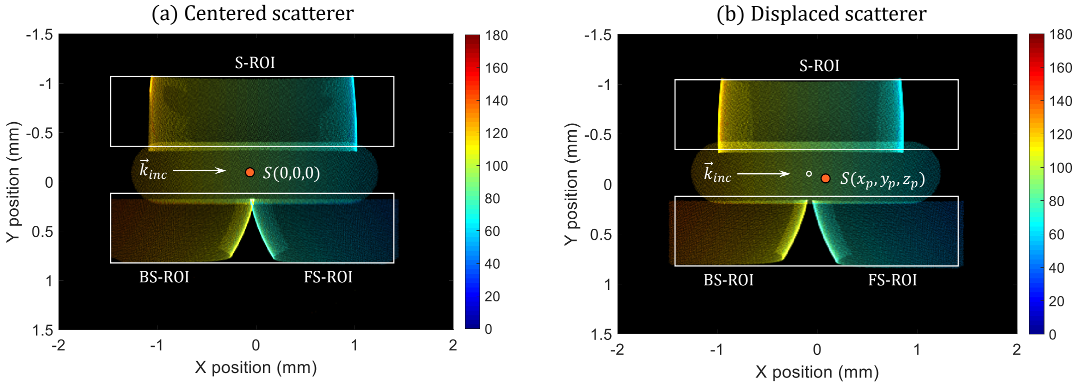

Figure III.33: Angular response (in degrees) of the second iteration optical system evaluating (a) a centered scatterer and (b) a displaced scatterer.

We have drawn white rectangles, that correspond to the two submatrixes. Again, we verify that the S-ROI falls on a first half matrix and that the FS and BS ROIs share the second half matrix. Thanks to the new design of both the optical piece and the cloaker, we do not observe evidence of cross-talk effects in the retina. Moreover, the total FoV was increased up to 110°. The position insensitivity appears to be maintained, as pixels are coloured the same in both subfigures. The transformation of the pupil's image of each subsystem is much fainter than in the previous design. Indeed, the optical path of scattered rays is longer, thus the relative displacement is smaller. Based on those simulations, the new design appears much better than our first iteration, and is fully compatible with our holed retina

III.5.4 Characterization of the advanced system

The characterizations of the second iteration optical piece are performed in the same fashion as for the lens-less setup (see, Section II.3), by using the Creapyx motherboard that drives the holed retina, and the aerosol test bench (see, Appendix D) that provides a continuous flow of calibrated particles, which are commercially available PSL spheres in our case.

A photography of the characterization setup is given in Figure III.34. The optical piece is sitting on the lower shell (cloaker) that properly aligns it with the holed retina below. As explained earlier, the downward illumination is provided by the illumination module (standard 0.5 inch lens tube, with a LD and aspheric lenses, see Appendix G), and redirected horizontally toward the muzzle of the air channel using a 45° mirror.

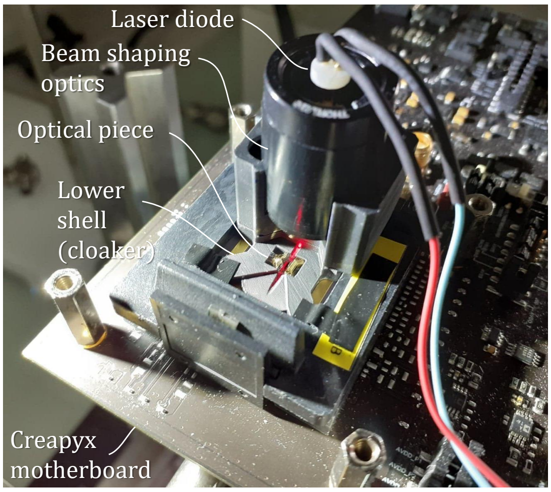

Figure III.34: *Photography of the characterization setup.*

In the photography we see that, despite the diaphragm, a large portion of stray light comes toward the optical piece, hitting some of its diopters.

Then, we take a reference image, using the holed retina when no aerosol is injected in the channel. Such a reference is presented in Figure III.35, and will be used as an offset to be automatically subtracted to future images. We notice that, a portion of the lower half matrix is impacted by stray light (the half matrix that evaluates the FS and BS ROIs), but not to a great extend.

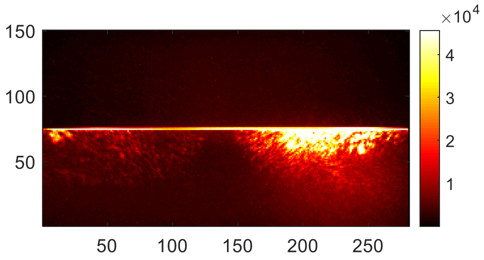

Figure III.35: *Reference image without particle.*

Given the visible amount of stray light hitting the optical piece, and the reasonable amount that ends up on the retina, one might argue that the anti-stray-light designs were successful, at least for our given illumination setup.

As described in Section II.3, we record bursts of 32 images, in global shutter (GS) mode, and we follow the standard deviation of the full image (with its reference subtracted)[16]. Then, an image is saved when its standard deviation reaches a given threshold.

We must note that such a setup is not perfect, notably in terms of robustness against misplacements, at least in its current state. Indeed, 3D printed pieces have not been drawn with carefully optimized tolerances. This results in a play on most of the elements, making the relative alignment of the air channel, the cloaker, the optical piece, the 45° mirror, and the illumination module not very robust. In the near future, such a setup could be greatly improved by conducting a proper calibration of the printer.

Despite the use of a not very robust set-up, we were able to detect single PSL particles of 3 µm and 830 nm. Examples of representatives signatures that can be experimentally recorded are given in Figure III.36(a,b)[17]. Hopefully, once a correct alignment is found, the images obtained are quite repeatable for

---

[16] Unlike the lens-less setup reported in Chapter II, not only the 'forward' matrix is evaluated, because the scattering the signature is projected in a more even way.

[17] We see, in experimental images, that the signature is quite rough, it might be an indication of small surface irregularities. If so, it could be a way to discriminate smooth particles such as droplets.

a given aerosol, both in terms of brightness and patterns. This can already give us confidence that the signature is weakly impacted by particle position, due to the Fourier-domain imaging setup.

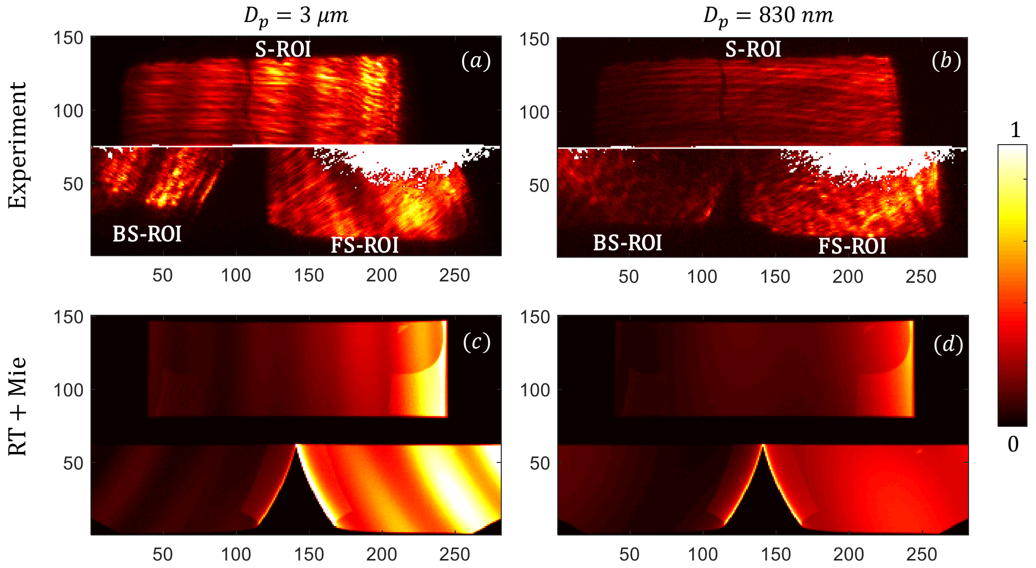

Figure III.36: Experimental images of scattering signatures of PSL spheres: (a) 3 µm *and (b)* 830 nm*; compared with associated computed signatures: (c, d) respectively.*

We observe three separated areas, that correspond to the S-ROI on the upper half matrix (rows 76 to 150); the BS and FS-ROIs on the lower half matrix (rows 1 to 75). We notice that the positions of such ROIs are slightly translated compared to what was expected, due to the alignment problems mentioned above. The white pixels correspond to pixels from the reference image that reached a certain threshold, that were removed from the image processing, in order to be less sensitive to Poissonian-type noises.

The scattering signatures of large spheres, such as the 3 µm PSL, exhibit a number of Mie's oscillation, whereas the 830 nm PSL does not (at least within the evaluated FoV). This effect is predicted by the Lorenz-Mie theory (see, Section I.3), and be can be found on the RT simulations for the associated PSL diameters (see, subfigures (c, d)). The oscillation of 3 µm PSL signatures facilitates the interpretation of such a recorded signature. For didactic reasons, we are going to focus in particular on this specific image Figure III.36(a):
We observe several vertical oscillations on the S-ROI, whereas those on the BS and FS ROIs are slanted by ±30°, which was expected by design. Those oscillations follows the iso-θ, which are defined as the trajectories on the retina that correspond to the rays scattered with the same scattering angle.
In order to reconstruct a scattering signature from the recorded image, we perform the same procedure as described in Section III.3.2, here we quickly recall the basic steps. By using a computed angle map, as shown in Figure III.33(a), one can associate each pixel of the retina to a scattering angle. For a given scattering angle (with a tolerance of 1°), a mean value of the intensity carried by those associated pixels can be calculated which then results in a sub-scattering signature reconstructed within the sub-FoV of each ROIs. In this case, the ROIs are misaligned with respect to the retina, thus we had to manually translate the angle map to best fit with the recorded image. Due to this effect, the BS ROI was cropped, resulting in a loss of FoV for very high angles. Still, the total FoV is quite wide, about 85°.

Before plotting those sub-signatures together, we had to perform a correction, that consists in having a multiplicative factor for each sub-signature. This step is motivated by the fact that the relative brightness of the ROIs are not consistent to what was expected: this can be seen especially with the BS-ROI (Figure III.36(a)) that is much brighter than expected (Figure III.36(c)). Hopefully, this correction appears to be very repeatable between the different recorded images, and could be easily found through a calibration campaign. We believe that it could be imputed to misalignment errors of the apertures with respect to the subsystems' pupils, that may create an uneven loss of photometry between the ROIs.

Finally, we merge those sub-signatures, by running a sliding average over the areas of overlap of the subFoVs, as explained in Section III.3.2. We insist on the fact that the reconstruction step is particularly resource-efficient in terms of computing capabilities, especially when applying only matrix operations (which are optimized by MATLAB, our data processing tool).

In Figure III.37, we plot the merged scattering signatures, alongside the theoretical signature of a 3 µm PSL sphere illuminated by a 637 nm wavelength beam, computed using the Lorenz-Mie theory.

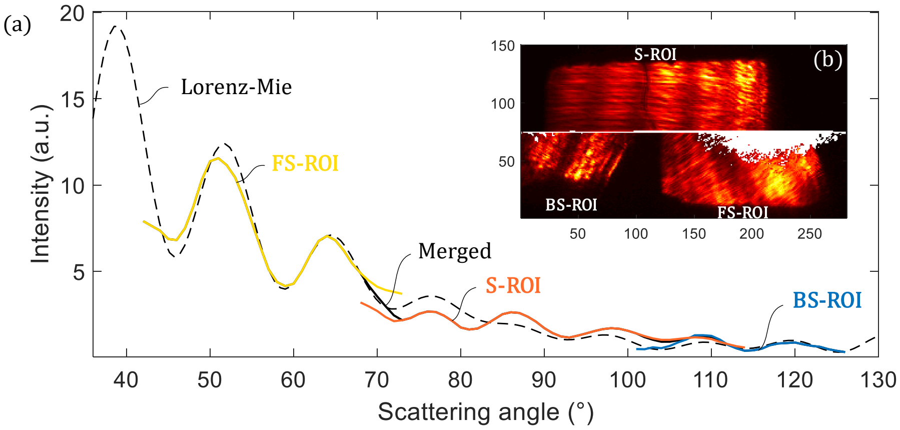

Figure III.37: *(a) Reconstructed signature from experimental image plotted with the theoretical signature. (b) Experimental image of a* 3 µm *PSL used for the reconstruction.*

Based on such a representative plot, we find that the reconstructed signature is surprisingly faithful with the theoretical one, especially with the position and frequency of the Mie's oscillations in the plot (those were not corrected). This gives us confidence that such an architecture of the sensor and reconstruction procedure is well suited for our application. However, to conclude on this point, we will have to conduct a proper statistical study, over a wide number of PSL diameters, with blind reconstructions. To do so, we will have to make our setup more robust. In the near future, the 3D printing of the cloaker would be optimized; then, the next step would be to integrate directly both the cloaker (with its optimized apertures) and the optical piece on-top the CMOS at wafer scale, in order to achieve optimal alignments.

Note that, we've modelled the Mie's scattering using circular polarization illumination conditions, even if the LD should be polarized linearly (or at least elliptically). We've made this approximation because polarizations effects on the scattering signatures are not predominant in our conditions, and because we integrate each scattering angle over the iso-θ, meaning that the polarization effects (carried by the azimuthal angle, found along those iso-θ) are mitigated. Nevertheless, it could be interesting in the future to study more carefully those polarizations effects.

In addition, a study on a larger number of particles, and on a larger diameter range could allow us to conclude on the detection limit, in terms of particle size. We can already determine with which SNR (Signal to Noise Ratio) we have detected 3 µm and 830 nm PSL. We calculate the SNR from the standard deviation of the images taken in a 32-image burst. We note that the PSL of 3 µm were detected with an SNR of about 825, while the PSL of 830 nm (which scatter less intensely) were detected with an SNR of about 145[18]. Those values are quite high already, thus we can realistically expect that we can measure smaller particle sizes using such a setup. In addition, the SNR should be further improved by optimizing the illumination system so that the amount of stray light is minimized.

---

[18] Those values were quite constant between images obtained from the same PSL diameter, meaning that the brightness and patterns of the recorded signatures are most likely much more repeatable that for the lens-less setup.

III.6 Discussion about particle identification

We recall that the principle of measuring a scattering signature is to find certain parameters of the particles that compose an aerosol, such as diameter D_p and refractive index n. To do so, we have to compare the image recorded experimentally, with a prediction from a model, usually based on the Lorenz-Mie theory and a geometrical transformation; and finally, perform the inverse problem. Such an exercise was already attempted in Section II.4 for the lens-less setup[19]. The optimization schematic used for the lens-less setup, and the Fourier-domain setup is presented in Figure III.38.

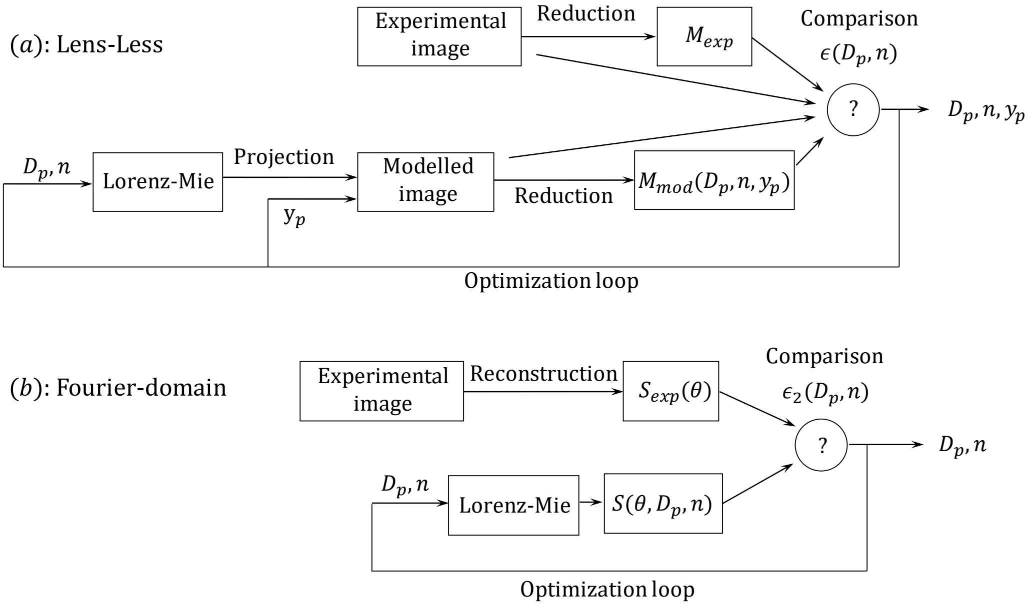

Figure III.38: Schematic of the optimization procedure used for the lens-less setup (a) and the Fourier-domain setup (b).

The general idea between both setups is to find a way to compare data retrieved from an experimental image with data from a modelled one. In Section II.4, we've developed a procedure to reduce an image (either experimental or modelled) in order to compare those. Such a procedure is schematized in subfigure (a). This procedure requires a prior computation of the modelled image. All these steps, which are relatively expensive in calculation, must be called regularly in an optimization loop. Moreover, as the image obtained depends on geometrical parameters such as the position of the particle y_p, these must be taken into account in the optimization.

In the Fourier-domain setup, the procedure (schematized in subfigure (b)) is simplified. It requires to perform the simple step of signature reconstruction $S_{exp}(\theta)$, and this only once. The computed signature $S(\theta, D_p, n)$ is retrieved directly from the Lorenz-Mie theory, and it's the only step within the optimization loop. The minimization criterion $\epsilon_2(D_p, n)$ is also much simpler than previously, which is a simple mean of a one-dimensional deviation function:

$$\epsilon_2(D_p, n) \propto \int_{\theta \in FoV} |S_{exp}(\theta) - S(\theta, D_p, n)| d\theta \qquad \text{(III.2)}$$

In the future, one could test different definitions for ϵ_2, using for instance an euclidean norm instead of a simple deviation. It could also be interesting to implement ponderations at the center of each sub-FoV where the aberrations are soft.

---

[19] We encourage the reader to get familiar with this section, in order to fully understand the present discussion.

We are now going to study the accuracy of such a procedure, in its capacity to find the correct values of D_p and n. In Section II.4, we've already plotted the map of the minimization criterion $\epsilon(D_p, n)$, used to find the correct parameters of a 3 µm PSL. For didactic reasons and for the sake of comparison, we are only considering the case of the sibling 3 µm PSL. The test images are found in Figure II.24 for the lens-less projection, and in Figure III.36(a) for the Fourier-domain projection. The maps of both minimization criteria are plotted in Figure III.39 as a function of the particle diameter D_p and n.

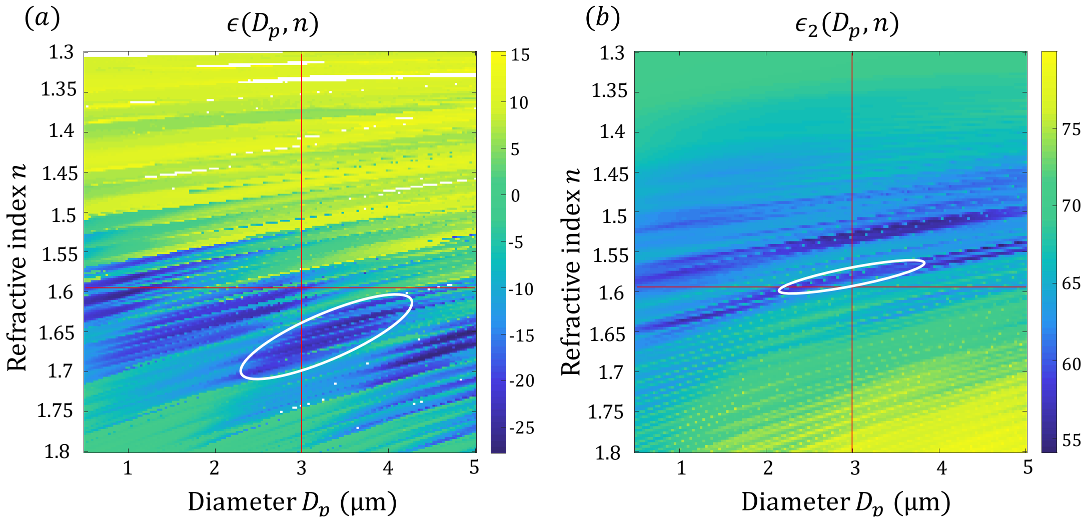

Figure III.39: *Map of our minimization criterion versus particle diameter and refractive index in logarithmic scale used for the lens-less setup (a) and the Fourier-domain setup (b).*

We draw the targeted parameters as red lines, and the reasonable local minima as a white contour. The accuracy of a procedure is judged by the extent of such a contour, and its distance from the targeted parameters. In addition, we are also interested in local minima, *i.e.* their number and prominence, for the reason that they can induce important errors in the estimation of the desired parameters.

We already discussed that, the procedure used in the lens-less setup was rather bad in view of these different judgment criteria (see, subfigure (a)). In comparison, the procedure for the Fourier-domain setup appears more successful (see, subfigure (b)), at least for the test case of a 3 µm PSL. We judge however that such a procedure is to be improved, not least because the precision is still insufficient, in particular by the fact that the valley of the local minimum is very elongated in one direction, and by the presence of another local minimum.

The direction of elongation of the local minima seems to be preserved, after comparison of the two methods. It would seem that this defect comes from the fact that similar scattering signatures can be obtained for different couples (D_p, n); and that a simple measurement of the scattering signature only allows to find a kind of optical diameter (that combines both D_p and n). We believe that it is possible to solve this limitation by simultaneously evaluating the optical diameter of the same particle (of fixed geometric diameter D_p) in two different ways, for example by recording a dichromatic scattering signature.

Then, another way to improve this procedure is, for example, to make the assembly more robust, as explained previously. Other elements could also help to reduce the uncertainty in the retrieval for parameters D_p and n, such as using the overall image brightness as a starting point for the optimization.

Again, the simple use of a 3 µm PSL example is far from sufficient to conclude on the accuracy of the procedure. To do so, we will have to perform a proper statistical study on a large number of particles, and over a wide range of diameters and types of particles (organic, inorganic, aqueous, irregular).

III.7 Chapter conclusion

In conclusion for this chapter, we have designed a second prototype that features a miniature, monolithic refracto-reflective system suited for the optical pre-treatment of scattering signatures. This design is applied to our family of PM sensors prototypes that uses holed retinae. It addresses the various areas of improvements for miniature PM sensors, that were identified Chapter II: such as the ability to collect more flux from the scatterer (with viewing angles where scattering is usually strong), particle's position insensitivity, ultra-wide FoV and simplified image processing. It features a monolithic assembly of five compact optical subsystems arranged around an air channel, that are folded onto a coincidental focal plane (see, Section III.1).

We present a state-of-the-art fabrication process for a glass prototype that was developed by FEMTOprint, that consists in the direct, 3D writing on glass, using a femtosecond laser inscription, a selective etching and local surface polishing, followed by a selective mirror deposition process. To achieve cost effectiveness for eventual volume production, we propose a replication process that uses silicone rubber molds and epoxy as the replication media (see, Section III.2).

Preliminary tests have shown good results reconstructing scattering signatures within a FoV of 90°, with very little computing cost. We have obtained repeatable signatures from a canned aerosol, that fits well with the Lorenz-Mie theory (see, Section III.3). However, the design proposed was unable to function when mated with the holed retina, as it showed critical design flaws. Its main issue is that the system was too sensitive to stray light from the source: making the retina blind to scattered light from particles (see, Section III.4).

An advanced design is then proposed in Section III.5, which is a second iteration built upon the return of experience provided by our first iteration. Such advanced optical piece, includes a free-form surface and shows greater performances in all fields. In particular, it features elements that prevents stray-light sensitivity and is fully compatible with the holed retina presented in Chapter II.

With the new design, we were able to test the complete assembly, which includes the second iteration glass piece, an optimized cloaker, and the holed retina, using calibrated aerosols. We were able to measure the scattering signature (optically processed) of single particles of polystyrene beads of different sizes. We were then able to test the reconstruction procedure of the scattering signature, which is particularly faithful to a theoretical signature. This gave promising results in solving the inverse problem, which consists in finding the size and refractive index of a particle using a theoretical particle scattering model, such as the Lorenz-Mie theory (see, Section III.6).

However, in order to conclude on the performance of such a system, we will have to carry out more in-depth tests on an assembly that needs to be made more robust. For example, it would be interesting to record signatures from a larger quantity of particles in order to perform a statistical study. Such a study would allow us, for example, to relate the detection rate to a particle concentration. We would also test our device on calibrated particles of various sizes, which would allow us to experimentally estimate a Limit of Detection (LoD) in size. Then, in order to be more representative of a real aerosol, we would perform those tests on a larger variety of particle types (such as organic, inorganic, aqueous, irregular particles).

IV

Perturbation of a PCM-based vertical cavity

Chapter content

IV.1 Concept architecture and general principles

In this chapter, a third prototype will be presented, designed with a more forward looking approach compared to the previous ones, presented in Chapters II and III. We will explore a way to detect and analyze particles with enhanced sensitivity by means of optical micro-cavities. Such structures can be manufactured using conventional micro-fabrication techniques for planar photonics. In the future, we hope to make these photonic structures conjointly with CMOS optronic chips (such as our holed retina presented in Chapter II). Amongst the different possible cavities, we are particularly interested in dielectric Fabry-Perot (FP) Vertical Cavities (VC), which are formed with two planar dielectric mirrors assembled parallel and on top of each other. The dielectric mirrors themselves are designed with a certain periodicity in the dielectric structure. In particular, a Distributed Bragg Reflector (DBR) is made by a periodic alternation of thin films with different refractive indexes; and a Photonic Crystal Membrane (PCM) is made by etching a periodic pattern on a dielectric slab. More details on DBRs, PCMs and VCs will be discussed in Section IV.2.

Here, we use the high intracavity optical intensity of such vertical cavities to enhance the sensitivity of an optical sensor: an open VC cavity is particularly relevant because a fluidic channel carrying an aerosol, fits in the space between the two mirrors (DBRs or PCMs[1]). We illuminate the system from the top, transmitting through an upper mirror and generating a vertical cavity mode. Then, particles circulate horizontally between the two mirrors, and can deliberately perturb such cavity mode. The effects of the interaction between the particle and the cavity mode is measured by transmission imaging of what we call the 'cavity-perturbation scattering signature'. The recording and analysis of the transmitted pattern could be used to retrieve properties of the particle such as its diameter and refractive index, in a manner similar to what was presented in Chapter II and III. We present in Figure IV.1, an artistic view of the prototype of a PM sensor made with a DBR and a PCM as the top and bottom reflectors respectively.

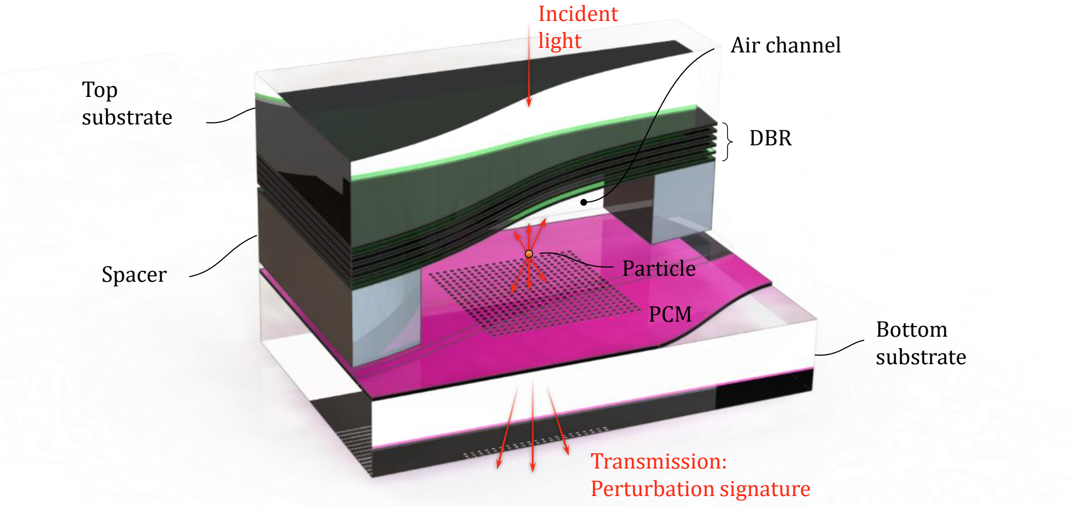

Figure IV.1: *Artistic view of the third prototype, made with an open VC formed by a DBR and a PCM (partial cross-sectional view).*

A PCM is itself a resonant structure, that is very sensitive to the inclination of the illumination beam, resulting in a rich modification of the reflected and transmitted pattern, for both intensity and phase. This part will be detailed in more details in the following. This sensitivity is usually considered as a parasitic effect that designers try to avoid (and that is not found with DBRs), but it could prove useful when applied to sensors. A PCM coupled with a VC allows us to intertwine the perturbation effects that a particle creates on the VC mode, and its repercussions on a transmission pattern, enriched by a PCM. In short, we don't measure a particle's scattering signature directly but the indirect effects of a scatterer

---

[1] A more conventional use of PhCs applied to PM sensors is to have particles interact with the evanescent field of a defect cavity [66]. We will not discuss defect cavity PhCs here. For more information, the reader is invited to consult the reference [159].

on a cavity mode.

Thus, the architecture we choose for such prototype is the following: a PCM is used as the bottom reflector, facing an imaging module at the back of the VC, that can record the cavity-perturbation scattering signature of a particle within the VC mode. This imaging setup can be a simple lens-less setup (see, Chapter II) with a CMOS image sensor directly in contact with the back side of the bottom substrate; or it can be a Fourier-domain imaging setup (see, Chapter III) that will be described later in Section IV.6.4. The top reflector is a DBR instead of a second PCM, because of its extended lateral dimensions: this setups removes the need for horizontal alignment of the two mirrors. An illumination module is facing the DBR top reflector, at the front of the VC.

We show in Figure IV.2, a schematic that illustrates the general principle of a PM sensor that uses a PCM-based vertical cavity (PCM-VC). Such an embodiment is described in more depth in patent [127]. In the absence of a particle, the excited (vertical) mode is centered on the Γ point of the PCM's reciprocal space, *i.e.* in normal incidence (see, Section IV.2.2). In the following we abusively call such a cavity mode, a 'Γ mode'. The unperturbed cavity signature is that of the Γ cavity mode.

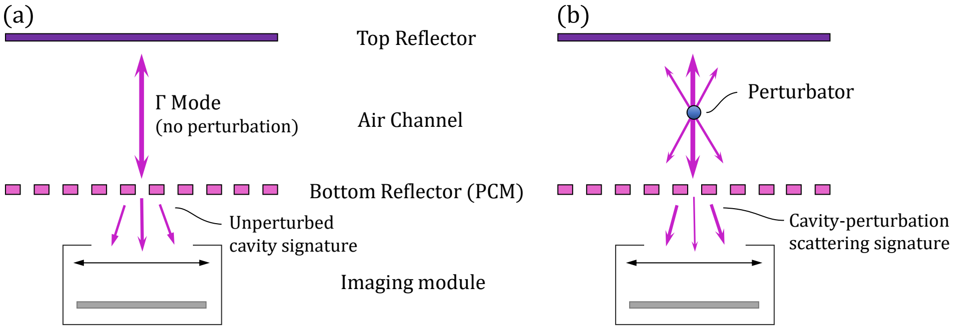

Figure IV.2: *General principles behind the mesurement of a cavity-perturbation scattering signature in a PCM-VC.*

In the presence of at least one particle, the cavity mode is perturbed: the vertical Γ mode is partially extinguished and transverse higher order FP modes appear. This cavity mode perturbation is highly dependent on the scattering signature of the perturbator (related to its size and refractive index). This perturbed cavity mode then modifies the pattern transmitted by the PCM, *i.e.* the cavity-perturbation scattering signature, that is recorded by the imaging module. Such a signature is characteristic of cavity itself but also the nature of the perturbation and therefore could allow the classification of the particle(s) present in the cavity. The effects of a scatterer on a cavity mode are illustrated in Figure IV.3 with a 2D-FDTD simulation of the perturbation of such a VC.

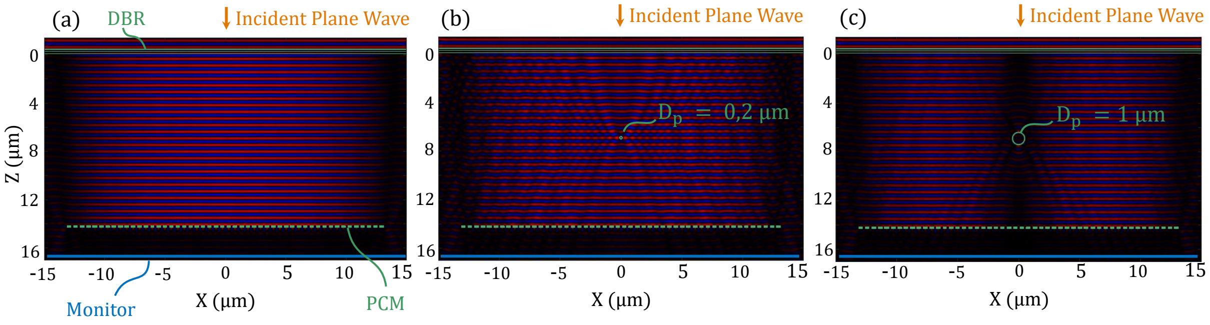

Figure IV.3: *FDTD simulation (E_y field) of a DBR/PCM VC without perturbation (a), with a* 0.2 μm *scatterer (b) and with a* 1 μm *scatterer (c), when illuminated by a P polarization (or TE polarization).*

We can see for instance that for a small perturbation (see, subfigure (b)), the vertical mode (Γ) is weakly extinguished while higher order FP modes are excited. Then, for a coarse perturbator, the main effect is the important attenuation of the vertical mode. A detailed interpretation of the phenomenon will be discussed in Section IV.4. These perturbations are presumably extremely sensitive, and would allow the detection of very small particles, which is particularly difficult with conventional light scattering methods (see, Chapter II and III).

IV.2 Introduction to dielectric mirrors

IV.2.1 Photonic Band Gaps reflectors

Passive optical devices are commonly designed to perform a given transformation of light. To do so, we commonly engineer a certain volume with a spatially variant dielectric function $\epsilon(x, y, z)$. The refractive index n is the square root of ϵ, in the following we will discuss n and ϵ alike. The most simple example of passive optical device is the spherical diopter: characterized by the discontinuity of the refractive index along a spherical surface is used to design focusing optics (principle of a lens). Then, if we reduce the size of these dielectric patterns down to the order of the wavelength, we're beginning to derive some interesting properties from these photonic structures. To cite only one example, we can design single-mode waveguides [160] made with small core with a high index surrounded by a low index cladding. More generally, a structuring of the dielectric material at the wavelength scale allows to quantify the discrete allowed modes (just like the waveguide), and therefore defines bands of forbidden modes: what is called a Photonic Band Gap (PBG) [161]. In this document, we will mainly focus on PBG structures that can perform a wide field of functions, and more specifically: reflectors.

Let us consider a dielectric material in which we have created a periodic structuration, when the period is within the order of magnitude of the wavelength in the medium (sometimes referred as the Bragg regime[2]). Devices created with a periodic dielectric function are widely called Photonic Crystals (PC, or PhC) [159, 165]. A periodic pattern can be repeated in several directions to create 1D [166], 2D [167] or 3D [168–171] PhCs. Examples of PhCs found in literature are presented in Figure IV.4.

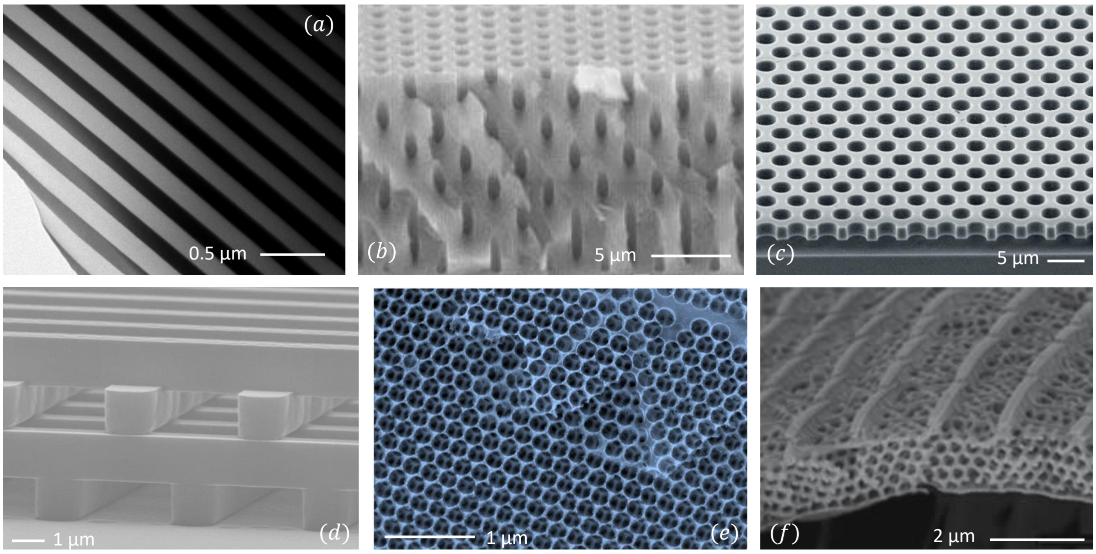

Figure IV.4: Examples of PhCs, electronic microscopy images found in literature. (a) 1D PhC [166]. (b) 2D PhC [167]. (c) 2D PhC on a slab [172]. (d) Wood-pile 3D PhC [169]. (e) Inverse opal 3D PhC [171]. Natural 3D PhC found in Vaga sp. butterfly's wing [173].

---

[2] Beyond the Bragg regime, is the Sub-Wavelength Grating (SWG) regime [162] where light becomes only sensitive of a average refractive index. This way one can access a continuum of refractive indexes using only two materials [163, 164].

By analogy with the physics of electron waves in semiconductor crystals, the behaviour of electromagnetic waves in a PhC can be described by Bloch modes [174–176] (waves that are delocalized over the span of the crystal, which results from the folding of the guided mode due to the periodicity of the lattice) and the field of study can be restricted to the first Brillouin zone in the reciprocal space (wavevector space), by plotting the photonic band diagram. In semiconductors, the geometry of the crystal's lattice can generate an energy band gap that forbids the propagation of electrons. Concepts and terminologies stemming from solid-state physics and semiconductor physics are not developed intentionally, the reader is encouraged to consult the references [177, 178] if needed. Thus, by analogy, a PBG structure is a particular use of a PhC, with specific geometrical conditions on the lattice, that allows the generation of a band gap in the photonic band diagram.

For simplicity, we will first describe the case of a 1D-PhC mirror, widely refereed as a Distributed Bragg Reflector (DBR), which is an alternating and periodic stacking of dielectric thin films of index n_1 and $n_2 > n_1$. We plot its photonic band diagram in Figure IV.5.

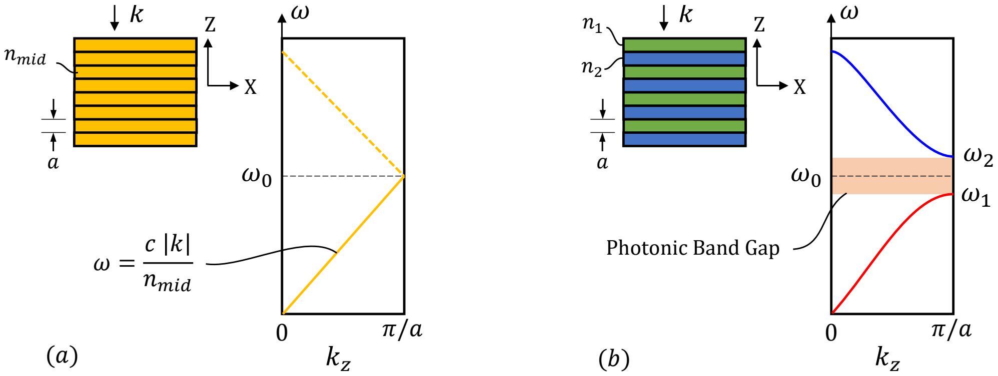

Figure IV.5: *Illustration of the formation of a PBG created by the modulation of the refractive index in the Bragg regime.*

We will discuss briefly on the formation of such a PBG. If we artificially create a periodicity a in uniform material of average index n_{mid}, then the band diagram is written $\omega = c|k|/n_{mid}$. No PBG is observed, as light propagates in a uniform medium. In the case of DBR, the electromagnetic field couples to the alternating dielectric layers in even (pulsating ω_1 modes) and odd (pulsating ω_2 modes) modes. Between these even and odd modes, no electromagnetic wave can propagate: this creates a PBG for the pulsations $\omega_1 < \omega < \omega_2$. In this range, the light is thus reflected, we explain in this way the reflectivity plateau of a DBR (see, Section IV.3.2). In the same way, 2D and 3D PhCs can exhibit PBGs, in specific cases (such as the angle of incidence).

IV.2.2 Periodicity on a slab: the PCM reflector

In the field of planar photonics, one of the most simple structure is the slab, or planar waveguide. This structure is made of a film with a thickness h, and infinitely extended in the X and Y directions. Such a structure is particularly adapted to the technologies of manufacturing. It is made with a high index core n_{core} surrounded by low index cladding n_{clad} (see, Figure IV.6(a)). It allows to restrict the propagation of light in the plane of the slab. This one direction of confinement is called a refractive guiding, which is a generalization of the total internal reflection guiding well known in classical optics. In these conditions, light behaviour can be described by a 2D free-space-like propagation in a material with a refractive index n_{eff} (effective index of a slab mode). The slab is a key concept in this chapter, thus we want to give some of its principles, while taking an intuitive perspective. Let's first consider a plane wave that is not confined in the slab, we will try to figure out its band diagram (which is the pulsation ω of the excitation EM versus the parallel wave vector $k_{||}$). Such band diagram is schematically drawn in Figure IV.6(b).

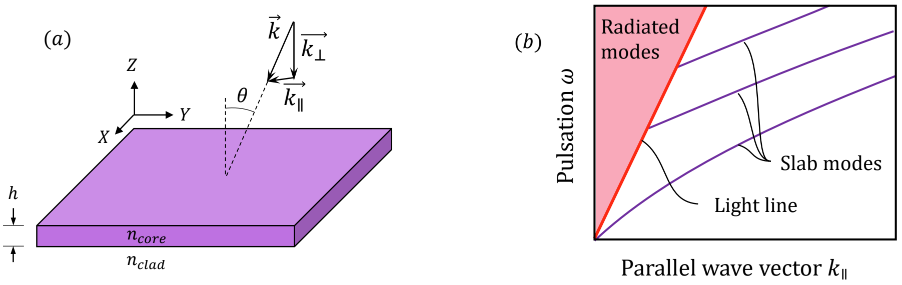

Figure IV.6: *(a) Schematic of a slab. (b) Band diagram of a slab.*

In free space, the pulsation is $\omega = c\,|k| = c\sqrt{k_\perp^2 + k_{||}^2}$, where $k_\perp$ and $k_{||}$ are the perpendicular and parallel components of the wave vector k, see Figure IV.6(a). We don't wish to dive into great details[3], but there is a condition on the wave vector that dictates if the wave is guided or not: high values of $k_\perp$ (compared to $k_{||}$) correspond to waves that have a low polar angle θ. Borrowing concepts from the geometric optics, the guiding conditions is not respected until a certain critical angle. In our case, it corresponds to the limit between guided modes and radiated modes, which is called the 'light-line' $\omega = ck_{||}/n_{core}$, drawn in red in Figure IV.6(b). The light cone (shaded area) correspond to a continuum of waves above the light line, we call radiated modes. Guided modes are below the light lines: here, there is only a discrete amount of possible modes because of the finite thickness of the slab.

From a slab, we can again generate a periodicity (1D or 2D) to create a new kind of PhCs: Photonic Crystal Membrane (PCM)[4]. An example of a PCM was given in Figure IV.4(c). There are a large variety of periodic structures that can be etched through the slab, Figure IV.7 gives examples of three different lattices: (a) The 1D lattice is a periodic succession of bars of the core material, that repeats in one direction and that are extended in the perpendicular direction. 2D PCM can also be made with lattices of holes where the core material is removed periodically. We give examples of two of the most usual lattice symmetries: (b) square and (c) triangular. The use of holes is rather widespread, because such an elementary cell is easily drawn with classical positive resist lithography techniques. Of course, other elementary cells can be drawn and etched, such as circular rods [179] or any arbitrary shaped elementary cell. The lattice symmetry is chosen according to the desired symmetry of the PCM's response. For more details on the possibilities, one can consult general references on symmetrical group theory [180].

---

[3] For more information, see [159].

[4] It is also possible to generate a 1D periodicity on a linear waveguide, creating a linear PhC.

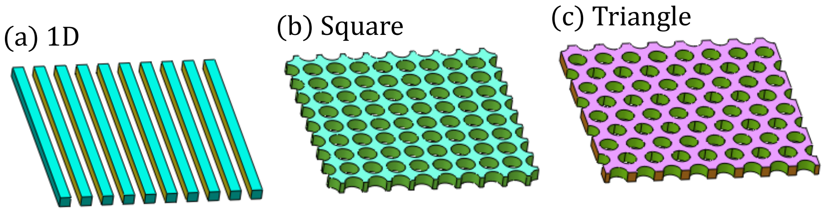

Figure IV.7: *Example of PCM lattices: (a) 1D lattice, (b) Square lattice of circular holes, (c) Triangular lattice of circular holes.*

The engineering of a periodic structure allows the presence of Bloch modes in the slab, that are either below, or above the light line. The former optical modes correspond to Bloch modes that are confined within the slab by refractive effects, which is the preferred mode of operation for in-plane photonic circuits, where slab modes are not allowed to interact with radiated modes: this is known as diffractive confinement. If a Bloch mode is above the light line, then it becomes possible to be coupled with the continuum of radiated modes (out-of-plane mode of operation): the structured slab can thus operate in both confined and radiated regime [181]. In this document, we will mainly focus on a particular PCM operating above the light-line which could be used as a reflector for reasons that will be detailed below.

A PCM reflector has a specific mode of operation: an out-of-plane incident light (normal or oblique) can be coupled with a guided Bloch mode. Such coupling translates into a resonance observed in the reflectance (and transmittance) spectrum. It happens when there is matching of both the wavelength and the parallel wavevector $k_{||}$ of the incident wave and the guided mode. This resonance is called a Fano resonance[5] [183,184]: it exhibit a Lorentzian shape (both symmetrical and asymmetrical[6], depending on the symmetry of the guided mode) in the PCM spectrum. The mechanism is explained simply as following: an incident wave that propagates in the $+Z$ direction excites a membrane mode that can then radiate light out of the plane. In reflective mode, the radiated part that propagates along $+Z$ is in phase-opposition with the incident wave and the $-Z$ is in phase: this results in a reflection phenomenon. Operating a Bloch mode above the light line and tailoring of the different characteristic of a PCM reflector is possible by shaping those Fano resonances (such as spectral and angular reflectivity). We do so by optimizing the geometrical parameters of the PCM. Several factors have to be taken into account such as the materials, the thickness of the membrane and the periodic structure itself (lattice symmetry, shape and size of the unitary cell). That's coupled-mode engineering. Section IV.3.3 will explain in more depth how to design such a PCM reflector.

---

[5] Fano resonances are not only found in PCMs, many physical systems that have coupled oscillators can exhibit those Fano resonances [182].

[6] Showing a transmission peak close to a reflection peak.

IV.2.3 Dielectric Vertical Cavities (VC)

A Fabry-Perot (FP) cavity is an optical resonator that features two mirrors M_1 and M_2 facing each other and spaced by a given distance d [146, 185]. A schematic view of such optical system is given in Figure IV.8(a).

It can be interpreted as an optical transmission system that features a feedback loop (see, subfigure (b)). At each loop, an EM wave loses in intensity while travelling within the cavity, notably caused by the reflectivity coefficient of the mirrors r_1 and r_2. Light also propagates trough a distance $2d$ during a full round trip, resulting in a phase shift by $\varphi = 4\pi n_m d/\lambda$ (λ is the operating wavelength and n_m is the refractive index of the intracavity medium). For certain wavelengths, loops are in phase: in such case, optical intensity within the cavity builds up by constructive interference. For this reason, a FP cavity can be interpreted as a device that can 'store' electromagnetic radiation. A more detailed description of a FP resonator will be provided in Section IV.4.1.

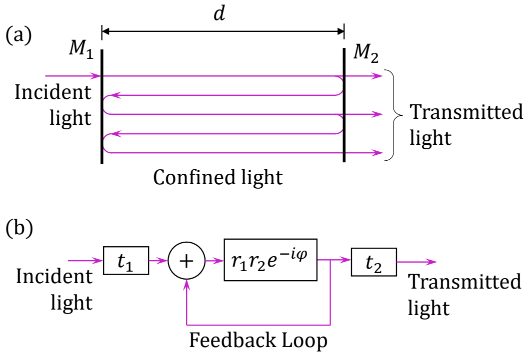

Figure IV.8: (a) Schematic description of a FP cavity. (b) Interpretation as a feedback system.

Such a resonator has been extensively used in many optical systems such as interferometers, spectrometers, lasers [186], non linear devices [187], and sensors [59, 60]. Developments on micro-fabricated optical devices and very low-loss dielectric mirrors led to the birth of Vertical Cavities (VC). This particular FP resonator is constituted by two dielectric planar reflectors made by thin film deposition, one on-top of the other. Among those reflectors, one can imagine DBRs and PCMs as part of VCs, as illustrated in Figure IV.9.

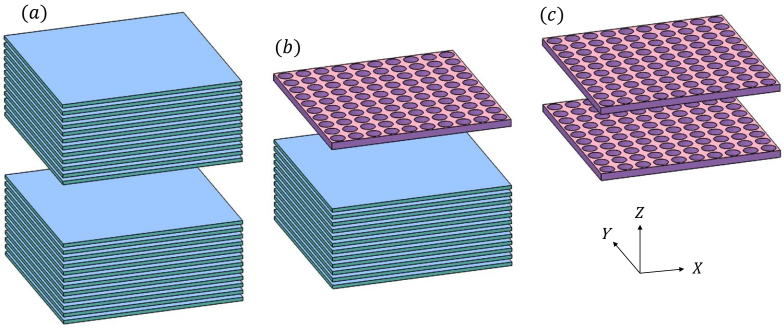

Figure IV.9: Illustration of VC variants involving DBRs and PCMs: (a) DBR-VC, (b) hybrid PCM/DBR-VC, (c) PCM-VC.

DBR stacks (1D-PhCs) where first used in VCs, as it can be made using mature technological steps (thin film deposition) and can achieve an arbitrary amount of reflectivity by adding more stacks. DBR-based VC (DBR-VC) [188], shown in subfigure (a), were a key step toward the miniaturization of optical cavities, which has made it possible for VCSELs (Vertical Cavity Surface Emitting Lasers) to flourish [189, 190]. This latter device remains the main application for VCs. Compared to DBRs, PCMs shows new advantages, notably in terms of compactness, the number of steps needed for fabrication and the overall design freedom which is essential if one wants a very specific spectral, angular and polarization response. Thus, it makes great sense attempting to implement PCM into VCs, using hybrid PCM/DBR-VC (Figure IV.9(b)) or using a double PCM cavity (Figure IV.9(c)). Examples of PCM-based VC made in-house are presented in Figure IV.10.

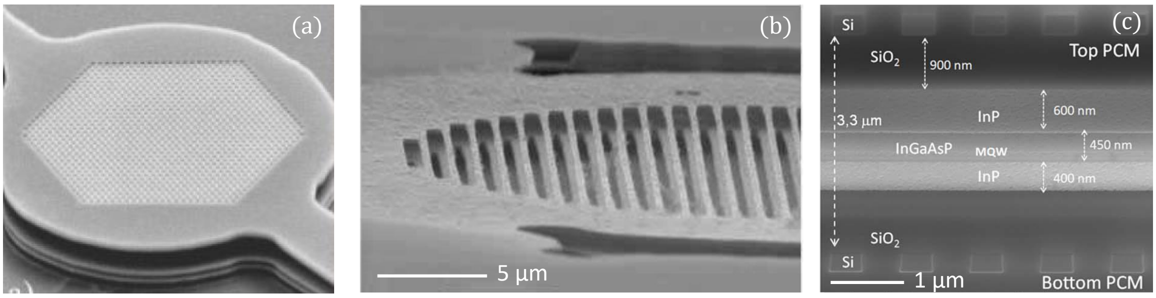

Figure IV.10: *SEM images of PCM-based VC: (a) Hybrid DBR/PCM-VC [181], (b) double PCM-VC [191], (c) PC-VCSEL made with a double PCM-VC [192].*

These compact resonant structures have several applications. For instance, as a MOEMS (Micro-Opto-Electro-Mechanical System) filter [193], that is able to modify the distance that separates the mirrors by electrostatic attraction of doped materials when a voltage is applied to them. We can also take advantage of the high intensity at given wavelengths within the cavity to insert an active medium and fabricate PCM-based VCSELs (PC-VCSEL)[7] [192, 197, 198].

---

[7] Note that the term PCSEL (Photonic Crystal Surface Emitting Laser) is sometimes used to refer to such structures, but also to surface emitting Bloch mode lasers with a single PCM [194–196]. Thus, our preference for the more specific term PC-VCSEL.

IV.3 Design of dielectric mirrors

IV.3.1 Choice of wavelength and materials

The important parameters involved in the choice of materials for dielectric mirrors are mainly the operating wavelength and the complex refractive indexes at this wavelength. The index contrast between the core and the cladding material has to be strong, in order to ensure a good efficiency of both refractive and diffractive effects which are critical for creating a large an efficient reflectivity plateau. Then, our materials should offer a very good transparency at the operating wavelength because our resonant structures stores a important optical intensity, in both the core and cladding material.

In Chapters II and III, the operating wavelength was $\lambda = 635$ nm, and was selected after finding a compromise between the efficiency of the scattering phenomenon and the cost of the sources. Here, we to take into account new constrains because we introduce new materials that comes with their independent set of specifications. At $\lambda = 635$ nm, we didn't find available materials in our micro-fabrication platform that was transparent, with sufficient index contrast. For instance, the main materials used in silicon photonics are incompatible with our application: SOI (Si/SiO_2) is not transparent in the visible range; silicon nitride on silica (Si_3N_4/SiO_2) or titanium oxide on silica (TiO_2/SiO_2) doesn't have a good index contrast, at least for PCMs applications[8]. Traditionally, PCM function in the NIR range, at telecommunication wavelength. We cannot operate in this range because we need to record a cavity-perturbation scattering signature from a particle using a CMOS image sensor, that are not sensitive to wavelengths beyond $\lambda \simeq 1$ µm.

The new compromise we have found is on the NIR spectral range, around $\lambda = 850$ nm, building upon the developments of optical free-space telecommunications, where efficient AlGaAs VCSEL or LED sources (commercially available for a few cents) can communicate by conventional CMOS photodiodes. At this wavelength, we found appropriate materials: hydrogenated amorphous silicon (a-Si:H, later refereed as aSi) can be used as the slab media for our PCMs and silicon nitride for the DBRs. We give in Figure IV.11; the measured complex refractive index ($n + ik$) of aSi, Si_3N_4 and SiO_2 cladding that are available in our microfabrication platform at Leti.

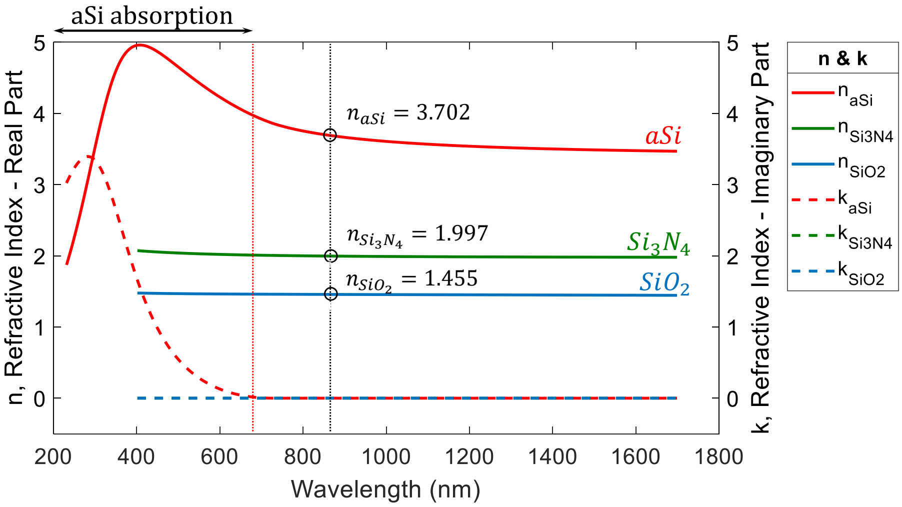

Figure IV.11: *Ellipsometric measurements of complex refractive index of aSi, Si_3N_4 and SiO_2 available at Leti.*

As seen in Figure IV.11, this specific aSi becomes transparent beyond $\lambda = 700$ nm and has a quite high real refractive index $n_{aSi} = 3.702$ at $\lambda = 850$ nm. Such characteristics are well suited for our PCMs. The substrate has to be transparent, because our PM sensor prototype operates in transmission mode: we choose a standard Borofloat 33 glass (BF33) substrate, with a refractive index of $n_{BF33} = 1.465$ at our operating wavelength.

---

[8] No successful design of PCM was achieved with Si_3N_4 and TiO_2 in terms of spectral and angular acceptance. However, we could obtain fairly good DBRs designs with Si_3N_4/SiO_2, see hereafter.

IV.3.2 Design of a DBR

A conventional DBR reflector is an alternation of two dielectric materials stacked as thin films onto a substrate.

The design such DBR stack is quite trivial: from an interferometric standpoint, a thin film alternation must transmit an EM wave (of operating wavelength λ_0) in phase opposition and reflect this wave in phase. The layers must be a quarter-wave thick (modulo one wavelength[a] for higher order DBRs) so that each alternation is a half wave thick. This specific design of layer stack is often called a quarter-wave DBR. If h_1 and h_2 are the thicknesses of the thin layers of the alternating materials of indexes n_1 and $n_2 > n_1$. Then these thicknesses are calculated as follows:

$$h_1 = \lambda_0 / 4n_1 \qquad\qquad h_2 = \lambda_0 / 4n_2 \tag{IV.1}$$

A geometric schematic of the structure, showing the layers and the thicknesses are shown in Figure IV.12.

---

[a] Here, wavelength are given within a material of refractive index n.

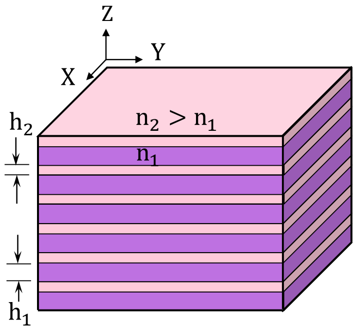

Figure IV.12: *Geometric parameters of the DBR stack.*

The energy reflectance of such mirror is at 100 % for a infinite stack of non lossy materials, a finite number of alternating layers does impact such reflectance. For example, Figure IV.13(a) gives three reflectance spectra of a mirror DBR for three different stacks: the more layers are stacked, the better is the reflectivity. We also see that adding more layers improves the definition of the reflectivity plateau. This design allows us to design an almost arbitrary reflectivity[9]. Moreover the width of the reflectivity plateau (both spectral and angular) will be all the more important as the index contrast between the thin layers is high.

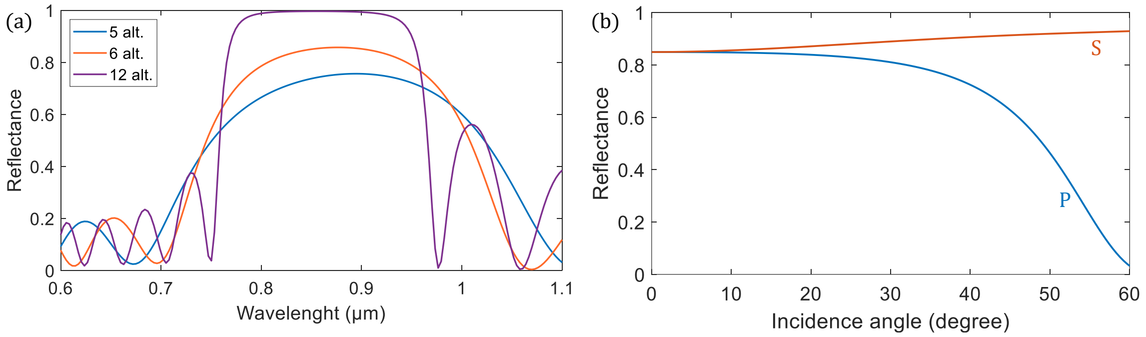

Figure IV.13: *(a) Reflectivity spectra of a DBR mirror consisting of 5, 6 and 12 alternating thin film layers of SiO_2 and Si_3N_4. (b) Angular reflectivity of a 6 alternating layers of SiO_2 and Si_3N_4, under P and S polarization. Both curves were calculated using the Abelès matrix formalism.*

In our case, we want to keep a good reflectivity for high angles, coming from a scatterer. As explained in the previous section, an alternation of Si_3N_4 and SiO_2 on a BF33 substrate is used, as it provides sufficient index contrast. For the operating wavelength $\lambda_0 = 850$ nm, we design a DBR made of 6 alternation (total of 12 layers): $h_{Si_3N_4} = 106$ nm and $h_{SiO_2} = 146$ nm. In Figure IV.13(a), we provide (a) the reflectance spectra, and (b) the angular reflectance, for both P and S polarization. Note that polarization effects appear when the DBR is operated at oblique incidence. For the perpendicular polarization (S), the more the DBR mirror is illuminated at shallow incidence, the more reflective it is. The curves plotted in Figure IV.13 were calculated using our in-house Abelès matrix calculator, which is detailed in Appendix J. Details on the fabrication of such mirror will be provided in Section IV.5.2. Characterizations will then follow in Section IV.6.2.

---

[9] Typically we will try to adapt the number of alternations to have a mirror with a reflectivity close to that of the PCM in the case of the hybrid vertical cavity.

IV.3.3 Design rules for wide-band PCM reflectors

As explained earlier in Section IV.2.2, in order to design a PCM mirror, one has to design a PhC operating with a Bloch mode above the light-line, so that the incident light can interact with such mode while exhibiting a Fano resonance in the reflectivity spectrum. Tailoring such a spectrum amounts to engineer the coupling between a slab mode and a radiated mode: shaping the position, width and coupling efficiency of a Fano resonance. This means adapting the geometrical parameters of the PCM, (such as materials, thickness of the slab, period and size of the periodic pattern), which impacts its band diagram and thus its reflectivity spectrum.

In classic PCM mirror designs, we start with a mono-mode slab at the operating wavelength: meaning that only one mode can be confined vertically in the slab. This defines the thickness h of the membrane. Then, one has to select the lattice symmetry of the periodic structure such as 1D, square, triangular *etc.* (see, Section IV.2.2). We usually select high symmetry unit cell such as circular holes[a]. An example of unitary cell is given in Figure IV.14. In these considerations, we define two geometrical parameters: the period P and the size of the pattern D (or the Filling Factor (FF)). The FF is the surface fraction of the core material, which is directly related to the diameter of the circular hole, alongside the period P (see, Table IV.1).

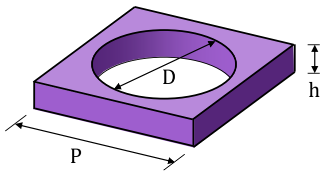

Figure IV.14: *Geometric definition of a unitary cell: example of a square lattice of holes.*

Now, let us consider the three conventional periodic patterns that we will use to design our PCM reflectors: 1D, periodic holes arranged in square ($\pi/2$ symmetry) and triangular ($\pi/3$ symmetry) lattices. We give in Figure IV.15 the geometric definitions of those unitary cells.

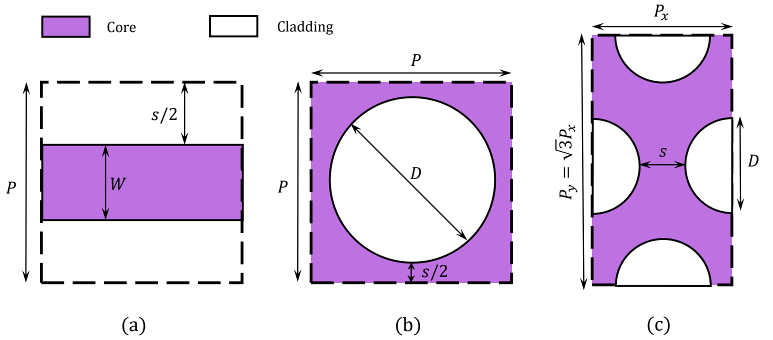

(a) (b) (c)

Figure IV.15: *Illustration of the geometrical parameters of the (a) 1D, (b) 2D square lattice and (c) 2D triangular lattice.*

The size of the periodic pattern W (width of the 1D pattern) and D (diameter of the holes) are linked to the two key parameters P and FF involved in the design of the mirror. Table IV.1 summarizes the relationships between W, D, P and FF for all three lattices. Demonstration is trivial.

Lattice	*Size of pattern*
(a) 1D	$W = FF \cdot P$
(b) Square (holes)	$D = 2P\sqrt{(1-FF)/\pi}$
(c) Triangular (holes)	$D = P_x\sqrt{2\sqrt{3}(1-FF)/\pi}$

Table IV.1: *Relationship between the size of patterns, the period and filling factor of different types of lattices.*

Note, that the resolution of the lithography usually limits the range the realistic geometric parameters (see, Section IV.5). We usually consider the smallest detail in the pattern, which is the size of the pattern (W or D), or the spacing between two elementary patterns (defined as s in Figure IV.15). It can be shown geometrically that, this limitation impacts the the square lattice much more than the triangular lattice, reducing the range of design possibilities. The symmetry of a lattice defines the symmetry of a PCM's reflectivity: notably in terms of polarization and angular dependence. In the following, we will

---

[a] Breaking the symmetry of the unitary cell can, however, lead to interesting proprieties and provides additional freedom in the design process.

discuss the specificities of the 1D and 2D-square designs, while the 2D-triangle will only be discussed in Appendix H.

Tuning the two remaining parameters (P and FF) allow us to engineer a Fano resonance, by setting its spectral position and width. However, this design limits the reflective band by the possible width of a single Fano resonance. This limitation can be overstepped by considering a multimode slab. Indeed, the reflectance spectrum can be broadened by merging two of those resonances [199]. In order to obtain this phenomenon, it is necessary to have a slab with at least two modes in the vertical direction. That is to say, a slab that admits one vertical oscillation. The advantageous h thickness of the membrane is around :

$$h = \lambda/2n_{mid} \qquad\qquad n_{mid} = \sqrt{FF \cdot n_2^2 + (1 - FF)n_1^2} \tag{IV.2}$$

Where n_{mid} is the average membrane index and FF is the Filling Factor. For aSi membranes encapsulated in SiO_2, an avantageous thickness is $h_{aSi} = 180$ nm, for $FF \simeq 50$ %. This way, the incident light at one edge of the operating wavelength range can couple with the fundamental slab mode (first Fano resonance); and the same should happen with a second slab mode in the other edge of the wavelength range. We will see in the following that, for reasons of technological hazards, we have a membrane thickness of $h_{aSi} = 180$ nm, which is not optimal.

In this section, we will try to provide simple guidelines on the design of such membranes. First, one needs to compute a PCM's spectrum for a given geometry of the membrane. For instance, FDTD simulations of a unitary cell with periodic boundaries could be a relevant choice. In our case, we prefer to use the RCWA method (Rigorous Coupled-Wave Analysis) [200, 201]. This extremely fast semi-analytical method, based on Bloch's theorem and Fourier decomposition of EM fields into harmonic series, is used to calculate the response to a plane wave of a periodic photonic system[10]. With this rapid simulation tool, it is possible to design a mirror by easily varying the geometric parameters and evaluating their impact on the reflectivity spectrum of the PCM, thus maximizing the width of the reflectivity plateau.

Changing the period P allows for example to roughly shift the operating wavelength of the mirror. Then, we will try to bring together two Fano resonances in order to obtain a reflectivity plateau. To do this, the filling factor FF must be modified: the resonances can be broadened by having the FF of the membrane close to 50 % (sharpest modulation of refractive index): this improves the coupling efficiency of slab modes (in-plane) and the radiated modes (out-of-plane). Note that changing FF will also shift the Fano resonances. Ideally, P and FF are adjusted iteratively until a convincing reflectivity spectrum is obtained. In Figure IV.16, we give an example of how two Fano resonances can be merged by tuning FF, in the case of a 1D-PCM wideband reflector.

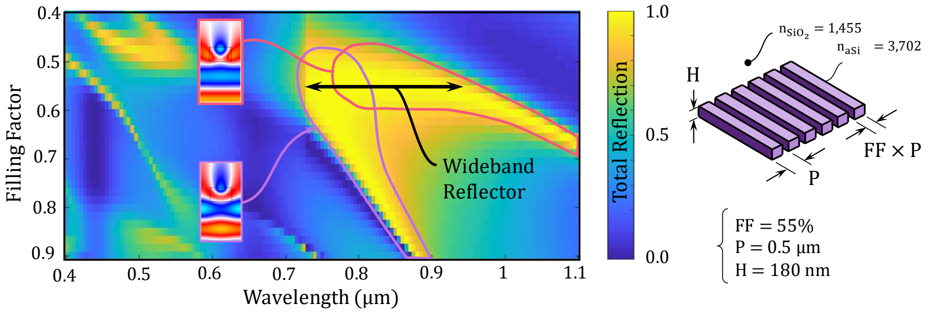

Figure IV.16: *Wideband mirror obtained by the merging of two Fano resonances done by modifying the FF of a 1D-PCM (aSi/SiO_2). Calculated by RCWA.*

Note that these design rules can also be applied to other symmetries than 1D, for instance square or triangular lattice of holes.

---

[10] The main disadvantage of these methods is that they cannot quantify lateral optical losses due to the finite pupil of the PCM mirror.

IV.3.4 Design of 1D and 2D PCM mirrors

Following the design methodology discussed above, we design a 1D-PCM mirror that exhibit the reflectivity spectrum presented in Figure IV.17. The mirror is designed to operate with the S-polarization. As a recall, S-polarization refers to the case were the polarization plane is coplanar with the tangential plane. This spectrum is obtained with a RCWA simulation (DiffractMOD, RSoft photonic suite), where the PCM is excited by an S-polarized plane wave at normal incidence.

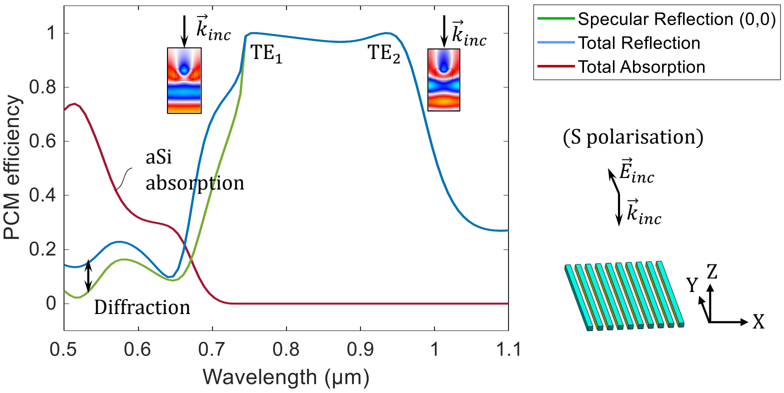

Figure IV.17: Reflectivity spectrum at normal incidence of a 1D-PCM mirror simulated with the RCWA method.

We plot the total energy reflectance spectrum R, which correspond to the total of energy reflected in the same hemisphere as the incident plane wave; the specular reflectance spectrum $R_{(0,0)}$ (or diffraction order (0,0)), which corresponds to the energy reflected as a plane wave that propagated accordingly to the Descartes' law of reflection; and the total absorption spectrum, which is the energy that was neither reflected in one hemisphere nor transmitted in the other hemisphere. A difference between the total and specular reflectance is observed when the wavelength becomes small enough compared to the periodic structure to allow diffraction effects. It means that the incident light is scattered following privileged directions, accordingly to Bragg's law of diffraction. When $R = R_{(0,0)}$, the mirrors acts mostly like a conventional mirror.

This mirror was obtained with a PCM from a 169 nm thick aSi/SiO_2 membrane structured with a 1D periodicity along X. The geometric parameters are $P = 0.51$ µm and $FF = 54$ %. A wide reflectance plateau is well observed, obtained by merging the two Fano resonances TE$_1$ and TE$_2$. We recall that, the membrane thickness is not optimal due to technological hazards. We have however adapted our geometrical parameters a much as possible, however the flatness of the reflectivity plateau remain less efficient than if we had the desired membrane thickness.

Note that, in this document, we describe the polarization using the TE/TM convention for confined slab modes (such as Bloch modes) on one hand. TE and TM stand for Transverse-Electric and Transverse-Magnetic respectively. In our case, Bloch modes carried by an electric field E_y, are denoted TE. We abusively extend this designation for the associated Fano resonances. On the other hand, we use the S and P polarization convention to refer to radiated modes that propagate in free space (see, Appendix A).

Let us quickly return to the design methodology for PCM reflectors: Figure IV.18 shows the influence of FF and P on the reflectance spectra.

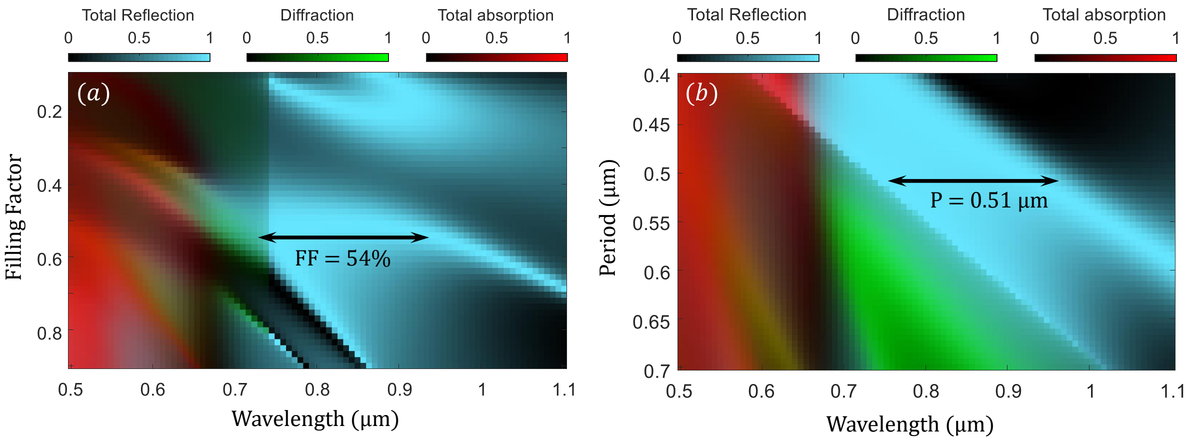

Figure IV.18: *Reflectance spectrum of a 1D-PCM mirror while modifying (a) the filling factor when* $P = 0.51$ µm *and (b) the period when* $FF = 54$ %.

The total reflectivity is displayed in blue, the absorption in red and the difference between total reflectivity and specular reflection, *i.e.* diffraction, in green. Those three spectra are displayed simultaneously on an RGB image to make it easier to read the behaviour of the PCM. The human eye easily interprets the color mixtures and visualizes the areas of interest. The objective is to maximize the width of the reflectivity plateau by avoiding areas that exhibit absorption and diffraction. As explained earlier, changing the period roughly shift the operation spectral ranges; and the filling factors allows for merging the two Fano resonances, which is clearly visible in subfigure IV.18(a).

We recall that our angular and polarization convention is defined in Appendix A.

Using the same color code as in Figure IV.18, we plot in Figure IV.19(a) the reflectivity spectrum at normal incidence of the 1D-PCM as a function of the polarization angle ϕ_p (polar plot), also calculated using RCWA. As seen in the plot, a reflectivity plateau is well defined at the S-polarization, but it degrades progressively as the polarization angle rotates toward the P-polarization. Note, that another Fano resonance appears in the P-polarized spectrum, but will not be used. This dependence in polarization was to be expected, considering the 1D periodicity of the mirror. We will see in the following how to design PCM mirrors that are polarization independent, using a 2D periodicity.

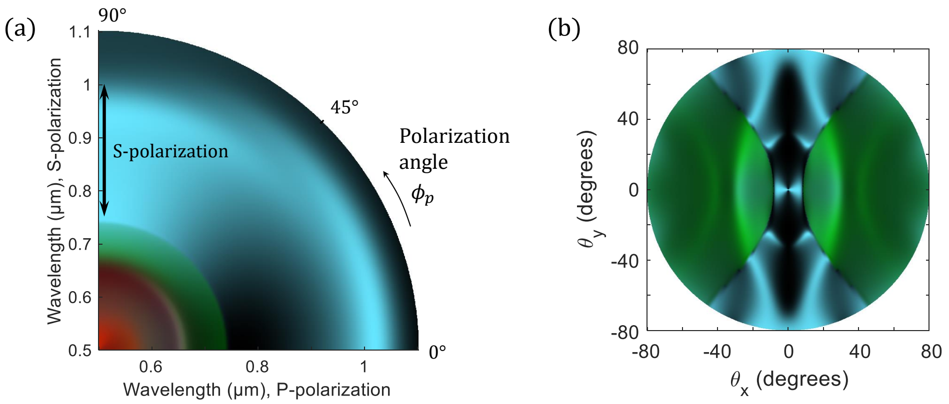

Figure IV.19: *(a) Polarization dependence in the reflectivity spectrum of the 1D-PCM. (b) Angular reflectivity of the 1D-PCM at* $\lambda = 850$ nm.

Then, we plot in Figure IV.19(b) the angular reflectivity of the 1D-PCM, calculated with a S-polarized incident plane wave at $\lambda = 850$ nm. We see that the diagram is only symmetrical by a π rotation, which is consistent with the PCM's symmetry. The central blue spot correspond to the specular reflection around normal conditions of illumination. This spot is shaped like a bow-tie, showing a larger angular acceptance perpendicular to the bars, which is expected because the modulation of the refractive index is stronger in this direction. Further away in this same direction, a second lobe appears for high θ_x angles, exhibiting diffraction effects (green map).

Again, we apply the design methodology described in Section IV.3.3, but for a square lattice of holes 2D-PCM. With the same membrane thickness $h_{aSi} = 169$ nm (non-optimal), we've obtained the following geometrical parameters: $FF = 44$ % and $P = 0.560$ µm.

At normal incidence, such a spectrum is polarization independent (ϕ_p invariant). This effect is made possible by the 2D periodicity of high symmetry unit cells, holes in our case[11]. The associated spectrum is presented in Figure IV.20(a). This show a drop in reflectance (not found in the 1D-PCM design), in the form of a fine resonance. This effects is due to a parasitic Fano resonances that manage to couple within the more complex 2D structure.

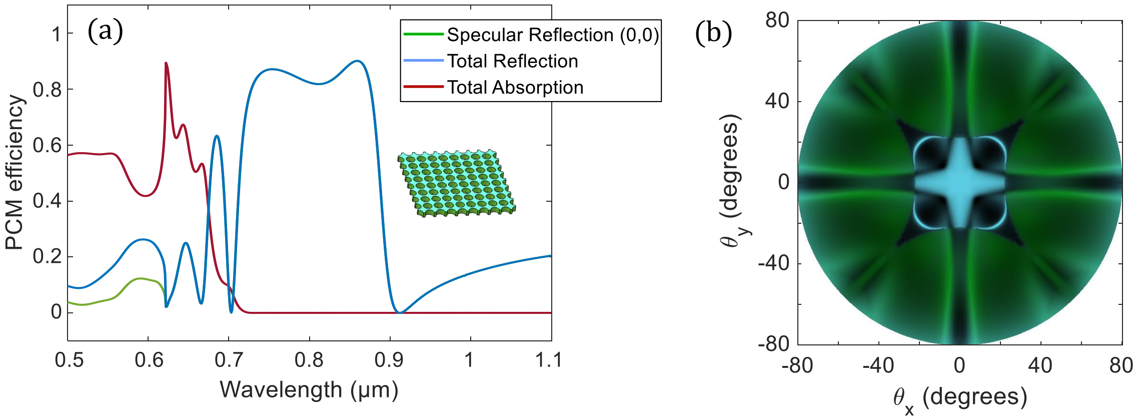

Figure IV.20: (a) Reflectivity spectrum at normal incidence of the square lattice 2D-PCM mirror. (b) Angular reflectivity at $\lambda = 850$ nm.

Then, we plot in Figure IV.20(b), the angular reflectance for an S polarization (or, equivalently, a P polarization), showing the angular behaviour of the mirror both in terms of specular reflection and diffraction (following the same colour code: blue and green respectively), and calculated with RCWA at $\lambda = 850$ nm. The figure exhibit a large cross-shaped region around normal incidence, where the mirror operates with specular reflection (central blue area). Note that this region is slightly more extended is the directions where the holes meets their firsts neighbours (X and Y): *i.e.* when the modulation of the refractive index is stronger. Then, following the directions of the second neighbours (45° azimuth), we observe four shapes that resemble the petals of a flower, where diffraction effects are predominant. We note that the figure perfectly respects the $\pi/2$ azimuthal symmetry of the lattice.

Note that the case of a triangular lattice of holes will not be discussed in the main body of the manuscripts, as it does not provides new insights toward the understanding of the perturbation phenomenon of a PCM based VC. Additionnal details in the design and characterization of a triangular lattice PCM are provided in Appendix H.

---

[11] Note that the polarization dependence can be tuned by breaking the symmetry of the unit cell [202].

IV.4 Perturbation of Fabry-Perot

In this section, we will model a Fabry-Perot (FP) cavity consisting of two dielectric mirrors (DBR or PCM). The goal is to determine the spectral[12], but also, the angular responses, carried by higher order FP modes of such a cavity.

Then, we will study the influence of a dielectric particle within this cavity. We will model both the extinction of the vertical mode (the Γ mode) and the energy transfer between the Γ mode and the higher order modes. In particular, we will try to model how the angular energy transfer is made possible by the phenomenon of light scattering by a particle.

Such a model will borrow concepts and mathematical tools from the Lorenz-Mie theory (see, Appendix B) and the Fourier's formulation of wave optics and diffraction, especially when applied to particle scattering (see, Appendix F). Both appendixes are to be considered as prerequisites for an optimal understanding of the following sections.

IV.4.1 FP cavity without pertubation

In this subsection, we will first model a basic FP cavity, which was introduced in Section IV.2.3, using the Fourier's formulation of wave optics and diffraction.

First, let us consider a FP cavity, made of two mirrors M_1 and M_2 with infinite lateral dimensions, and separated by a distance d in an intracavity medium of refractive index n_m. In such conditions, no lateral loss are considered. We express the propagation of a wave through a round trip within the cavity, in Fourier domain.

A round trip is divided into four events: a first free-space propagation by a distance d, a first reflection by the mirror M_2, a second free-space propagation by a distance d, and a second reflection by the mirror M_1. We define $F_{1,5}(\nu_x, \nu_y)$ as the waves, in Fourier domain, between those four events, as schematized in Figure IV.21.

$$\begin{cases} F_2(\nu_x,\nu_y) & = & \mathscr{H}_d(\nu_x,\nu_y) \cdot F_1(\nu_x,\nu_y) \\ F_3(\nu_x,\nu_y) & = & \mathscr{R}_2(\nu_x,\nu_y) \cdot F_2(\nu_x,\nu_y) \\ F_4(\nu_x,\nu_y) & = & \mathscr{H}_d(\nu_x,\nu_y) \cdot F_3(\nu_x,\nu_y) \\ F_5(\nu_x,\nu_y) & = & \mathscr{R}_1(\nu_x,\nu_y) \cdot F_4(\nu_x,\nu_y) \end{cases} \tag{IV.3}$$

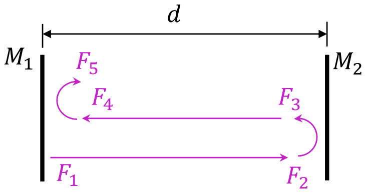

Figure IV.21: *Schematic of a round trip propagation within a FP cavity.*

Here, (ν_x, ν_y) are the sagittal and tangential spatial frequencies (given in μm^{-1}). $\mathscr{R}_{1,2}(\nu_x, \nu_y)$ are the Optical Transfer Functions (OTF) of the mirrors which quantifies their reflection coefficients (and, in some cases, the phase shift induced by a reflection[13]). We clarify the difference between the OTF of the mirrors ($\mathscr{R}_{1,2}(\nu_x, \nu_y)$) which applies the complex function of the wave, the reflection coefficients ($r_{1,2}$) at the amplitude of the latter, and the energy reflectance ($R_{1,2} = |\mathscr{R}_{1,2}|^2$) which applies to energy of the wave[14]. Those functions can be computed using models such as the Abelès matrix method (see, Appendix J) for DBRs, the coupled mode theory for PCMs, or more generally imported from RCWA simulations. Then, $\mathscr{H}_d(\nu_x, \nu_y)$ is the OTF of a free space propagation by a distance d, expressed as:

$$\mathscr{H}_d(\nu_x, \nu_y) = \exp\left[i2\pi n_m d\sqrt{1/\lambda^2 - \nu_x^2 - \nu_y^2}\right] \tag{IV.4}$$

It should be noted that the refractive index n_m of the intracavity medium can exhibit an imaginary part, which can create a loss of modulation[15] (equivalent to a Beer-Lambert attenuation) within the propagation domain ($\nu^2 < 1/\lambda^2$), with $\nu = \sqrt{\nu_x^2 + \nu_y^2}$ the axial spatial frequency. We then define $\mathscr{H}_R(\nu_x, \nu_y)$, the OTF of a single round trip, expressed as:

$$\mathscr{H}_R(\nu_x, \nu_y) = \mathscr{R}_1(\nu_x, \nu_y) \cdot \mathscr{R}_2(\nu_x, \nu_y) \cdot \mathscr{H}_{2d}(\nu_x, \nu_y) \tag{IV.5}$$

---

[12] Note that, in the schematics of this chapter, the rays or wavefronts are drawn purple. Indeed, in an intuitive representation, NIR is associated with purple because it excites both red and blue pixels of common CMOS cameras.

[13] Which can happen in certain scenarios, such as a reflection made by a diffractive element, or more specifically, a PCM.

[14] The same applies for the transmission mode, whith t, $\mathscr{T}$, and T

[15] We exclude the case of gain materials for the sake of simplicity.

As suggested previously, in Section IV.2.3, such cavity is interpreted as an optical transmission system that features a feedback loop where part of the radiation is lost at each loop. Such system is schematized in Figure IV.22, using a block diagram.

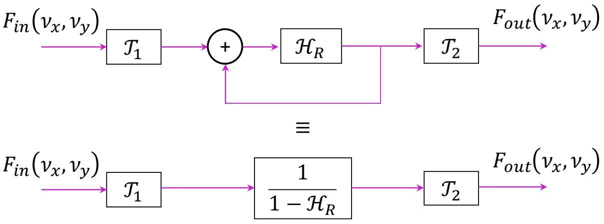

Figure IV.22: *Representation of a FP cavity using a block diagram, and its reduced diagram.*

Here, $F_{in}(\nu_x,\nu_y)$ and $F_{out}(\nu_x,\nu_y)$ are the input and output waves, in Fourier domain; $\mathscr{T}_{1,2}$ are the OTF of the two mirrors in transmission mode. At each loop, the wave is multiplied by $\mathscr{H}_R$, the OTF of a round trip. It is common to reduce such feedback loop into a single block, as shown in Figure IV.22's bottom diagram. Hence, we express the OTF of the FP cavity $\mathscr{H}_{FP}(\nu_x,\nu_y)$ as:

$$\mathscr{H}_{FP}(\nu_x,\nu_y) = \frac{1}{1-\mathscr{H}_R(\nu_x,\nu_y)} \tag{IV.6}$$

In Figure IV.23, we plot the modulus and argument of $\mathscr{H}_{FP}$ as a function of the spacial frequencies. This cavity example is 15 µm long, and illuminated at a wavelength that resonate at the Γ mode around 850 nm.

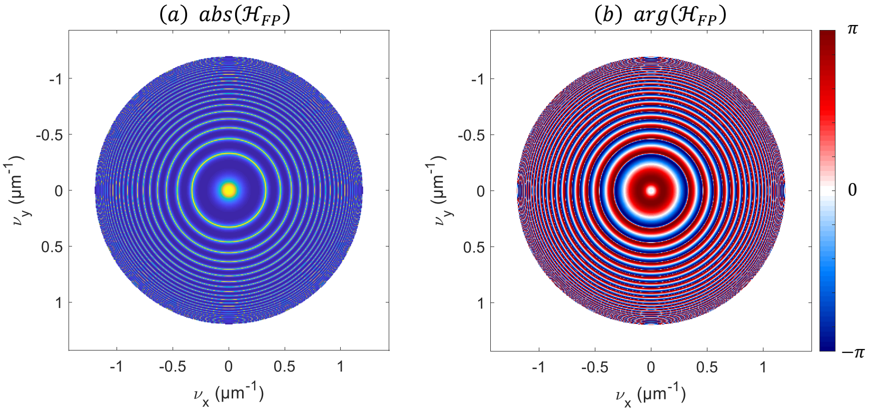

Figure IV.23: *(a) Modulus and (b) argument of $\mathscr{H}_{FP}$.*

The FP rings are clearly visible in subfigure (a), which correspond to the higher order cavity modes. The quality factor of a cavity mode can be deduced from the thickness of the corresponding ring[16]. It should be noted that the high spacial frequencies, beyond the propagation domain ($\nu^2 < 1/\lambda^2$), are not computed. Indeed, we did not find any interest in extending our study beyond this frontier. The domain that correspond to those high spacial frequencies are drawn in white.

We will now take into account the finite lateral dimensions of the mirrors, which induces noticeable losses, especially with our PCM mirrors that are limited in size due to our writing process. Those lateral losses are even more critical when studying high scattering angles. The higher the angle of incidence, the higher the lateral losses: the quality factor of the FP resonances is thus degraded. Therefore, the cavity perturbation scattering signature resulting from high scattering angles will be analyzed with less sensitivity.

---

[16] The quality factor Q is the wavelength divided by the spectral width of the resonance, which is also related to the angular width.

A classical approach to this problem is to calculate $h(x,y,x',y')$ the Point Spread Function (PSF) of a round trip in the Fresnel approximation [203].

$$u_2(x,y) = \iint_{\mathbb{R}^2} h(x,y,x',y') \cdot u_1(x',y')dx'dy' \tag{IV.7}$$

Where $u_{1,2}(x,y)$ are waves before and after a round trip. Then one must solve the following eigenvalues problem:

$$\iint_{\mathbb{R}^2} h(x,y,x',y') \cdot u(x',y')dx'dy' = \mu \cdot u(x,y) \tag{IV.8}$$

Where $\arg \mu = m2\pi$ and $m \in \mathbb{Z}$. The eigenvalues $u(x,y)$ are the cavity modes. However, this approach is particularly computationally heavy, especially for high order cavity modes, where classical eigenvalue equation solvers converge poorly [204]. Moreover, the implementation of an intermediate diffracting plane, such as a sphere equivalent planar obstacle, has proved to be particularly difficult both in terms of formulation and computation. Indeed, an exact formulation takes a form that involves cascaded integrals.

Another simpler approach, known as the 'clip approximation', is to estimate the amount of optical radiation lost during a round trip by quantifying the fraction of the beam reflected by the pupil of each mirror as an effective reflectivity [203]. In our case, we implement a modified 'clip approximation' by considering the overlap of the waves f_1 and f_2, before and after a round trip. This approximation also takes into account the angle of incidence of the wave (and thus its spatial frequency).

We model this part by considering the mirror M_1 with infinite lateral dimensions (M_1 is usually a large DBR reflector), and M_2 with a square pupil sized by W_2. The model of lateral losses is illustrated in Figure IV.24.

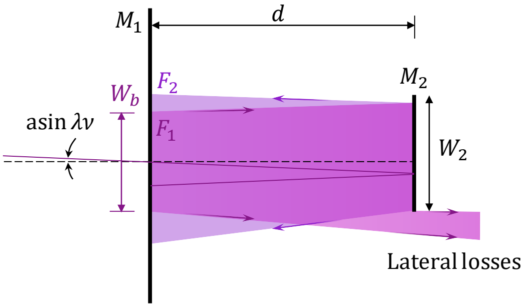

Figure IV.24: *Geometry of the lateral losses with the modified 'clip approximation'. For readability reasons, the geometry of the problem is represented only in 1D.*

We consider f_1 (wave before a round trip) as a Gaussian beam. It is usually a good approximation for a FP cavity mode. We write $F_1 = \mathscr{F}\{f_1(x,y)\} = \exp(-(\pi \cdot W_b/2)^2 \cdot (\nu_x^2 + \nu_y^2))$, which is a Gaussian beam, sized by W_b, expressed in Fourier domain. Then, the wave $F_2 = \mathscr{F}\{f_2\}$ after a round trip is calculated as such:

$$F_2 = \mathscr{H}_d \cdot (P_{M_2} * (\mathscr{H}_d \cdot F_1)) \tag{IV.9}$$

Where P_{M_2} is the Fourier transform of the pupil[17] of M_2, and $*$ is the operator of convolution. The proof for this equation is left for the reader, who might want to express the propagation during a round trip in real space, and then apply the Fourier transform. In order to obtain the overlap of f_1 and f_2 (denoted $\mathscr{R}_d$), we perform an equivalent operation, which is the cross correlation:

$$\mathscr{R}_d(x',y') = |f_1(x,y) \otimes_{x,y} f_2(x-x',y-y')| \tag{IV.10}$$

The operator $\otimes_{x,y}$ is the 2D cross-correlation, which is equivalent to a correlation with a transverse translation. One can convert such translation correlation into a deflection using a simple change of

---

[17] In the case of a square pupil, P_{M_2} simply becomes a product of two orthogonal cardinal sinuses.

variables: this leads to the effective reflection OTF $\mathscr{R}_d(\nu_x, \nu_y)$, that takes into account the lateral losses using the modified 'clip approximation'.

$$\mathscr{R}_d(\nu_x, \nu_y) = \mathscr{R}_d \left(\frac{1}{\lambda} \text{atan} \frac{x'}{d}, \frac{1}{\lambda} \text{atan} \frac{y'}{d} \right) \tag{IV.11}$$

Such effective reflectivity can then be implemented into the OTF of a round trip $\mathscr{H}_R(\nu_x, \nu_y)$, alongside the other two reflection OTF ($\mathscr{R}_{1,2}$).

IV.4.2 Particle induced extinction of the Γ mode

We will now introduce a particle within the cavity. This particle is a uniform dielectric sphere that will introduce additional losses, as well as scattering, which is quantified using the Lorenz-Mie theory. Such a particle, will be referred to as the perturbator in the following.

In our model, we will make the following approximation: the sole fundamental mode (Γ mode) is subjected to extinction. It then generates scattering toward higher order FP modes. We will therefore consider the Γ mode separately; then, the higher order modes, which are based on the intensity of the Γ mode, will be studied in the next section.

As a reminder, the Lorenz-Mie theory allows to calculate an extinction cross section $C_{ext}(\chi)$ of a particle. This quantity quantifies the power drawn from an incident beam in relation to its section, which is then dissipated ($C_{abs}(\chi)$) or scattered in other directions ($C_{scat}(\chi)$, given in µm^2).

$$C_{ext}(\chi) = C_{abs}(\chi) + C_{scat}(\chi) = W_{ext}/I_\Gamma \tag{IV.12}$$

W_{ext} is the optical power lost by the Γ mode due to the perturbator. I_Γ is the intensity of the Γ mode that illuminates the particle before undergoing losses. The perturbator will be abusively referred to as the letter χ, which is the adimensional size factor.

During a passage of the mode Γ in the cavity, we quantify $A_s(\chi)$. It is the ratio of the intensity of the mode Γ after having undergone the extinction and this same intensity in the absence of particle:

$$A_s(\chi) = 1 - \frac{C_{ext}(\chi)}{\Sigma_\Gamma} \tag{IV.13}$$

The section of the mode Γ, denoted Σ_Γ, is derived from the previous calculations, obtained in the absence of a perturbator.

Based on observations from FDTD simulations (which are not shown here), we will introduce a phase shift phenomenon arising from interaction between the mode Γ and the perturbator. A naive, but telling, interpretation would be to attribute this phase shift to the path of light inside the particle. Let $\widetilde{S}(\nu_x, \nu_y)$ be the scattering signature, defined in Appendix F. We also define the phase scattering signature:

$$\varphi_s(\nu_x, \nu_y) = \arg(\widetilde{S}(\nu_x, \nu_y)) - \pi/2 \tag{IV.14}$$

The subtraction by $\pi/2$ will be explained in the following. The phase shift of Γ, denoted $\varphi_{s,\Gamma}$, can be retrieved trough the argument of such signature, when the deviation is null: $\varphi_{s,\Gamma} = \varphi_s(0,0)$.

Finally, we can extend our formulation of $\mathscr{H}_{R,\Gamma}$, the OTF of a round trip travelled by the mode Γ, in the presence of a perturbator:

$$\mathscr{H}_{R,\Gamma} = \mathscr{R}_1\mathscr{R}_2\mathscr{R}_d \cdot \mathscr{H}_{2d} \cdot (A_s(\chi)e^{i\varphi_{s,\Gamma}})^2 \tag{IV.15}$$

We plot in Figure IV.25, spectra of Γ intensity for different size of perturbators, using $|\mathscr{H}_{R,\Gamma}|^2$, where $\mathscr{H}_{R,\Gamma}$ is the modified round trip OTF.

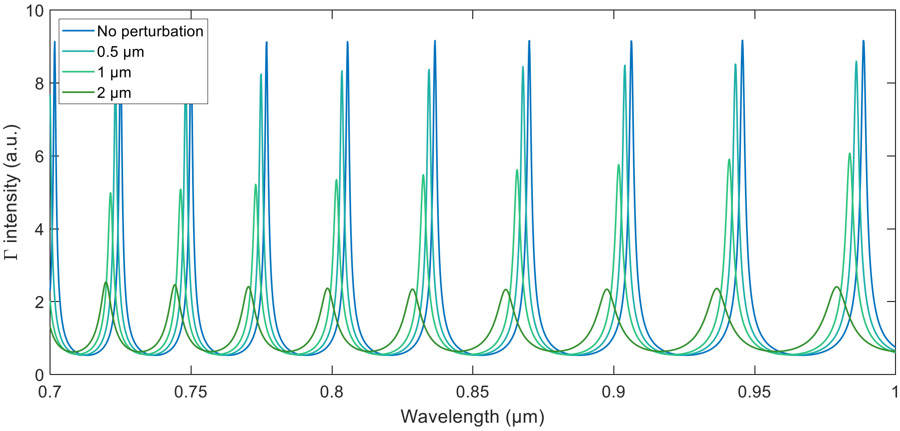

Figure IV.25: *Spectra of Γ intensity for different size of perturbators.*

The additional losses attributed to $A_s(\chi)^2$ have the effect of degrading the quality factor of the FP resonances (Γ modes) and reducing its intensity while the phase shift $2\varphi_{s,\Gamma}$ has the effect of shifting those resonances.

In should be noted that, in this model, the particle is delocalized and the Γ mode is extended throughout the space bounded by the two mirrors. There are no spatial considerations, but rather spatial frequency (angular) considerations because the cavity perturbation signature is analysed in far-field, and the particle is at a random (or unspecified) position. Only the fact that the particle has been encountered twice during a Γ mode round trip in the cavity is of interest to us, without considering the position of the encounter. However, the extinction of Γ is most certainly underestimated because the Γ mode is extinguished locally on a vertical cylinder with a cross section close to the effective cross section of the particle (as seen in FDTD simulations) and not distributed over the whole lateral extent of the mirrors.

IV.4.3 Energy transfer toward higher order cavity modes

We would remind that the cavity is illuminated at normal incidence, i.e. only the Γ mode resonates, the higher order modes are initially not excited. Then, the scattering phenomenon (off-axis deflection) induced by the scatterer allows an energy transfer from the Γ mode to the higher order modes.

Figure IV.26 gives a schematic representation of an energy transfer from a fundamental mode to higher order modes ($\Gamma \rightarrow \nu_i$).

Since the transfer of energy is made possible by the phenomenon of scattering, which must be carried out with intense illumination, the phenomenon of cascaded energy transfer from the ν_i modes to the ν_j modes ($\nu_i \rightarrow \nu_j$) is neglected. Indeed, this transfer should be based on a FP resonance ν_i which is much fainter than the Γ mode.

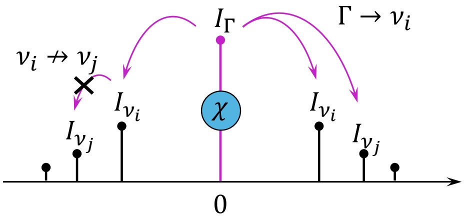

Figure IV.26: Schematic representation of the energy transfer between the mode Γ toward the higher orders ν_i.

The Lorenz-Mie theory is again used to quantify the efficiency of this energy transfer. We recall the expression of scattering matrix $s(\theta)$ which links the P and S components of the incident and scattered fields, in the far-field approximation[18]:

$$\begin{pmatrix} U^P_{inc}(\theta) \\ U^S_{inc}(\theta) \end{pmatrix} = \frac{e^{ikr}}{-ikr} \begin{pmatrix} s_{11}(\theta) & 0 \\ 0 & s_{22}(\theta) \end{pmatrix} \begin{pmatrix} U^P_{scat}(\theta) \\ U^S_{scat}(\theta) \end{pmatrix} \tag{IV.16}$$

We also recall that these coefficients are complex: their amplitude $|s_{11}(\theta)|^2$ and $|s_{22}(\theta)|^2$ quantify the angular distribution of the scattered energy; their phase $\arg(s_{11}(\theta))$ and $\arg(s_{22}(\theta))$ quantifies the phase shift induced by the scattering. In Figure IV.27, we plot the argument and amplitude of the diagonal components of such matrix as a function of the scattering angle θ and the cylinder[19] diameter D_p.

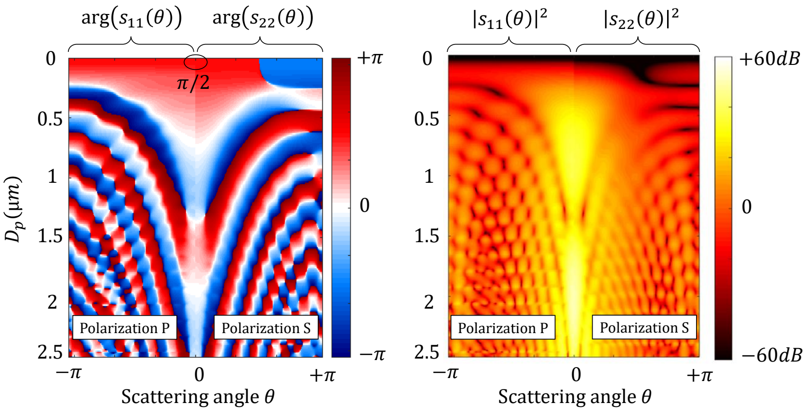

Figure IV.27: Plot of the argument and amplitude of the diagonal components of the scattering matrix $s(\theta)$ as a function of the scattering angle θ and the cylinder diameter D_p.

From equation (IV.16), one can build the scattering signature $\widetilde{S}(\nu_x, \nu_y)$ using a simple geometric change of variables, and by correcting its intensity using the scattering cross section $C_{scat}(\chi)$. Proper definition of $\widetilde{S}(\nu_x, \nu_y)$ is provided in Appendix F. By doing so, it is equivalent to inserting the sphere-equivalent planar obstacle inside the cavity.

---

[18] Note that θ is used for both the angle of incidence and the scattering angle, because it is the same polar angle.

[19] This specific calculation was made using the 2D Mie's theory, which calculates the scattering of an infinite cylinder instead of a sphere [83]. Those plots are similar to those of a sphere.

The phase scattering signature $\varphi_s(\nu_x, \nu_y)$ must be corrected by a subtraction by $\pi/2$, as previously mentioned in equation (IV.14). A quick justification for this correction is given: for a particle diameter tending towards 0, the argument of the diagonal coefficients of the scattering matrix at $\theta = 0$ is equal to $\pi/2$, as seen in Figure IV.27. Let us return to the equations IV.16 to explain this term: the phase term $\exp(-ikr)$ is related to the propagation of a spherical wave, which is already taken into account in the model. We also notice the decay term of a spherical wave $-1/ikr$ which is a pure imaginary: this is why we must subtract the phase of this pure imaginary $(-\pi/2)$.

Then, since the Γ mode is a stationary wave that can be decomposed into a propagative wave and a counter-propagative wave, we must consider both the scattering and backscattering phenomena. So we define $\widetilde{S}_{f+b}(\nu_x, \nu_y)$ as the total scattering signature, composed of the forward scattering $\widetilde{S}_f$ and backscattering signature $\widetilde{S}_b$[20], written as $\widetilde{S}_{f+b} = \widetilde{S}_f + \widetilde{S}_b$.

We provide, in Figure IV.28, a geometrical representation of our perturbed FP model, where the sphere-equivalent obstacle is inserted inside the cavity, delimited by the two mirrors $M_{1,2}$.

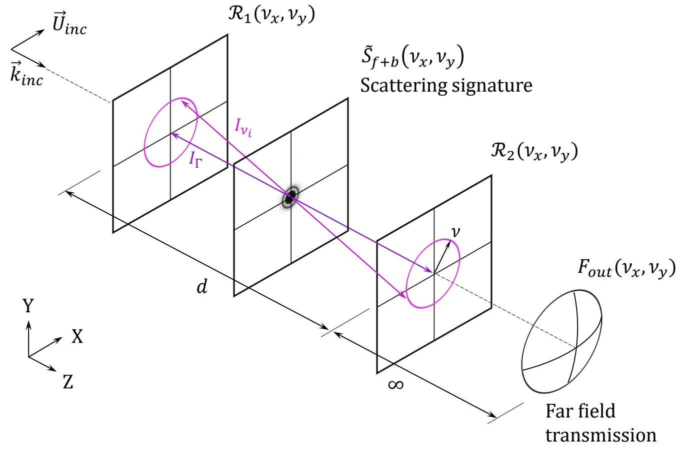

Figure IV.28: *Geometrical representation of the perturbed FP model.*

We will translate the scattering phenomenon, to integrate it into our FP model. To do so, we use our feedback loop system, and consider two sources, as shown in Figure IV.28. A first real source comes from the vertical illumination by a Gaussian beam (denoted F_{in}), that excites the Γ mode. A second fictional source $\widetilde{S}_{f+b}(\nu_x, \nu_y)$, which is injected within the cavity, represents the scatterer, is proportional to the intensity of the Γ mode (denoted F_Γ). Both sources will interact with the FP cavity.

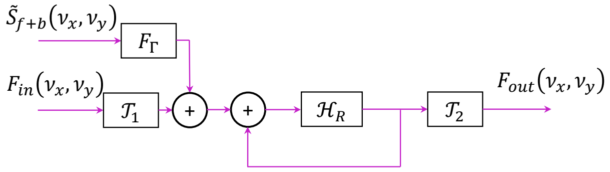

Figure IV.29: *Block diagram of the perturbed FP cavity, using two sources.*

By the superposition theorem, which applies to linear systems, like ours, we can consider these sources separately, and *in fine* add them together.

$$F_{out} = F_{in} \cdot \mathscr{T}_1 \cdot \mathscr{T}_2 \cdot \mathscr{H}_{FP,\Gamma} + F_\Gamma \cdot \widetilde{S}_{f+b} \cdot \mathscr{T}_2 \cdot \mathscr{H}_{FP} \tag{IV.17}$$

With $\mathscr{T}_{1,2}(\nu_x, \nu_y)$, the OTF of the mirrors $M_{1,2}$ in transmission mode. Then, the resulting image is simply obtained with $I_{out} \propto \text{abs}(F_{out})^2$.

---

[20] From the Lorenz-Mie theory, one can simply reverse the scattering signature, such as $S_f(\theta) = S_b(\pi - \theta)$.

IV.4.4 Results and discussion

In Figure IV.30, examples of modelled cavity perturbation scattering signatures are given, for three diameters of perturbators.

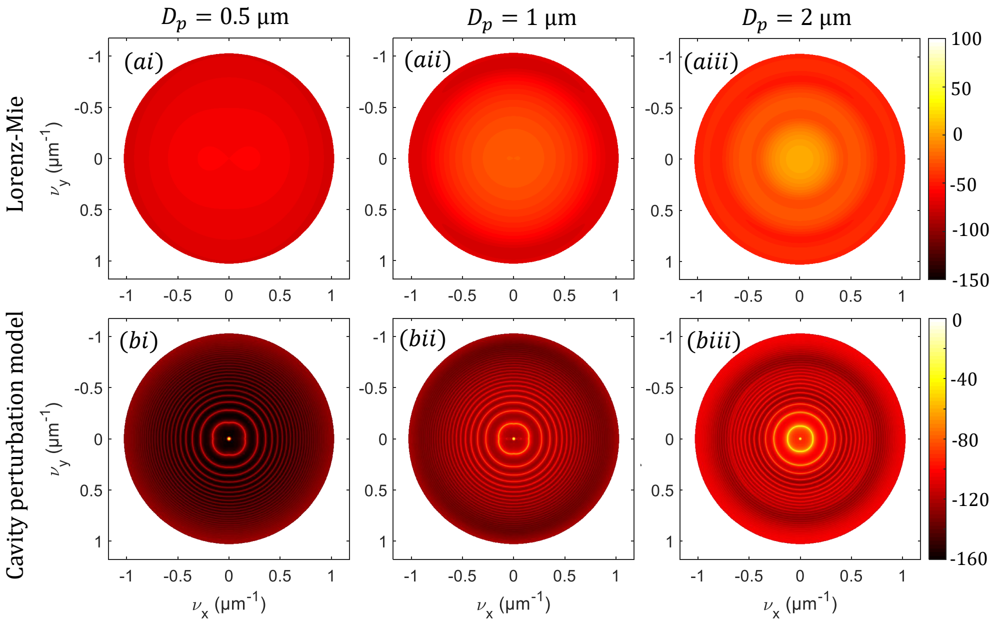

Figure IV.30: (a) Lorenz-Mie computations of scattering signatures for (i) 0.5 µm, (ii) 1 µm, and (iii) 2 µm. (b) Associated modelled cavity perturbation scattering signatures. Color axis is given is decibels.

A scattering signature has, depending on the particle size, one or more scattering lobes that resemble slow varying concentric rings. The polarization dependence of the Mie scattering is responsible for the non-circular aspect of these rings. A very sensitive image sensor would be able to detect the intensity of these scattering lobes but not their phase shift.

In our case, we observe Mie scattering through a resonant cavity, we will be able to observe the transmission of these scattering lobes, if they validate the resonance conditions of the FP cavity. Scattering is the phenomenon at the origin of energy transfer between FP modes. We have just seen that this transfer is done with a phase shift. This phase shift will modify the condition of the resonance of a FP mode, in terms of spacial frequency (both angular and spectral). The scattering lobes appear clearly with slow variations as wide spaced rings while the FP modes appear as intense thin rings. The spacing of these FP rings depends on the length of the cavity and are generally much smaller than scattering lobes can be. The radii of these rings are first related to the order of these modes (which are specific to the optical length of the cavity alone), these radii are then shifted by the phase shift acquired during scattering.

Several overlapping phenomena can be observed: rings (FP modes) modulated by Mie's oscillations and by mirror efficiencies.

Unfortunately, such a 3D model does not allow the intelligible understanding of effects that depend on the particle diameter. Moreover, due to computing capabilities, it is particularly difficult to simulate the perturbation of a long cavity using volumetric numerical methods such as 3D-FDTD. However, the dimensions of the problem can be reduced, since both our geometry and hypothesis are mainly based on the P and S polarization planes. For this reason, we can afford to reduce our field of study to the XZ and YZ planes. Thus, we will evaluate the cavity perturbation scattering signature only on the sagittal and tangential axis.

In Figure IV.31(a), the abscissa axis represent the signature in S and P polarization, for the positive and then negative polar angles θ respectively. One thus obtains a line for a given particle diameter, which can be stacked by varying the particle diameter along the ordinate axis. The intensity of the signature is displayed using a colored axis, in logarithmic scale.

In this 2D model, we no longer consider a sphere but an infinite cylinder[21] in the axis not considered. This cylinder is inside a DBR/DBR cavity (3 alt. aSi/SiO_2 optimized for 850 nm). The intra-cavity medium has a refractive index of 1.45, and the cylinder has an index contrast of 0.7. The Γ mode is excited at the nearest FP resonance around 850 nm.

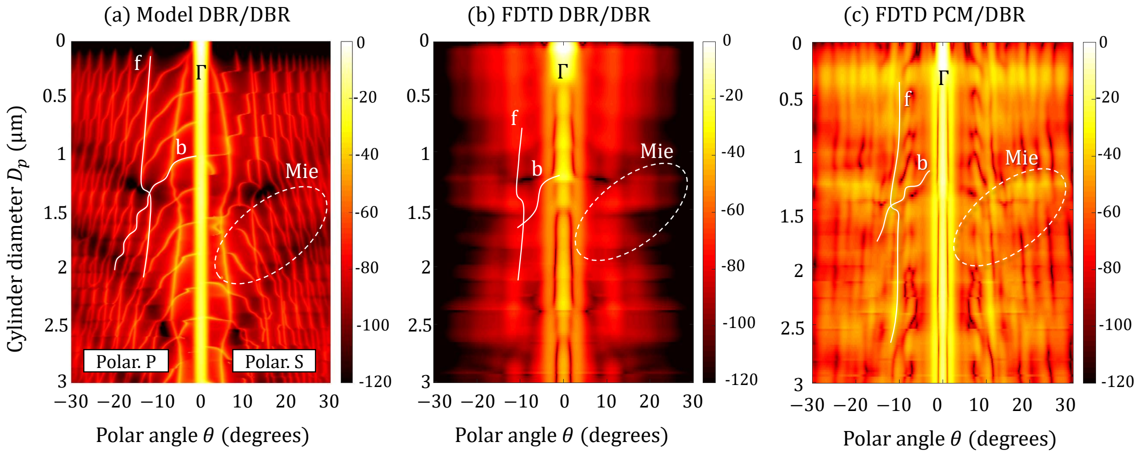

Figure IV.31: *Representation of the cavity perturbation scattering signature as a function of the perturbation diameter obtained with (a) the 2D model with a DBR/DBR cavity, (b) a 2D-FDTD simulation with a DBR/DBR cavity and (c) a 2D-FDTD simulation with a PCM/DBR cavity.*

In this graph, we observe a vertical intense line, which corresponds to the Γ mode. Its intensity varies according to the extinction efficiency of the cylinder, which depends on the diameter D_p. Then, we recognize fine lines corresponding to the FP resonances excited by the phenomena of scattering and backscattering (on the graph: f and b respectively). These resonances are based on the intensity of the Γ mode, as explained above and are modulated by the Mie's oscillations (on the graph, circled in white, with a dotted line). The fact that these lines are not vertical comes from the fact that the resonance conditions are modified by the phase signature φ_s of the particle, in particular the backscattering lines where the phase signature is very rich.

---

[21] See, 2D-Mie theory for cylinders [83].

For comparison, we simulate this DBR/DBR cavity, using a 2D-FDTD simulation. Here, we only simulate the P polarisation. The cavity perturbation scattering signature is derived from the simulation, using a near-field / far-field transformation. This transformation consists in averaging the Poynting vector per unit of solid angle, and assuming a spherical wave type decay (in $1/r$). Results are presented in subfigure (b), in the same fashion as for the 2D-model. Characteristics present in the model are recognized, in particular the f and b resonances, modulated by the Mie's oscillations, and shifted by the phase signature of the perturbator. However, these characteristics are largely overestimated in the model, compared to the FDTD simulation. Explanation for such a difference may come from, for example, the fact that we assume a delocalized perturbator, which causes an extended extinction of the Γ mode, and from the assumption that a higher order FP mode is always phase shifted the same way at each cavity round trip. Such a study, while failing to provide quantitative predictions of a cavity perturbation scattering signature, at least allows to point out some of the mechanisms that come into play when an FP cavity is perturbed by a particle (Γ mode extinction, phase-shifted scattering and backscattering resonances, *etc.*). Possible improvements for the model will have to improve on the formulation of our hypothesis.

Finally, subfigure (c) present the results of the same 2D-FDTD simulation but with a PCM/DBR cavity. The bottom mirror M_2 is a 1D-PCM operating at the P polarization, aroung 850 nm: $h = 0.2$ µm, $P = 0.5$ µm and $FF = 55$ %. By comparing subfigures (b) and (c), we can see directly that the simple fact of replacing the M2 mirror, from a DBR to a PCM had a strong positive impact on the signature.

First, we notice that the scattering efficiency is all the stronger as the extinction of the Γ mode is weak, *i.e.* for small particles, which are generally difficult to detect in out-of-cavity setup.

Then, the scattering and backscattering resonances are found much more intense and sharper than previous, as well as their phase-shift curves. It is as if scattering and phase shift effects were sustained by the cavity when it operates in higher FP orders. We suppose that the cavity/particle interaction is improved when the PCM is used at oblique incidence, presenting a rich reflectivity response, especially in terms of phase. This may allow to modify the resonance conditions of higher order FP modes when they are perturbed by the particle. In order to properly model the coupled interaction of a cavity composed of a PCM with a particle, it will certainly be necessary to model the behavior of a PCM, for example by means of the coupled mode theory [205,206].

IV.5 Fabrication of mirrors and cavities

IV.5.1 Fabrication of PCM mirrors

Our specific application needs a transparent substrate around 850 nm because we have an optical transmission systems, as explained earlier. For this reason we start our process with a glass substrate: 725 µm thick Borofloat 33 (BF33) 200 mm wafer supplied by Planoptik. Using such substrate in our 200 mm microfabrication platform is not standard. Indeed, most machines are designed to operate on non transparent substrates such as silicon. In order to use these machines we have performed an opacification step on the back-face of the glass substrate, by depositing a 100 nm Titanium adhesion layer followed by a 500 nm Silicon Nitride (SiN) layer. After this step, we can start depositing the stack needed to fabricate our PCM reflectors on the front face.

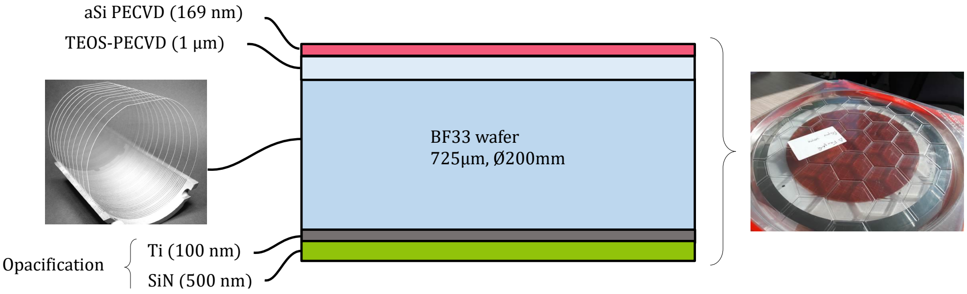

Figure IV.32: *Base stack for the process of the PCM mirrors (not to scale).*

Before the core layer, we first deposit a 1 µm thick SiO_2 bottom cladding (or BOX, standing for Buried OXide) by PECVD (Plasma Enhanced Chemical Vapor Deposition) using TEOS (TetraEthyl OrthoSilicate) at 400°, as a silicon source. This layer allows to compensate the slight refractive index mismatch between SiO_2 and BF33, which is $\Delta n = 0.02$. This oxide layer allows to guarantee a good top-down symmetry of the PCM[22]. This step can, however, be considered questionable, future PCM mirrors designs may instead forego the BOX.

Then, the core layer of hydrogenated amorphous silicon (a-Si:H, simply refereed as aSi) is deposited by PECVD at 350 °C, $h_{aSi} = 169$ nm ± 1.2 std. We must note that, the thick oxide layer, followed by the aSi slab, strains the glass wafer, resulting in a significant bow, which is measured at an average of 90 µm after the oxide deposition and 154 µm after aSi deposition. Indeed, amorphous silicon is well known for its tendency to strain wafers due to its high Young's modulus[23]. Note that we could not measure the bow after the de-opacification step. For this reason, we do not have information on the strain caused by the opacification layer on the back side. The base stack for the process of the PCM mirrors is presented in Figure IV.32.

---

[22] A PCM that is not symmetrical above and below the plane can exhibit more diffraction losses.

[23] The Young's modulus of SiO_2 is -80 MPa, while that of aSi is -750 MPa

Then, we can draw the lithography mask than contains those PCM reflectors. In order to compensate the fabrication errors that would result in the modification of the PCM's geometry, we draw several variants of the targeted design, by modifying P and FF following the ranges given in Table IV.2. This mask will be drawn into our device by e-beam lithography.

Lattice	*Targeted FF*	*Range FF*	*Targeted P*	*Range P*
(a) 1D	54 %	44 – 64 %	.510 µm	.46 – .56 µm
(b) Square (holes)	44 %	40 – 50 %	.425 µm	.40 – .45 µm
(c) Triangular (holes)	62 %	57 – 67 %	.560 µm	.51 – .61 µm

Table IV.2: *Geometrical parameters for* 169 nm *thick aSi membranes: targeted design and range of parameters.*

A 1D-PCM is quite easy and quick to pattern, because it's made only with a succession of rectangles. However, 2D-PCMs are much more complicated: indeed, contrary to a 1D pattern which can be drawn in a single line, the electron beam must be switched off/on and then moved to each 2D pattern (not to mention the large number of circles to be drawn. For this reason, we were able to draw large 1D-PCMs that have a square pupil sized by 200 µm × 200 µm; 2D-PCMs are smaller, with a pupil of 100 µm × 100 µm. Figure IV.33 present the mask used to pattern our PCM mirror designs.

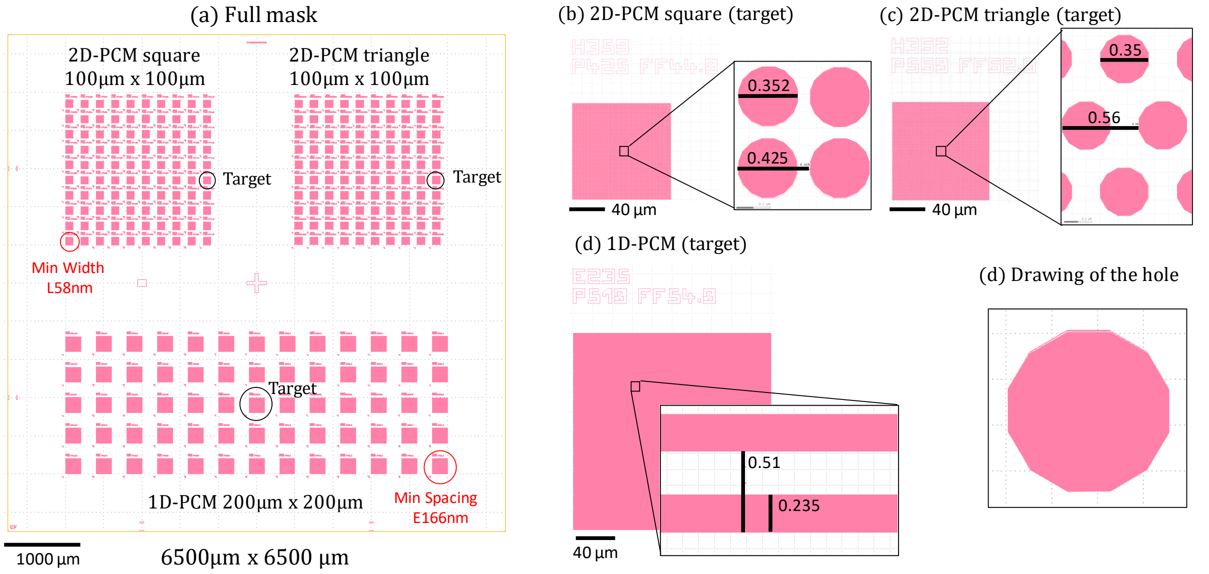

Figure IV.33: *Description of the lithography mask. (a) Full view of the mask, (b) View of the 2D-PCM square targeted design, (c) View of the 2D-PCM triangle targeted design, (d) View of the hole.*

In order to minimize the writing time of the e-beam step, a first rule is to define a path that minimizes the distance travelled by the scanning electron beam between each unitary pattern. Then, a second rule concerns the unitary pattern itself, a circular hole in our case: a circle has to be approximated by a regular polygon (see, Figure IV.33(d)). The more vertices we use, the better the circle will be defined, but the writing time will explode. We choose a 12 vertices regular polygon because it appears like a good compromise. Additionally the polygon should exhibit the same symmetry than the lattice, a 12 vertices polygon does show both a $\pi/2$ symmetry (square lattice) and a $\pi/3$ symmetry (triangular lattice). Finally, the vertices of two neighbors holes should not be facing each other, in order to limit the proximity effects during the writing step with the e-beam.

Ontop of the aSi layer, we deposit a 100 nm silica hard mask (SiH_4 PECVD, 300 °C). Then we deposit the e-beam positive resist (CAP112, 200 nm), by spin coating. An electron beam then fractures the resist, shaping the PCMs (see, Figure IV.34). The fractured resist is removed, exposing the underlying silica hard mask, that can be dry etched selectively (RIE with CF_4/O_2 gaz). Once the hard mask is etched, the resist is no longer needed, and thus stripped. Finally we etch the aSi layer (ICP-RIE with $HBr/Cl_2/CF_4$), reproducing the patterns of the hard mask.

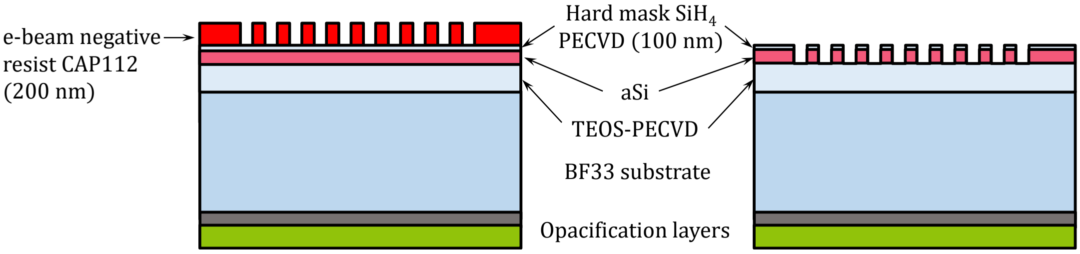

Figure IV.34: *Schematic view of the lithography and etching steps (not to scale).*

After the etching step, we have noticed problems of field stitching as seen in Figure IV.35. The imperfect stitching effects are aggravated by charge effects, specifically considering the insulating nature of the substrate (glass in our case). Such an artifact is indeed particularly noticeable at the frontier of two fields, where we can clearly see that the patterns are not connecting correctly.

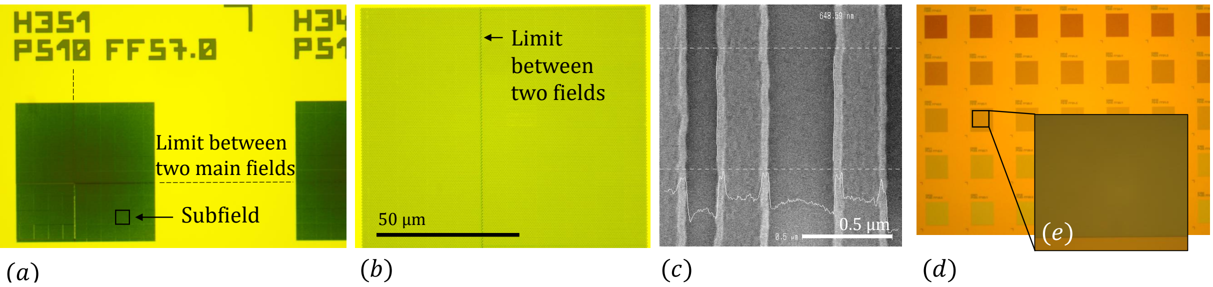

Figure IV.35: *(a) Optical view showing the frontiers of main fields and subfields. (b) Zoomed optical view of a frontier between two fields. (c) SEM view of a 1D-PCM showing that the period is locally broken at the frontier of the fields. (d) Wide and (e) zoomed optical view of the PCM designs written on a silicon wafer.*

In Figure IV.35(a), we can distinguish a main field, that crosses a PCM, as well as the smaller subfields (8.8 µm). This effects breaks the periodicity locally, creating defects within the PCM (see, subfigure (e)). Hopefully, not all PCMs are impacted by the bad stitching between two main fields, which are more critical than those for subfields. In order to confirm that this artifact is due to charge effects, we have tested our design on the same lithography step, but on a silicon wafer. Figure IV.35(d,e) are optical views of our PCM written on a silicon wafer, that does not exhibit the problems of field stitching observed on glass. We could not afford a new fabrication run to correct this issue. We had to report this artifact for those who would want to try the same thing in the future. A proposed solution would be the deposition a thin conducting layer (such as Ti, TiN or Al) below or above the resist layer, in order to properly evacuates the electrons. Alternatively, one can use a conductive e-beam resist specialized for insulating substrates, such as ESPACER 300 by Showa Denko K.K..

To prevent particle soiling within the holes of our PCM mirrors, and to ensure the vertical symmetry we cover the structured aSi layer with a silica top cladding deposited by HDP-CVD (High Density Plasma Chemical Vapor Deposition) at 400°[24]. This new layer is then planarized by CMP (Chemical-Mechanical Planarization), this prevents a periodic pattern to form above the PCM, that would generate parasitic diffractive effects. Finally, the opacification layer on the back face is removed. Figure IV.36(a,b) shows the result of the PCM mirrors after the desopacification step.

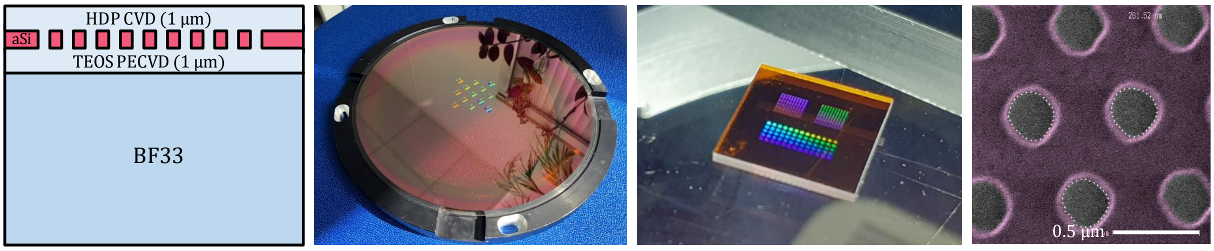

(a) (b) (c) (d)

Figure IV.36: (a) Schematic cross-cut view of the fabricated PCM reflector (not to scale). (b) Photography of the photonic chips on the glass wafer. (c) Photography of a diced chip. (d) SEM picture of a triangle lattice PCM (colorized).

The final photonic chip containing our PCM mirrors is obtained by dicing the 200 mm glass wafer, as shown in Figure IV.36(c). We notice the rainbow effects created by the arrays of PCMs that individually diffract lights when seen at high angles. The varying geometries of the PCMs results in the colouring of the mirrors, as seen in Figure IV.37, that can be useful to identify quickly a PCM among the group.

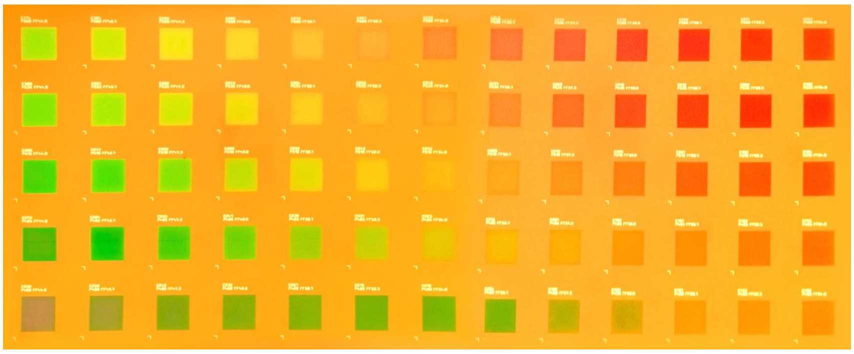

Figure IV.37: Optical transmission image of the 1D-PCM group, showing a nice color palette.

---

[24] Note that, we exceeded our thermal budget during this step, considering we deposited the aSi layer at 350°: this is not problematic as we knew that this specific aSi would not crystallize at 400°. As a backup, we've tried a top cladding made by SiH_4 PECVD, at 300 °C: after investigation, we didn't notice any difference between these two alternative steps. This step is known to cover efficiently inside small holes like in our PCM.

IV.5.2 Fabrication of DBRs

Distributed Feedback Reflectors were fabricated on our usual glass substrate (725 µm thick BF33). Prior to any steps, the glass wafer was diced into 2 cm × 4 cm samples, in order to roughly respect the dimensions of a microscope slide. The deposition step were performed at the PTA micro-fabrication platform at Grenoble, France, on a 4 inch PVD (Physical Vapor Deposition) coating machine. As explained earlier, the deposition consists in 6 alternation of Si_3N_4 and SiO_2 ($h_{Si_3N_4} = 106$ nm and $h_{SiO_2} = 146$ nm). Alternatively, we have also fabricated similar DBRs with 7 alternations, designed for 830 nm instead of 850 nm. Figure IV.38 show a schematic view of the stack, alongside a photography of fabricated reflectors.

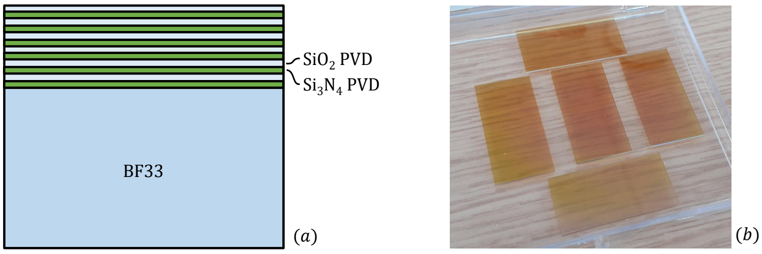

Figure IV.38: *(a) Schematic view of the DBR (not to scale). (b) Photography of fabricated DBRs.*

The photography in IV.38(a) show the mirrors as they were arranged on the sample holder of the PVD machine. The mirrors have a reddish hue thanks to their reflectivity around the NIR region. However, we notice that the mirror in the center is coloured with a deeper red, which is indicative of a slight non-uniformity of the deposit.

IV.5.3 Cavity assembly

The main element required for the assembly of the cavities is the spacer. We choose to fabricate the spacer from a calibrated 50 µm stainless steel foil (from h+s Präzisionsfolien). The opening between the two mirrors and the fluidic channel[25] is drilled out using a Ytterbium fiber laser driller (Trotec Speedy 400 flexx). Note that, the drilling process must spread out using multiple passes in order to prevent the foil from warping itself due to localized heating[26]. Figure IV.39(a) shows a photography of the stainless steel spacer next to the PCM and DBR mirrors.

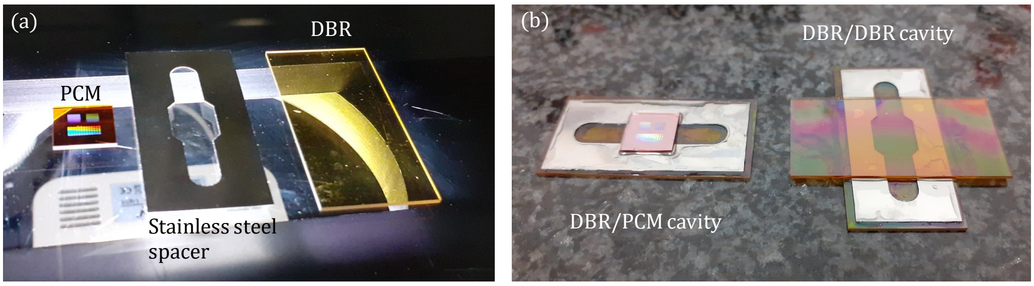

Figure IV.39: (a) Photography of the stainless steel spacer next to the PCM and DBR mirrors. (b) Assembled PCM/DBR and DBR/DBR cavities.

The stack that includes the two mirrors and the spacer must be assembled by maintaining a certain pressure. However, in use, such cavities (especially PCM cavities, which can be 100 µm wide) must be accessible with a short working distance, for example to be at the focal plane of a microscope objective (see, Section IV.6.4, hereafter). We didn't found a robust design with thin enough clamps to maintain sufficient pressure. Instead, we chose to glue the different elements of the stack (UV-Polytec glue), while the pressure is maintained by a rigid steel clamp. After polymerization, the clamp pressure is released.

In the following, we measured (from the free spectral range of a cavity spectrum) a cavity length of $d = 119$ µm for a DBR/DBR cavity and $d = 115$ µm for a PCM/DBR cavity. Those cavities are much longer than the 50 µm width of the steel spacer: we believe that the glue is stretched back after the release of the clamp pressure. Nevertheless, this assembly method allows full access to the back face of the top mirror. Figure IV.39(b) show a photography of the assembled PCM/DBR and DBR/DBR cavities.

We were also able to estimate the misalignment between the two mirrors, using a visible laser pointer, and measuring the deflection, induced by the misalignment, for the multiple reflections. This deflection is measured at long distance (about 10 m), and correspond to a misalinment of the order of the mrad, or below.

Note that those cavities can be disassembled by immersing them in an acetone bath. After this step, the mirrors and the spacer must be properly cleaned.

---

[25] Note that, a functional air convention system could not be developed within the allotted time.

[26] The warping of steel is an effect that prevent us from using thinner spacers.

IV.6 Characterization

IV.6.1 Vertical transmission micro-spectrometer

We use a micro-spectrometer to measure the mirrors and cavities spectra. This instrument, shown in Figure IV.40 allows for the measurement of vertical reflectance and transmittance spectra of samples sized by 20 µm. These measurements can be automated at wafer scale (200 mm). This instrument was developed prior to this work, but is well suited for testing our devices with few modifications. The reflectance measurement needs a calibrated reference sample with high reflectivity, and can accurately measure a sample's spectrum that is less reflective than the reference. For PCM and DBR mirrors, we could not obtain reasonable reflectance spectra. Hopefully, transmittance measurements does provide reliable data: we are most interested in these measurements as it is suited to our device architecture. Indeed, to make spectral measurement, we only need to take a background and a reference spectra of the source without the sample.

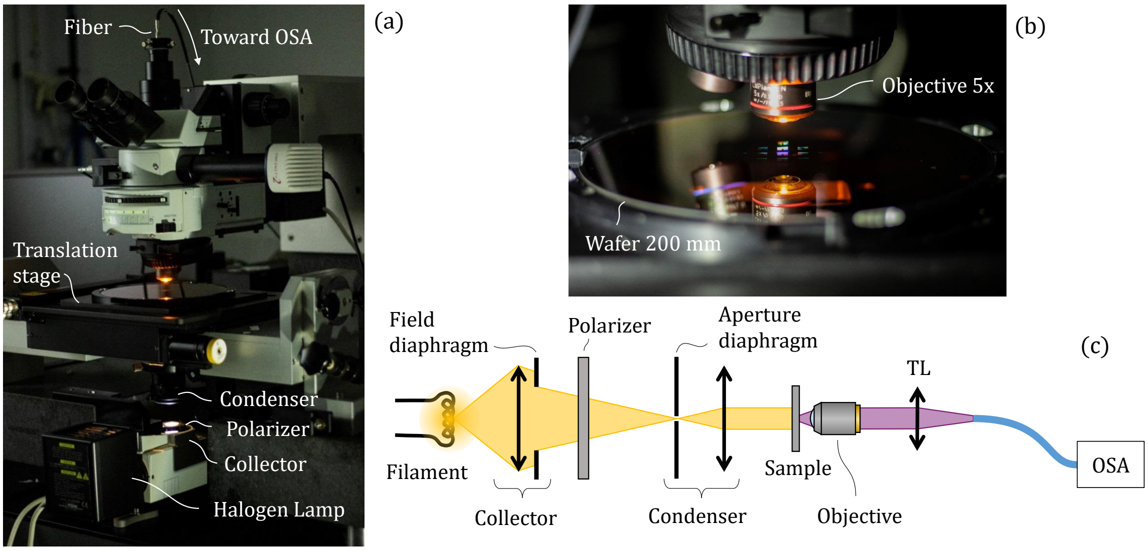

Figure IV.40: Photographs of the micro-spectrometer bench.(a) Full view. (b) Close-up view. (c) Simplified schematic of the optical setup.

We will now briefly describe the transmittance setup, with the support of the full view in subfigure IV.40(a). The source is a halogen lamp providing a broadband, white illumination covering the whole visible and NIR spectral range (up to 950 nm). Illumination of the sample is achieved using the Köhler setup [207], which consists in a collector doublet with a field diaphragm and a condenser doublet with an aperture diaphragm. Such a setup provides uniform illumination from the halogen lamp's filament and allows to properly collimate the beam by closing the aperture diaphragm mounted with the condenser doublet. We add a polarizer between the collector and the condenser in order to measure polarization dependent spectrum. The illumination beam is coloured yellow in subfigure (c).

Subfigure IV.40(b) shows a close-up view of the area around the sample. The latter is mounted on a motorized translation (X,Y,Z) stage that can hold a 200 mm wafer. The transmitted beam is collected by the microscopy setup (the sampled beam is coloured purple in subfigure (c)), using a microscope objective (Plan-Apochromat. x5). The image of the sample is focused, by a microscope Tube Lens (TL), to a 100 µm core multimode fiber. The fiber's core is magnified by the microscope objective so that the surface collected is 20 µm. Finally, the fiber relays the transmitted light to an optical spectrum analyzer (OSA) where the light is diffracted by a grating and cast on a CCD camera (Andor Newton, SR-303i-B).

IV.6.2 Dielectric mirrors transmittance spectra

We usually consider the spectrum $1-T$ that resemble the energy reflectance spectrum R but integrates the absorbed and diffracted energy. In the case of a DBR constituted of two materials (silicon nitride and silica) that does not absorb at our spectral range, and does not diffract light, we can safely consider $1-T \simeq R$. In Figure IV.41, we present the $1-T$ spectrum of a fabricated DBR compared with the targeted reflectance spectrum computed using the Abelès matrix method (see, Appendix J).

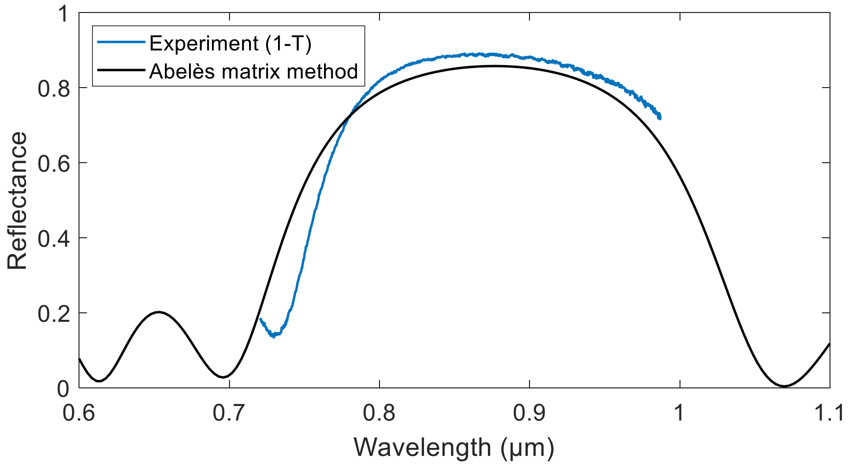

Figure IV.41: *Comparison of measured and calculated (Abelès method) DBR spectrum.*

We verify that the measured spectrum is consistent with the calculated one. Slight differences are likely caused by small inaccuracies during the PVD deposition process.

Then, we measure the PCM's transmittance spectra. As explained earlier, we are able to measure the polarization dependent transmittance $T_{S/P}$ spectra of every single PCM mirrors within a full 200 mm wafer. Every PCM is repeated throughout 13 chips contained in the wafer: we define the mean transmittance $\langle T \rangle$ and its standard deviation $\mathrm{std}(T)$. In Figure IV.42, we plot $1-\langle T_S \rangle$ (first line), $1-\langle T_P \rangle$ (second line) and $\mathrm{std}(T_S)$ (third line). Each line contains all 65 spectra from each individual 1D-PCM contained in one chip. These spectra are regrouped in five subplots (five columns) that correspond to 5 periods. Each subplot is the spectrum as a function of the PCM's Filling Factor (FF).

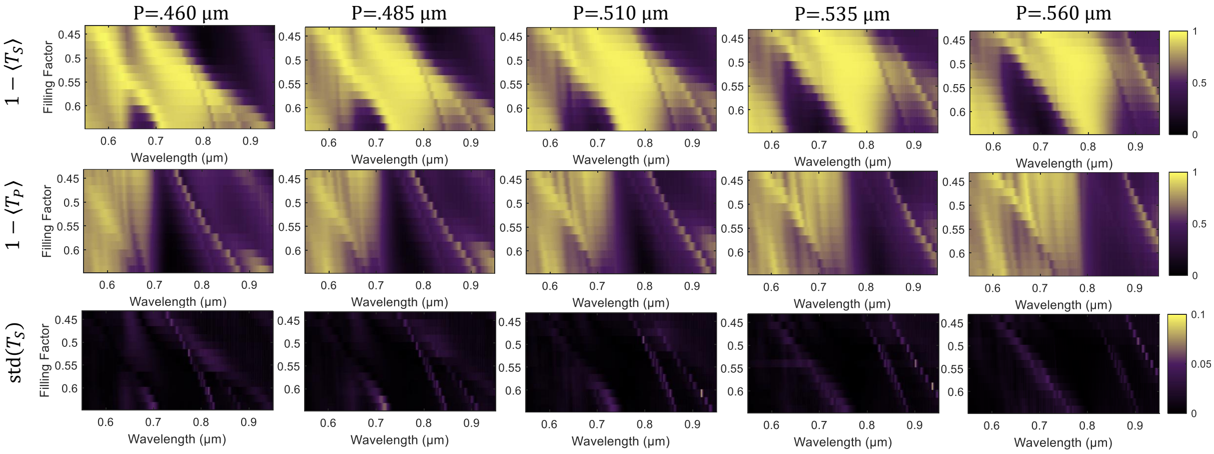

Figure IV.42: *Polarization dependent mean transmission spectra of all 1D-PCM, and example of standard deviation transmission spectra.*

The first line shows the $1-\langle T_S \rangle$ spectra, which are measured in the S polarization (operating polarization). We observe a transmission drop that are likely the reflectance plateau that depends on FF and P. The second line shows the $1-\langle T_P \rangle$ spectra (P polarization). We verify that our 1D-PCM are polarization dependent. The third line shows the standard deviation spectra $\mathrm{std}(T_S)$ calculated from the 13 chips illuminated with the S polarization[27]. We see that the main source of deviation originates from the fine Fano resonances that are a slightly shifted. Fortunately, the mirrors working range are not impacted by these resonances which gives us a very good uniformity throughout the wafer: the order of magnitude is about a few percent in transmittance. This measurement is made for both polarization and for all PCM mirrors (1D and 2D), for readability reasons, we only plot $\text{std}(T_S)$ for the 1D design, but similar results were obtained with the other designs and polarization.

Then, we present in Figure IV.43 the $1 - \langle T_{S/P} \rangle$ spectra obtained from a 100 square lattice 2D-PCM, averaged over 13 chips.

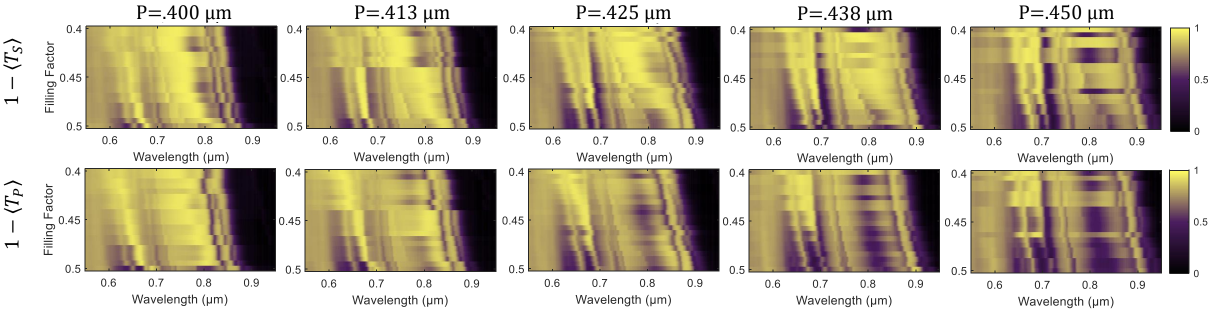

Figure IV.43: Mean transmission spectra of all 2D-PCM, square lattice.

As before, the first line shows the $1 - \langle T_S \rangle$ spectra while the second line shows the $1 - \langle T_P \rangle$ spectra. We expect that such design is independent of the polarization, when illuminated at normal incidence. However, we do observe polarization dependencies, especially for larger periods, where the reflectance gets degradated at the P-polarization. We believe this artifact is due the e-beam writing process that could have drawn non symmetrical holes[28]. Another comment is that the measured spectra does not seem to be modified continuously when varying the two geometric parameters (FF and P): this can be explained by the fact that square lattices are the hardest of our designs to manufacture. We will see in Appendix H that the triangular design presents a much better independence in terms of polarization, due to the less aggressive geometrical parameters.

---

[27] Such measurement is important if one want to manufacture a large number of these mirrors to assemble PM sensors at industrial scale.

[28] The e-beam path is generally horizontal, which can result in the writing of a slightly ellipical hole, which breaks the symmetry of the PCM [202].

IV.6.3 Cavity spectra

In Figure IV.44, we present the reflectance spectrum of an unperturbed DBR/DBR cavity. It shows clear FP resonances, in the forms of Lorentzian shaped reflectance drops. The specific shape of DBR reflectance is found by following the envelope of those resonances.

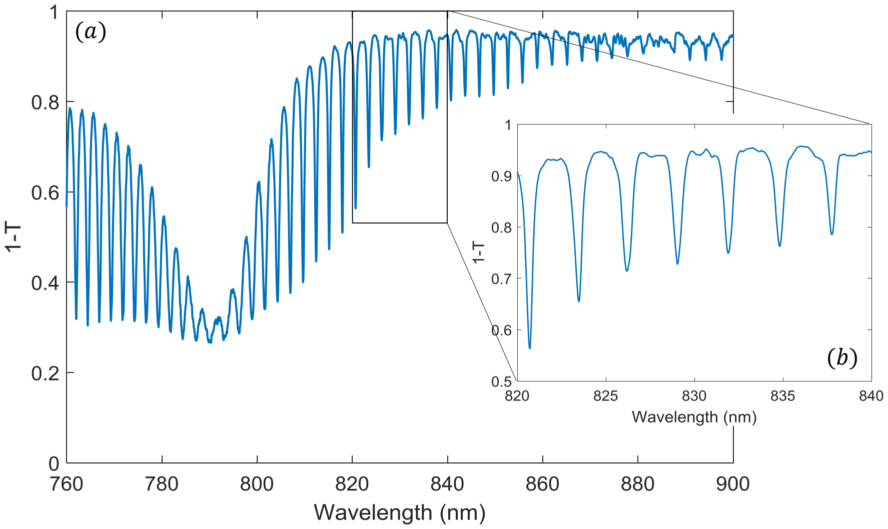

Figure IV.44: *Unperturbed DBR/DBR cavity spectrum: (a) Full measured spectral range. (b) Zoom on the range of interest.*

Subfigure (b) shows the FP resonances around the spectral range of interest (*i.e.* around $\lambda_0 = 830\,\text{nm}$). Using the free spectral range (FSR) formula $\Delta\lambda_{FSR} \simeq \lambda_0^2/2d$, we can derive the measured cavity length $d = 119\,\mu\text{m}$, which is much higher than the width of the spacer (50 µm), which results from the gluing process, as explained earlier.

The question now arises as to the impact of a particle-induced perturbation on such a spectrum. During the preparation of this manuscript, we did not have time to develop a fully functional air fluidic system that would have allowed an aerosol to circulate the cavity. However, our instrument allows us to reduce our sampling area down to 20 µm, and thus measure the perturbation induced by a single dust (less than 20 µm in size) naturally sedimented inside the cavity. Figure IV.45 shows measured spectra, resulting from the cavity perturbation of three dusts of different size.

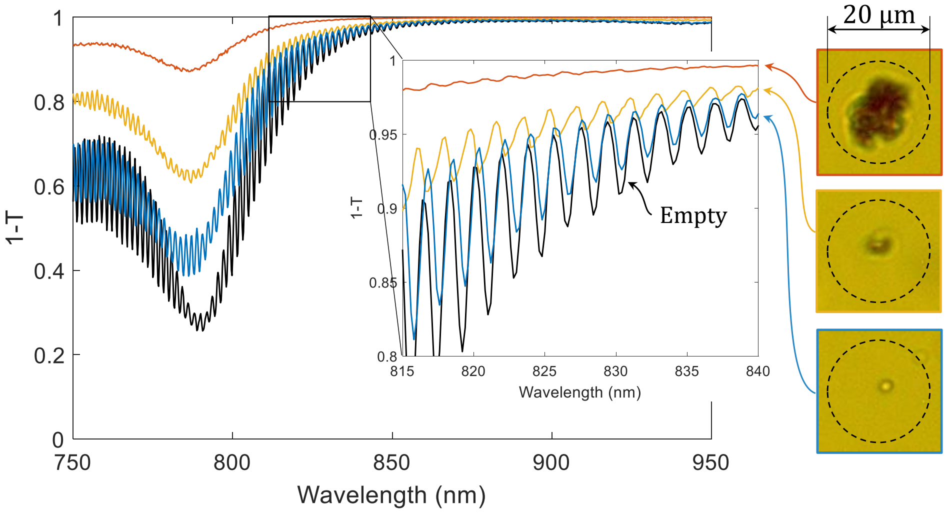

Figure IV.45: *Dust-induced perturbation of a DBR/DBR cavity, for three different sized-dust (coloured lines), compared with the unpertubed spectrum (black line).*

We have selected three neighbouring dusts (in order to compare them, and to avoid the effects of spatial non-uniformity of the mirrors) of different sizes[29] and with low aspect ratios. Optical images of the sampled dust are presented in Figure IV.45, the dotted black circle represent the sampled surface.

We notice that the larger the size of the dust, the more the FP resonances lose in quality (loss of contrast on the spectrum). This effect is due to the fact that the presence of dust induces optical losses in the vertical cavity mode, the only one being measured by the instrument. Previously, we had called this effect the extinction of the Γ mode. For the largest dust, the extinction effect is such that there is almost no transmission ($1 - T \simeq 1$).

Then, we notice that the resonances of the perturbed cavity spectra are shifted with respect to the unperturbed one, while keeping the same FSR. This is consistent with our previously suggested hypothesis that the Γ mode undergoes a phase shift when it passes through a particle. However, this effect remains difficult to quantify, because of our large cavity length (which induces a small FSR). In future studies, we could attempt to reduce the cavity length (while allowing a good air flow between the mirrors) in order to better spectrally isolate those FP resonances, and thus better quantify the phase shift effects.

The important point that prevents us from pursuing our interpretation of the perturbed spectra is that we could not carry out these measurements with calibrated particles (*e.g.* PSL beads). Indeed, neither the full geometry nor the complex refractive index of the dust is known. We have indeed encountered difficulties in depositing hydrosol droplets and drying them without having the particles aggregating during this stage. If one wants to achieve such a deposition, more sophisticated processes will have to be implemented, including for instance a dilution and a pressured atomization step followed by a droplet impact on the targetted surface.

---

[29] Red, yellow and blue curves, in decreasing order of size.

Then, we measure the polarized transmittance spectra (presented as $1 - T_S$ in Figure IV.46) of all 65 1D-PCM/DBR cavities. The presentation of the results is done in the same way as for Figure IV.42.

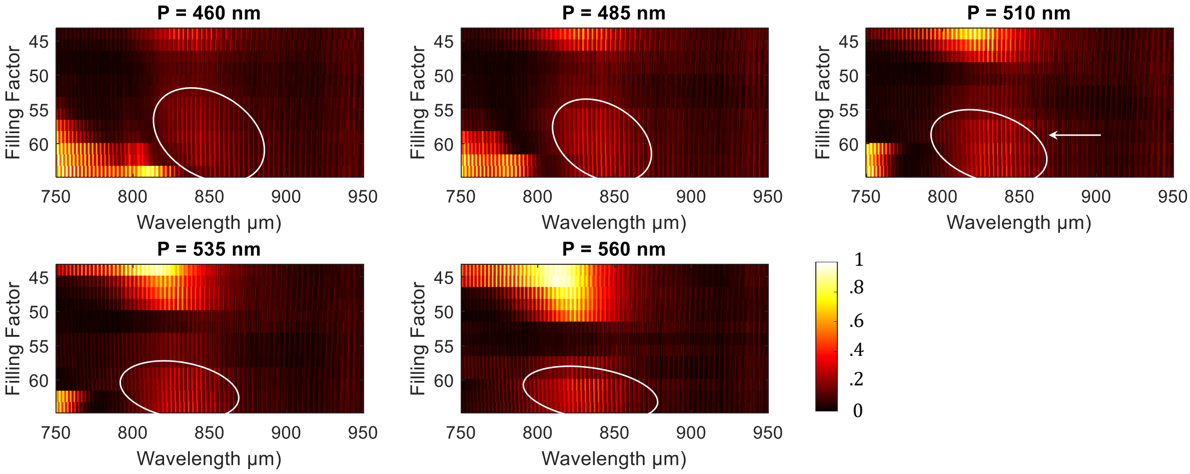

Figure IV.46: Polarized transmission spectra $(1 - T_S)$ of all 1D-PCM/DBR cavities.

We have circled in white the areas of interest, were we observe sharp FP resonances, that correspond to the operating areas of both the 1D-PCM mirrors and the DBR. In this way, we can determine which PCMs allow us to obtain satisfactory cavities. For example, we select one of the PCMs (white arrow), and draw its $1 - T_S$ spectrum in Figure IV.47. Its geometric parameters are $FF = 57.33$ % and $P = 0.51$ µm.

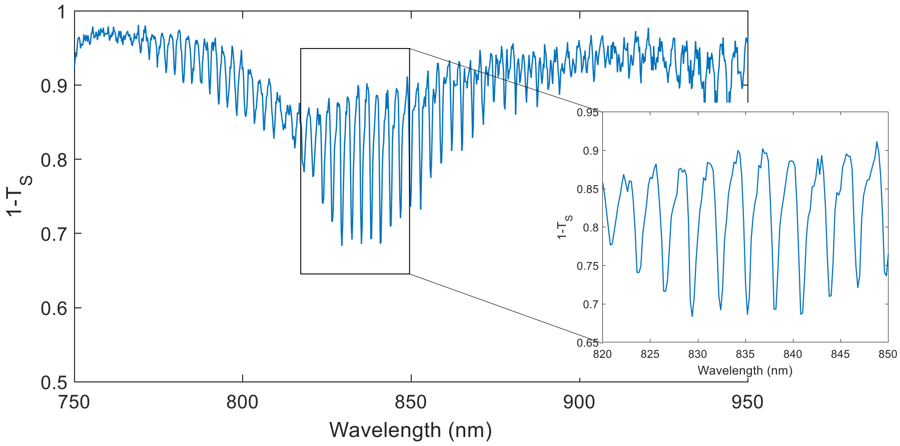

Figure IV.47: Polarized transmission spectra $(1 - T_S)$ of a single 1D-PCM/DBR cavity.

Here again, sharp FP resonances are observed. However the contrast is weaker than for the DBR/DBR cavity, indeed the 1D-PCM reflectivity is lower and the pupil limited to 200 µm allows for more lateral losses. The cavity length, derived from the FSR, is $d = 115$ µm, which is very close to that obtained with the DBR/DBR cavity (which was to be expected because the assembly method is identical).

IV.6.4 Fourier-domain imaging microscope

After recording spectra of the dielectric mirrors and cavities, the next important characterizations are the angular images of PCM or cavity perturbation scattering signatures: meaning we have to develop a Fourier microscopy imaging setup, with specific requirements. Indeed, a Fourier image should be recorded while aiming (in real space) at a specific PCM mirror (sized by 100 µm or 200 µm) within the photonic chip. In order to properly sample the correct area, a spatial filtering has to be performed. Such a microscope is presented in Figure IV.48.

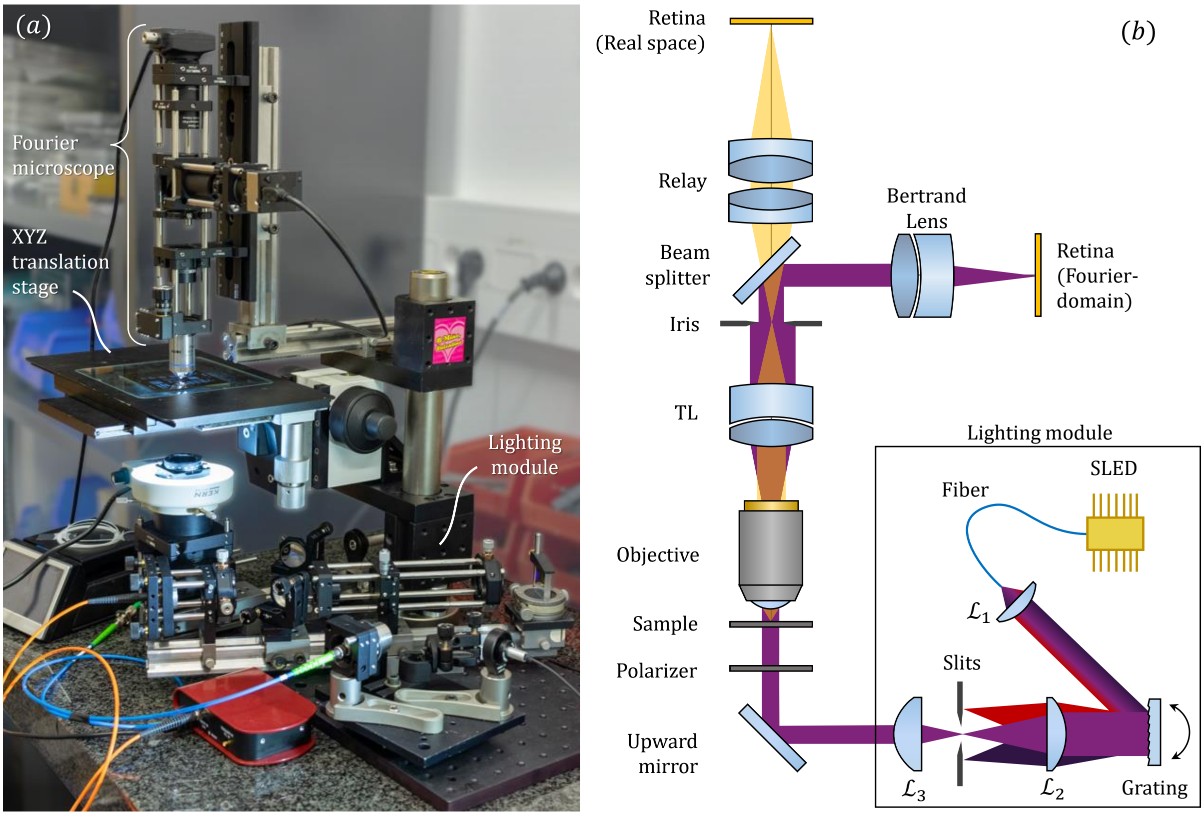

Figure IV.48: *(a) Photography of the full bench. (b) Schematic of the full optical system.*

The imaging part, which is a modified microscopy setup, allows to make simultaneous images of a sample in both Fourier and real space. The optical system is separated toward two paths, using a beam splitter (BS), leading to two retinae. It is placed after an intermediate image plane (with a proper magnification) where an iris is used to perform a spatial filtering of the sampled area. The optical system is schematized in subfigure (b), and precisely described in Appendix K.1, alongside RT simulations.

This imaging setup is assembled vertically in a fashion similar to a transmission optical microscope, with a microscope XYZ translation stage and a bottom lighting system, as photographed in subfigure (a). Such a configuration makes easier the manipulation and observation of our samples, compared with a full horizontal configuration.

The lighting system, framed in subfigure (b), is designed modular, and can be placed next to the microscope and easily injected upward using a simple redirection mirror. It can illuminate our samples with a collimated beam, polarized linearly. An illumination ring provides white light for brightly coloured images in the real space domain. In our configuration, the lighting system is constituted by a broadband NIR SLED, and a monochromator. Such a setup allows us to tune the illumination wavelength (as well as the spectral bandwidth), this in order to match a specific Fabry-Perot (FP) resonance. Precise details on the design and characterization of the lighting system is provided in Appendix K.2.

IV.6.5 Cavity perturbation in Fourier domain

We use the Fourier-domain microscope in order to record the transmission image of the DBR/DBR cavity (without perturbation), while being illuminated at normal incidence, at $\lambda = 830$ nm. We had expected to get a single dot at the center of the retina, with possibly faint FP rings, caused by parasitic scattering. However, we've obtained a train of dots[30], aligned in one direction, from the center and fading away toward an edge, as seen in Figure IV.49(a). Those dots are spaced by about 1°.

Note that the angular correspondence of pixels is derived from RT simulations (see, Appendix figure K.1), and validated experimentally using diffractive targets (USAF 1951 target). The following Fourier-domain images are stretched in order to compensate the barrel distortions of our Fourier-domain microscope.

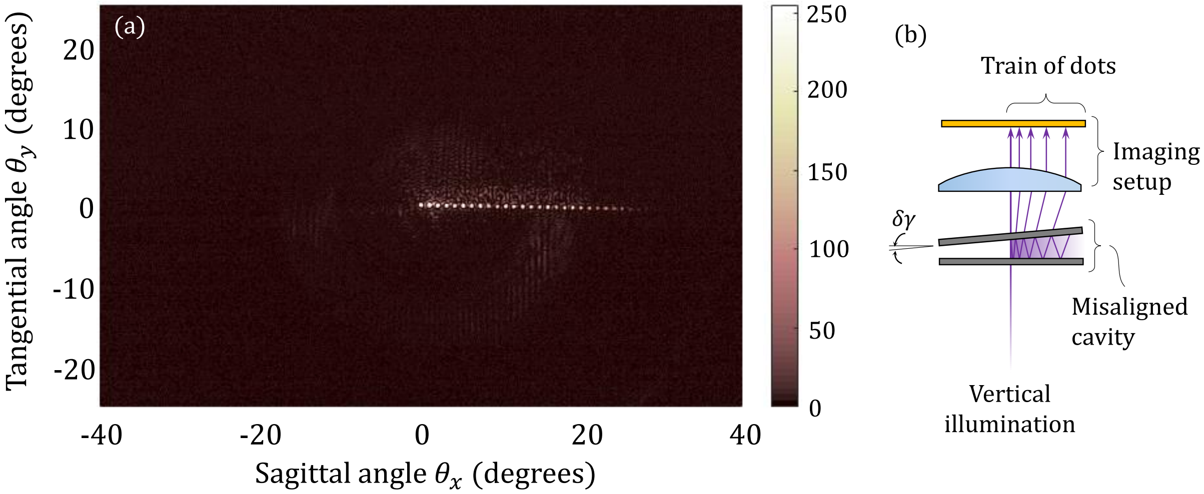

Figure IV.49: (a)Fourier-domain image of the DBR/DBR cavity illuminated at normal incidence. (b) Schematic of the proposed mechanism behind the formation of a train of dots.

We notice, that the direction of the train of dots is only related to the orientation of the DBR/DBR cavity. This leads us to believe that this train is caused by a misalignment between the mirrors (wedged cavity), which causes successive deflections in one direction (see, Figure IV.49(b)). If only geometrical effects are considered, then the spacing between the different points of the train should be equal to the misalignment $\delta\gamma$ previously estimated at $\delta\gamma \simeq 1$ mrad, which is not consistent with the measured spacing (about 1°). We also noticed that the spacing of the dots is dependent on the wavelength, with can be tuned by rotating the grating of our monochromator (see, Appendix K.2). The latter part leads us to believe that the measured dots are the results of interferometric mechanisms (not purely geometric), and could very likely be transmitted cavity resonances. We must note that the resonances conditions of a wedged cavity aren't fully understood yet, and are not the same of that of the off-axis FP cavity.

This transmission figure, in the form of a train of dots, is very different from what was originally planned and modelled. Hoverer, it appears that those dots are the results of cavity resonances; thus, it might be interesting to study how such resonances could be perturbed.

---

[30] Note that the spread of dots is mainly due to the quality of the collimation of the incident beam, and not much the PSF of our imaging system.

As explained earlier, we could not develop a fully functional air convection system, in order to test such a cavity with a calibrated aerosol. Thus, we apply the same methodology as in Figure IV.45, which is to study the perturbation induced by uncalibrated dust (that have sedimented inside the cavity). Once again, we have a spatial filtering system (iris in an intermediate image plane) that allows us to sample the rays coming from an area where a single dust is encountered.

In Figure IV.50, we provide examples of the cavity transmission of our DBR/DBR cavity, when perturbed by two different dust.

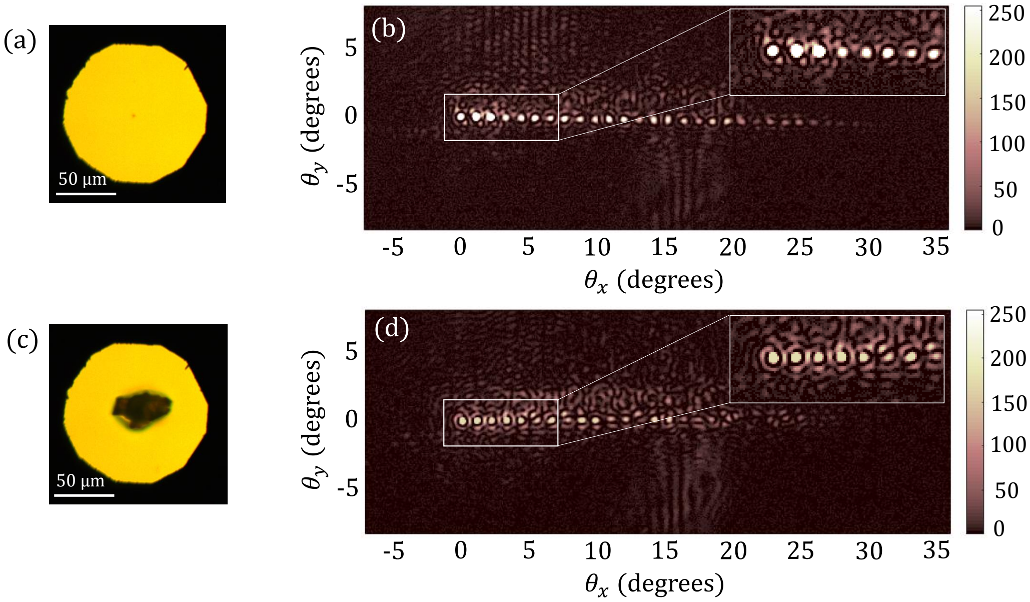

Figure IV.50: *Real-space images of (a) a small dust, and (c) a coarse dust inside the cavity. (b,d) Associated Fourier-domain images of the cavity perturbation.*

Subfigures (a,c) show the real-space images of two dust in the cavity which are very different in size, which are meant to illustrate cases of weak and strong perturbations. The black polygonal frame seen in real space images is the iris (at the intermediate image plane of the microscope), that allows for the spatial filtering of Fourier-domain images. Subfigures (b,d) show the associated Fourier-domain images.

On one hand, for the weak perturbation (small dust), the intensity of the dots are weakly impacted compared with the unperturbed image (see, Figure IV.49(a)), meaning that the extinction effects are weak. However, we observe luminous lobes around each dot, which could very likely be caused by scattering effects.

On the other hand, for the strong perturbation (coarse dust), the dots have dropped in brightness due to extinction effects. Then, we can clearly see what we interpret as scattering lobes around each dots, which are much brighter than those made by the small dust. The fact that these scattering lobes are thin (unlike Mie-like scattering lobes) could be an indicator that those are new resonant modes, excited and phase shifted by scattering.

We also notice important interference effects at the vicinity of the train of dots that resemble speckle effects. The rough nature of those large dust in term of surface irregularities (and maybe also volume porosities), could lead to those speckle-like interference effects.

The Fourier-domain image carries most of its information in the axis of the train of dots. Here, we've oriented the sample so that this axis is aligned with the sagittal axis. Then, we can reduced the dimension of the Fourier-domain image into a line, by evaluating it only along its sagittal axis. In order to explore further the dust size dependence on those reduced Fourier-domain lines, we can stack various lines (corresponding to various dust) as shown in Figure IV.51(b).

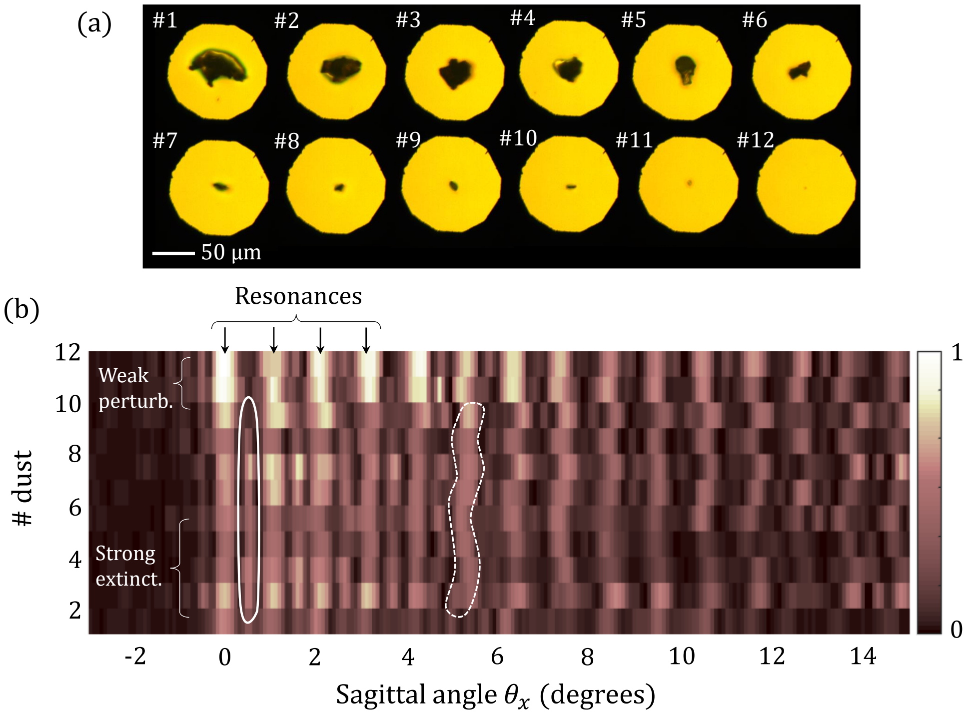

Figure IV.51: *(a) Real-space images of 12 dust indexed in decreasing size. (b) Line-cut (sagittal axis) of the associated Fourier-domain images.*

We select 12 different dusts, associated real-space images are shown in Figure IV.51(b). All 12 dust are indexed in decreasing order in size. The stack of lines in subfigure (b) shows various regions where perturbation effects can be seen. The resonance dots are here seen as roughly vertical columns, following those columns allows to find hints on the dust size dependent effects.

For small dust, we see that the resonances are still very bright, meaning that the extinction effects are weak. Then, the larger the dust is, the stronger those effects gets. In this stack of line, we can observe resonant scattering effects, in the form of roughly vertical columns between the resonances, as circled in white (solid contour). Then we can glimpse what we interpret as phase shifting effects that result in a bending of resonances, which are stronger for high sagittal angles, as seen circled in white (dotted contour).

As previously discussed, the fact that we have not been able to carry out such measurements with calibrated particles limits us in our analysis and interpretation of the results, as we do not have the possibility of knowing the true nature and geometry of the dusts, in addition to not being able to precisely determine their size. Future studies should be able to be carried out with calibrated particles (*e.g.* PSL beads).

Nevertheless, as a qualitative point, it should be remembered that there seems to be the expected effects when a cavity mode is perturbed by dust: *i.e.* extinction, scattering to other resonant modes and phase shift.

IV.7 Chapter conclusion

In conclusion to this chapter, we have designed a third prototype, with a forward looking approach. It consists in an open dielectric vertical cavity (VC), where particles are allowed to disturb a cavity mode, by crossing the space between the two parallel mirrors. Such a structure would allow to measure a cavity perturbation scattering signature, by transmission imaging, in order to detect and characterize particles. This, with enhanced sensitivity, by taking advantage of the high power density inside the resonant optical cavity.

The purpose of such a prototype is not to provide a functional PM sensor, but to pave the way toward a future sensor that has a great sensitivity, a strong capacity for aerosol characterization and a significant potential for integration and miniaturization. The main goal of such a study is to better understand the mechanisms involved when a particle disturbs a cavity mode, notably in terms of the modification of resonance conditions (both spectral and angular). We also study the impact of different types of mirrors, such as distributed feedback reflectors (DBRs) and photonic crystal membrane (PCM) mirrors.

First, Sections from IV.2 to IV.4 are a kind of paper study on DBRs and PCMs dielectric mirrors, in terms of working principles, and designs; as well as on dielectric VCs. In particular, Section IV.4 reports a model that formulates hypothesis on the perturbation of such a VC: extinction of the fundamental mode, and the excitation of phase-shifted resonant scattering modes. The model is then compared with FDTD simulations, showing much better performances for the PCM/DBR cavity in terms of its sensitivity to perturbation compared with the DBR/DBR cavity.

Then, Section IV.5 reports the fabrication of dielectric mirrors (DBRs and PCMs) on a 200 mm transparent glass wafers, made using conventional micro-fabrication techniques for integrated photonics. We have then explored preliminary assembly techniques.

Finally, Section IV.6 describes the development of optical benches used to characterize the spectral and angular behaviour of such micro-cavities, involving a vertical transmission micro-spectrometer and a vertical transmission Fourier-domain microscope. Then, we report preliminary characterization results of the perturbation of VCs, induced by uncalibrated dusts, which tend to confirm our hypothesis

There is still a lot of work to be done on this subject. Firstly, it will be necessary to improve the formulation of the cavity perturbation model and to take into account the specificities of DBRs and PCMs in order to best fit the FDTD calculations, and thus to have *in fine* a prediction capability for a cavity-perturbation scattering signature. Next, cavity assembly methods will be improved to ensure good control of cavity length and mirror alignment. Then, we will try to implement a functional air convention system in the cavity. Finally, those future cavities will have to be tested with calibrated aerosol, such as PSL beads.

This knowledge could, in the future, help us design an open active cavity, where the fundamental mode is excited by optical or even electrical pumping.

Conclusion and perspectives

During the preparation of this manuscript, we sought to make our contribution for the scientific community in the development of tomorrow's Particulate Matter (PM) sensors *'on-a-chip'*, which should be miniaturized, portable and inexpensive while being at the same time sensitive and accurate. The development of such sensors is a new effort, which must address the current sanitary and environmental issues related to air quality monitoring. When tackling a new topic, some questions must be asked: what should such a sensor look like, which designs are successful, which ones are not? What are the difficulties we did not imagine we would encounter? We believe that answering those questions would come to through a path-finding phase, and we had the privilege to walk down this path, in search for the beginnings of those answers.

Chapter I is an introduction to the topic. It provides an overview of the environmental and sanitary issues raised by PM pollution, and underlines the importance of having the capability to monitor ambient air quality, using widely distributed networks of inexpensive and portable sensors. Various PM sensing techniques are reviewed, and we show that OPCs (optical particle counters) are very good candidates for miniaturization and integration. Then, we review light-scattering theories and methods, in order to better understand how particles interact with light. This knowledge helps us see how the architecture of the sensor can be optimized. In other words, see how to maximize the sensitivity and accuracy in the characterization of aerosols, both in terms of measurement and data process. At the end of this general introduction, we choose to measure the scattering signature (angular scattering efficiency) of single particles, and this by several methods of imaging, and then process this image relying on the Lorenz-Mie theory. Based on this, we explore different optical setups and imaging modes, through the design of three prototypes, which are targeting at different levels of maturity.

A first prototype is described in Chapter II. Here, the scattering signature is evaluated by the means of a lens-less setup, and recorded using a unconventional CMOS image sensor. Such an imager chip is made with a vertical traversing fluidic channel, and named 'holed retina'. We report the design fabrication of the holed retina at wafer level (200 mm). The lens-less setup is then described, and features a cloaker (3D printed piece designed for stray light protection). Using this setup, we present experimental signatures recorded using calibrated polystyrene beads. These images are highly dependent on the position of the scatterer, and in agreement with modelled signatures. The latter can be computed using both the Lorenz-Mie theory and a radiometric projection model. Finally, an image analysis procedure is described, which allows to classify particles, by fitting a best modelled signature to the experimental one. An estimation of both the diameter and the refractive index of a particle can be made, but the accuracy is to be improved, mainly because the lens-less setup provides a projected signature that is highly dependent of the position of the scatterer and with a quite narrow field of view (FoV).

The second prototype, described in Chapter III, is an improved version of the first prototype. The limited FoV and the position dependency is addressed, by switching the lens-less projection to a Fourier-domain imaging setup. Such a setup is a kind of optical pre-processing that makes image processing much robust and simpler. It is achieved using a millimeter-sized, monolithic assembly of refracto-reflective optical sub-systems arranged around the fluidic channel. Each sub-system is designed to focus the scattering signature from a particle into a given area on the holed retina, providing an angular image, independent on the position of the scatterer and with a very wide FoV when combining all sub-systems. We report, notably, a state of the art fabrication process that involves the direct 3D writing on glass. We describe the optical setup involving an optimized cloaker and a compact illumination module. We provide examples of experimental images and reconstructed signatures from calibrated polystyrene beads. A simplified analysis procedure suggests that the accuracy of the particle characterization has been greatly improved compared to the lens-less setup.

Finally, the third prototype described in Chapter IV, is the result of a forward looking approach, where the aerosol is detected and characterized inside a resonant optical cavity, that comprises photonic crystal membrane (PCM) mirrors and distributed feedback reflectors (DBRs). A cavity mode is deliberately perturbed, and characterized through transmission imaging, by recording the 'cavity perturbation scattering signature'. The mechanisms involved in such a perturbation is studied first theoretically, by using a wave propagation model and FDTD simulations. It appears that PCM based cavities are especially sensitive to such a perturbation, and could be well suited to cavity-enhanced PM sensors. Next, we report the design and fabrication of PCM and DBR mirrors on glass substrates using conventional photonic manufacturing techniques, followed by the assembly of the cavity. Preliminary experimental studies are performed, in order to characterize the cavity perturbation induced by a particle through its spectral and angular effects, using dedicated benches. Those theoretical and experimental studies suggest the following perturbation mechanisms: extinction of the fundamental mode, energy transfers toward higher order resonant modes, and phase shifting.

Those prototypes should be considered as firsts attempts, in an iterative design methodology, paving the way toward future PM sensors. For the continuation of the work, we suggest several improvements. Firstly on the holed retina, the packaging and driving hardware should be improved, for instance with the use of an ASIC. Proper fluidic, and aerodynamic study should be performed, in order to implement an efficient air convection system. On the optical part, it could be interesting to manufacture and assemble cloakers and miniature optical systems for both beam forming and Fourier-domain imaging at wafer scale. Then, for the cavity-enhanced prototype specifically, more developments will have to be made concerning the cavity assembly process, and the implementation of a proper fluidic system. At each iteration of prototypes, we could perform proper statistical studies on a wide size range of calibrated particles, in order to determine its specifications (repeatability, sensitivity, particle size range, accuracy *etc.*). Lastly, in order to be more representative of a real aerosol, we could perform those tests with a larger variety of particle types (such as organic, inorganic, aqueous, irregular particles); and *in fine*, on field studies.

To whoever has made it this far, we hope you had a pleasant reading, and we wish you best of luck for your new sensor ;)

A

Appendixes

Appendix content

A Conventions: normalization, polarization and geometry

In this manuscript, we rely on concepts and tools originating from various fields of optics (geometrical or wave optics, electromagnetism), leading to as many different definitions and conventions. For the sake of consistency, we will agree on certain conventions throughout this manuscript, which are listed hereafter.

A.1 Normalization in linear optical systems

Here we study only linear optical systems[1]: this allows us to derive results from illumination conditions that are written from a linear combination of particular illumination conditions, by studying the optical system only from these inputs.

In our electro-magnetic (EM) theories, we usually start with Maxwell's equations in harmonic regime [208], and in particular, its curl equations:

$$\left\{ \begin{array}{rcl} \nabla \times \overrightarrow{E} & = & i\omega\mu \overrightarrow{H} \\ \nabla \times \overrightarrow{H} & = & -i\omega\epsilon_m \overrightarrow{E} \end{array} \right. \tag{A.1}$$

By applying the curl operator again, the vector Helmholtz propagation equations are easily obtained:

$$\left\{ \begin{array}{rcl} (\nabla^2 + k_m^2)\overrightarrow{E} & = & \overrightarrow{0} \\ (\nabla^2 + k_m^2)\overrightarrow{H} & = & \overrightarrow{0} \end{array} \right. \tag{A.2}$$

With $k_m^2 = \omega^2\epsilon_m\mu$ the wave-vector in the surrounding medium. From those equations, it is clear that the electric $\overrightarrow{E}$ and magnetic $\overrightarrow{H}$ field vectors behave in the same way, in terms of propagation. Thus, one can define a unitless, normalized optical wave $\overrightarrow{U}$ that satisfies the vector Helmholtz equation.

$$(\nabla^2 + k_m^2)\overrightarrow{U} = \overrightarrow{0} \tag{A.3}$$

Then, one can find $\overrightarrow{U}_{out}$, the output of a linear optical system, from an input $\overrightarrow{U}_{in}$. In this document, we will mainly consider imaging systems with normalized images, so the use of such a normalized optical wave is sufficient for us. If a quantitative study is needed, one can simply find the output unit from a given input unit. For instance, one can define an incident electric field as $\overrightarrow{E}_{in} = E_0\overrightarrow{U}_{in}$, where E_0 is given in V/m. Then, the output electric field is simply $\overrightarrow{E}_{out} = E_0\overrightarrow{U}_{out}$, given accurately in V/m. In a similar manner, if the incident intensity is I_0, given in W/m^2, then out output intensity is $I_0 \cdot \|\overrightarrow{U}_{out}\|^2$, also given in W/m^2.

---

[1] If g_1 and g_2 are the output of the optical system when excited by the respective inputs f_1 and f_2, then output of the linear optical system is $(c \cdot g_1 + g_2)$ when excited by the combined input $(c \cdot f_1 + f_2)$. With c a scalar.

A.2 Polarization

Knowing that any illumination field can be expanded into a series of plane waves, we will consider throughout this document that linear optical systems are illuminated a plane wave, with a linear polarization. Let $\overrightarrow{U}_{inc}$ be a monochromatic (wavelength λ) plane wave, that propagates in the Z direction in a surrounding media of refractive index n_m, and carried by a unitary vector $\overrightarrow{p}$, orthogonal to $\overrightarrow{z}$:

$$\overrightarrow{U}_{inc} = \exp(ik_m z)\overrightarrow{p} \tag{A.4}$$

Where $k_m = 2\pi n_m/\lambda$ is the wave-vector. Here we omit the supposed harmonic time variation in $\exp(-i\omega t)$ because our sensors are not sensitive to it in the optical range. Note that the optical wave is written as a complex harmonic instead of the usual real cosine, simply because it simplifies formulations and calculations.

We define the transverse plane $(0, \overrightarrow{x}, \overrightarrow{y})$, sagittal plane as $(0, \overrightarrow{x}, \overrightarrow{z})$ and the tangential plane as $(0, \overrightarrow{y}, \overrightarrow{z})$. The polarization plane is defined as the plane $(0, \overrightarrow{p}, \overrightarrow{z})$. The polarization angle ϕ_p is defined as the angle between the sagittal plane and the polarization plane, as illustrated in Figure A.1.

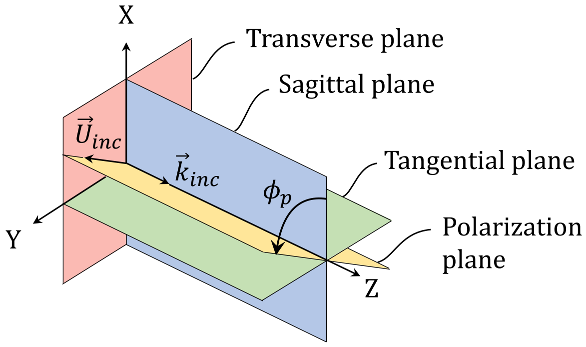

Figure A.1: Definition of the polarization plane.

Using the linear principles discussed above, we will mainly consider two orthogonal polarizations: the P-polarization refers to the case were the polarization plane is coplanar with the sagittal plane ($\phi_p = 0$, parallel); the S-polarization is defined in the same way, but according to the tangential plane ($\phi_p = \pi/2$, perpendicular), *mutatis mutandis*. In this way, we can describe the behaviour of an optical system when illuminated by a source with an arbitrary polarization state (circular, elliptical, linear), by considering its behaviour only with a P and S polarized illumination.

Note that this definition of polarization state is purely geometrical here, using only a fictional normalized vector field $\overrightarrow{U}$, instead of the usual EM fields $(\overrightarrow{E}, \overrightarrow{H})$. We have chosen to avoid as much as possible physical considerations, in order to simplify the formulation (and interpretation) of our different models.

In practice, in order to coincide with experiments and EM simulations (*e.g.* FDTD), we consider *in fine* that the P polarization corresponds to the case where the electric field is carried by the sagittal axis (X axis).

A.3 Coordinate systems and spherical angles

In this document, we will agree on the following coordinate systems. It is considered, unless otherwise specified, that the optical axis is carried by the Z-axis. As shown in Figure A.1, we define the different planes (transverse, sagittal and tangential). The angles of our spherical coordinate system are illustrated in Figure A.2.

The polar angle θ (associated to the scattering angle, in scattering theories) is the angle between the optical axis and the wave-vector (or the direction of a ray);
the azimuthal angle ϕ is the angle between the sagittal axis and the wave-vector, projected onto the transverse plane.
θ_x and θ_y are the sagittal and tangential angles respectively, which are the projections of the polar angle θ onto the sagittal and tangential planes respectively[a].
This convention for spherical angles is different from the canonical one. This choice was made in order to remain consistent with the convention adopted in light scattering theories and Fourier's optics.

---

[a] The polar angles when $\phi = 0$ and $\phi = \pi/2$, respectively.

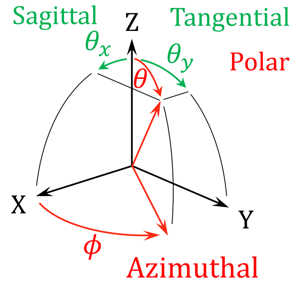

Figure A.2: Convention of spherical angles.

In Chapters II and III, the holed retina is studied. We consider the columns and lines axis of the pixel matrix as the X and Y axis, because it makes more sense for the image analysis. In those chapters, the illumination axis is parallel to the matrix, and thus the Cartesian coordinate system must be permuted (see, Figure I.16). In Chapter II, the optical axis is Y, the sagittal is X and the tangential is Z. In Chapter III, only when the holed retina is considered, the optical axis is X, the sagittal is Y and the tangential is Z.

The spherical angles are defined accordingly[2].

---

[2] To avoid confusion, spherical angles definitions are defined using the optical axis, sagittal and tangential axis; and not the X,Y,Z denomination.

B Introduction to the Lorenz-Mie theory

B.1 Position of the problem

The Lorenz-Mie theory is an analytical resolution of Maxwell's equations applicable to the problem of electro-magnetic (EM) scattering by a sphere of arbitrary diameter and complex refractive index. It allows to evaluate EM fields at any point in space and integral quantities, such as the extinction ans scattering efficiencies. This theory was first formulated by Gustav Mie in 1908 [209]; however, it will be described using the modernized formulation of Bohren and Huffman [82]. The subsections that follow will simply summarize the main points of the demonstration, which are detailed in this reference book.

Let us consider a dielectric spherical particle of radius a, of complex refractive index n_s, surrounded by a medium of index n_m and illuminated by a P-polarized plane wave that propagates in the Z direction, expressed by its optical vector field $\overrightarrow{U}_{inc}$:

$$\overrightarrow{U}_{inc} = \exp\left(i\frac{2\pi n_m}{\lambda}z\right)\overrightarrow{x} \tag{B.1}$$

Such a particle is reduce the sphere to its size factor χ:

$$\chi = \frac{2\pi n_m a}{\lambda} \tag{B.2}$$

B.2 Helmholtz equations of propagation

We recall the Helmholtz vector equation :

$$(\nabla^2 + k_m^2)\overrightarrow{U} = \overrightarrow{0} \tag{B.3}$$

Solving this equations usually starts by considering the scalar Helmholtz equation:

$$(\nabla^2 + k_m^2)\psi = 0 \tag{B.4}$$

From scalar solutions $\psi_{l,m}$ (with $m \in \mathbb{N}$, $l \in [0,m]$) we can build independent solutions of the Helmholtz vector equations $(\overrightarrow{L}, \overrightarrow{M}, \overrightarrow{N})_{l,m}$:

$$\left\{\begin{array}{lcl} \overrightarrow{L}_{l,m} & = & \nabla\psi_{l,m} \\ \overrightarrow{M}_{l,m} & = & \nabla\times\overrightarrow{r}\psi_{l,m} \\ \overrightarrow{N}_{l,m} & = & k_m^{-1}\nabla\times\overrightarrow{M}_{l,m} \end{array}\right. \tag{B.5}$$

We can verify that $(\overrightarrow{L}, \overrightarrow{M}, \overrightarrow{N})_{l,m}$ form a complete basis for the solutions of the vector Helmholtz equation. One the one hand, $\overrightarrow{L}_{l,m}$ is a purely longitudinal solution, which is omitted in the following. On the other hand, $\overrightarrow{M}_{l,m}$ and $\overrightarrow{N}_{l,m}$ are solenoidal solutions, which means they verify Maxwell's divergence equations. The Helmholtz scalar equation usually have to be re-written in a new system of coordinate, relevant with the geometry of the problem[3]. In the case of the scattering by a small object (with a small aspect ratio) we solve the Helmholtz scalar equation in spherical coordinates, by considering a special solution with separate variables[4]:

$$\psi(r,\theta,\phi) = R(r)\Theta(\theta)\Phi(\phi) \tag{B.6}$$

Thus it becomes possible to separate the scalar equation into three classical equations involving $R(r)$, $\Theta(\theta)$ and $\Phi(\phi)$ independently. This allows us to explicit the solution of the scalar equation:

$$\psi_{l,m}^{(k)}(r,\theta,\phi) = \sqrt{\frac{2}{\pi}}Z_l^{(k)}(k_m r)P_l^m e^{im\phi} \tag{B.7}$$

---

[3] This scalar solution is known in 11 coordinate systems [210].

[4] It is possible to show that the orthogonality of the variables (r,θ,ϕ) is verified in the case of a sphere.

With $k = 1, 2, 3$ and $Z_l^{(k)}$ which can be either spherical Bessel or Hankel functions [211]:

i A spherical Bessel function of the first kind $Z_l^{(1)} = j_l$

ii A spherical Bessel function of the second kind $Z_l^{(2)} = y_l$

iii A spherical Hankel function of the first kind $Z_l^{(3)} = h^{(1)} = j_l + iy_l$

And with P_l^m the associated Legendre polynomial of degree l and order m [211]. We then construct the even (e) and odd (o) solutions of the scalar equation:

$$\begin{cases} \psi_{l,m,e}^{(k)}(r,\theta,\phi) & = & \sqrt{\frac{2}{\pi}} Z_l^{(k)}(k_m r) P_l^m \cos(im\phi) \\ \psi_{l,m,o}^{(k)}(r,\theta,\phi) & = & \sqrt{\frac{2}{\pi}} Z_l^{(k)}(k_m r) P_l^m \sin(im\phi) \end{cases} \tag{B.8}$$

B.3 A basis of spherical harmonics

In EM problems solved in the spherical coordinate system, the following angular functions are commonly defined:

$$\Pi_{l,m}(\theta) = m\frac{P_l^m(\cos\theta)}{\sin\theta} \qquad T_{l,m}(\theta) = \frac{dP_l^m(\cos\theta)}{d\theta} \tag{B.9}$$

These functions will allow us to describe the angular distributions of the scattered intensities. From $\psi_{l,m,p}^{(k)}$ we generate the vector basis of spherical harmonics (also known as SWVF, standing for Spherical Wave Vector Functions) of Maxwell's equations:

$$\begin{cases} \overrightarrow{M}_{l,m,p}^{(k)} & = & \nabla \times \overrightarrow{r}\psi_{l,m,p}^{(k)} \\ \overrightarrow{N}_{l,m,p}^{(k)} & = & k_m^{-1}\nabla \times \overrightarrow{M}_{l,m,p}^{(k)} \end{cases} \tag{B.10}$$

With $p = e, o$ and $k = 1, 2, 3$.

Knowing the expression of scalar solutions, one can explicit the vectors $\overrightarrow{M}_{l,m,p}^{(k)}$ and $\overrightarrow{N}_{l,m,p}^{(k)}$ in spherical coordinates, using the notations $z = k_m r$, and $[\,\cdot\,]' = d/dz$.

$$\overrightarrow{M}_{l,m,e}^{(k)} = \begin{bmatrix} O \\ -\sin(m\phi)\Pi_{l,m}(\theta)Z_l^{(k)}(z) \\ -\cos(m\phi)T_{l,m}(\theta)Z_l^{(k)}(z) \end{bmatrix}_{(r,\theta,\phi)} \qquad \overrightarrow{N}_{l,m,e}^{(k)} = \begin{bmatrix} \frac{l(l+1)}{m}\cos(m\phi)\sin(\theta)\Pi_{l,m}(\theta)\frac{Z_l^{(k)}(z)}{z} \\ \cos(m\phi)T_{l,m}(\theta)\frac{[zZ_l^{(k)}(z)]'}{z} \\ -\sin(m\phi)\Pi_{l,m}(\theta)\frac{[zZ_l^{(k)}(z)]'}{z} \end{bmatrix}_{(r,\theta,\phi)} \tag{B.11a}$$

$$\overrightarrow{M}_{l,m,o}^{(k)} = \begin{bmatrix} O \\ \cos(m\phi)\Pi_{l,m}(\theta)Z_l^{(k)}(z) \\ -\sin(m\phi)T_{l,m}(\theta)Z_l^{(k)}(z) \end{bmatrix}_{(r,\theta,\phi)} \qquad \overrightarrow{N}_{l,m,o}^{(k)} = \begin{bmatrix} \frac{l(l+1)}{m}\sin(m\phi)\sin(\theta)\Pi_{l,m}(\theta)\frac{Z_l^{(k)}(z)}{z} \\ \sin(m\phi)T_{l,m}(\theta)\frac{[zZ_l^{(k)}(z)]'}{z} \\ \cos(m\phi)\Pi_{l,m}(\theta)\frac{[zZ_l^{(k)}(z)]'}{z} \end{bmatrix}_{(r,\theta,\phi)} \tag{B.11b}$$

B.4 SWVF expansion of an incident plane wave

We previously wrote that $\overrightarrow{M}^{(k)}_{l,m,p}$ and $\overrightarrow{N}^{(k)}_{l,m,p}$ form a complete basis for the solutions of Maxwell's equations. This is why the incident field can be expanded into a vector series of spherical harmonics. This expansion was first proposed by Hansen, in 1935 [212].

$$\overrightarrow{U}_{inc} = \sum_{l,m,k,p} B^{(k)}_{l,m,p} \overrightarrow{M}^{(k)}_{l,m,p} + A^{(k)}_{l,m,p} \overrightarrow{N}^{(k)}_{l,m,p} \tag{B.12}$$

The incident field is *a priori* known, it is now a question of determining the coefficients $A^{(k)}_{l,m,p}$ and $B^{(k)}_{l,m,p}$. Until now, we have considered an arbitrary incident field. It is possible to simplify the expressions of the coefficients $A^{(k)}_{l,m,p}$ and $B^{(k)}_{l,m,p}$ in the case of an incident P-polarized plane wave, expressed as:

$$\overrightarrow{U}_{inc} = \exp\left(i\frac{2\pi n_m}{\lambda}z\right)\overrightarrow{x} \tag{B.13}$$

In these considerations it can be shown (after very long calculations) that :

i All terms except for $m = 1$ disappear,

ii All terms except for $k = 1$ disappear, thus $Z^{(1)}_l = j_l$

iii $B^{(1)}_{l,m,e} = A^{(1)}_{l,m,o} = 0$

iv $B^{(1)}_{l,m,o} = -A^{(1)}_{l,m,e} = i^l \frac{2l+1}{l(l+1)} = U_l$

Which in the end results in:

$$\overrightarrow{U}_{inc} = \sum_{l} U_l(\overrightarrow{M}^{(1)}_{l,1,o} + \overrightarrow{N}^{(1)}_{l,1,e}) \tag{B.14}$$

We notice that the series is rapidly converging: the series can be truncated at $l_{max} = \chi + 4\chi^{1/3} + 2$, as proposed by Bohren & Huffman.

B.5 Determination of internal and scattered fields

Up to this point, we have only discussed the general case where a plane wave has not encountered any obstacle. We will now determine the internal and scattered fields of a spherical particle. As explained in Section I.3, the relationships between the different coefficients of the expansion are then determined using the boundary conditions at the particle surface. Assuming there is no surface current, tangential components of the vector field are continuous at those interfaces [81]. With simple geometries like spheres, internal $\overrightarrow{U}_{int}$ and scattered $\overrightarrow{U}_{scat}$ fields can be analytically expressed with simplified boundary conditions, were $r = a$:

$$(\overrightarrow{U}_{inc} + \overrightarrow{U}_{int} + \overrightarrow{U}_{scat}) \times \overrightarrow{e}_r = \overrightarrow{0} \tag{B.15}$$

These conditions allow us to determine (again after long calculations) the shape of the internal and scattered fields:

$$\overrightarrow{U}_{int} = \sum_l U_l (c_l \overrightarrow{M}^{(1)}_{l,1,o} - i d_l \overrightarrow{N}^{(1)}_{l,1,e}) \qquad \overrightarrow{U}_{scat} = \sum_l U_l (i a_l \overrightarrow{N}^{(3)}_{l,1,e} - b_l \overrightarrow{M}^{(3)}_{l,1,o}) \tag{B.16a}$$

For simplification, we introduce the Ricatti-Bessel functions [211]:

$$\begin{cases} \psi_l(z) & = & z j_l(z) \\ \xi_l(z) & = & z h_l^{(1)}(z) \end{cases} \tag{B.17}$$

Then, we give the expressions of Mie's coefficients $(a, b, c, d)_l$

$$a_l = \frac{m\psi_l(m\chi)\psi_l'(\chi) - \psi_l(\chi)\psi_l'(m\chi)}{m\psi_l(m\chi)\xi_l'(\chi) - m\xi_l(\chi)\psi_l'(m\chi)} \tag{B.18}$$

$$b_l = \frac{m\psi_l(m\chi)\psi_l'(\chi) - m\psi_l(\chi)\psi_l'(m\chi)}{\psi_l(m\chi)\xi_l'(\chi) - m\xi_l(\chi)\psi_l'(m\chi)} \tag{B.19}$$

$$c_l = \frac{m\psi_l(\chi)\xi_l'(\chi) - m\xi_l(\chi)\psi_l'(\chi)}{\psi_l(m\chi)\xi_l'(\chi) - m\xi_l(\chi)\psi_l'(m\chi)} \tag{B.20}$$

$$d_l = \frac{m\psi_l(\chi)\xi_l'(\chi) - m\xi_l(\chi)\psi_l'(\chi)}{m\psi_l(m\chi)\xi_l'(\chi) - \xi_l(\chi)\psi_l'(m\chi)} \tag{B.21}$$

With, as a reminder, the size factor $\chi = 2\pi n_m a/\lambda$ and the ratio of refractive index $m = n_s/n_m$. The subscripts s refers to the sphere whereas m refers to the surrounding medium.

B.6 Cross sections and Mie's efficiencies

Evaluating the internal and scattered Poynting vector integrated over a sphere, we can calculate the extinction C_{ext} and scattering C_{scat} cross sections (given in µm^2) defined as following:

$$\begin{aligned} C_{scat} &= W_{scat}/I_{inc} \\ C_{ext} &= W_{ext}/I_{inc} \end{aligned} \quad (B.22)$$

One can also define a backscattering cross section C_{bscat} [213], integrated over the backward hemisphere:

$$C_{bscat} = W_{bscat}/I_{inc} \quad (B.23)$$

With I_{inc} the intensity of the incoming wave (in W/m^2), W_{scat},W_{ext},W_{bscat} respectively the scattered, attenuated and back-scattered powers (in W). Mie's efficiencies are commonly defined as a dimensionless parameter reduced to the geometric cross-sectional area of the particle with radius a:

$$\begin{aligned} Q_{scat} &= C_{scat}/\pi a^2 \\ Q_{ext} &= C_{ext}/\pi a^2 \\ Q_{bscat} &= C_{bscat}/\pi a^2 \end{aligned} \quad (B.24)$$

These efficiencies can be calculated from the Mie coefficients according to the following formulas:

$$Q_{scat} = \frac{2}{\chi^2}\sum_l (2l+1)(|a_l|^2 + |b_l|^2) \quad (B.25)$$

$$Q_{ext} = \frac{2}{\chi^2}\sum_l (2l+1)\Re(a_l + b_l) \quad (B.26)$$

$$Q_{bscat} = \frac{1}{\chi^2}|\sum_l (2l+1)(-1)^l(a_l - b_l)|^2 \quad (B.27)$$

B.7 Far field distribution of scattered intensity

Let the scattering matrix $s(\theta)$ which links the P and S components of the incident and scattered fields, in the far-field approximation:

$$\begin{pmatrix} U^P_{inc}(\theta) \\ U^S_{inc}(\theta) \end{pmatrix} = \frac{e^{ikr}}{-ikr}\begin{pmatrix} s_{11}(\theta) & 0 \\ 0 & s_{22}(\theta) \end{pmatrix}\begin{pmatrix} U^P_{scat}(\theta) \\ U^S_{scat}(\theta) \end{pmatrix} \quad (B.28)$$

With the angular scattered distribution:

$$s_{11}(\theta) = \sum_l \frac{2l+1}{l(l+1)}(a_l\Pi_l(\theta) + b_l T_l(\theta)) \qquad s_{22}(\theta) = \sum_l \frac{2l+1}{l(l+1)}(a_l T_l(\theta) + b_l\Pi_l(\theta)) \quad (B.29)$$

The scattering matrix $s(\theta)$ is diagonal: that is, $s_{12} = s_{21} = 0$. Which means, *ex hypothesi*, that there is no depolarization of the scattered fields with respect to the incident fields.

In the case of unpolarized light (*i.e.* azimuthal ϕ invariance), the angular intensity distribution becomes $S(\theta) = |s_{11}(\theta)|^2 + |s_{22}(\theta)|^2$. If the incident plane wave has a polarization angle ϕ_p, then it will suffice to include the 2×2 rotation matrix R_{ϕ_p} in the matrix product given in equation (B.28).

C Partial occultation of scattering signatures

C.1 Shadowed signatures

A shadow can appear on the retina when part of the scattering signature is occulted by the cloaker, as seen in experimental images (see, Figure II.22). This event occurs when the particle is situated far from the center of the detection area so that the cloaker comes within the FoV, causing this partial occultation. The geometry of such an event is illustrated in Figure C.2(a).

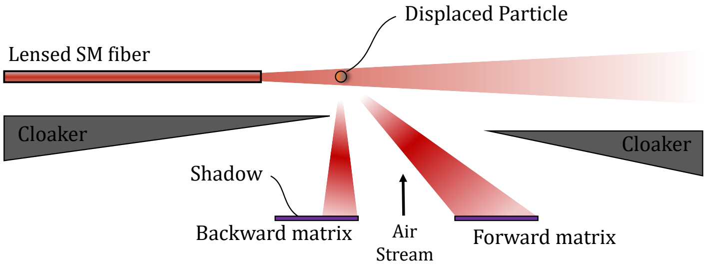

Figure C.1: *Origin of shadows.*

We will now describe how we can automatically detect one or more shadows on an image. If the shadow is predominant, the image is removed from future image processing. An image showing multiple shadows can be analyzed to detect the presence of several particles. It should be noted that on one hand, the 'forward' matrix contains the maximum amount of information, the scattering intensity and its variations being stronger in this region. On the other hand, the 'backward' matrix generally contains shadow figures, as for example in Figure C.2(a). It will be important to take this into account.

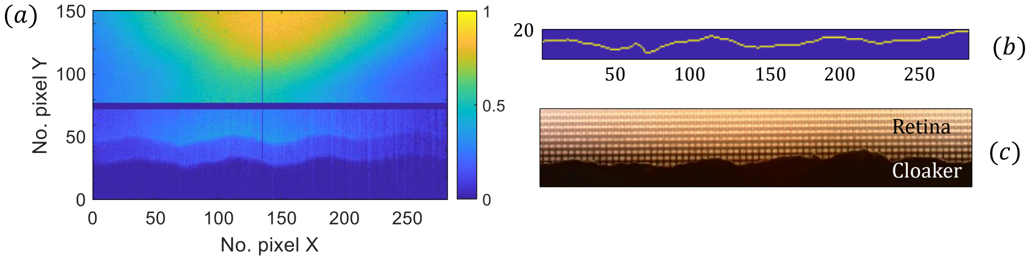

Figure C.2: *(a) Example of a shadowed image. (b) Contour of the reference shadow. (c) Optical view of the edge of the cloaker.*

In this section, we are going to focus mainly on shadows created by the edge of the cloaker above the backward matrix as theses shadows are more frequent due to the geometry of the cloaker. The method can be applied for the other edge, as they do appear, with much less frequency. Note that in some rare examples, the edge of the shadow above the backward matrix can appear in the forward region, and *vice versa*.

The edge of the cloaker has a specific shape, depending on the 3D printing (see, Figure C.2(c)) and therefore unique to each sensor. The contour of the shadow created by the edge of a cloaker (see, Figure C.2(b)) can be easily obtained using a 'well shadowed' reference image, by applying a Sobel filter [214, 215][5].

---

[5] By calculating the gradient of the intensity of each pixel of the image, one can deduce the direction of the variation of intensity and thus we deduce the points where the variation is strong, which can correspond to a contour.

To illustrate the different interesting cases in this section, three images have been chosen (see, Figure C.3).

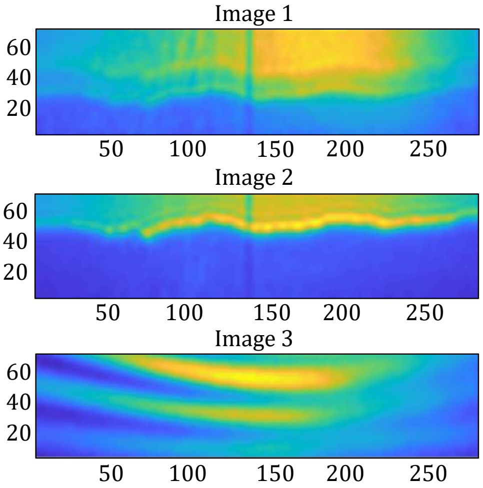

#	*Particle*	*Comment*
1	190 nm PSL	Several shadows
2	720 nm PSL	Single shadow
3	5 µm PSL	Flat and thin lobes

Figure C.3: *Image examples for shadow detection.*

In order to detect the shadow on any image, a binary image is formed from the contour detection of the previously blurred image (Gaussian blur filter, $\sigma = 2$ pixels), using the Sobel filter. The binary image of detected contours is correlated with the contour of the reference shadow on each line. A peak on the correlation curve therefore corresponds to a shadow pattern similar to the reference shadow. The number of peaks above a certain threshold is therefore associated with the number of detected shadows. The contours and calculated correlations of images 1, 2, and 3 are shown in Figure C.4; two shadow figures are detected for images 1 and 2, and none for image 3.

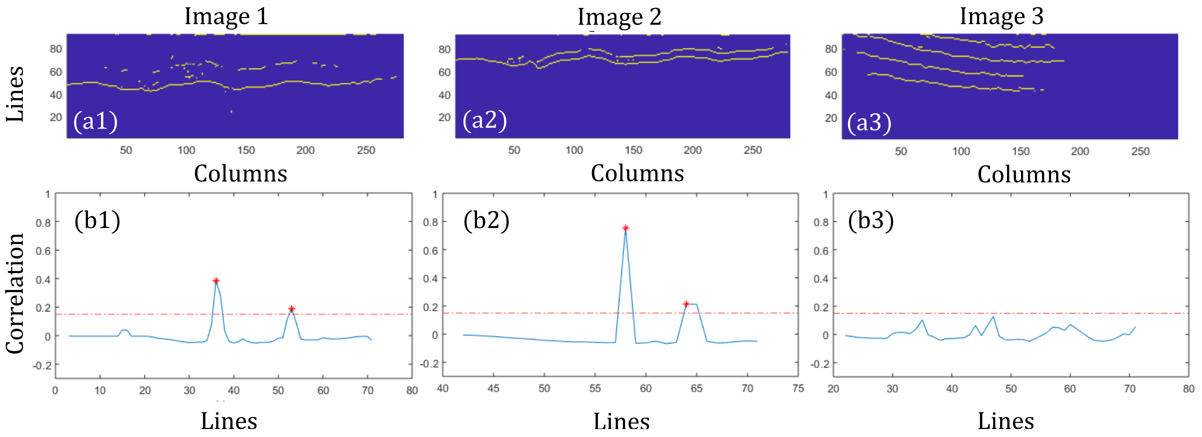

Figure C.4: *(a) Contours of images (1,2,3) and (b) correlation with reference shadow.*

The detected contour in image 2 shows two shadows when there is only one: it is very likely a diffraction pattern created by the edge of the cloaker, with equidistant contours (between 6 and 8 pixels). If two peaks are close, they are then considered as a single peak, which cancels the errors in the number of detected shadows resulting from this diffraction. Thus, two shadows are detected for image 1, and only one for image 2. Based on tests performed over about 50 different images, this algorithm correctly detects all the shadow patterns, without false detection.

C.2 Scattering through a slit

In this section, we present an alternative sensor [138], similar to the one presented in Chapter II, but with an extended glass channel covered with a gold layer, see Figure C.5. An optical fiber is placed on top of the gold layer, that acts as a cloaker by protecting the holed retina of stray light from the fiber.

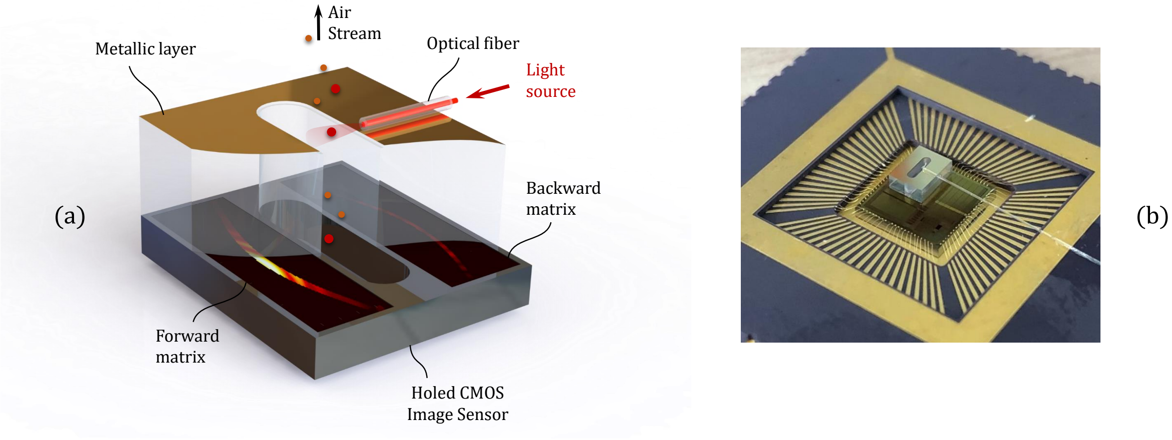

Figure C.5: *(a) Rendering of the alternative sensor. (b) Photography of the alternative sensor.*

The canal is manufactured according to the same principles as for the holed retina, *i.e.* at wafer scale and using microfabrication technologies.

This air channel is fabricated from a glass substrate (Borofloat 33 glass wafer, 1 mm thick, 200 mm diameter). The glass wafer was covered by a metallic layer (10 nm titanium + 100 nm gold, see our metallization process on glass, in Section III.2.3). The metallic layer acts like a cloaker and reduces the sensitivity to parasitic effects such as electrostatic charges carried by aerosols. The fluidic channel was then drilled at wafer level using a femtosecond NIR laser following the same oblong profile as the holed retina. At last, each glass part was cut off and placed on top of the detection areas using a 'pick-and-place' process. The final device is shown in Figure C.6.

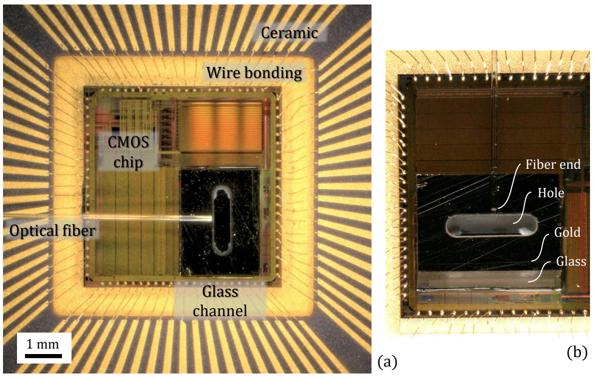

Figure C.6: *(a) Top view of the final device. (b) Tilted view of the sensing area.*

During the laser drilling process, part of the metallic layer is removed at the vicinity of the air channel (see, Figure C.7(e)). SEM images presented in Figure C.7(c,d) show that this layer was peeled off by about 30 µm around the channel, forming a slit. Figure C.7(a) is a RT simulation, were an isotropic scatterer is placed at the sensing area. We show that the slit allows for some of the scattered rays to be refracted within the glass substrate. These rays forms in the retina two luminous arcs, resulting from the deformation of the slit by refractive effects, as seen in subfigure (b).

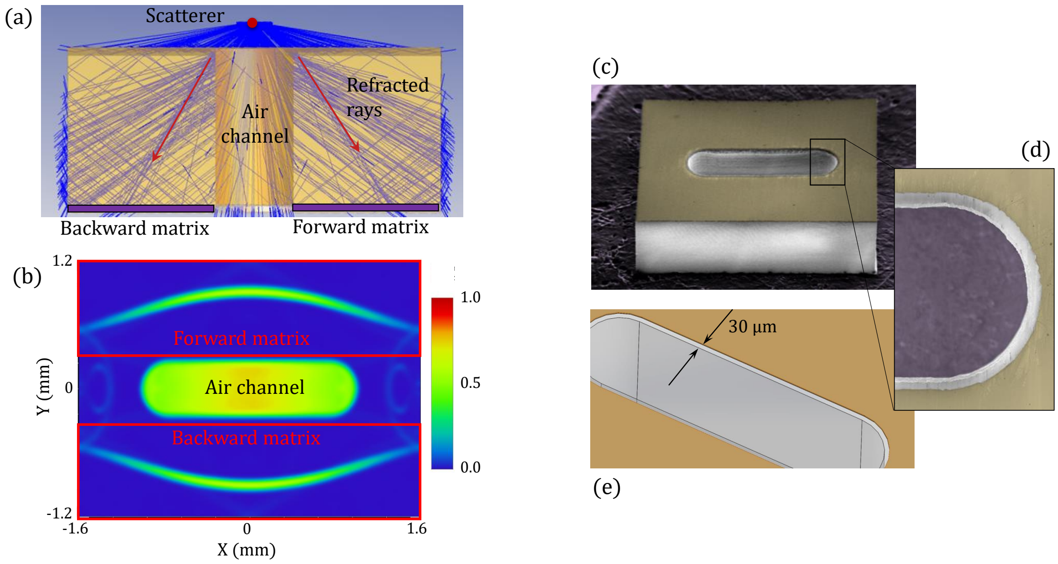

Figure C.7: (a) RT simulation of the alternative setup. (b) Resulting illuminance on the imager plane. (c) Tilted SEM image of the glass channel (colorized). (d) Zoomed SEM image of the slit (colorized). (e) 3D drawing of the slit.

We have developed a modified version of the radiometric model previously described in Section II.2. Details on this modified model are not discussed here. However, if the reader wishes to re-write this model, here are some hints: for each pixel of the retina, the associated scattering angle must be calculated by back tracing the scattered rays, taking into account the deviation induced by refraction. An intermediary plane can be defined (metallic layer plane). In this plane, a geometrical condition (geometry of the slit) must be applied whether or not the scattered ray should pass or be blocked by the metallic layer, in the form of a boolean image. The rest of the model is identical as described in Section II.2.

Figure C.8 shows examples of experimental images taken with PSL spheres (using the aerosol bench described in Appendix D, in the same fashion as in Section II.3) compared with images computed with the modified model. In this section, the illumination beam is wider than in Section II.3 as we use a fiber with a wider NA = 0.1. On each image, we observe two luminous arcs structured with fringes (forward and backward scattering arcs). These arcs are the images of the scattering signatures seen trough the two slits and deformed by refraction. The lobes along theses arcs are the iso-θ. These observations are in good agreement with our modified analytical model.

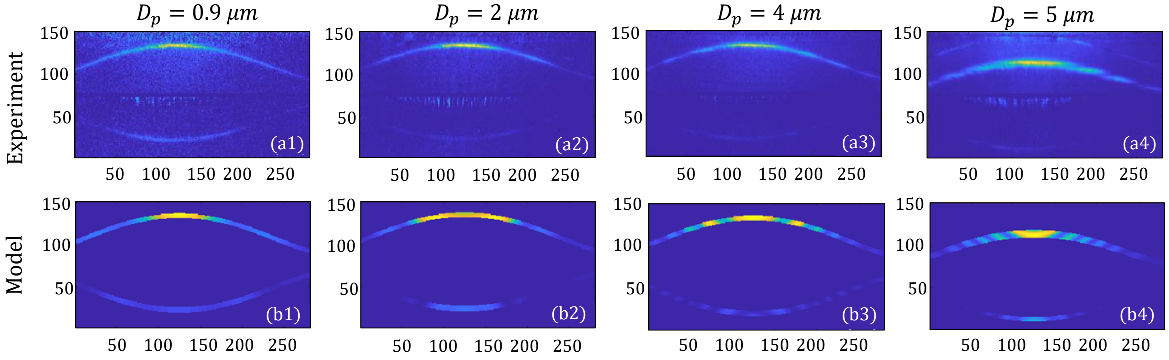

Figure C.8: (1) Experimental signature of PSL spheres. (2) Associated modeled images for different PSL diameters: (a) 0.9 µm, *(b)* 2 µm, *(c)* 4 µm, *(d)* 5 µm.

What is interesting about these arcs is that they carry information about the position of the scatterer in an easily analyzable way. A translation of X and Y (parallel to the retina and the metallic layer) results in the translation of the arcs; a translation of Z (vertical direction) results in the spacing and curvature of the two arcs, as seen in Figure C.9

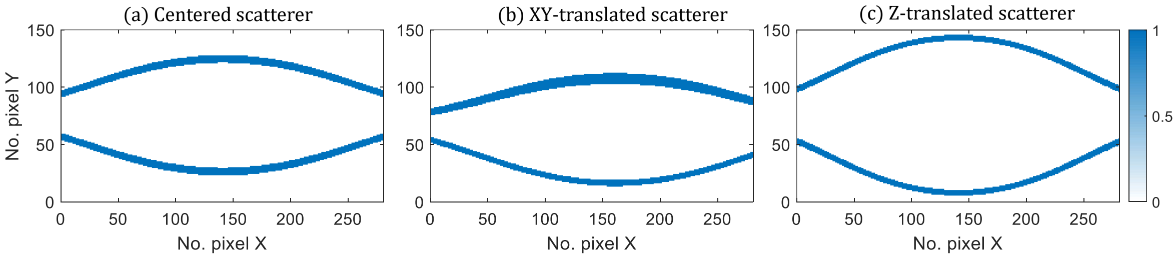

Figure C.9: *Calculated arcs (binary images) formed by a centered (a), XY-translated (b), Z-translated scatterer (c).*

In an event of coincidence, when several particles are detected at a time, it becomes possible to detect and analyze independently the individual scattering signatures seen along these arcs. Indeed, depending of the individual position of the particles, associated arcs are formed in separate regions of the retina. Figure C.10 shows an experimental demonstration of multiple detection within a same image recording.

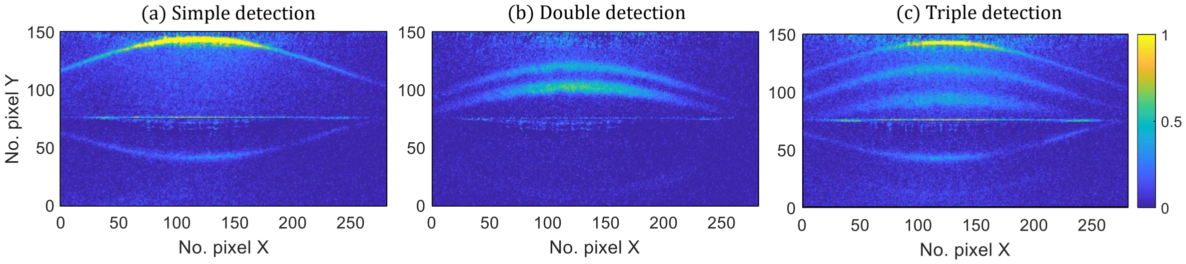

Figure C.10: *Experimental demonstration of multiple detections. (a) Simple detection. (b) Double detection. (c) Triple detection.*

Being able to detect and analyze signatures from multiple particles simultaneously is a tremendous advantage compared with conventional OPC designs. Indeed, the latter usually try to avoids those coincidence events as it affects the counting accuracy: the solution usually chosen involves of a pre-dilution of the sampled aerosol, which adds complexity to the system and lower its sensitivity. In our case, a multiple detection event is fortunate, because we can count and analyze several particles without having to record additional images, and then saving on the energy cost needed to drive the retina.

C.3 Engineered occultations: bright and dark reticles

We have discussed in Sections C.1 and C.2 examples of two very different forms of partial occultations of scattering signatures. The former is what we can call a 'bright' occultation as it allows us to recognize a shadow figure while a large portion of the retina can be used to image and analyze a scattering signature. In the case of a coincidence event, several shadows can be detected, allowing us to count particles. However, we observe a superposition of scattering signatures, making the image processing harder (or impossible). The second type of occultation, discussed in Section C.2 is what we call a 'dark' occultation as the scattering signature is projected through only a small surface. While it reduces the surface of analysis of the signature, it allows for the individual analysis of multiple scattering signatures as they can be projected on different areas on the retina.

In both case, whether it is the edge of a shadow or the deformed image of a slit, an analysis of the occultation figure provides information on the position of the scatterer with allegedly great accuracy, by back tracing rays. This is a clear advantage as the scattered position has been shown in II.4 to be an important unknown, impacting the complexity and accuracy of the image processing.

Felix culpa, both occultation types were not initially planned and designed, but stemmed from manufacturing errors. However, we can take advantage of this artifact engineer optimized occultations, by designing reticles (bright or dark) which would make the data processing easier and more accurate. Examples of bright and dark reticles are discussed precisely in patent [129]. We will not discuss here the different configurations and design principle for reticles, but we give in Figure C.11 an example of embodiment to illustrate the general idea behind those reticles.

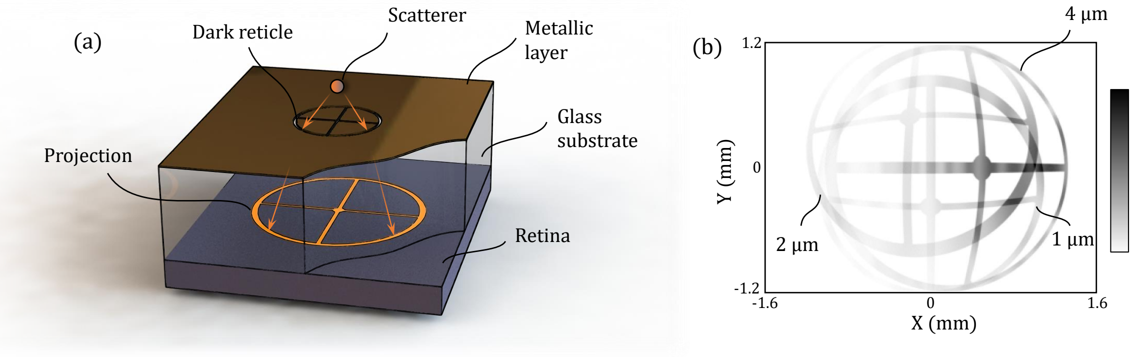

Figure C.11: (a) Example of an imaging system with a dark reticle. (b) Detection of three occulted scattering signatures projected through the same dark reticle (RT simulation).

Figure C.11(a) shows an example of a scattering imaging system that uses a dark reticle formed by a combination of pinholes and slits. The shape in inspired by a rifle scope crosshair which makes the determination of the scattered position easy by considering the position and magnification of the crosshair. The analysis of the scattering signature is evaluated on the outer ring, which is a shape adapted for the observation of Mie's oscillations[6]. Here, we did not include a vertical air channel for readability reasons. Figure C.11(b) shows a RT simulation of the occulted projection formed by three scatterers (PSL 4 µm, 2 µm and 1 µm), that can then be analyzed individually.

---

[6] Note that the optimized shape is perpendicular to the iso-θ. With parallel projection, iso-θ are hyperbolae. Thus, the optimized reticle shape is elliptical.

D Aerosol test bench

The different prototypes of PM sensors we develop are tested on a calibrated aerosol test bench (Constant Output Atomizer Model 3076 by TSI) that delivers a continuous stream of particles toward our sensor under test. This test bench is hosted by CEA's Nano-Safety Platform (PNS, in french) at Grenoble, France. Presented in Figure D.1, it is made up of various elements placed under a fume cupboard:

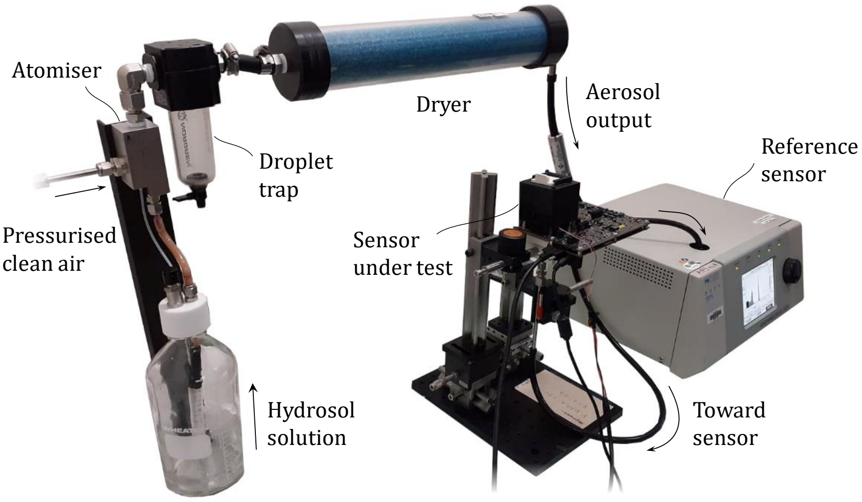

Figure D.1: Photograph of the continuous aerosol dispenser.

The aerosol is suspended in a previously prepared water solution. At this stage, we speak of hydrosol instead of aerosol. This preparation is carried out by diluting calibrated particles with ultra pure water. Generally, the particles used are comercially available monodisperse polystyrene beads (PSL).

Large droplets of hydrosol are extracted from the container by the Venturi effect using a pressurised air flow and are fed to an atomizer located above the container. These large droplets are impacted on a wall of the atomizer where each droplet will be broken into smaller bits, with good repeatability. The larger droplets fall back into the solution container while the smaller ones are carried up by the pressurized air flow to the next part of the generator. The various parameters of the bench are adjusted so that, statistically, each of these small droplets contains no more than a single particle. An optional step is to place a trap (U-shaped pipe) that removes the excessively large residual droplets.

The flow of wet particles then passes through a dryer, made of silica gel. If there are more than one particle per droplet, then aggregates will be generated. At the outlet of the dryer, we obtain a calibrated flow of particles.

This flow is usually separated into two outputs. A reference output feeds a commercial aerosol analyzer that characterizes the particle flow: we use the Aerodynamic Particle Sizer APS Spectrometer 3321 by TSI. A second output feeds, via a silicone tube, our prototype PM sensor under test.

E Supplementary material on image processing

E.1 Image reduction algorithm

In this appendix, we will discuss how to extract parameters from the iso-θ in order to build the matrix M_{im} that represents the reduced image. The first step in the recovery of information is the detection of minima and maxima curves (or ridges and valleys).

To do this, we go through the columns of the image and recover the positions of the local extrema as shown in Figure E.1(a).
We then recognize the curves, by evaluating the presence of an extremum close from one column to another: if there is, then we consider the two extrema points as part of the same iso-θ. We remove the isolated points, and we automatically connect the pieces of iso-θ truncated by the image, which allows us to model these curves by 2nd order polynomials as shown in Figure E.1(b). Note that this fit is a simplification, as iso-θ are in theory conical curves of the type $a_1X^2 + a_2Y^2 + a_3XY + a_4X + a_5Y + a_6 = 0$. We use the following color code: red for ridges and green for valleys.

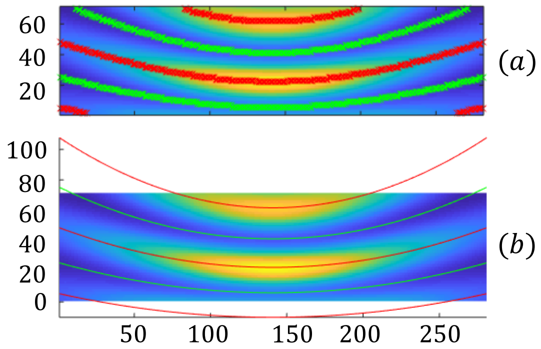

Figure E.1: (a) Detection of extrema, (b) Polynomial fit of iso-θ.

Another interesting information that completes the polynomial fit of iso-θ is the width of the iso-θ. L_{iso} is defined as the mean width of the peak at 25% of maximum along the normal at iso-θ (see, Figure E.2). The importance of this information stems from the visual importance we attach to the width of these lobes, which allows us to differentiate images.

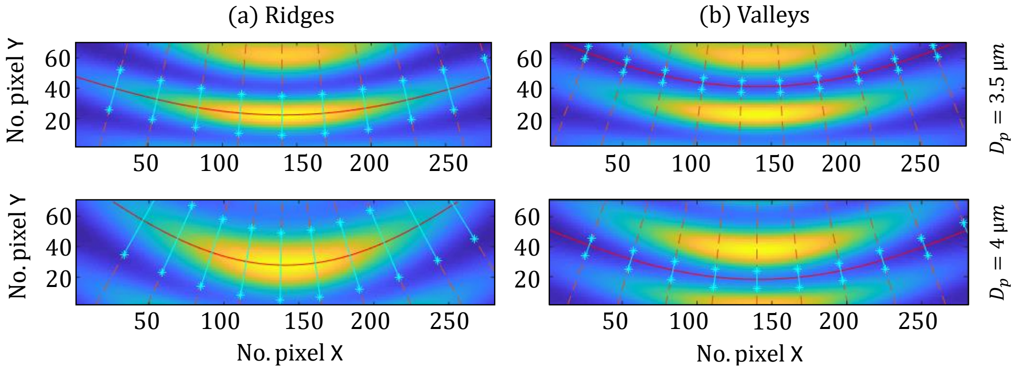

Figure E.2: Recovery of L_{iso} for (a) ridges and (b) valleys.

Then, we define $m = 1$ or $m = -1$ depending if the iso-θ is a ridge or a valley. Finally, we build the matrix M_{im} which contains N_{iso} lines that represent all the iso-θ detected (N_{iso} being the number of curves). The columns represent all three 2nd order polynomial fit as well as L_{iso} and m.

$$M_{im} = \begin{pmatrix} p2_1 & p1_1 & p0_1 & L_{iso_1} & m_1 \\ \vdots & \vdots & \vdots & \vdots & \vdots \\ p2_{N_{iso}} & p1_{N_{iso}} & p0_{N_{iso}} & L_{iso_{N_{iso}}} & m_{N_{iso}} \end{pmatrix} \tag{E.1}$$

E.2 Minimization criterion

In this appendix, we discuss our strategies used to fit experimental images with modelled ones.
We have observed that the naive strategy of trying to maximize the two-dimensional correlation between experimental and modeled images fails to deliver the expected particle parameters (apart from being computationally heavy). Indeed, the correlation appears to be very sensitive to noise and errors induced by stray light as well as poor modelling of the true vignette effects. Our chosen strategy consists in comparing simplified images by focusing only on the iso-θ (ridge and valleys only). From an image, either experimental or modelled, we extract relevant information on N_{iso} iso-θ detected such as the curvature and the width of the iso-θ. With these parameters, we can build the matrix M_{im} sized by $(N_{iso} \times 5)$ that represents the reduced image. Details on how we extract theses parameters were reported in Appendix E.1.

For a given experimental image I_{exp}, we generate modeled images $I_{mod}(D_p, n)$ with the aim of fitting I_{exp}. The modeled image depends on geometrical parameters: in our case, y_p is the only non-negligible parameter. To overcome this dependence, we generate a model with an artificial high number of lines so that the experimental image can be translated vertically to best match the model (horizontal translation, rotation and magnification can be applied for other geometrical parameters). The experimental image I_{exp} is reduced into the matrix M_{exp}. In a concern for simplification, we only consider the forward submatrix as it contains sufficient information on the signature, for now. The large modeled image $I_{mod}(D_p, n)$ is also reduced into the matrix $M_{mod}(D_p, n)$, which generally has a greater number of lines (*i.e.* more iso-θ detected). In order to compare those matrixes, we crop $M_{mod}(D_p, n)$ to match the size of M_{exp} into several cropped $\widetilde{M}_{mod}(D_p, n)$. We exclude comparisons between ridge and valleys, and we keep the cropped matrix that best compares with M_{exp}, which is equivalent to a y_p fit. The matrix comparison criterion $N_\epsilon(D_p, n)$ is the following:

$$N_\epsilon(D_p, n) = \|(\widetilde{M}_{mod}(D_p, n) - M_{exp}) \times D_{pond}\|_2 \tag{E.2}$$

The $\|\cdot\|_2$ stands for the euclidean norm. D_{pond} is the 5×5 diagonal matrix of ponderation that normalizes each column with M_{exp} and gives a $1/3$ ponderation for the columns associated to all three polynomial coefficients. We then calculate $R_2(D_p, n)$, which is the 2D correlation factor between the experimental image and the modeled image translated by the fitted parameter y_p. Finally, we define our minimization criterion:

$$\epsilon(D_p, n) = N_\epsilon \times (1 - R_2) \tag{E.3}$$

F Fourier's optics applied to particle scattering

F.1 Brief introduction to Fourier's optics

In this section, we aim to briefly introduce the Fourier's harmonic description of light, based on references [145, 146]. In 1822, Joseph Fourier found that a complex signal can be expanded into harmonic functions [216]. The same principle applies to optical signals, where an arbitrary wave can be considered as a superposition of plane waves. In other words, plane waves form a integral basis for the whole set of optical waves. Let $u(x,y)$ be an arbitrary wave, we can write equation (F.1):

$$u(x,y) = \iint_{\mathbb{R}^2} F(\nu_x,\nu_y) e^{-i2\pi(\nu_x x+\nu_y y)}\, d\nu_x\, d\nu_y \tag{F.1}$$

(ν_x,ν_y) are the sagittal and tangential spatial frequencies, given in this document in μm^{-1} (but sometimes given in cycles/mm). For axially symmetrical optical systems, we also define the radial spatial frequency $\nu = \sqrt{\nu_x^2+\nu_y^2}$, suited for 1D calculations. Spatial frequencies are associated with the propagation angle θ (polar angle) of the plane wave with respect to the optical axis, as $\theta = \text{asin}(\lambda\nu)$. We usually consider small angles, so that $\sin\theta \simeq \theta$: this is known as the paraxial approximation, then we can write $\nu \simeq \theta/\lambda$. The coefficients in the integral basis $F(\nu_x,\nu_y)$ in equation (F.1) are the two-dimensional Fourier transform of $u(x,y)$:

$$F(\nu_x,\nu_y) = \mathscr{F}\left\{u(x,y)\right\} = \iint_{\mathbb{R}^2} u(x,y) e^{i2\pi(\nu_x x+\nu_y y)}\, dx\, dy \tag{F.2}$$

The advantage of this transformation is that it bridges the spatial domain with the angular domain. It can prove useful describing linear, and translation invariant optical systems. Such systems can describe free space propagation or thin lenses for example. In the spatial domain, let us consider a linear, translation invariant optical system $h(x,y)$, if $f(x,y)$ and $g(x,y)$ are input and output waves (respectively) traversing the optical system (see, Figure F.1), then we can write:

$$g(x,y) = h(x,y) * f(x,y) \tag{F.3}$$

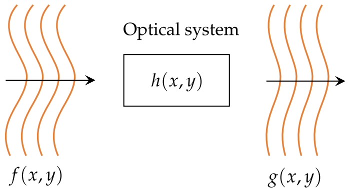

Figure F.1: *Transmission of a wave through an optical system.*

Where $*$ is the operator of convolution. $h(x,y)$ is called the Point Spread Function (PSF) of the optical system[7]. In the Fourier domain, describing such optical system becomes much easier as computationally heavy convolutions becomes simple products, especially for cascaded systems. Let $F(\nu_x,\nu_y)$ and $G(\nu_x,\nu_y)$ be the Fourier transform of $f(x,y)$ and $g(x,y)$, we can write:

$$G(\nu_x,\nu_y) = \mathscr{H}(\nu_x,\nu_y)\cdot F(\nu_x,\nu_y) \tag{F.4}$$

$\mathscr{H}(\nu_x,\nu_y)$ is the Fourier transform of $h(x,y)$, it is called the Optical Transfer Function (OTF) of the optical system. It's common to break down this complex function in two real functions:

$$\mathscr{H}(\nu_x,\nu_y) \;=\; \mathscr{M}(\nu_x,\nu_y)e^{i\mathscr{P}(\nu_x,\nu_y)} \tag{F.5}$$

$\mathscr{M}(\nu_x,\nu_y)$ is the modulus of the OTF, which is widely known as the Modulation Transfer Function (MTF): it quantifies the loss of contrast induced by an optical system as a function of the spatial frequency (*i.e.* the finesse of detail). $\mathscr{P}(\nu_x,\nu_y)$ is the phase of the OTF, called the Phase Transfer Function (PTF or PhTF). The latter is less used, but can be useful to describe phase sensitive systems such as interferometers.

---

[7] It gives the response of the optical system illuminated by a point.

A linear, translation invariant optical system can be described by its OTF. In some simple cases, this function can be expressed analytically. As a relevant example, we can calculate the OTF of free space propagation $\mathscr{H}_d(\nu_x, \nu_y)$ after a distance d in a medium of refractive index n_m:

$$\mathscr{H}_d(\nu_x, \nu_y) = \exp\left[-i2\pi n_m d\sqrt{1/\lambda^2 - \nu_x^2 - \nu_y^2}\right] = \exp\left[-i2\pi n_m d\sqrt{1/\lambda^2 - \nu^2}\right] \quad \text{(F.6)}$$

This expression is exact, not to be confused with the Fresnel's propagator that is calculated under the Fresnel approximation. We usually define a domain where $\nu^2 < 1/\lambda^2$ called the propagation domain. Under such conditions, (if n_m is real, meaning that the propagation media is not absorbing), a wave is phase-shifted by the argument of $\mathscr{H}_d$ but its magnitude is not altered. Beyond the propagation domain, $\mathscr{H}_d(\nu_x, \nu_y)$ decays exponentially as the argument below the square root becomes negative. The wave is then called an evanescent wave. It means that waves with high angle (*i.e.* with axial spatial frequencies beyond $1/\lambda$) can't propagate.

We can calculate several other OTF's, here we are most interested in describing the scattering of spheres (or other scatterers) using this formalism.

F.2 Fourier's formulation of Mie's theory

The Lorenz-Mie theory, in its simplest form, describes the light scattering by a sphere illuminated by a plane wave aligned with the optical axis. This case is illustrated in Figure F.2(a).

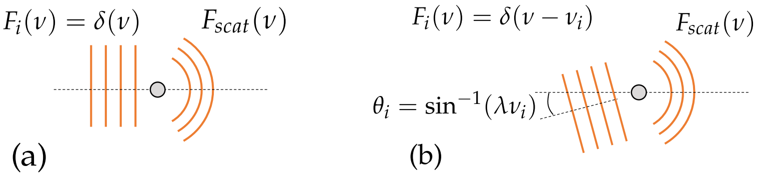

Figure F.2: *(a) Illustration of scattering of an axial plane wave. (b) Illustration of scattering of a tilted plane wave.*

Let us give a description in the Fourier domain (1D axisymmetrical for simplification). We consider an incident axial plane wave, written $F_i(\nu) = \delta(\nu)$. The normalized scattering signature $S(\theta)$ is calculated by Lorenz-Mie theory (or other scattering theories), the intensity is $C_{scat} \cdot |S(\theta)|^2/\Sigma$, with Σ the section of the incident beam (see, Appendix B).

For simplification, we define $\widetilde{S}(\nu) = (C_{scat}/\Sigma)^{1/2} \cdot S(\text{asin}(\lambda\nu))$. The scattered wave is then written $F_{scat}(\nu) = \widetilde{S}(\nu)$. We can trivially write:

$$F_{scat}(\nu) = \widetilde{S}(\nu) = \delta(\nu) * \widetilde{S}(\nu) = F_i(\nu) * \widetilde{S}(\nu) \quad \text{(F.7)}$$

Now, let's consider a plane wave tilted by an angle $\theta_i = \text{asin}(\lambda\nu_i)$ as in Figure F.2(b). The tilted incoming wave is $F_i(\nu) = \delta(\nu - \nu_i)$. By rotation of the case (a), we can write the scattered wave as:

$$F_{scat}(\nu) = \delta(\nu) * \widetilde{S}(\nu - \nu_i) = \delta(\nu - \nu_i) * \widetilde{S}(\nu) = F_i(\nu) * \widetilde{S}(\nu) \quad \text{(F.8)}$$

We obtain the same result as in (a). Finally, we can rightfully generalize this result with an arbitrary wave, as plane waves form an integral basis of the whole optical wave set.

$$F_{scat}(\nu_x, \nu_y) = F_i(\nu_x, \nu_y) * \widetilde{S}(\nu_x, \nu_y) \quad \text{(F.9)}$$

Note that, here we've made no approximation that could restrict the domain of spatial frequencies. Let now discuss this result in the spatial domain by taking the inverse Fourier transform $\mathscr{F}^{-1}$ of the incoming wave $u_i(x, y)$ and the scattered wave $u_{scat}(x, y)$:

$$u_i(x, y) = \mathscr{F}^{-1}\left\{F_i(\nu_x, \nu_y)\right\} \quad \text{(F.10)}$$

$$u_{scat}(x, y) = \mathscr{F}^{-1}\left\{F_i(\nu_x, \nu_y) * \widetilde{S}(\nu_x, \nu_y)\right\} = u_i(x, y) \cdot \mathscr{F}^{-1}\left\{\widetilde{S}(\nu_x, \nu_y)\right\} \quad \text{(F.11)}$$

This is equivalent to the case where a wave $u_i(x,y)$ gets diffracted by a planar obstacle $P_\chi(x,y) = \mathscr{F}^{-1}\left\{\widetilde{S}(\nu_x,\nu_y)\right\}$. We plot in Figure F.3 the modulus of the equivalent planar obstacles $P_\chi(x,y)$ of PSL spheres (refractive index $n_{PSL} = 1.5875$ [84]) illuminated by a polarized[8] incident plane wave of wavelength $\lambda = 635$ nm.

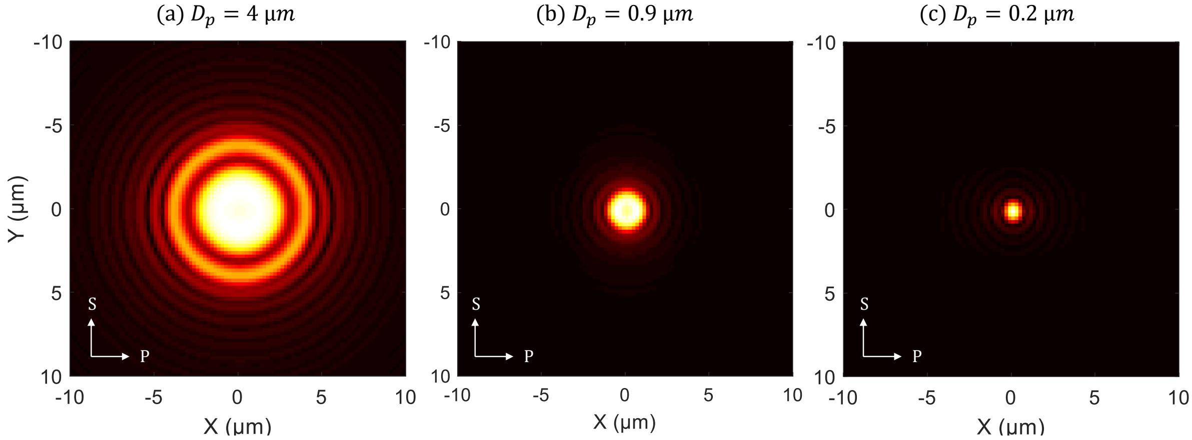

Figure F.3: Modulus of the equivalent planar obstacles of PSL spheres with different diameters (a) 4 μm, *(b)* 0.9 μm *and (c)* 0.2 μm.

We observe that the modulus of planar-equivalent obstacles $P_\chi(x,y)$ of a sphere (semi-transparent transmission profile) is very different from a disc. Still, the overall size of the obstacle appears consistent with the diameter of the particle, but show additional ripples. The phase part (not shown here) of this obstacle show similar ripple effects. This formulation can be extended to other scattering theories or methods, providing that one can express a scattering signature $S(\theta)$.

F.3 Optical Fourier transform of scattering signatures

It is commonly known that it is possible to perform an optical Fourier Transform using the d-f lens setup. This assertion can be easily demonstrated graphically, using the ray construction rules. Here, we will develop this argument using the formalism of Fourier optics, for consistency reasons. We will take as a reference the book [146], that gives the expression of the image $g(x,y)$ of an object plane $f(x,y)$ through a lens, in the d-f setup:

$$g(x,y) = \frac{1}{\lambda f} e^{-ik(d+f)} e^{i\pi\frac{(x^2+y^2)(d-f)}{\lambda f^2}} F(\frac{x}{\lambda f}, \frac{y}{\lambda f}) \tag{F.12}$$

With $F(\nu_x,\nu_y) = \mathscr{F}\{f(x,y)\}(\nu_x,\nu_y)$ the Fourier transform of the image plane $f(x,y)$. Under incoherent illumination, a image sensor is sensitive to the module squared of the image $g(x,y)$. In this case, we obtain a Fourier transform of the object plane.

$$I(x,y) = |g(x,y)|^2 = \frac{1}{|\lambda f|^2} |F(\frac{x}{\lambda f}, \frac{y}{\lambda f})|^2 \tag{F.13}$$

As a side note, we can consider the particular case f-f, where the object plane is at the object focal plane the the lens (*i.e.* $d = f$). In this case, the phase part ($\exp(i\pi(x^2+y^2)(d-f)/\lambda f^2)$) of equation (F.12) is erased. The image $g(x,y)$ is proportional to the Fourier Transform $F(\nu_x,\nu_y)$ of the object plane $f(x,y)$.

---

[8] Our polarization convention is given in Appendix A.

Going back to the general d-f setup, we now consider a scattering particle in the object plane. The particle is at the spatial coordinates (x_p, y_p, z_p). According to the previous section, and by adding a transverse translation by (x_p, y_p), we have:

$$f(x,y) = \delta(x - x_p, y - y_p) * P_\chi(x,y) \tag{F.14}$$

As a recall, $P_\chi(x,y) = \mathscr{F}^{-1}\left\{\widetilde{S}(\nu_x,\nu_y)\right\}$ is the equivalent planar obstacle of a sphere. The Fourier transform of $f(x,y)$ is simply

$$F(\nu_x,\nu_y) \;=\; \mathscr{F}\{f(x,y)\}(\nu_x,\nu_y) = e^{i2\pi(\nu_x x_p + \nu_y y_p)}\widetilde{S}(\nu_x,\nu_y) \tag{F.15}$$

We observe that the effect of the position of the particle is only carried by the phase of $F(\nu_x,\nu_y)$. This part is removed by taking the intensity, meaning that we lose the information on the particle's position:

$$|F(\nu_x,\nu_y)|^2 \;=\; |\widetilde{S}(\nu_x,\nu_y)|^2 \tag{F.16}$$

Applying equation (F.13) we obtain the image we would see on an image sensor in the image focal plane (IFP) of a lens, with is proportional to the scattering signature:

$$I(x,y) = |g(x,y)|^2 = \frac{1}{|\lambda f|^2}|\widetilde{S}(\frac{x}{\lambda f},\frac{y}{\lambda f})|^2 \tag{F.17}$$

Such setup, applied to particle's scattering signature imaging in the Fourier domain is illustrated in Figure F.4.

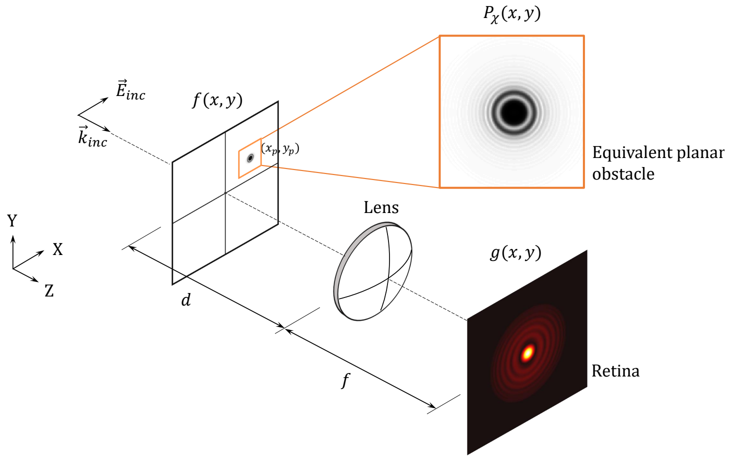

Figure F.4: Schematic of the d-f setup applied to particle's scattering signature imaging in the Fourier domain.

G Compact illumination module

In this appendix, we will describe the downward illumination module used in Section III.5.3 designed to operate with our PM sensors based on holed retinae (weather it is the lens-less setup as in Chapter II, the Fourier-domain setup as in Chapter III or a possible future assembly involving engineered reticles as described in Appendix C). Its main goal is to provide a focused beam just above the muzzle of the air channel, using a 45° mirror.

Such an illumination system is realized by assembling commercially available optical elements such as a Laser Diode (LD) that provides 5 mW of optical power at a wavelength of 637 nm (Thorlabs, L637P5); a collimation aspheric lens $\mathscr{L}_1$ (Thorlabs, C330TMD-B, $f_1 = 3.1$ mm); and a focusing aspheric lens $\mathscr{L}_2$ (Thorlabs, C280TMD-B, $f_2 = 18.4$ mm). All those elements are contained within a standard lens tube for 0.5 inch optics (Thorlabs, SM05M10), that has an outer diameter of 17.78 mm.

This module is presented in Figure G.1.

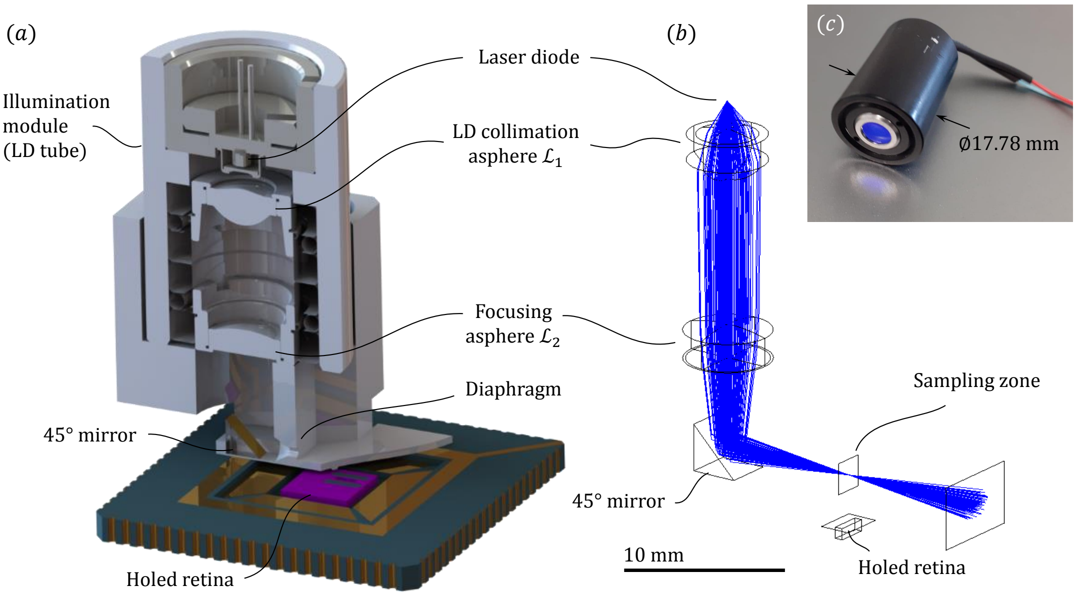

Figure G.1: (a) 3D view of the full assembly involving the illumination tube, a blank cloaker and the holed retina (partial cross sectional view). (b) RT simulation of the formation of the illumination beam. (c) Photography of the illumination tube.

The $\mathscr{L}_{1,2}$ lens system is designed to properly form a focused beam above the fluidic channel from the bare LD. First, the $\mathscr{L}_1$ collimation asphere is chosen with a high numerical aperture, in order to capture and collimate most of the radiation from the source; then, $\mathscr{L}_2$ focuses the beam in the aerosol sampling zone. An important matter to take into account in the choice of lenses is the angular magnification of the system: if θ_1 and θ_2 are polar angles from the source and to the focal point respectively, then the relation between the two angles is given by the equation (demonstration is trivial):

$$\frac{\tan(\theta_2)}{\tan(\theta_1)} = \frac{f_1}{f_2} \tag{G.1}$$

The LD provides a Gaussian beam with a typical divergence of 8° (FWHM) for its slow axis and 34° (FWHM) for its fast axis. At the focal point, using equation (G.1), the divergence becomes 1.36° (FWHM) for its slow axis and 6.48° (FWHM) for its fast axis.

One can reasonably consider that when passing through the aspherical lens system, the beam is still Gaussian. We recall that, for a Gaussian beam, the steeper the divergence is, the smaller the waist and the shorter the Rayleigh distance are [146]. The waist and Rayleigh distance roughly define the particle sampling volume (denoted V_s). A small volume allows to have a high optical power density and thus a bright scattering phenomena (which can allow to detect small particles). On the other hand, a low sampling volume reduces the probability of detecting a particle. The lens system used, and its consequence on the extend of sampling volume seems to be experimentally a good compromise, pending further study to determine an optimal configuration with a custom optical system.

Note that the Lorenz-Mie theory is regularly called upon, which is valid when the illumination is a plane wave. It can reasonably be considered as valid in the region bounded by the Rayleigh distance.

Finally, it should be noted that the LD provides a linearly polarized (or at least strongly elliptical) illumination. The polarization angle ϕ_p can be advantageously rotated simply by turning the tube around its axis.

H 2D-PCM Triangular lattice

This section will provides information about the triangular lattice of holes 2D-PCM that was designed, fabricated and tested, alongside the other two PCM designs. Although this specific lattice does not bring any additional element to the operating principle of the VC, especially in terms of polarization dependency (already achieved by the square lattice), it allows to relax some technological constraints (especially on the gap between the holes).

In the same fashion as in Section IV.3.4, we compute the spectral and angular response of the triangular lattice design: $h = 180$ nm, $FF = 56$ %, $P = 0.560$ µm (see, Figure H.1).

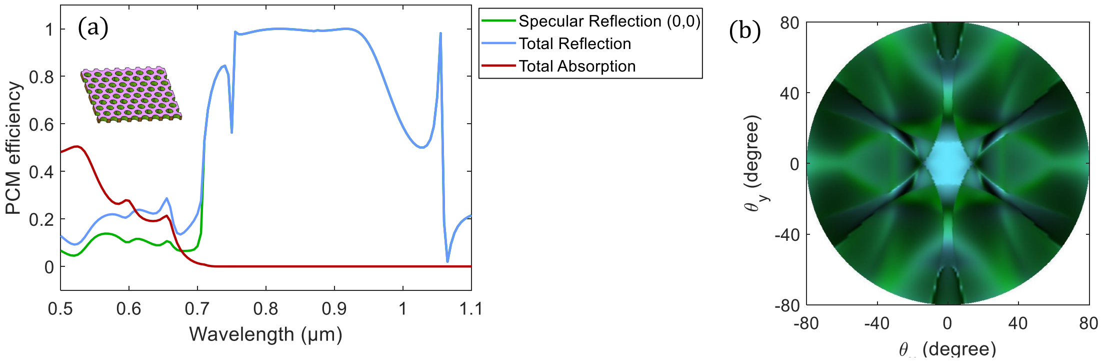

Figure H.1: (a) Reflectivity spectrum at normal incidence of the triangular lattice 2D-PCM mirror. (b) Angular reflectivity at $\lambda = 850$ *nm.*

Again, parasitic Fano resonance are seen in the normal incidence spectrum (subfigure (a)). In the angular reflectivity map (subfigure (b)), we can see the expected $\pi/3$ symmetry, that is present both in the six diffraction petals (green map) and in the central specular area that is shaped like an hexagon (blue map). Note that the vertices of this hexagon are aligned with the first neighbors holes of the lattice.

After fabrication of a 100 variants of the triangular lattice design, we measure the transmittance spectra of all variants: shown in Figure H.2 the $1 - \langle T_{S/P} \rangle$. The disposition of subplots is the same as for the 1D and 2D square mirrors (see, Figure IV.43).

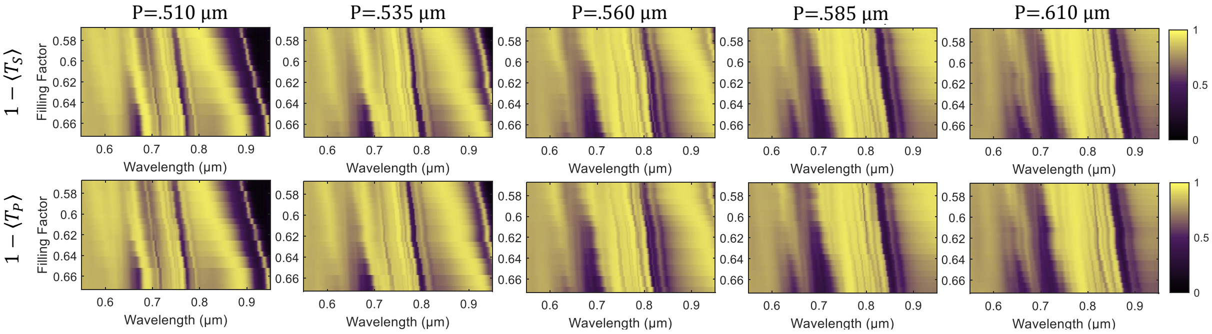

Figure H.2: Mean transmission spectra of all 2D-PCM, triangular lattice.

The measured polarized spectra are almost identical, showing a much better polarization independence than for the square lattice. This is certainly due to the fact that the critical dimensions are less aggressive.

J Abelès matrix method

The Abelès matrix method (or optical transfer matrix method), first proposed by Florin Abelès in 1948 [217], is a method extensively used to model the electromagnetic propagation of waves through a stratified medium, such as a DBR (Distributed Bragg Reflector). In this section, we will briefly summarize the method, on the basis of reformulations found in references [218,219].

The starting point of the method is based on the calculation of the reflexion and transmission of a plane wave at the interface of two dielectric media. When there are multiple interfaces, as in stratified media, the multiple reflections and transmissions throughout the different layers can interfere constructively of destructively. By using the continuity conditions of the wave at the interfaces of a single layer [81], the Abelès matrix method allows to describe this wave within the layer, using a simple 2 × 2 matrix. Then, the full description of the layered stack can be described by the product of each individual layer matrixes.

In this formulation, the wave is calculated with the wave basis U^+ and U^-. Which correspond to the part of the field that propagates along the Z axis, and the counter-propagating part, respectively. The optical configuration is defined in Figure J.1, showing the arbitrary stack of N layers, of arbitrary thicknesses. As explained earlier, we can show that the relation between the incident wave U_0^+, reflected wave U_0^- and transmitted wave U_{N+1}^+ is given by this simple matrix product, as expressed in equation (J.1):

$$\begin{pmatrix} U_0^+ \\ U_0^- \end{pmatrix} = \frac{1}{\prod_{j=1}^{N+1} t_j} \prod_{j=1}^{N+1} C_j \begin{pmatrix} U_{N+1}^+ \\ U_{N+1}^- \end{pmatrix} \tag{J.1}$$

Where C_j is the 2 × 2 matrix associated to the j-th layer, which will be expressed in the following. The scalar coefficients t_j are the Fresnel's transmission coefficients.

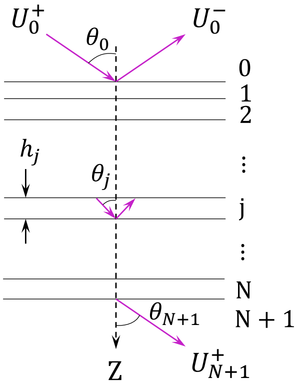

Figure J.1: *Geometrical definitions of the stack.*

The Fresnel's reflection and transmission coefficients r_j and t_j respectively, between the $(j-1)$-th and j-th layer can be easily expressed, using the complex reflective indexes (n_{j-1} and n_j) and the angles (θ_{j-1} and θ_j), for both P and S polarization (parallel and perpendicular, respectively) [220].

$$r_{j,P} = \frac{n_{j-1}\cos\theta_j - n_j\cos\theta_{j-1}}{n_{j-1}\cos\theta_j + n_j\cos\theta_{j-1}} \qquad t_{j,P} = \frac{2n_{j-1}\cos\theta_{j-1}}{n_{j-1}\cos\theta_j + n_j\cos\theta_{j-1}} \tag{J.2}$$

$$r_{j,S} = \frac{n_{j-1}\cos\theta_{j-1} - n_j\cos\theta_j}{n_{j-1}\cos\theta_{j-1} + n_j\cos\theta_j} \qquad t_{j,S} = \frac{2n_{j-1}\cos\theta_{j-1}}{n_{j-1}\cos\theta_{j-1} + n_j\cos\theta_j} \tag{J.3}$$

Naturally, the angles θ_j follows the Snell-Descartes law:

$$n_0 \sin\theta_0 = n_j \sin\theta_j \tag{J.4}$$

Then, we define δ_j, the optical length between the $(j-1)$-th and j-th interfaces, which expresses a phase (or an modulation if n_j exhibit an imaginary part).

$$\delta_0 = 0 \qquad \delta_j = (2\pi/\lambda) n_j \cos\theta_j h_j \tag{J.5}$$

Where h_j is the thickness of the j-th layer, and λ is the wavelength in the vacuum. Finally we can express C_j, the 2 × 2 matrix associated to the j-th layer:

$$C_j = \begin{pmatrix} \exp(-i\delta_{j-1}) & r_j \exp(-i\delta_{j-1}) \\ r_j \exp(i\delta_{j-1}) & \exp(i\delta_{j-1}) \end{pmatrix} \tag{J.6}$$

Note that this matrix can be expressed with the reflection coefficients r_j in either P or S polarization. Going back to equation (J.1), we express the product of the individual layer matrixes as:

$$C = \prod_{j=1}^{N+1} C_j = \begin{pmatrix} a & b \\ c & d \end{pmatrix} \tag{J.7}$$

We can consider $U_{N+1}^{-} = 0$, because we don't input light from the back of the stack. By doing so, we obtain a very convenient expression for the total reflection r and transmission t coefficients.

$$r = \frac{U_0^-}{U_0^+} = \frac{c}{a} \qquad\qquad t = \frac{U_{N+1}^+}{U_0^+} = \frac{\prod_{j=1}^{N+1} t_j}{a} \tag{J.8}$$

The energy reflectance R is simply $R = |r|^2$. If, the stack is not absorbing, the energy transmittance is $T = 1 - R$. If the stack is absorbing, the formula is slightly more complex, and is polarization dependent:

$$T_S = \Re\left(\frac{n_{N+1}\cos\theta_{N+1}}{n_0\cos\theta_0}\right)|t_S|^2 \qquad\qquad T_P = \Re\left(\frac{n_{N+1}^*\cos\theta_{N+1}}{n_0^*\cos\theta_0}\right)|t_P|^2 \tag{J.9}$$

Where, $*$ stands for the complex conjugate, and $\Re$ for the real part.

Now let us consider the specific case of the DBR, constituted by an alternation of two dielectric layers on a substrate. We can compute the transfer matrixes of the two layers C_1 and C_2 once. Then, if N_{alt} is the number of alternations, we can write:

$$C = C_{first} \times (C_1 \times C_2)^{N_{alt}} \times C_{last} \tag{J.10}$$

Where, C_{first} and C_{last} correspond to the first and last interfaces respectively. Generally, it refers to the air above the stack and the substrate below.

K Supplementary material on the Fourier microscope

K.1 Design of the dual space optical microscopy setup.

In this appendix, we will describe precisely the optical design of the dual space (real and Fourier's) microscopy setup. We take inspiration from reference [221] in terms of optical design principles and methods, using RT tools (Zemax Optics Studio, Sequential mode). The real space microscopy imaging setup allows to aim correctly at a specific PCM (sized by 100 µm or 200 µm) within the photonic chip. We present a design in Figure K.1. The optical system is designed achromatic at the NIR range (mirrors' working range), extending in the visible range as much as possible. The real space path is optimized achromatic in the visible range. The different optical paths (Real vs Fourier domain) can be separated using either a Beam Splitter (BS) or dichroic mirror.

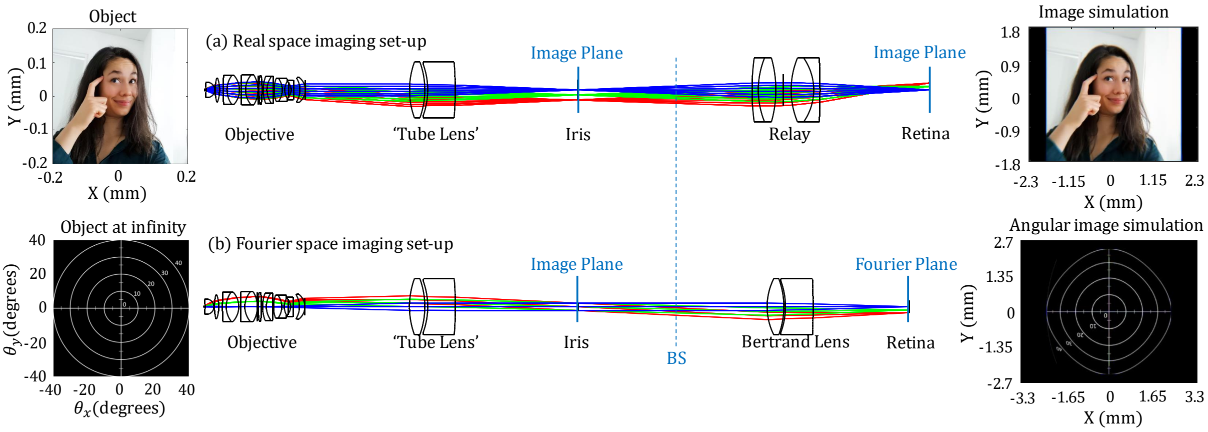

Figure K.1: *RT simulation of the modified microscopy setup (a) in real space imaging mode and (b) in Fourier domain mode.*

We use a modified microscopy optical setup with an infinity corrected microscope objective (Olympus Plan-Apochromat. 40X, NA=0.65)[9] associated with a Tube Lens (TL). Due the lack of available TLs for infinitely corrected microscope objectives with short focal length, we choose to use a simple achromatic pair instead (Thorlabs, ACA254-060-B, $f = 60$ mm). We have an intermediate image plane where classic microscope objectives have the image sensor, we have an iris instead in order to select the rays coming from the PCM specifically. This part is common to both real and Fourier paths.

Now detailing the real space (visible) optical path (see, Figure K.1(a)). The image plane is re-imaged on a color sensitive CMOS image sensor[10], Rolling Shutter (Thorlabs, DCC1645C) using a magnified relay lens system: an achromatic doublet pair optimized for the visible range (Thorlabs, MAP105075-A, $f_1 = 50$ mm, $f_2 = 75$ mm). Figure K.1(a) shows an image simulation with a picture of Marine made in the same fashion than in Figure III.6, we verify that the magnification is correct to image a PCM sized by 100 µm, with very good image quality.

We step back at the object to detail the Fourier path (see, Figure K.1(b)). In this part, rays are traced from an object seen at infinity for given angles and with an aperture that corresponds to the size of the sample. The planes where these parallel object rays are focused are the Fourier planes. The TL is used to collimate the Back Focal Plane (BFP) of the objective in order to perform an angular magnification. In most infinity corrected microscope objectives, the BFP is inside the objective and highly curved [221]. We don't use a conventional infinitely corrected TL, but we still manage to obtain a decent optical system, with limited field curvature aberrations. The distance between the TL and the objective is of important matter in this case as the FFP (Front Focal Plane) of the TL should be co-planar with the BFP of the objective. Thus, the need for a specific TL's focal distance (hardly found with conventional TLs). In the

---

[9] Zemax files for the microscope objective were obtained from a participatory database for Zemax lens files built using patent [222] filed by Olympus as a reference. Zemax files for every other optical elements were found on Thorlabs Zemax's catalog.

[10] We use a color sensor as the color of the PCM is an important visual information making sure we are aiming at the right PCM within the photonic chip, as seen in Figure IV.37.

intermediate image plane, the rays coming from the PCM are selected spatially by the iris, as explained above. Finally, the Fourier plane is focused on a Global Shutter, monochromatic CMOS image sensor (Thorlabs, DCC1240) using a Bertrand Lens[11]: we choose a simple achromatic pair (Thorlabs, ACA254-060-B, $f = 50$ mm). Figure K.1(b) shows an angular image simulation with an angle graduated reticle. We observe barrel distortions, that could be easily taken into account in image processing.

A concern one might have with this setup is that the Γ mode (unperturbed transmitted mode) could bloom the retina in the Fourier setup, making our measurement blind to scattering effects on the cavities. A solution one can adopt is to add relay optics to image an intermediate Fourier plane where a blocking element is placed instead. This solution adds additional elements that significantly increase alignments difficulties and the overall size of the microscope optical setup. We chose instead to use a Cassegrain microscope objective[12] (Thorlabs, LMM-40X-UVV) as an alternate optical setup where the on-axis light is blocked by the secondary mirror as seen in Figure K.2(a-c).

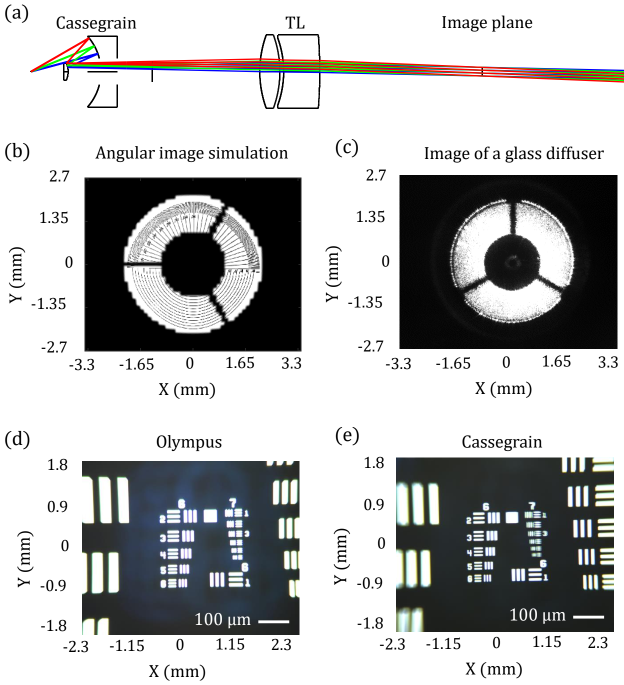

Figure K.2: (a) RT simulation of the alternate microscopy setup, Fourier path. (b) Angular image simulation. (c) Fourier-domain image of a glass diffuser. (d, e) Real space image of the USAF 1951 target obtained with the Olympus and the Cassegrain objective.

This objective offers a longer working distance but the FoV in Fourier domain is degraded compared to the previous setup. This is mainly due to the fact theta the secondary mirror (and its arms) is blocking part of the field, as it can be seen in subfigures (a, b, c). This limitation is acceptable considering that the system becomes only sensitive to high-angles scattering effects. Subfigure (b) shows an image simulation in the Fourier domain[13], while subfigure (c) shows an experimental image obtained with a glass diffuser (Thorlabs, DG20-120), which is among the closest we can get from a perfect isotropic scatterer. Finally, the real-space image (subfigure (d, e)) quality shows degradation compared with the previous setup, which are mainly due to field curvature aberrations caused by the Cassegrain objective (which are not present in Plan-Apochromat. objectives). Considering that the real space image is only used to aim at a specific PCM, image quality is not of great deal, and the effect of field curvature would be mitigated by closing the iris on the intermediate image plane. The two alternate setup will both be used depending on the experimental conditions (brightness of Γ mode and available working distance).

---

[11] The term Bertrand Lens is generally used to refer to lenses that forms an image of the BFP of a microscope objective.

[12] A Cassegrain is a reflective objective composed of an annular primary concave mirror and a secondary convex mirror.

[13] The pupil appears pixelated in this simulation: this is due to the limited sampling of the spatially variant PSF of the Fourier setup

K.2 Lighting system for the Fourier microscope

This section describes the lighting system that provides illumination for the Fourier imaging microscope described in Section IV.6.4. The lighting system includes a wideband SLED and a monochromator, such design stems from the need for a widely tunable source in terms of wavelength and spectral bandwidth. This part is critical if one wants to match a specific Fabry-Perot (FP) resonance. We choose not to use a tunable laser because we needed to remain under certain laser safety condition, so that our bench can be used outside an optical laboratory, for instance alongside the aerosol test bench described in Appendix D. The lighting system is presented in Figure K.3.

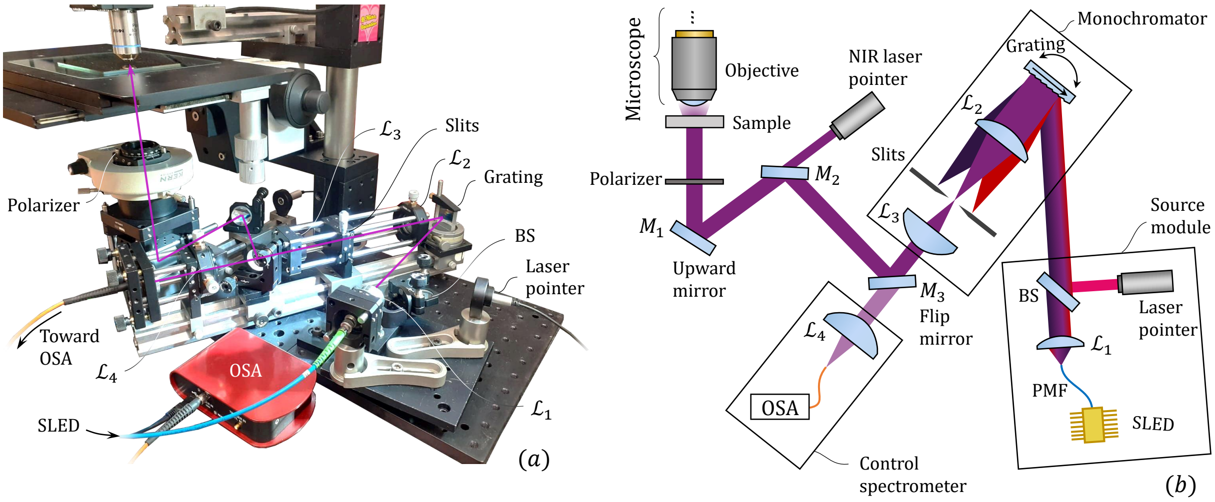

Figure K.3: (a) Photography of lighting system. (b) Schematic of the optical setup.

The source itself, is modular, and can be easily swapped as long as it provides a collimated beam of reasonable size (typically less than 1 inch). In our case, as our primary source, we use a SLED (Thorlabs, SLD830A20) that operate in the NIR region from 790 nm to 880 nm, and that can provide a total of 26 mW of optical power. The SLD is coupled with a single mode (SM) optical fiber, and collimated with a fiber collimator (Thorlabs, F810APC-780), referred in Figure K.3 as $\mathscr{L}_1$. The shaped NIR polychromatic beam is a collimated beam sized by 7.5 mm. We noticed that the beam delivered by the SLED had a sharply elliptical polarization. For this reason, we used a Polarization-Maintaining Fiber (PMF, PM780-HP) between the SLED and the $\mathscr{L}_1$ collimator, then we mounted the collimator on a rotating mount, in order to roughly adjust the polarization state of the beam. We also align a laser pointer (780 nm) with our primary beam using a flip beam splitter (BS). The laser pointer is only used during alignment operations.

The monochromator is constituted by a blazed reflective grating (Thorlabs, GR25-0608). Such a grating is designed to maximize the diffraction efficiency for both polarizations at a given diffraction order, here the order -1, around the blaze wavelength (750 nm). The optimal configuration, called Littrow configuration [223], consists in having the blaze angle (13°) as the angle of incidence. This configuration is not practical since the diffracted rays are reflected in the direction of incidence. However, we will try to get as close as possible to the Littrow configuration, while taking into account the space constraints[14]. Here, we use an angle of incidence of 32°, which is the best we could get.

The diffracted beams, which are spread out in the sagittal plane (OXZ) by the grating (depending on the wavelength) are then focused on the image focal plane (IFP) of the $\mathscr{L}_2$ lens. The radiation from the primary source is spread out along the sagittal axis of the focal plane (horizontal axis); the longer the focal length, the greater the spread will be. By taking into consideration the compactness constraints, we selected $f_2 = 100$ mm. Variable slits are placed in such focal plane, in order to select the desired wavelength and spectral width.

---

[14] especially lens frames that block the beam when the angles used are too small.

Figure K.4(b, c) shows images focused on the plane of the slits. When the slits are open (see, subfigure (b)), we observe the spreading of the polychromatic source[15] along the sagittal axis, as explained above. Closing the slits (see, subfigure (c)), and rotating the grating allows us to select a specific wavelength, by modifying both the incidence and diffraction angle.

The selected radiation is then re-collimated using the $\mathscr{L}_3$ lens. the focal length of the $\mathscr{L}_3$ lens ($f_3 = 40$ mm) is chosen according to the desired output beam diameter. Indeed, the magnification of the afocal lens system $\mathscr{L}_2 - \mathscr{L}_3$ is $-f_2/f_3 = -0.4$, meaning that the 7.5 mm beam delivered by the fiber collimator L1 is narrowed to a 3 mm output beam.

The output beam is redirected upward to the microscope using set of mirrors (M_{1-3}). In order to control the wavelength and the spectral width of the output beam, we've added a control path toward a reference OSA (Optical Spectrum Analyzer). This optical path is can be separated using a beam sampler, or in our case, a flip mirror (M_3). The control spectrometer path is constituted by a focusing lens $\mathscr{L}_4$ (75 mm) that concentrates the sampled beam to an optical fiber plugged into the reference OSA (Thorlabs, CCS175, Czerny-Turner CCD spectrometer). Figure K.4(a) shows the spectrum of the output beam, before and after closing the slits (respectively, blue[16] and orange curves).

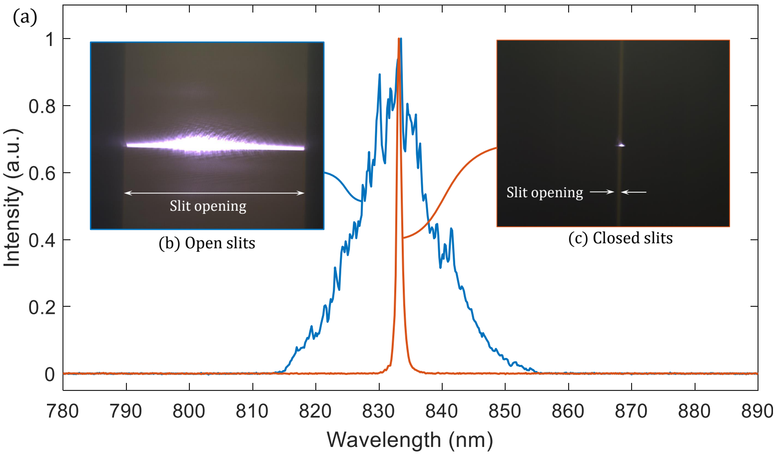

Figure K.4: (a) Spectrum of the output beam, before (blue curve) and after (orange curve) closing the slits. (b, c) Color images focused on the slit plane when open (b) and closed (c).

Finally, the beam crossed a polarizer mounted on a rotation stage, just before the sample in order to purify the polarization state of the illumination beam.

Alternatively, we can use a simple laser source (for instance a collimated VSEL source at 850 nm) that can bypass the monochromator. Such configuration can be useful for alignment/calibration operations, or to perform simple measurements that don't require the monochromator. Such a configuration can be switch on simply by removing the M_2 mirror (see, Figure K.3).

---

[15] Note that the image was taken with a color CMOS image sensor without IR filter. Is such sensor, both red and blue pixels react to NIR radiation, thus NIR 'color' appear purple.

[16] Note that the blue curve is not to be mistaken with the SLED spectrum. Only a portion of the beam, spread by the grating, can be injected into the OSA's fiber.

Scientific production

Part of the work presented in this manuscript was published in scientific journals and conference proceedings:

[1] **Jobert, G.**, Barritault, P., Fournier, M., Monpeurt, C., Boutami, S., Jamois, C., Bernasconi, P., Lovera, A., Braga, D., Seassal, C., Miniature optical particle counter and analyzer involving a fluidic-optronic CMOS chip coupled with a millimeter-sized glass optical system. Sensors, vol. 21, no. 9, p. 3181, May 2021. https://www.mdpi.com/1424-8220/21/9/3181

[2] **Jobert, G.**, Barritault, P., Fournier, M., Boutami, S., Jobert, D., Marchant, A., Michelot, J., Monsinjon, P., Lienhard, P., Nicoletti, S., Miniature particulate matter counter and analyzer based on lens-free imaging of light scattering signatures with a holed image sensor. Sens. Actuators Rep. 100010. 2020. https://doi.org/10.1016/j.snr.2020.100010

[3] **Jobert, G.**, Fournier, M., Boutami, S., Jamois, C., Lovera, A., Braga, D., Seassal, C., Millimeter-sized particle sensor using a wide field of view monolithic lens assembly for light scattering analysis in Fourier domain. Presented at the Photonic Instrumentation Engineering VII, SPIE, San Francisco, United States, p. 24. 2020. https://doi.org/10.1117/12.2544185

[4] Fournier, M., Barritault, P., **Jobert, G.**, Marchant, A., Boutami, S., Michelot, J., Lienhard, P., Nicoletti, S., Duraffourg, L., A miniaturized optical sensor for particulate matter detection. Presented at the Photonic Instrumentation Engineering VII, SPIE, San Francisco, United States, p. 43. 2020. https://doi.org/10.1117/12.2546128

[5] **Jobert, G.**, Fournier, M., Barritault, P., Boutami, S., Auger, J., Maillard, A., Michelot, J., Lienhard, P., Nicoletti, S., Duraffourg, L., A Miniaturized Optical Sensor for Fire Smoke Detection. Presented at the 20th International Conference on Solid-State Sensors, Actuators and Microsystems & Eurosensors XXXIII (TRANSDUCERS & EUROSENSORS XXXIII), IEEE, Berlin, Germany, pp. 1144–1149. 2019. https://doi.org/10.1109/TRANSDUCERS.2019.8808611

[6] Boutami, S., **Jobert, G.**, Barritault, P., Coutard, J.-G., Fournier, M., Fédéli, J.-M., Labeye, P., Marchant, A., Skubich, J., Teulle, A., Lartigue, O., Lorent, E., Glière, A., Constancias, C., Nicoletti, S., Jamois, C., Seassal, C., Duraffourg, L., Visible to mid-infrared integrated sensors for air quality measurement. Presented at the Optical Sensing, Imaging, and Photon Counting: From X-Rays to THz 2019, SPIE, San Diego, United States, p. 25. 2019. https://doi.org/10.1117/12.2529262

Several patents were also filed, during the preparation of the manuscript. Some of them relate to a side project, not directly associated with particle sensors.

[1] **Jobert, G.**, Optical particle detector, 2018, EP3598102, US20200033246, FR3083864.

[2] **Jobert, G.**, Boutami, S., Fournier, M., Seassal, C., Optical particle detector, 2018, WO2020128105, FR3090873.

[3] **Jobert, G.**, Optical particle sensor, 2019, EP3671179, FR3090874.

[4] **Jobert, G.**, Barritault, P., Fournier, M., Detecteur multi-particules, 2019, FR1911949.

[5] Boutami, S., Fournier, M., **Jobert, G.**, Jamois, C., Seassal, C., Détecteur optique de particules et procédé de fabrication, 2020, FR2009545

[6] **Jobert, G.**, Monpeurt C., Dispositif de répartition de lumière basé sur un guide d'onde planaire, 2020, FR2005622

[7] Monpeurt C., Dupoy, M., Beurrier-Bousquet, M., **Jobert, G.**, Composant optique pour un dispositif d'imagerie interférométrique, 2020, FR2013816

[8] **Jobert, G.**, Monpeurt C., Composant optique pour un dispositif interférométrique d'imagerie ATR, 2020, FR2013817

[9] Monpeurt C., **Jobert, G.**, Mathieu, G., Dupoy, M., Lartigues, O., Dispositif pour produire un faisceau lumineux polychromatique par combinaison de plusieurs faisceaux lumineux individuels (*pending*)

Bibliography

[1] G. B. Hamra, N. Guha, A. Cohen, F. Laden, O. Raaschou-Nielsen, J. M. Samet, P. Vineis, F. Forastiere, P. Saldiva, T. Yorifuji, and D. Loomis, "Outdoor Particulate Matter Exposure and Lung Cancer: A Systematic Review and Meta-Analysis," *Environmental Health Perspectives*, Jun. 2014. [Online]. Available: http://ehp.niehs.nih.gov/1408092

[2] J. O. Anderson, J. G. Thundiyil, and A. Stolbach, "Clearing the Air: A Review of the Effects of Particulate Matter Air Pollution on Human Health," *Journal of Medical Toxicology*, vol. 8, no. 2, pp. 166–175, Jun. 2012. [Online]. Available: http://link.springer.com/10.1007/s13181-011-0203-1

[3] S. A. Cormier, S. Lomnicki, W. Backes, and B. Dellinger, "Origin and Health Impacts of Emissions of Toxic By-Products and Fine Particles from Combustion and Thermal Treatment of Hazardous Wastes and Materials," *Environmental Health Perspectives*, vol. 114, no. 6, pp. 810–817, Jun. 2006. [Online]. Available: https://www.ncbi.nlm.nih.gov/pmc/articles/PMC1480527/

[4] A. J. Cohen, J. M. Samet, K. Straif, and International Agency for Research on Cancer, *Air pollution and cancer*. Lyon: International Agency for Research on Cancer, 2013, oCLC: 993948851. [Online]. Available: http://publications.iarc.fr/Book-And-Report-Series/Iarc-Scientific-Publications/Air-Pollution-And-Cancer-2013

[5] P. Vineis and K. Husgafvel-Pursiainen, "Air pollution and cancer: biomarker studies in human populations †," *Carcinogenesis*, vol. 26, no. 11, pp. 1846–1855, Nov. 2005. [Online]. Available: http://academic.oup.com/carcin/article/26/11/1846/2476064/Air-pollution-and-cancer-biomarker-studies-in

[6] United States Environmental Protection Agency, "Integrated Science Assessment for Particulate Matter (External Review Draft, 2018)," U.S. Environmental Protection Agency, Washington, DC, Tech. Rep., 2018. [Online]. Available: https://cfpub.epa.gov/ncea/isa/recordisplay.cfm?deid=341593

[7] V. Howard, "Statement of Evidence: Particulate Emission and Health (An Bord Plenala, Proposed Ringaskiddy Waste-to-Energy Facility)," 2009. [Online]. Available: http://www.durhamenvironmentwatch.org/Incinerator%20Health/CVHRingaskiddyEvidenceFinal1.pdf

[8] C. Sioutas, R. J. Delfino, and M. Singh, "Exposure Assessment for Atmospheric Ultrafine Particles (UFPs) and Implications in Epidemiologic Research," *Environmental Health Perspectives*, vol. 113, no. 8, pp. 947–955, Aug. 2005. [Online]. Available: https://ehp.niehs.nih.gov/doi/10.1289/ehp.7939

[9] S. Fuzzi, U. Baltensperger, K. Carslaw, S. Decesari, H. Denier van der Gon, M. C. Facchini, D. Fowler, I. Koren, B. Langford, U. Lohmann, E. Nemitz, S. Pandis, I. Riipinen, Y. Rudich, M. Schaap, J. G. Slowik, D. V. Spracklen, E. Vignati, M. Wild, M. Williams, and S. Gilardoni, "Particulate matter, air quality and climate: lessons learned and future needs," *Atmospheric Chemistry and Physics*, vol. 15, no. 14, pp. 8217–8299, Jul. 2015. [Online]. Available: https://www.atmos-chem-phys.net/15/8217/2015/

[10] "Clouds and Aerosols," in *Climate Change 2013 - The Physical Science Basis*, Intergovernmental Panel on Climate Change, Ed. Cambridge: Cambridge University Press, 2014, pp. 571–658. [Online]. Available: https://www.cambridge.org/core/product/identifier/CBO9781107415324A024/type/book_part

[11] M. Z. Jacobson, "Control of fossil-fuel particulate black carbon and organic matter, possibly the most effective method of slowing global warming," *Journal of Geophysical Research*, vol. 107, no. D19, p. 4410, 2002. [Online]. Available: http://doi.wiley.com/10.1029/2001JD001376

[12] T. C. Bond, S. J. Doherty, D. W. Fahey, P. M. Forster, T. Berntsen, B. J. DeAngelo, M. G. Flanner, S. Ghan, B. Kärcher, D. Koch, S. Kinne, Y. Kondo, P. K. Quinn, M. C. Sarofim, M. G. Schultz, M. Schulz, C. Venkataraman, H. Zhang, S. Zhang, N. Bellouin, S. K. Guttikunda, P. K. Hopke, M. Z. Jacobson, J. W. Kaiser, Z. Klimont, U. Lohmann, J. P. Schwarz, D. Shindell, T. Storelvmo, S. G. Warren, and C. S. Zender, "Bounding the role of black carbon in the climate system: A scientific assessment: BLACK CARBON IN THE CLIMATE SYSTEM," *Journal of Geophysical Research: Atmospheres*, vol. 118, no. 11, pp. 5380–5552, Jun. 2013. [Online]. Available: http://doi.wiley.com/10.1002/jgrd.50171

[13] V. Ramanathan and G. Carmichael, "Global and regional climate changes due to black carbon," *Nature Geoscience*, vol. 1, no. 4, pp. 221–227, Apr. 2008. [Online]. Available: http://www.nature.com/articles/ngeo156

[14] C. Wang, "A modeling study on the climate impacts of black carbon aerosols: CLIMATE ASPECTS OF BLACK CARBON," *Journal of Geophysical Research: Atmospheres*, vol. 109, no. D3, pp. n/a–n/a, Feb. 2004. [Online]. Available: http://doi.wiley.com/10.1029/2003JD004084

[15] G. Lonati, S. Ozgen, G. Ripamonti, S. Cernuschi, and M. Giugliano, "Pedestrian Exposure to Size-Resolved Particles in Milan," *Journal of the Air & Waste Management Association*, vol. 61, no. 11, pp. 1273–1280, Nov. 2011. [Online]. Available: https://www.tandfonline.com/doi/full/10.1080/10473289.2011.617650

[16] P. Penttinen, K. Timonen, P. Tiittanen, A. Mirme, J. Ruuskanen, and J. Pekkanen, "Ultrafine particles in urban air and respiratory health among adult asthmatics," *European Respiratory Journal*, vol. 17, no. 3, pp. 428–435, Mar. 2001. [Online]. Available: http://erj.ersjournals.com/content/17/3/428

[17] S. D. Lowther, K. C. Jones, X. Wang, J. D. Whyatt, O. Wild, and D. Booker, "Particulate Matter Measurement Indoors: A Review of Metrics, Sensors, Needs, and Applications," *Environmental Science & Technology*, vol. 53, no. 20, pp. 11 644–11 656, Oct. 2019. [Online]. Available: https://pubs.acs.org/doi/10.1021/acs.est.9b03425

[18] N. Janssen, Ed., *Health effects of black carbon*. Copenhagen: World Health Organization, Regional Office for Europe, 2012, oCLC: 930804705.

[19] D. Jaggard, C. Hill, R. Shorthill, D. Stuart, M. Glantz, F. Rosswog, B. Taggart, and S. Hammond, "Light scattering from particles of regular and irregular shape," *Atmospheric Environment (1967)*, vol. 15, no. 12, pp. 2511–2519, 1981.

[20] M. I. Mishchenko, L. D. Travis, and A. A. Lacis, *Multiple Scattering of Light by Particles: Radiative Transfer and Coherent Backscattering*. Cambridge University Press, 2006.

[21] I. Perera and C. Litton, "A Detailed Study of the Properties of Smoke Particles Produced from both Flaming and Non-Flaming Combustion of Common Mine Combustibles," *Fire Safety Science*, vol. 10, pp. 213–226, 2011. [Online]. Available: http://www.iafss.org/publications/fss/10/213

[22] A. Hoffer, A. Tóth, I. Nyirő-Kósa, M. Pósfai, and A. Gelencsér, "Light absorption properties of laboratory-generated tar ball particles," *Atmos. Chem. Phys.*, vol. 16, no. 1, pp. 239–246, Jan. 2016. [Online]. Available: https://www.atmos-chem-phys.net/16/239/2016/

[23] F.-X. Ouf, *Caractérisation des aérosols émis lors d'un incendie*. Rouen, Jan. 2006. [Online]. Available: http://www.theses.fr/2006ROUES003

[24] M. Wozniak, "Diffusion Limited Aggregation (DLA) algorithm of DLA / TEM software ver . - Semantic Scholar," 2013. [Online]. Available: /paper/Diffusion-Limited-Aggregation-(-DLA-)-algorithm-of-Wozniak/59e707311c84e76f48d5abbf13fca43873b37edb

[25] K. T. Whitby, W. E. Clark, V. A. Marple, G. M. Sverdrup, G. J. Sem, K. Willeke, B. Y. H. Liu, and D. Y. H. Pui, "Characterization of California aerosols—I. Size distributions of freeway aerosol," *Atmospheric Environment (1967)*, vol. 9, no. 5, pp. 463–482, May 1975. [Online]. Available: http://www.sciencedirect.com/science/article/pii/0004698175901079

[26] S. M. Wall, W. John, and J. L. Ondo, "Measurement of aerosol size distributions for nitrate and major ionic species," *Atmospheric Environment (1967)*, vol. 22, no. 8, pp. 1649–1656, Jan. 1988. [Online]. Available: http://www.sciencedirect.com/science/article/pii/0004698188903927

[27] F. Tampieri and C. Tomasi, "Size distribution models of fog and cloud droplets and their volume extinction coefficients at visible and infrared wavelengths," *pure and applied geophysics*, vol. 114, no. 4, pp. 571–586, Jul. 1976. [Online]. Available: https://link.springer.com/article/10.1007/BF00875651

[28] S. Amaral, J. de Carvalho, M. Costa, and C. Pinheiro, "An Overview of Particulate Matter Measurement Instruments," *Atmosphere*, vol. 6, no. 9, pp. 1327–1345, Sep. 2015. [Online]. Available: http://www.mdpi.com/2073-4433/6/9/1327

[29] E. Sage, A. Brenac, T. Alava, R. Morel, C. Dupré, M. Hanay, M. Roukes, L. Duraffourg, C. Masselon, and S. Hentz, "Neutral particle mass spectrometry with nanomechanical systems," *Nature Communications*, vol. 6, 2015.

[30] H. G. Craighead, "Nanoelectromechanical Systems," *Science*, vol. 290, no. 5496, pp. 1532–1535, Nov. 2000. [Online]. Available: http://science.sciencemag.org/content/290/5496/1532

[31] I. Paprotny, F. Doering, P. A. Solomon, R. M. White, and L. A. Gundel, "Microfabricated air-microfluidic sensor for personal monitoring of airborne particulate matter: Design, fabrication, and experimental results," *Sensors and Actuators A: Physical*, vol. 201, pp. 506–516, Oct. 2013. [Online]. Available: http://www.sciencedirect.com/science/article/pii/S0924424712007637

[32] S. Thomas, M. Cole, F. H. Villa-López, and J. W. Gardner, "High frequency surface acoustic wave resonator-based sensor for particulate matter detection," *Sensors and Actuators A: Physical*, vol. 244, pp. 138–145, Jun. 2016. [Online]. Available: http://www.sciencedirect.com/science/article/pii/S0924424716301480

[33] J. Liu, W. Hao, M. Liu, Y. Liang, and S. He, "A Novel Particulate Matter 2.5 Sensor Based on Surface Acoustic Wave Technology," *Applied Sciences*, vol. 8, no. 1, p. 82, Jan. 2018. [Online]. Available: http://www.mdpi.com/2076-3417/8/1/82

[34] K. Takahashi, H. Minoura, and K. Sakamoto, "Examination of discrepancies between beta-attenuation and gravimetric methods for the monitoring of particulate matter," *Atmospheric Environment*, vol. 42, no. 21, pp. 5232–5240, Jul. 2008. [Online]. Available: https://linkinghub.elsevier.com/retrieve/pii/S1352231008002379

[35] D. Schweizer, R. Cisneros, and G. Shaw, "A comparative analysis of temporary and permanent beta attenuation monitors: The importance of understanding data and equipment limitations when creating PM 2.5 air quality health advisories," *Atmospheric Pollution Research*, vol. 7, no. 5, pp. 865–875, Sep. 2016. [Online]. Available: https://linkinghub.elsevier.com/retrieve/pii/S1309104215300581

[36] J. Newman, "Modified Theory For The Characterization Of Ionization Smoke Detectors," *Fire Safety Science*, vol. 4, pp. 785–792, 1994. [Online]. Available: http://www.iafss.org/publications/fss/4/785

[37] P. P. Hairston, F. D. Dorman, G. J. Sem, and J. K. Agarwal, “Apparatus for measuring particle sizes and velocities,” Patent US5 561 515 A 1996-10-01 [US5 561 515] - US5 467 913 A 1995-11-21 [US5 467 913], Nov., 1995, archive Location: 84417774. [Online]. Available: https://permalink.orbit.com/RenderStaticFirstPage?XPN=ZhkC%252BIS0MLvjCoOEB2EWlnfDUqlXTJ5uwQdFuycu4uk%3D%26n%3D1&id=0&base=

[38] M. Fierz, C. Houle, P. Steigmeier, and H. Burtscher, “Design, Calibration, and Field Performance of a Miniature Diffusion Size Classifier,” *Aerosol Science and Technology*, vol. 45, no. 1, pp. 1–10, Jan. 2011. [Online]. Available: http://www.tandfonline.com/doi/abs/10.1080/02786826.2010.516283

[39] S. Clavaguera, M. Pourprix, and Q. Renot, “Device for collecting particles contained in an aerosol, comprising electrometres to determine nanoparticle concentration and particle size,” (EP3328547) Contracting States: AL AT BE BG CH CY CZ DE DK EE ES FI FR GB GR HR HU IE IS IT LI LT LU LV MC MK MT NL NO PL PT RO RS SE SI SK SM TR Patent EP3 328 547 B1 2019-10-23 [EP3 328 547] - EP3 328 547 A1 2018-06-06 [EP3 328 547] - WO2017/017 183 A1 2017-02-02 [WO201 717 183] - US20 180 200 726 A1 2018-07-19 [US20 180 200 726] - FR3 039 434 B1 2018-02-16 [FR3 039 434] - FR3 039 434 A1 2017-02-03 [FR3 039 434] - CN107 921 443 B 2020-03-20 [CN107 921 443B] - CN107 921 443 A 2018-04-17 [CN107 921 443], Feb., 2017, archive Location: 75259081. [Online]. Available: https://permalink.orbit.com/RenderStaticFirstPage?XPN=bCxIhwEsz3fdGqGyRhNS9XfDUqlXTJ5uwQdFuycu4uk%3D%26n%3D1&id=0&base=

[40] S. Clavaguera, A. Guiot, M. Pourprix, and N. Daniel, “Selective aerosol particle collecting method and device, according to particle size,” (EP3328548) Contracting States: AL AT BE BG CH CY CZ DE DK EE ES FI FR GB GR HR HU IE IS IT LI LT LU LV MC MK MT NL NO PL PT RO RS SE SI SK SM TR Patent EP3 328 548 B1 2019-12-18 [EP3 328 548] - EP3 328 548 A1 2018-06-06 [EP3 328 548] - WO2017/017 179 A1 2017-02-02 [WO201 717 179] - US20 180 200 727 A1 2018-07-19 [US20 180 200 727] - FR3 039 435 B1 2017-08-18 [FR3 039 435] - FR3 039 435 A1 2017-02-03 [FR3 039 435] - CN107 921 444 A 2018-04-17 [CN107 921 444], Feb., 2017, archive Location: 75259094. [Online]. Available: https://permalink.orbit.com/RenderStaticFirstPage?XPN=bCxIhwEsz3cbWDK85JFymXfDUqlXTJ5uwQdFuycu4uk%3D%26n%3D1&id=0&base=

[41] R. Lee, J. Caldwell, and G. Morgan, “The evaluation of methods for measuring suspended particulates in air,” *Atmospheric Environment (1967)*, vol. 6, no. 9, pp. 593–622, Sep. 1972. [Online]. Available: https://linkinghub.elsevier.com/retrieve/pii/0004698172900212

[42] J.-B. Renard, C. Thaury, J.-L. Mineau, and B. Gaubicher, “Small-angle light scattering by airborne particulates: Environnement S.A. continuous particulate monitor,” *Measurement Science and Technology*, vol. 21, no. 8, p. 085901, Aug. 2010. [Online]. Available: http://stacks.iop.org/0957-0233/21/i=8/a=085901?key=crossref.053061db356062750c6dda54f18dcb84

[43] J. H. Vincent, *Aerosol Sampling*. Chichester, UK: John Wiley & Sons, Ltd, Mar. 2007. [Online]. Available: http://doi.wiley.com/10.1002/9780470060230

[44] O. Mahdavipour, D. Fahimi, and I. Paprotny, “Microfabricated Air-Microfluidics Virtual Impactor with Groove-Based Envelope-Flow Particle Focusing System,” in *2019 20th International Conference on Solid-State Sensors, Actuators and Microsystems & Eurosensors XXXIII (TRANSDUCERS & EUROSENSORS XXXIII)*. Berlin, Germany: IEEE, Jun. 2019, pp. 805–808. [Online]. Available: https://ieeexplore.ieee.org/document/8808503/

[45] J. Tryner, C. Quinn, B. C. Windom, and J. Volckens, “Design and evaluation of a portable PM $_{2.5}$ monitor featuring a low-cost sensor in line with an active filter sampler,” *Environmental Science: Processes & Impacts*, vol. 21, no. 8, pp. 1403–1415, 2019. [Online]. Available: http://xlink.rsc.org/?DOI=C9EM00234K

[46] S. Wang, X. Xiao, T. Deng, A. Chen, and M. Zhu, “A Sauter mean diameter sensor for fire smoke detection,” *Sensors and Actuators B: Chemical*, vol. 281, pp. 920–932, Feb. 2019. [Online]. Available: https://linkinghub.elsevier.com/retrieve/pii/S0925400518319750

[47] J.-B. Renard, F. Dulac, G. Berthet, T. Lurton, D. Vignelles, F. Jégou, T. Tonnelier, M. Jeannot, B. Couté, R. Akiki, N. Verdier, M. Mallet, F. Gensdarmes, P. Charpentier, S. Mesmin, V. Duverger, J.-C. Dupont, T. Elias, V. Crenn, J. Sciare, P. Zieger, M. Salter, T. Roberts, J. Giacomoni, M. Gobbi, E. Hamonou, H. Olafsson, P. Dagsson-Waldhauserova, C. Camy-Peyret, C. Mazel, T. Décamps, M. Piringer, J. Surcin, and D. Daugeron, “LOAC: a small aerosol optical counter/sizer for ground-based and balloon measurements of the size distribution and nature of atmospheric particles – Part 1: Principle of measurements and instrument evaluation,” *Atmospheric Measurement Techniques*, vol. 9, no. 4, pp. 1721–1742, Apr. 2016. [Online]. Available: https://www.atmos-meas-tech.net/9/1721/2016/

[48] Wenjia Shao, Hongjian Zhang, and Hongliang Zhou, “Fine Particle Sensor Based on Multi-Angle Light Scattering and Data Fusion,” *Sensors*, vol. 17, no. 5, p. 1033, May 2017. [Online]. Available: http://www.mdpi.com/1424-8220/17/5/1033

[49] G. W. Mulholland and M. Y. Choi, “Measurement of the mass specific extinction coefficient for acetylene and ethene smoke using the large agglomerate optics facility,” *Symposium (International) on Combustion*, vol. 27, no. 1, pp. 1515–1522, Jan. 1998. [Online]. Available: https://linkinghub.elsevier.com/retrieve/pii/S0082078498805596

[50] G. Kullenberg, “Scattering of light by Sargasso Sea water,” *Deep Sea Research and Oceanographic Abstracts*, vol. 15, no. 4, pp. 423–432, Aug. 1968. [Online]. Available: https://linkinghub.elsevier.com/retrieve/pii/0011747168900508

[51] M. Bartholdi, G. C. Salzman, R. D. Hiebert, and M. Kerker, “Differential light scattering photometer for rapid analysis of single particles in flow,” *Applied Optics*, vol. 19, no. 10, p. 1573, May 1980. [Online]. Available: https://www.osapublishing.org/abstract.cfm?URI=ao-19-10-1573

[52] Y. Agrawal and H. Pottsmith, “Instruments for particle size and settling velocity observations in sediment transport,” *Marine Geology*, vol. 168, no. 1-4, pp. 89–114, Aug. 2000. [Online]. Available: https://linkinghub.elsevier.com/retrieve/pii/S002532270000044X

[53] M. Heim, B. J. Mullins, H. Umhauer, and G. Kasper, “Performance evaluation of three optical particle counters with an efficient “multimodal” calibration method,” *Journal of Aerosol Science*, vol. 39, no. 12, pp. 1019–1031, Dec. 2008. [Online]. Available: https://linkinghub.elsevier.com/retrieve/pii/S0021850208001365

[54] Y.-L. Pan, A. Kalume, C. Wang, and J. L. Santarpia, "Opto-aerodynamic focusing of aerosol particles," *Aerosol Science and Technology*, vol. 52, no. 1, pp. 13–18, Jan. 2018. [Online]. Available: https://www.tandfonline.com/doi/full/10.1080/02786826.2017.1367090

[55] T. Njalsson and I. Novosselov, "Design and optimization of a compact low-cost optical particle sizer," *Journal of Aerosol Science*, vol. 119, pp. 1–12, May 2018. [Online]. Available: https://linkinghub.elsevier.com/retrieve/pii/S0021850217302331

[56] F. C. Cheong, B. S. Rémi Dreyfus, J. Amato-Grill, K. Xiao, L. Dixon, and D. G. Grier, "Flow visualization and flow cytometry with holographic video microscopy," *Optics Express*, vol. 17, no. 15, p. 13071, Jul. 2009. [Online]. Available: https://www.osapublishing.org/abstract.cfm?URI=oe-17-15-13071

[57] G. Brunnhofer, A. Bergmann, A. Klug, and M. Kraft, "Design and Validation of a Holographic Particle Counter," *Sensors*, vol. 19, no. 22, p. 4899, Nov. 2019. [Online]. Available: https://www.mdpi.com/1424-8220/19/22/4899

[58] Y.-C. Wu, A. Shiledar, Y.-C. Li, J. Wong, S. Feng, X. Chen, C. Chen, K. Jin, S. Janamian, Z. Yang, Z. S. Ballard, Z. Göröcs, A. Feizi, and A. Ozcan, "Air quality monitoring using mobile microscopy and machine learning," *Light: Science & Applications*, vol. 6, no. 9, pp. e17 046–e17 046, Sep. 2017. [Online]. Available: http://www.nature.com/articles/lsa201746

[59] M. Mader, J. Reichel, T. W. Hänsch, and D. Hunger, "A scanning cavity microscope," *Nature Communications*, vol. 6, no. 1, p. 7249, Nov. 2015. [Online]. Available: http://www.nature.com/articles/ncomms8249

[60] T. D. Gordon, N. L. Wagner, M. S. Richardson, D. C. Law, D. Wolfe, E. W. Eloranta, C. A. Brock, F. Erdesz, and D. M. Murphy, "Design of a Novel Open-Path Aerosol Extinction Cavity Ringdown Spectrometer," *Aerosol Science and Technology*, vol. 49, no. 9, pp. 717–726, Sep. 2015. [Online]. Available: http://www.tandfonline.com/doi/full/10.1080/02786826.2015.1066753

[61] F. Kalantarifard, P. Elahi, G. Makey, O. M. Maragò, F. O. Ilday, and G. Volpe, "Intracavity optical trapping of microscopic particles in a ring-cavity fiber laser," *Nature Communications*, vol. 10, no. 1, p. 2683, Dec. 2019. [Online]. Available: http://www.nature.com/articles/s41467-019-10662-7

[62] Z. Gong, Y.-L. Pan, G. Videen, and C. Wang, "Optical trapping and manipulation of single particles in air: Principles, technical details, and applications," *Journal of Quantitative Spectroscopy and Radiative Transfer*, vol. 214, pp. 94–119, Jul. 2018. [Online]. Available: https://linkinghub.elsevier.com/retrieve/pii/S002240731830044X

[63] X. Xu, C. Cheng, Y. Zhang, H. Lei, and B. Li, "Dual focused coherent beams for three-dimensional optical trapping and continuous rotation of metallic nanostructures," *Scientific Reports*, vol. 6, no. 1, p. 29449, Sep. 2016. [Online]. Available: http://www.nature.com/articles/srep29449

[64] K. J. Vahala, "Optical microcavities," *Nature*, vol. 424, no. 6950, pp. 839–846, Aug. 2003. [Online]. Available: http://www.nature.com/articles/nature01939

[65] A. A. P. Trichet, P. R. Dolan, D. James, G. M. Hughes, C. Vallance, and J. M. Smith, "Nanoparticle Trapping and Characterization Using Open Microcavities," *Nano Letters*, vol. 16, no. 10, pp. 6172–6177, Oct. 2016. [Online]. Available: https://pubs.acs.org/doi/10.1021/acs.nanolett.6b02433

[66] Q. Quan, D. L. Floyd, I. B. Burgess, P. B. Deotare, I. W. Frank, S. K. Y. Tang, R. Ilic, and M. Loncar, "Single particle detection in CMOS compatible photonic crystal nanobeam cavities," *Optics Express*, vol. 21, no. 26, p. 32225, Dec. 2013. [Online]. Available: https://www.osapublishing.org/oe/abstract.cfm?uri=oe-21-26-32225

[67] K. Saurav and N. Le Thomas, "Probing the fundamental detection limit of photonic crystal cavities," *Optica*, vol. 4, no. 7, p. 757, Jul. 2017. [Online]. Available: https://www.osapublishing.org/abstract.cfm?URI=optica-4-7-757

[68] D. Choudhary, A. Mossa, M. Jadhav, and C. Cecconi, "Bio-Molecular Applications of Recent Developments in Optical Tweezers," *Biomolecules*, vol. 9, no. 1, p. 23, Jan. 2019. [Online]. Available: http://www.mdpi.com/2218-273X/9/1/23

[69] M. Tardif, J.-B. Jager, P. R. Marcoux, K. Uchiyamada, E. Picard, E. Hadji, and D. Peyrade, "Single-cell bacterium identification with a SOI optical microcavity," *Applied Physics Letters*, vol. 109, no. 13, p. 133510, Sep. 2016. [Online]. Available: http://aip.scitation.org/doi/10.1063/1.4963070

[70] E. Sage, M. Sansa, S. Fostner, M. Defoort, M. Gély, A. K. Naik, R. Morel, L. Duraffourg, M. L. Roukes, T. Alava, G. Jourdan, E. Colinet, C. Masselon, A. Brenac, and S. Hentz, "Single-particle mass spectrometry with arrays of frequency-addressed nanomechanical resonators," *Nature Communications*, vol. 9, no. 1, p. 3283, Dec. 2018. [Online]. Available: http://www.nature.com/articles/s41467-018-05783-4

[71] D. Weinert, T. Cleary, G. Mulholland, and P. Beever, "Light Scattering Characteristics And Size Distribution Of Smoke And Nuisance Aerosols," *Fire Safety Science*, vol. 7, pp. 209–220, 2003. [Online]. Available: http://www.iafss.org/publications/fss/7/209

[72] H. Volten, O. Muñoz, E. Rol, H. De, W. Vassen, J. Hovenier, K. Muinonen, and T. Nousiainen, "Scattering matrices of mineral aerosol particles at 441.6 nm and 632.8 nm," *Journal of Geophysical Research Atmospheres*, vol. 106, no. D15, pp. 17 375–17 401, 2001.

[73] L. Rayleigh, "On the electromagnetic theory of light," *The London, Edinburgh, and Dublin Philosophical Magazine and Journal of Science*, vol. 12, no. 73, pp. 81–101, Aug. 1881. [Online]. Available: https://www.tandfonline.com/doi/full/10.1080/14786448108627074

[74] Y. Grynko and Y. G. Shkuratov, "Light scattering from particulate surfaces in geometrical optics approximation," in *Light Scattering Reviews 3*, A. A. Kokhanovsky, Ed. Berlin, Heidelberg: Springer Berlin Heidelberg, 2008, pp. 329–382. [Online]. Available: http://link.springer.com/10.1007/978-3-540-48546-9_9

[75] J.-M. Jin, *The finite element method in electromagnetics*, third edition ed. Hoboken. New Jersey: John Wiley & Sons Inc, 2014.

[76] A. Taflove, "Review of the formulation and applications of the finite-difference time-domain method for numerical modeling of electromagnetic wave interactions with arbitrary structures," *Wave Motion*, vol. 10, no. 6, pp. 547–582, Dec. 1988. [Online]. Available: https://linkinghub.elsevier.com/retrieve/pii/0165212588900121

[77] P. Yang and K. N. Liou, “Finite-difference time domain method for light scattering by small ice crystals in three-dimensional space,” *Journal of the Optical Society of America A*, vol. 13, no. 10, p. 2072, Oct. 1996. [Online]. Available: https://www.osapublishing.org/abstract.cfm?URI=josaa-13-10-2072

[78] S. Rao, D. Wilton, and A. Glisson, “Electromagnetic scattering by surfaces of arbitrary shape,” *IEEE Transactions on Antennas and Propagation*, vol. 30, no. 3, pp. 409–418, May 1982. [Online]. Available: http://ieeexplore.ieee.org/document/1142818/

[79] F. J. García de Abajo and A. Howie, “Retarded field calculation of electron energy loss in inhomogeneous dielectrics,” *Physical Review B*, vol. 65, no. 11, p. 115418, Mar. 2002. [Online]. Available: https://link.aps.org/doi/10.1103/PhysRevB.65.115418

[80] F. Frezza, F. Mangini, and N. Tedeschi, “Introduction to electromagnetic scattering: tutorial,” *Journal of the Optical Society of America A*, vol. 35, no. 1, p. 163, Jan. 2018. [Online]. Available: https://www.osapublishing.org/abstract.cfm?URI=josaa-35-1-163

[81] M. Born and E. Wolf, *Principles of optics: electromagnetic theory of propagation, interference and diffraction of light*, 7th ed. Cambridge ; New York: Cambridge University Press, 1999.

[82] C. F. Bohren and D. R. Huffman, *Absorption and scattering of light by small particles*. Wiley, 1983.

[83] H. C. v. d. Hulst, *Light Scattering by Small Particles*. Dover Publications, 1981.

[84] N. Sultanova, S. Kasarova, and I. Nikolov, “Dispersion Properties of Optical Polymers,” *Acta Physica Polonica A*, vol. 116, no. 4, pp. 585–587, Oct. 2009. [Online]. Available: http://przyrbwn.icm.edu.pl/APP/PDF/116/a116z442.pdf

[85] M. J. Pilat and D. S. Ensor, “Plume opacity and particulate mass concentration,” *Atmospheric Environment (1967)*, vol. 4, no. 2, pp. 163–173, Mar. 1970. [Online]. Available: https://linkinghub.elsevier.com/retrieve/pii/0004698170900065

[86] D. B. Curtis, M. Aycibin, M. A. Young, V. H. Grassian, and P. D. Kleiber, “Simultaneous measurement of light-scattering properties and particle size distribution for aerosols: Application to ammonium sulfate and quartz aerosol particles,” *Atmospheric Environment*, vol. 41, no. 22, pp. 4748–4758, Jul. 2007. [Online]. Available: http://www.sciencedirect.com/science/article/pii/S1352231007002701

[87] M. I. Mishchenko and L. D. Travis, “Electromagnetic Scattering by Nonspherical Particles,” in *Exploring the Atmosphere by Remote Sensing Techniques*, R. Guzzi, Ed. Berlin, Heidelberg: Springer Berlin Heidelberg, 2003, vol. 607, pp. 77–127, series Title: Lecture Notes in Physics. [Online]. Available: http://link.springer.com/10.1007/3-540-36536-2_4

[88] G. Gouesbet and G. Gréhan, *Generalized Lorenz-Mie theories*. Berlin Heidelberg: Springer, 2011, oCLC: 712460566.

[89] S. Asano and G. Yamamoto, “Light Scattering by a Spheroidal Particle,” *Applied Optics*, vol. 14, no. 1, pp. 29–49, Jan. 1975. [Online]. Available: https://www.osapublishing.org/abstract.cfm?uri=ao-14-1-29

[90] K. A. Fuller, “Scattering and absorption cross sections of compounded spheres II Calculations for external aggregation,” *Journal of the Optical Society of America A*, vol. 12, no. 5, p. 881, May 1995. [Online]. Available: https://www.osapublishing.org/abstract.cfm?URI=josaa-12-5-881

[91] K. Sertel and J. Volakis, “Multilevel fast multipole method solution of volume integral equations using parametric geometry modeling,” in *IEEE Antennas and Propagation Society International Symposium. 2001 Digest. Held in conjunction with: USNC/URSI National Radio Science Meeting (Cat. No.01CH37229)*, vol. 3. Boston, MA, USA: IEEE, 2001, pp. 786–789. [Online]. Available: http://ieeexplore.ieee.org/document/960215/

[92] M. Fall, S. Boutami, A. Glière, B. Stout, and J. Hazart, “Multilevel fast multipole method based on a potential formulation for 3D electromagnetic scattering problems,” *Journal of the Optical Society of America A*, vol. 30, no. 6, p. 1273, Jun. 2013. [Online]. Available: https://www.osapublishing.org/abstract.cfm?URI=josaa-30-6-1273

[93] P. Waterman, “Matrix formulation of electromagnetic scattering,” *Proceedings of the IEEE*, vol. 53, no. 8, pp. 805–812, 1965. [Online]. Available: http://ieeexplore.ieee.org/document/1445988/

[94] M. I. Mishchenko, L. D. Travis, and D. W. Mackowski, “T-matrix computations of light scattering by nonspherical particles: A review,” *Journal of Quantitative Spectroscopy and Radiative Transfer*, vol. 55, no. 5, pp. 535–575, May 1996. [Online]. Available: http://www.sciencedirect.com/science/article/pii/0022407396000027

[95] M. I. Mishchenko, L. D. Travis, and A. A. Lacis, *Scattering, absorption, and emission of light by small particles*. Cambridge ; New York: Cambridge University Press, 2002, oCLC: ocm48932103.

[96] R. Tazaki, H. Tanaka, S. Okuzumi, A. Kataoka, and H. Nomura, “Light Scattering by Fractal Dust Aggregates. I. Angular Dependence of Scattering,” *The Astrophysical Journal*, vol. 823, no. 2, p. 70, 2016. [Online]. Available: http://stacks.iop.org/0004-637X/823/i=2/a=70

[97] R. Botet, P. Rannou, and M. Cabane, “Mean-field approximation of Mie scattering by fractal aggregates of identical spheres,” *Applied Optics*, vol. 36, no. 33, pp. 8791–8797, Nov. 1997. [Online]. Available: https://www.osapublishing.org/abstract.cfm?uri=ao-36-33-8791

[98] C. M. Sorensen, “Light Scattering by Fractal Aggregates: A Review,” *Aerosol Science and Technology*, vol. 35, no. 2, pp. 648–687, Jan. 2001. [Online]. Available: http://www.tandfonline.com/doi/abs/10.1080/02786820117868

[99] P. H. McMurry, M. F. Shepherd, J. S. Vickery, and NARSTO, Eds., *Particulate matter science for policy makers: a NARSTO assessment*. Cambridge: Cambridge University Press, 2004, oCLC: ocm56643495.

[100] B. C. Singer and W. W. Delp, “Response of consumer and research grade indoor air quality monitors to residential sources of fine particles,” *Indoor Air*, vol. 28, no. 4, pp. 624–639, Jul. 2018. [Online]. Available: http://doi.wiley.com/10.1111/ina.12463

[101] M. Kaliszewski, M. Włodarski, J. Młyńczak, and K. Kopczyński, “Comparison of Low-Cost Particulate Matter Sensors for Indoor Air Monitoring during COVID-19 Lockdown,” *Sensors*, p. 17, 2020.

[102] M. Budde, R. El Masri, T. Riedel, and M. Beigl, "Enabling low-cost particulate matter measurement for participatory sensing scenarios," in *Proceedings of the 12th International Conference on Mobile and Ubiquitous Multimedia - MUM '13*. Luleå, Sweden: ACM Press, 2013, pp. 1–10. [Online]. Available: http://dl.acm.org/citation.cfm?doid=2541831.2541859

[103] R. Jayaratne, X. Liu, P. Thai, M. Dunbabin, and L. Morawska, "The influence of humidity on the performance of a low-cost air particle mass sensor and the effect of atmospheric fog," *Atmospheric Measurement Techniques*, vol. 11, no. 8, pp. 4883–4890, Aug. 2018. [Online]. Available: https://www.atmos-meas-tech.net/11/4883/2018/

[104] G. Snider, C. L. Weagle, R. V. Martin, A. van Donkelaar, K. Conrad, D. Cunningham, C. Gordon, M. Zwicker, C. Akoshile, P. Artaxo, N. X. Anh, J. Brook, J. Dong, R. M. Garland, R. Greenwald, D. Griffith, K. He, B. N. Holben, R. Kahn, I. Koren, N. Lagrosas, P. Lestari, Z. Ma, J. Vanderlei Martins, E. J. Quel, Y. Rudich, A. Salam, S. N. Tripathi, C. Yu, Q. Zhang, Y. Zhang, M. Brauer, A. Cohen, M. D. Gibson, and Y. Liu, "SPARTAN: a global network to evaluate and enhance satellite-based estimates of ground-level particulate matter for global health applications," *Atmospheric Measurement Techniques*, vol. 8, no. 1, pp. 505–521, Jan. 2015. [Online]. Available: https://www.atmos-meas-tech.net/8/505/2015/

[105] E. A. Wendt, C. W. Quinn, D. D. Miller-Lionberg, J. Tryner, C. L&apos;Orange, B. Ford, A. P. Yalin, J. R. Pierce, S. Jathar, and J. Volckens, "A low-cost monitor for simultaneous measurement of fine particulate matter and aerosol optical depth &#8211; Part 1: Specifications and testing," *Atmospheric Measurement Techniques*, vol. 12, no. 10, pp. 5431–5441, Oct. 2019. [Online]. Available: https://www.atmos-meas-tech.net/12/5431/2019/

[106] T. N. T. Nguyen, V. H. Luu, V. H. Pham, Q. H. Bui, and T. K. O. Nguyen, "Particulate Matter Concentration Mapping from Satellite Imagery," in *TORUS 3 – Toward an Open Resource Using Services*, 1st ed., D. Laffly, Ed. Wiley, Apr. 2020, pp. 103–130. [Online]. Available: https://onlinelibrary.wiley.com/doi/abs/10.1002/9781119720522.ch5

[107] H. Liu, Q. Li, T. Shi, S. Hu, G. Wu, and Q. Zhou, "Application of Sentinel 2 MSI Images to Retrieve Suspended Particulate Matter Concentrations in Poyang Lake," *Remote Sensing*, vol. 9, no. 7, p. 761, Jul. 2017. [Online]. Available: http://www.mdpi.com/2072-4292/9/7/761

[108] A. van Donkelaar, R. V. Martin, M. Brauer, N. C. Hsu, R. A. Kahn, R. C. Levy, A. Lyapustin, A. M. Sayer, and D. M. Winker, "Global Estimates of Fine Particulate Matter using a Combined Geophysical-Statistical Method with Information from Satellites, Models, and Monitors," *Environmental Science & Technology*, vol. 50, no. 7, pp. 3762–3772, Apr. 2016. [Online]. Available: https://pubs.acs.org/doi/10.1021/acs.est.5b05833

[109] E. G. Snyder, T. H. Watkins, P. A. Solomon, E. D. Thoma, R. W. Williams, G. S. W. Hagler, D. Shelow, D. A. Hindin, V. J. Kilaru, and P. W. Preuss, "The Changing Paradigm of Air Pollution Monitoring," *Environmental Science & Technology*, vol. 47, no. 20, pp. 11 369–11 377, Oct. 2013. [Online]. Available: https://pubs.acs.org/doi/10.1021/es4022602

[110] Francesca Borghi, Andrea Spinazzè, Sabrina Rovelli, Davide Campagnolo, Luca Del Buono, Andrea Cattaneo, and Domenico Cavallo, "Miniaturized Monitors for Assessment of Exposure to Air Pollutants: A Review," *International Journal of Environmental Research and Public Health*, vol. 14, no. 8, p. 909, Aug. 2017. [Online]. Available: http://www.mdpi.com/1660-4601/14/8/909

[111] J. Li, "Recent advances in low-cost particulate matter sensor: calibration and application," Engineering and Applied Science Theses & Dissertations. 450., Washington University in St. Louis, May 2019. [Online]. Available: https://openscholarship.wustl.edu/eng_etds/450

[112] J. Li, S. K. Mattewal, S. Patel, and P. Biswas, "Evaluation of Nine Low-cost-sensor-based Particulate Matter Monitors," *Aerosol and Air Quality Research*, vol. 20, no. 2, pp. 254–270, 2020. [Online]. Available: http://www.aaqr.org/doi/10.4209/aaqr.2018.12.0485

[113] K. Kelly, J. Whitaker, A. Petty, C. Widmer, A. Dybwad, D. Sleeth, R. Martin, and A. Butterfield, "Ambient and laboratory evaluation of a low-cost particulate matter sensor," *Environmental Pollution*, vol. 221, pp. 491–500, Feb. 2017. [Online]. Available: https://linkinghub.elsevier.com/retrieve/pii/S026974911632718X

[114] H. Hojaiji, O. Goldstein, C. E. King, M. Sarrafzadeh, and M. Jerrett, "Design and calibration of a wearable and wireless research grade air quality monitoring system for real-time data collection," in *2017 IEEE Global Humanitarian Technology Conference (GHTC)*. San Jose, CA: IEEE, Oct. 2017, pp. 1–10. [Online]. Available: http://ieeexplore.ieee.org/document/8239308/

[115] O. Z. Olszewski, J. Kubik, and R. Houlihan, "Mems Micro-Pump for Air Sampling Application," in *2019 20th International Conference on Solid-State Sensors, Actuators and Microsystems & Eurosensors XXXIII (TRANSDUCERS & EUROSENSORS XXXIII)*. Berlin, Germany: IEEE, Jun. 2019, pp. 2017–2020. [Online]. Available: https://ieeexplore.ieee.org/document/8808627/

[116] W. Bogaerts and L. Chrostowski, "Silicon Photonics Circuit Design: Methods, Tools and Challenges," *Laser & Photonics Reviews*, vol. 12, no. 4, p. 1700237, Apr. 2018. [Online]. Available: http://doi.wiley.com/10.1002/lpor.201700237

[117] X. Li, E. Iervolino, F. Santagata, J. Wei, C. A. Yuan, P. Sarro, and G. Zhang, "Miniaturized particulate matter sensor for portable air quality monitoring devices," in *IEEE SENSORS 2014 Proceedings*. Valencia, Spain: IEEE, Nov. 2014, pp. 2151–2154. [Online]. Available: http://ieeexplore.ieee.org/lpdocs/epic03/wrapper.htm?arnumber=6985464

[118] M. Dong, E. Iervolino, F. Santagata, G. Zhang, and G. Zhang, "Silicon microfabrication based particulate matter sensor," *Sensors and Actuators A: Physical*, vol. 247, pp. 115–124, Aug. 2016. [Online]. Available: https://linkinghub.elsevier.com/retrieve/pii/S092442471630262X

[119] Y. Qiao, J. Tao, Y. Zhang, J. Qiu, X. Hong, J. Wu, and C.-H. Chen, "Sub-Micro Particle Matter Detection for Metal 3-D Printing Workshop," *IEEE Sensors Journal*, vol. 19, no. 13, pp. 4932–4939, Jul. 2019. [Online]. Available: https://ieeexplore.ieee.org/document/8654595/

[120] S. Boutami, G. Jobert, P. Barritault, J.-G. Coutard, M. Fournier, J.-M. Fédéli, P. Labeye, A. Marchant, J. Skubich, A. Teulle, O. Lartigue, E. Lorent, A. Glière, C. Constancias, S. Nicoletti, C. Jamois, C. Seassal, and L. Duraffourg, "Visible to mid-infrared integrated sensors for air quality measurement," in *Optical Sensing, Imaging, and Photon Counting: From X-Rays to THz 2019*, O. Mitrofanov, Ed. San Diego, United States: SPIE, Sep. 2019, p. 25. [Online]. Available: https://www.spiedigitallibrary.org/conference-proceedings-of-spie/11088/2529262/Visible-to-mid-infrared-integrated-sensors-for-air-quality-measurement/10.1117/12.2529262.full

[121] P. Barritault, M. Brun, O. Lartigue, J. Willemin, J.-L. Ouvrier-Buffet, S. Pocas, and S. Nicoletti, "Low power CO2 NDIR sensing using a micro-bolometer detector and a micro-hotplate IR-source," *Sensors and Actuators B: Chemical*, vol. 182, pp. 565–570, Jun. 2013. [Online]. Available: https://linkinghub.elsevier.com/retrieve/pii/S0925400513003298

[122] A. Glière, P. Barritault, A. Berthelot, C. Constancias, J.-G. Coutard, B. Desloges, L. Duraffourg, J.-M. Fedeli, M. Garcia, O. Lartigue, H. Lhermet, A. Marchant, J. Rouxel, J. Skubich, A. Teulle, T. Verdot, and S. Nicoletti, "Downsizing and Silicon Integration of Photoacoustic Gas Cells," *International Journal of Thermophysics*, vol. 41, no. 2, p. 16, Feb. 2020. [Online]. Available: http://link.springer.com/10.1007/s10765-019-2580-7

[123] S. Nicoletti, "Particle detector and method for manufacturing such a detector," (EP2596329) Contracting States: AL AT BE BG CH CY CZ DE DK EE ES FI FR GB GR HR HU IE IS IT LI LT LU LV MC MK MT NL NO PL PT RO RS SE SI SK SM TR Patent EP2 596 329 B1 2019-03-06 [EP2 596 329] - EP2 596 329 A1 2013-05-29 [EP2 596 329] - WO2012/011 052 A1 2012-01-26 [WO201 211 052] - US8 867 035 B2 2014-10-21 [US8 867 035] - US20 130 120 749 A1 2013-05-16 [US20 130 120 749] - US9 518 909 B2 2016-12-13 [US9 518 909] - US20 150 116 710 A1 2015-04-30 [US20 150 116 710] - FR2 963 101 B1 2013-02-15 [FR2 963 101] - FR2 963 101 A1 2012-01-27 [FR2 963 101], Jan., 2012. [Online]. Available: https://permalink.orbit.com/RenderStaticFirstPage?XPN=B5lJYIF%252BxRQ1zTc2PWcWRHfDUqlXTJ5uwQdFuycu4uk%3D%26n%3D1&id=0&base=

[124] S. Boutami and S. Nicoletti, "Optical detector of particles," (EP3574301) Contracting States: AL AT BE BG CH CY CZ DE DK EE ES FI FR GB GR HR HU IE IS IT LI LT LU LV MC MK MT NL NO PL PT RO RS SE SI SK SM TR - Extension States: BA ME Patent EP3 574 301 A1 2019-12-04 [EP3 574 301] - WO2018/138 223 A1 2018-08-02 [WO2 018 138 223] - FR3 062 209 A1 2018-07-27 [FR3 062 209] - KR10-2019-0 112 049A 2019-10-02 [KR20 190 112 049], Jul., 2018. [Online]. Available: https://permalink.orbit.com/RenderStaticFirstPage?XPN=MV%252BDvbBf%252F0Euw56Xk6cpNXfDUqlXTJ5uwQdFuycu4uk%3D%26n%3D1&id=0&base=

[125] S. Boutami, M. Dupoy, and J. Fedeli, "Optical particle detector," (EP3583402) Contracting States: AL AT BE BG CH CY CZ DE DK EE ES FI FR GB GR HR HU IE IS IT LI LT LU LV MC MK MT NL NO PL PT RO RS SE SI SK SM TR - Extension States: BA ME Patent EP3 583 402 A1 2019-12-25 [EP3 583 402] - WO2018/150 044 A1 2018-08-23 [WO2 018 150 044] - US20 200 049 617 A1 2020-02-13 [US20 200 049 617] - FR3 063 147 A1 2018-08-24 [FR3 063 147] - JP2 020 508 449 A 2020-03-19 [JP2 020 508 449] - KR10-2019-0 119 630A 2019-10-22 [KR20 190 119 630], Aug., 2018, archive Location: 80997650. [Online]. Available: https://permalink.orbit.com/RenderStaticFirstPage?XPN=GsdFZErKG%252BWseLHW8WjXjnfDUqlXTJ5uwQdFuycu4uk%3D%26n%3D1&id=0&base=

[126] G. Jobert, "Optical particle detector," (EP3598102) Contracting States: AL AT BE BG CH CY CZ DE DK EE ES FI FR GB GR HR HU IE IS IT LI LT LU LV MC MK MT NL NO PL PT RO RS SE SI SK SM TR - Extension States: BA ME Patent EP3 598 102 A1 2020-01-22 [EP3 598 102] - US20 200 033 246 A1 2020-01-30 [US20 200 033 246] - FR3 083 864 A1 2020-01-17 [FR3 083 864], Jan., 2020. [Online]. Available: https://permalink.orbit.com/RenderStaticFirstPage?XPN=oQ9aRAtEpMKseLHW8WjXjnfDUqlXTJ5uwQdFuycu4uk%3D%26n%3D1&id=0&base=

[127] G. Jobert, S. Boutami, M. Fournier, and C. Seassal, "Optical particle detector," (WO2020128105) National States: AE AG AL AM AO AT AU AZ BA BB BG BH BN BR BW BY BZ CA CH CL CN CO CR CU CZ DE DJ DK DM DO DZ EC EE EG ES FI GB GD GE GH GM GT HN HR HU ID IL IN IR IS JO JP KE KG KH KN KP KR KW KZ LA LC LK LR LS LU LY MA MD ME MG MK MN MW MX MY MZ NA NG NI NO NZ OM PA PE PG PH PL PT QA RO RS RU RW SA SC SD SE SG SK SL SM ST SV SY TH TJ TM TN TR TT TZ UA UG US UZ VC VN ZA ZM ZW - ARIPO: BW GH GM KE LR LS MW MZ NA RW SD SL SZ TZ UG ZM ZW - EAPO: AM AZ BY KG KZ RU TJ TM - EPO: AL AT BE BG CH CY CZ DE DK EE ES FI FR GB GR HR HU IE IS IT LT LU LV MC MK MT NL NO PL PT RO RS SE SI SK SM TR - OAPI: BF BJ CF CG CI CM GA GN GQ GW KM ML MR NE SN ST TD TG Patent WO2020/128 105 A1 2020-06-25 [WO2 020 128 105] - FR3 090 873 A1 2020-06-26 [FR3 090 873], Dec., 2018, archive Location: 89419298. [Online]. Available: https://permalink.orbit.com/RenderStaticFirstPage?XPN=clztOvdlzxYFvBFOc8lv2rmsLuw%252FR4oY%252BQgpgFzVRnM%3D%26n%3D1&id=0&base=

[128] G. Jobert, "Optical particle sensor," (EP3671179) Contracting States: AL AT BE BG CH CY CZ DE DK EE ES FI FR GB GR HR HU IE IS IT LI LT LU LV MC MK MT NL NO PL PT RO RS SE SI SK SM TR - Extension States: BA ME Patent EP3 671 179 A1 2020-06-24 [EP3 671 179] - FR3 090 874 A1 2020-06-26 [FR3 090 874], Dec., 2018, archive Location: 89415403. [Online]. Available: https://permalink.orbit.com/RenderStaticFirstPage?XPN=uy29K%252BhUFCE1zTc2PWcWRHfDUqlXTJ5uwQdFuycu4uk%3D%26n%3D1&id=0&base=

[129] G. Jobert, P. Barritault, and M. Fournier, "Detecteur multi-particules," France Patent B04 110 FR-DD19 480 HB, Oct., 2019.

[130] S. Boutami, M. Fournier, G. Jobert, C. Jamois, and C. Seassal, "Capteur PM optique petites particules," France Patent DD20 275 HB, 2020.

[131] G. Jobert, P. Barritault, M. Fournier, S. Boutami, D. Jobert, A. Marchant, J. Michelot, P. Monsinjon, P. Lienhard, and S. Nicoletti, "Miniature particulate matter counter and analyzer based on lens-free imaging of light scattering signatures with a holed image sensor," *Sensors and Actuators Reports*, p. 100010, May 2020. [Online]. Available: https://linkinghub.elsevier.com/retrieve/pii/S2666053920300072

[132] M. Fournier, P. Barritault, G. Jobert, A. Marchant, S. Boutami, J. Michelot, P. Lienhard, S. Nicoletti, and L. Duraffourg, "A miniaturized optical sensor for particulate matter detection," in *Photonic Instrumentation Engineering VII*, Y. Soskind and L. E. Busse, Eds. San Francisco, United States: SPIE, Mar. 2020, p. 43. [Online]. Available: https://www.spiedigitallibrary.org/conference-proceedings-of-spie/11287/2546128/A-miniaturized-optical-sensor-for-particulate-matter-detection/10.1117/12.2546128.full

[133] J. Michelot, P. Monsinjon, J. Caranana, A. Menard, M. Dubois, A. Lesire, C. Bouvier, S. Cohet, and S. Caranhac, “Creapyx: An Innovative Pixel Evaluation Platform,” Toulouse, France, Nov. 2015. [Online]. Available: http://www.pyxalis.com/pyxalis-wp/wp-download/publications/2015_PYXALIS_CNES_CREAPYX.pdf

[134] B. Dupont, J. Caranana, P. Pinoncely, J. Michelot, C. Bouvier, S. Cohet, P. Jourdain, and P. Monsinjon, “A dual-core highly programmable 120dB image sensor,” *Electronic Imaging*, vol. 2016, no. 12, pp. 1–3, Feb. 2016. [Online]. Available: http://www.ingentaconnect.com/content/10.2352/ISSN.2470-1173.2016.12.IMSE-261

[135] E. Herth, M. Baranski, D. Berlharet, S. Edmond, D. Bouville, L. E. Calvet, and C. Gorecki, “Fast ultra-deep silicon cavities: Toward isotropically etched spherical silicon molds using an ICP-DRIE,” *Journal of Vacuum Science & Technology B*, vol. 37, no. 2, p. 021206, Mar. 2019. [Online]. Available: http://avs.scitation.org/doi/10.1116/1.5081503

[136] P. B. Catrysse, X. Liu, and A. El Gamal, “QE reduction due to pixel vignetting in CMOS image sensors,” in *Proc. SPIE*, vol. 3965, 2000, pp. 420–430.

[137] R. Jaenicke, “The optical particle counter: Cross-sensitivity and coincidence,” *Journal of Aerosol Science*, vol. 3, no. 2, pp. 95–111, Mar. 1972. [Online]. Available: https://linkinghub.elsevier.com/retrieve/pii/0021850272901474

[138] G. Jobert, M. Fournier, P. Barritault, S. Boutami, J. Auger, A. Maillard, J. Michelot, P. Lienhard, S. Nicoletti, and L. Duraffourg, “A Miniaturized Optical Sensor for Fire Smoke Detection,” in *2019 20th International Conference on Solid-State Sensors, Actuators and Microsystems & Eurosensors XXXIII (TRANSDUCERS & EUROSENSORS XXXIII)*. Berlin, Germany: IEEE, Jun. 2019, pp. 1144–1149. [Online]. Available: https://ieeexplore.ieee.org/document/8808611/

[139] J. Pribošek and G. Röhrer, “Estimation of the Particle Sizing Error Due to Particle Position in an Integrated PM2.5 Optical Particle Counter,” *Proceedings*, vol. 2, no. 13, p. 850, Dec. 2018. [Online]. Available: http://www.mdpi.com/2504-3900/2/13/850

[140] S. H. Jones, M. D. King, and A. D. Ward, “Determining the unique refractive index properties of solid polystyrene aerosol using broadband Mie scattering from optically trapped beads,” *Physical Chemistry Chemical Physics*, vol. 15, no. 47, p. 20735, 2013. [Online]. Available: http://xlink.rsc.org/?DOI=c3cp53498g

[141] A. Yevick, M. Hannel, and D. G. Grier, “Machine-learning approach to holographic particle characterization,” *Optics Express*, vol. 22, no. 22, p. 26884, Nov. 2014. [Online]. Available: https://www.osapublishing.org/oe/abstract.cfm?uri=oe-22-22-26884

[142] R. H. Zerull, R. H. Giese, and K. Weiss, “Scattering Measurements Of Irregular Particles Vs. MIE-Theory,” R. M. A. Azzam and D. Coffeen, Eds., San Diego, Oct. 1977, pp. 191–199. [Online]. Available: http://proceedings.spiedigitallibrary.org/proceeding.aspx?articleid=1226620

[143] B. Mills, J. Grant-Jacob, S. Jain, Y. Xie, B. MacKay, M. McDonnell, M. Praeger, M. Loxham, D. Richardson, and R. Eason, “Particulate sensing using optical fibres and deep learning (Conference Presentation),” in *AI and Optical Data Sciences*, K.-i. Kitayama and B. Jalali, Eds. San Francisco, United States: SPIE, Mar. 2020, p. 27. [Online]. Available: https://www.spiedigitallibrary.org/conference-proceedings-of-spie/11299/2543951/Particulate-sensing-using-optical-fibres-and-deep-learning-Conference-Presentation/10.1117/12.2543951.full

[144] G. Jobert, M. Fournier, S. Boutami, C. Jamois, A. Lovera, D. Braga, and C. Seassal, “Millimeter-sized particle sensor using a wide field of view monolithic lens assembly for light scattering analysis in Fourier domain,” in *Photonic Instrumentation Engineering VII*, Y. Soskind and L. E. Busse, Eds. San Francisco, United States: SPIE, Mar. 2020, p. 24. [Online]. Available: https://www.spiedigitallibrary.org/conference-proceedings-of-spie/11287/2544185/Millimeter-sized-particle-sensor-using-a-wide-field-of-view/10.1117/12.2544185.full

[145] J. W. Goodman, *Introduction to Fourier Optics*. Roberts and Company Publishers, 2005.

[146] B. E. A. Saleh and M. C. Teich, *Fundamentals of Photonics*, ser. Wiley Series in Pure and Applied Optics, J. W. Goodman, Ed. New York, USA: John Wiley & Sons, Inc., Aug. 1991. [Online]. Available: http://doi.wiley.com/10.1002/0471213748

[147] G. D. Boreman, *Modulation transfer function in optical & electro-optical systems*, ser. Tutorial texts in optical engineering. Bellingham, Wash., USA: SPIE Press, 2001, no. v. TT 52.

[148] L. Li and A. Y. Yi, “Design and fabrication of a freeform microlens array for a compact large-field-of-view compound-eye camera,” *Applied Optics*, vol. 51, no. 12, p. 1843, Apr. 2012. [Online]. Available: https://www.osapublishing.org/abstract.cfm?URI=ao-51-12-1843

[149] M. Sortino, G. Totis, and E. Kuljanic, “Comparison of Injection Molding Technologies for the Production of Micro-optical Devices,” *Procedia Engineering*, vol. 69, pp. 1296–1305, 2014. [Online]. Available: https://linkinghub.elsevier.com/retrieve/pii/S1877705814003683

[150] S. Thiele, T. Gissibl, H. Giessen, and A. M. Herkommer, “Ultra-compact on-chip LED collimation optics by 3D femtosecond direct laser writing,” *Optics Letters*, vol. 41, no. 13, p. 3029, Jul. 2016. [Online]. Available: https://www.osapublishing.org/abstract.cfm?URI=ol-41-13-3029

[151] S. Thiele, K. Arzenbacher, T. Gissibl, H. Giessen, and A. M. Herkommer, “3D-printed eagle eye: Compound microlens system for foveated imaging,” *Science Advances*, vol. 3, no. 2, p. e1602655, Feb. 2017. [Online]. Available: https://advances.sciencemag.org/lookup/doi/10.1126/sciadv.1602655

[152] Y. Bellouard, “The Femtoprint Project,” *Journal of Laser Micro/Nanoengineering*, vol. 7, no. 1, pp. 1–10, Feb. 2012. [Online]. Available: http://www.jlps.gr.jp/jlmn/index.php?action=laser_volno&volno=701

[153] D. Krol, “Femtosecond laser modification of glass,” *Journal of Non-Crystalline Solids*, vol. 354, no. 2-9, pp. 416–424, Jan. 2008. [Online]. Available: https://linkinghub.elsevier.com/retrieve/pii/S0022309307010836

[154] C. A. Ross, D. G. MacLachlan, D. Choudhury, and R. R. Thomson, “Optimisation of ultrafast laser assisted etching in fused silica,” *Optics Express*, vol. 26, no. 19, p. 24343, Sep. 2018. [Online]. Available: https://www.osapublishing.org/abstract.cfm?URI=oe-26-19-24343

[155] V. Mourier, P. Revirand, G. Mauguen, and T. Fathallah, “Process for manufacturing an article with a complex shape with an organic or inorganic hardened material,” (EP2978579) Contracting States: AL AT BE BG CH CY CZ DE DK EE ES FI FR GB GR HR HU IE IS IT LI LT LU LV MC MK MT NL NO PL PT RO RS SE SI SK SM TR Patent EP2 978 579 B1 2017-04-12 [EP2 978 579] - EP2 978 579 A1 2016-02-03 [EP2 978 579] - WO2014/154 712 A1 2014-10-02 [WO2 014 154 712] - US20 160 039 123 A1 2016-02-11 [US20 160 039 123] - FR3 003 790 B1 2015-05-01 [FR3 003 790] - FR3 003 790 A1 2014-10-03 [FR3 003 790], Mar., 2014, archive Location: 67495341. [Online]. Available: https://permalink.orbit.com/RenderStaticFirstPage?XPN=KZ6z6zgty%252F41zTc2PWcWRHfDUqlXTJ5uwQdFuycu4uk%3D%26n%3D1&id=0&base=

[156] C. R. Company and D. R. Lide, Eds., *CRC handbook of chemistry and physics: a ready-reference book of chemical and physical data*, 85th ed. Boca Raton: CRC Press, 2004, oCLC: 249875978.

[157] G. Jobert, P. Barritault, M. Fournier, C. Monpeurt, S. Boutami, C. Jamois, P. Bernasconi, A. Lovera, D. Braga, and C. Seassal, “Miniature Optical Particle Counter and Analyzer Involving a Fluidic-Optronic CMOS Chip Coupled with a Millimeter-Sized Glass Optical System,” *Sensors*, vol. 21, no. 9, p. 3181, May 2021. [Online]. Available: https://www.mdpi.com/1424-8220/21/9/3181

[158] J. Ye, L. Chen, X. Li, Q. Yuan, and Z. Gao, “Review of optical freeform surface representation technique and its application,” *Optical Engineering*, vol. 56, no. 11, p. 1, Nov. 2017. [Online]. Available: https://www.spiedigitallibrary.org/journals/optical-engineering/volume-56/issue-11/110901/Review-of-optical-freeform-surface-representation-technique-and-its-application/10.1117/1.OE.56.11.110901.full

[159] J. D. Joannopoulos, S. G. Johnson, J. N. Winn, and R. D. Meade, *Photonic Crystals: Molding the Flow of Light, Second Edition*. Princeton University Press, Oct. 2011, google-Books-ID: QrTNslcjlZEC.

[160] A. W. Snyder and J. D. Love, *Optical Waveguide Theory*. Boston, MA: Springer US, 1984, oCLC: 852789587. [Online]. Available: http://dx.doi.org/10.1007/978-1-4613-2813-1

[161] E. Yablonovitch, “Photonic band-gap structures,” *Journal of the Optical Society of America B*, vol. 10, no. 2, p. 283, Feb. 1993. [Online]. Available: https://www.osapublishing.org/abstract.cfm?URI=josab-10-2-283

[162] C. Alonso-Ramos, X. Le Roux, J. Zhang, D. Benedikovic, V. Vakarin, E. Durán-Valdeiglesias, D. Oser, D. Pérez-Galacho, F. Mazeas, L. Labonté, S. Tanzilli, r. Cassan, D. Marris-Morini, P. Cheben, and L. Vivien, “Diffraction-less propagation beyond the sub-wavelength regime: a new type of nanophotonic waveguide,” *Scientific Reports*, vol. 9, no. 1, p. 5347, Dec. 2019. [Online]. Available: http://www.nature.com/articles/s41598-019-41810-0

[163] P. Cheben, P. J. Bock, J. H. Schmid, J. Lapointe, S. Janz, D.-X. Xu, A. Densmore, A. Delâge, B. Lamontagne, and T. J. Hall, “Refractive index engineering with subwavelength gratings for efficient microphotonic couplers and planar waveguide multiplexers,” *Optics Letters*, vol. 35, no. 15, p. 2526, Aug. 2010. [Online]. Available: https://www.osapublishing.org/abstract.cfm?URI=ol-35-15-2526

[164] W. T. Chen, A. Y. Zhu, and F. Capasso, “Flat optics with dispersion-engineered metasurfaces,” *Nature Reviews Materials*, vol. 5, no. 8, pp. 604–620, Aug. 2020. [Online]. Available: http://www.nature.com/articles/s41578-020-0203-3

[165] K. Busch, G. von Freymann, S. Linden, S. Mingaleev, L. Tkeshelashvili, and M. Wegener, “Periodic nanostructures for photonics,” *Physics Reports*, vol. 444, no. 3-6, pp. 101–202, Jun. 2007. [Online]. Available: https://linkinghub.elsevier.com/retrieve/pii/S0370157307000786

[166] G. M. Harry, M. R. Abernathy, A. E. Becerra-Toledo, H. Armandula, E. Black, K. Dooley, M. Eichenfield, C. Nwabugwu, A. Villar, D. R. M. Crooks, G. Cagnoli, J. Hough, C. R. How, I. MacLaren, P. Murray, S. Reid, S. Rowan, P. H. Sneddon, M. M. Fejer, R. Route, S. D. Penn, P. Ganau, J.-M. Mackowski, C. Michel, L. Pinard, and A. Remillieux, “Titania-doped tantala/silica coatings for gravitational-wave detection,” *Classical and Quantum Gravity*, vol. 24, no. 2, pp. 405–415, Jan. 2007. [Online]. Available: https://iopscience.iop.org/article/10.1088/0264-9381/24/2/008

[167] A. Chelnokov, S. David, Kang Wang, F. Marty, and J.-M. Lourtioz, “Fabrication of 2-D and 3-D silicon photonic crystals by deep etching,” *IEEE Journal of Selected Topics in Quantum Electronics*, vol. 8, no. 4, pp. 919–927, Jul. 2002. [Online]. Available: http://ieeexplore.ieee.org/document/1039483/

[168] E. Yablonovitch, “Inhibited Spontaneous Emission in Solid-State Physics and Electronics,” *Physical Review Letters*, vol. 58, no. 20, pp. 2059–2062, May 1987. [Online]. Available: https://link.aps.org/doi/10.1103/PhysRevLett.58.2059

[169] S. Y. Lin, J. G. Fleming, D. L. Hetherington, B. K. Smith, R. Biswas, K. M. Ho, M. M. Sigalas, W. Zubrzycki, S. R. Kurtz, and J. Bur, “A three-dimensional photonic crystal operating at infrared wavelengths,” *Nature*, vol. 394, no. 6690, pp. 251–253, Jul. 1998. [Online]. Available: http://www.nature.com/articles/28343

[170] Y. A. Vlasov, X.-Z. Bo, J. C. Sturm, and D. J. Norris, “On-chip natural assembly of silicon photonic bandgap crystals,” *Nature*, vol. 414, no. 6861, pp. 289–293, Nov. 2001. [Online]. Available: http://www.nature.com/articles/35104529

[171] M. Curti, J. Schneider, D. W. Bahnemann, and C. B. Mendive, “Inverse Opal Photonic Crystals as a Strategy to Improve Photocatalysis: Underexplored Questions,” *The Journal of Physical Chemistry Letters*, vol. 6, no. 19, pp. 3903–3910, Oct. 2015. [Online]. Available: https://pubs.acs.org/doi/10.1021/acs.jpclett.5b01353

[172] P. Reininger, S. Kalchmair, R. Gansch, A. M. Andrews, H. Detz, T. Zederbauer, S. I. Ahn, W. Schrenk, and G. Strasser, “Optimized photonic crystal design for quantum well infrared photodetectors,” H. R. Míguez, S. G. Romanov, L. C. Andreani, and C. Seassal, Eds., Brussels, Belgium, Jun. 2012, p. 84250A. [Online]. Available: http://proceedings.spiedigitallibrary.org/proceeding.aspx?doi=10.1117/12.923045

[173] V. L. Welch and J.-P. Vigneron, “Beyond butterflies—the diversity of biological photonic crystals,” *Optical and Quantum Electronics*, vol. 39, no. 4-6, pp. 295–303, Aug. 2007. [Online]. Available: http://link.springer.com/10.1007/s11082-007-9094-4

[174] F. Bloch, “Uber die Quantenmechanik der Elektronen in Kristallgittern,” *Zeitschrift fur Physik*, vol. 52, no. 7-8, pp. 555–600, Jul. 1929. [Online]. Available: http://link.springer.com/10.1007/BF01339455

[175] G. Malpuech, A. Kavokin, G. Panzarini, and A. Di Carlo, "Theory of photon Bloch oscillations in photonic crystals," *Physical Review B*, vol. 63, no. 3, p. 035108, Jan. 2001. [Online]. Available: https://link.aps.org/doi/10.1103/PhysRevB.63.035108

[176] J. Gazalet, S. Dupont, J. Kastelik, Q. Rolland, and B. Djafari-Rouhani, "A tutorial survey on waves propagating in periodic media: Electronic, photonic and phononic crystals. Perception of the Bloch theorem in both real and Fourier domains," *Wave Motion*, vol. 50, no. 3, pp. 619–654, Apr. 2013. [Online]. Available: https://linkinghub.elsevier.com/retrieve/pii/S0165212513000036

[177] C. Kittel, *Introduction to solid state physics*, 7th ed. New York: Wiley, 1996.

[178] S. Sze and K. K. Ng, *Physics of Semiconductor Devices*. Hoboken, NJ, USA: John Wiley & Sons, Inc., Oct. 2006. [Online]. Available: http://doi.wiley.com/10.1002/0470068329

[179] L. Ferrier, P. Rojo-Romeo, E. Drouard, X. Letatre, and P. Viktorovitch, "Slow Bloch mode confinement in 2D photonic crystals for surface operating devices," *Optics Express*, vol. 16, no. 5, p. 3136, 2008. [Online]. Available: https://www.osapublishing.org/oe/abstract.cfm?uri=oe-16-5-3136

[180] M. Tinkham, *Group theory and quantum mechanics*. Mineola, N.Y: Dover Publications, 2003.

[181] P. Viktorovitch, B. Ben Bakir, S. Boutami, J. L. Leclercq, X. Letartre, P. Rojo-Romeo, C. Seassal, M. Zussy, L. Di Cioccio, and J. Fedeli, "3D harnessing of light with 2.5D photonic crystals," *Laser & Photonics Reviews*, vol. 4, no. 3, pp. 401–413, Apr. 2010. [Online]. Available: http://doi.wiley.com/10.1002/lpor.200910009

[182] A. E. Miroshnichenko, S. Flach, and Y. S. Kivshar, "Fano resonances in nanoscale structures," *Reviews of Modern Physics*, vol. 82, no. 3, pp. 2257–2298, Aug. 2010. [Online]. Available: https://link.aps.org/doi/10.1103/RevModPhys.82.2257

[183] W. Zhou, D. Zhao, Y.-C. Shuai, H. Yang, S. Chuwongin, A. Chadha, J.-H. Seo, K. X. Wang, V. Liu, Z. Ma, and S. Fan, "Progress in 2D photonic crystal Fano resonance photonics," *Progress in Quantum Electronics*, vol. 38, no. 1, pp. 1–74, Jan. 2014. [Online]. Available: https://linkinghub.elsevier.com/retrieve/pii/S0079672714000020

[184] M. F. Limonov, M. V. Rybin, A. N. Poddubny, and Y. S. Kivshar, "Fano resonances in photonics," *Nature Photonics*, vol. 11, no. 9, pp. 543–554, Sep. 2017. [Online]. Available: http://www.nature.com/articles/nphoton.2017.142

[185] J.-B. A. Perot and C. Fabry, "On the Application of Interference Phenomena to the Solution of Various Problems of Spectroscopy and Metrology," *The Astrophysical Journal*, vol. 9, p. 87, Feb. 1899. [Online]. Available: http://adsabs.harvard.edu/doi/10.1086/140557

[186] A. Yariv, *Optical electronics*, 4th ed., ser. The Holt, Rinehart, and Winston series in electrical engineering. Philadelphia: Saunders College Pub, 1991, oCLC: 246754648.

[187] H. El Dirani, A. Kamel, M. Casale, S. Kerdiles, C. Monat, X. Letartre, M. Pu, L. K. Oxenløwe, K. Yvind, and C. Sciancalepore, "Annealing-free Si3N4 frequency combs for monolithic integration with Si photonics," *Applied Physics Letters*, vol. 113, no. 8, p. 081102, Aug. 2018. [Online]. Available: http://aip.scitation.org/doi/10.1063/1.5038795

[188] R. P. Stanley, R. Houdré, U. Oesterle, M. Gailhanou, and M. Ilegems, "Ultrahigh finesse microcavity with distributed Bragg reflectors," *Applied Physics Letters*, vol. 65, no. 15, pp. 1883–1885, Oct. 1994. [Online]. Available: http://aip.scitation.org/doi/10.1063/1.112877

[189] H. Soda, K.-i. Iga, C. Kitahara, and Y. Suematsu, "GaInAsP/InP Surface Emitting Injection Lasers," *Japanese Journal of Applied Physics*, vol. 18, no. 12, pp. 2329–2330, Dec. 1979. [Online]. Available: https://iopscience.iop.org/article/10.1143/JJAP.18.2329

[190] C. Hepburn, "Vertical Cavity Surface Emitting Lasers (VCSELs)." [Online]. Available: http://britneyspears.ac/physics/vcsels/vcsels.htm

[191] S. Boutami, B. Benbakir, X. Letartre, J. L. Leclercq, P. Regreny, and P. Viktorovitch, "Ultimate vertical Fabry-Perot cavity based on single-layer photonic crystal mirrors," *Optics Express*, vol. 15, no. 19, p. 12443, 2007. [Online]. Available: https://www.osapublishing.org/oe/abstract.cfm?uri=oe-15-19-12443

[192] C. Sciancalepore, B. Ben Bakir, C. Seassal, X. Letartre, J. Harduin, N. Olivier, J. Fedeli, and P. Viktorovitch, "Thermal, Modal, and Polarization Features of Double Photonic Crystal Vertical-Cavity Surface-Emitting Lasers," *IEEE Photonics Journal*, vol. 4, no. 2, pp. 399–410, Apr. 2012. [Online]. Available: http://ieeexplore.ieee.org/document/6159050/

[193] S. Boutami, B. Ben Bakir, J.-L. Leclercq, X. Letartre, P. Rojo-Romeo, M. Garrigues, P. Viktorovitch, I. Sagnes, L. Legratiet, and M. Strassner, "Highly selective and compact tunable MOEMS photonic crystal Fabry-Perot filter," *Optics Express*, vol. 14, no. 8, p. 3129, 2006. [Online]. Available: https://www.osapublishing.org/oe/abstract.cfm?uri=oe-14-8-3129

[194] J. Mouette, C. Seassal, X. Letartre, P. Rojo-Romeo, J.-L. Leclercq, P. Regreny, P. Viktorovitch, E. Jalaguier, P. Perreau, and H. Moriceau, "Very low threshold vertical emitting laser operation in InP graphite photonic crystal slab on silicon," *Electronics Letters*, vol. 39, no. 6, p. 526, 2003. [Online]. Available: https://digital-library.theiet.org/content/journals/10.1049/el_20030371

[195] L. Ferrier, O. El Daif, X. Letartre, P. Rojo Romeo, C. Seassal, R. Mazurczyk, and P. Viktorovitch, "Surface emitting microlaser based on 2D photonic crystal rod lattices," *Optics Express*, vol. 17, no. 12, p. 9780, Jun. 2009. [Online]. Available: https://www.osapublishing.org/oe/abstract.cfm?uri=oe-17-12-9780

[196] H.-Y. Lu, S.-C. Tian, C.-Z. Tong, L.-J. Wang, J.-M. Rong, C.-Y. Liu, H. Wang, S.-L. Shu, and L.-J. Wang, "Extracting more light for vertical emission: high power continuous wave operation of 1.3- \mu m quantum-dot photonic-crystal surface-emitting laser based on a flat band," *Light: Science & Applications*, vol. 8, no. 1, p. 108, Dec. 2019. [Online]. Available: http://www.nature.com/articles/s41377-019-0214-2

[197] S. Boutami, B. Benbakir, J.-L. Leclercq, and P. Viktorovitch, "Compact and polarization controlled 1.55 \mu m vertical-cavity surface-emitting laser using single-layer photonic crystal mirror," *Applied Physics Letters*, vol. 91, no. 7, p. 071105, Aug. 2007. [Online]. Available: http://aip.scitation.org/doi/10.1063/1.2771085

[198] C. Sciancalepore, B. B. Bakir, X. Letartre, J. Harduin, N. Olivier, C. Seassal, J.-M. Fedeli, and P. Viktorovitch, “CMOS-Compatible Ultra-Compact 1.55- \mu m Emitting VCSELs Using Double Photonic Crystal Mirrors,” *IEEE Photonics Technology Letters*, vol. 24, no. 6, pp. 455–457, Mar. 2012. [Online]. Available: https://ieeexplore.ieee.org/document/6109312/

[199] S. Boutami, “Microcavités optiques verticales a base de cristaux photoniques membranaires,” phdthesis, Ecole Centrale de Lyon, Ecully, Oct. 2007. [Online]. Available: https://tel.archives-ouvertes.fr/tel-00341736/document

[200] M. G. Moharam and T. K. Gaylord, “Rigorous coupled-wave analysis of planar-grating diffraction,” *Journal of the Optical Society of America*, vol. 71, no. 7, p. 811, Jul. 1981. [Online]. Available: https://www.osapublishing.org/abstract.cfm?URI=josa-71-7-811

[201] E. Popov and M. Nevière, “Maxwell equations in Fourier space: fast-converging formulation for diffraction by arbitrary shaped, periodic, anisotropic media,” *Journal of the Optical Society of America A*, vol. 18, no. 11, p. 2886, Nov. 2001. [Online]. Available: https://www.osapublishing.org/abstract.cfm?URI=josaa-18-11-2886

[202] S. Boutami, B. Bakir, H. Hattori, X. Letartre, J.-L. Leclercq, P. Rojo-Rome, M. Garrigues, C. Seassal, and P. Viktorovitch, “Broadband and compact 2-D photonic crystal reflectors with controllable polarization dependence,” *IEEE Photonics Technology Letters*, vol. 18, no. 7, pp. 835–837, Apr. 2006. [Online]. Available: http://ieeexplore.ieee.org/document/1608178/

[203] M. V. Poplavskiy, A. B. Matsko, H. Yamamoto, and S. P. Vyatchanin, “On fundamental diffraction limitation of finesse of a Fabry–Perot cavity,” *Journal of Optics*, vol. 20, no. 7, p. 075609, Jul. 2018. [Online]. Available: https://iopscience.iop.org/article/10.1088/2040-8986/aac7d4

[204] J. Benedikter, T. Hümmer, M. Mader, B. Schlederer, J. Reichel, T. W. Hänsch, and D. Hunger, “Transverse-mode coupling and diffraction loss in tunable Fabry–Pérot microcavities,” *New Journal of Physics*, vol. 17, no. 5, p. 053051, May 2015. [Online]. Available: https://iopscience.iop.org/article/10.1088/1367-2630/17/5/053051

[205] E. Waks and J. Vuckovic, “Coupled mode theory for photonic crystal cavity-waveguide interaction,” *Optics Express*, vol. 13, no. 13, pp. 5064–5073, 2005. [Online]. Available: https://doi.org/10.1364/OPEX.13.005064

[206] S. Fan, “Photonic crystal theory: Temporal coupled-mode formalism,” *Optical Fiber Telecommunication V A*, p. 160, 2008. [Online]. Available: https://doi.org/10.1016/B978-0-12-374171-4.00012-5

[207] J. Chaves, *Introduction to nonimaging optics*, second edition ed. Boca Raton: CRC Press/Taylor & Francis, 2016.

[208] J. C. Maxwell, “A dynamical theory of the electromagnetic field,” *Philosophical Transactions of the Royal Society of London*, vol. 155, pp. 459–512, Dec. 1865. [Online]. Available: https://royalsocietypublishing.org/doi/10.1098/rstl.1865.0008

[209] G. Mie, “Beiträge zur Optik trüber Medien, speziell kolloidaler Metallösungen,” *Annalen der Physik*, vol. 330, no. 3, pp. 377–445, 1908. [Online]. Available: http://doi.wiley.com/10.1002/andp.19083300302

[210] C. Jingyang, X. Penggen, and L. Shu, “Vector wave function expansion for solving electromagnetic scattering by buried objects,” *Journal of Electronics (China)*, vol. 8, no. 3, pp. 239–246, Jul. 1991. [Online]. Available: http://link.springer.com/10.1007/BF02778375

[211] M. Abramowitz and I. A. Stegun, Eds., *Handbook of mathematical functions: with formulas, graphs, and mathematical tables*, 9th ed., ser. Dover books on mathematics. New York, NY: Dover Publ, 2013, oCLC: 935935300.

[212] W. W. Hansen, “A New Type of Expansion in Radiation Problems,” *Physical Review*, vol. 47, no. 2, pp. 139–143, Jan. 1935. [Online]. Available: https://link.aps.org/doi/10.1103/PhysRev.47.139

[213] C. Matzler, “MATLAB functions for Mie scattering and absorption,” *IAP Res Rep*, vol. 8, Jul. 2002.

[214] R. O. Duda and P. E. Hart, *Pattern classification and scene analysis*. New York: Wiley, 1973.

[215] J. S. Lim, *Two-dimensional signal and image processing*, ser. Prentice Hall signal processing series. Englewood Cliffs, N.J: Prentice Hall, 1990.

[216] J. Fourier, *Théorie analytique de la chaleur*. Paris: Firmin Didot, père et fils, 1822.

[217] F. Abelès, “Sur la propagation des ondes électromagnétiques dans les milieux sratifiés,” *Annales de Physique*, vol. 12, no. 3, pp. 504–520, 1948. [Online]. Available: http://www.annphys.org/10.1051/anphys/194812030504

[218] K. Ohta and H. Ishida, “Matrix formalism for calculation of electric field intensity of light in stratified multilayered films,” *Applied Optics*, vol. 29, no. 13, p. 1952, May 1990. [Online]. Available: https://www.osapublishing.org/abstract.cfm?URI=ao-29-13-1952

[219] R. M. A.-G. Azzam and N. M. Bashara, *Ellipsometry and polarized light*, 4th ed., ser. North-Holland personal library. Amsterdam: Elsevier, 1999, oCLC: 247501433.

[220] A.-J. Fresnel, “Mémoire sur la loi des modifications que la réflexion imprime à la lumière polarisée,” French Academy of Sciences, Tech. Rep., Jan. 1823.

[221] J. A. Kurvits, M. Jiang, and R. Zia, “Comparative analysis of imaging configurations and objectives for Fourier microscopy,” *Journal of the Optical Society of America A*, vol. 32, no. 11, p. 2082, Nov. 2015. [Online]. Available: https://www.osapublishing.org/abstract.cfm?URI=josaa-32-11-2082

[222] M. Sakakura and Y. Fujimoto, “Objective lens system for microscope,” Patent US7 158 310 B2 2007-01-02 [US7 158 310] - US20 060 056 039 A1 2006-03-16 [US20 060 056 039] - JP4 633 405 B2 2010-11-26 [JP4 633 405] - JP4 633 406 B2 2010-11-26 [JP4 633 406] - JP2 006 065 023 A 2006-03-09 [JP2 006 065 023] - JP2 006 065 030 A 2006-03-09 [JP2 006 065 030], Mar., 2006, archive Location: 22654254. [Online]. Available: https://permalink.orbit.com/RenderStaticFirstPage?XPN=o4wfAOxQ3DXVNtz%252BuaPnF3fDUqlXTJ5uwQdFuycu4uk%3D%26n%3D1&id=0&base=

[223] C. Palmer, *Diffraction Grating Handbook*, 8th ed. MKS Newport, 2020.

Abstract

This thesis is a contribution to the scientific community for the development of tomorrow's optical Particulate Matter (PM) sensors *'on-a-chip'*, which should be miniaturized, portable and inexpensive while being at the same time sensitive and accurate. The development of such sensors addresses the current sanitary and environmental issues related to air quality monitoring. What should such a sensor look like, which designs are successful, which ones are not? What are the difficulties we did not imagine we would encounter? Those are the questions we have tried to answer, by exploring three novel designs of optical particle counters (OPCs).

A first prototype has been developed, and comprises a custom CMOS image sensor with a traversing air channel. A particle, flowing in the channel, crosses a light beam and a scatter a specific pattern, which is recorded by the image sensor in a lens-less configuration.

Then, an improved mode of imaging is studied with a second prototypes that involves a monolithic, millimeter-sized glass assembly of lenses and mirrors. This miniature optical system is directly coupled with the holed image sensor. For both the first and second prototypes, experimental images of calibrated polystyrene beads are used to retrieve the diameter and refractive index of particles, using dedicated image processing softwares.

Finally, by the means of a third prototype, we explore how an optical resonant cavity is perturbed by the presence of a particle. In particular, open vertical cavity that involves dielectric mirrors such as distributed Bragg reflectors and photonic crystal slab mirrors are studied. Understanding the mechanisms involved in the perturbation of the cavity, enables the design of a cavity-enhanced OPC, where the perturbed cavity mode is analyzed by transmission imaging.

Keywords : Particulate matter, optical particle counter, light-scattering, image sensors, image processing, optical resonators, dielectric mirrors, silicon micro-fabrication, glass micro-machining

Résumé

Cette thèse est une contribution à la communauté scientifique pour le développement des futures générations de capteurs optiques de particules fines sur puce, qui doivent être miniaturisés, portables et peu coûteux; et ce, en garantissant à la fois sensibilité et précision. Le développement de ces capteurs a pour objectif de répondre aux problématiques sanitaires et environnementales actuelles liées à la surveillance de la qualité de l'air.

À quoi doit ressembler un tel capteur? Quelles architectures fonctionnent? Lesquelles ne fonctionnent pas? Quelles sont les difficultés que nous n'imaginions pas rencontrer? Voilà les questions auxquelles nous avons tenté de répondre, en explorant trois nouvelles architectures de compteurs optiques de particules (OPCs).

Un premier prototype a été développé, et comprend un capteur d'image CMOS troué d'un canal fluidique d'air. Une particule, qui circule dans le canal, traverse un faisceau lumineux et diffuse un motif spécifique, qui est enregistré par le capteur d'images selon une configuration d'imagerie sans lentille.

Ensuite, via un second prototype, on étudie un mode d'imagerie amélioré qui implique une pièce monolithique en verre, de taille millimétrique, où sont assemblés des lentilles et des miroirs. Ce système optique miniature est directement couplé au capteur d'images troué. Pour les premier et second prototypes, des images expérimentales de billes de polystyrène calibrées sont utilisées pour retrouver le diamètre et l'indice de réfraction des particules, à l'aide de procédures de traitement d'image dédiées.

Enfin, au moyen d'un troisième prototype, nous étudions comment une cavité optique résonnante est perturbée par la présence d'une particule. En particulier, on étudie une cavité verticale ouverte qui comprend des miroirs diélectriques tels que des miroirs de Bragg et des miroirs minces à cristaux photoniques. La compréhension des mécanismes impliqués dans la perturbation de cavité permet de concevoir un OPC à haute sensibilité, où le mode de la cavité perturbée est analysé par imagerie en transmission.

Mots clés : Particules fines, compteur optique de particules, diffusion de la lumière, capteurs d'images, traitement d'images, résonateurs optiques, miroirs diélectriques, micro-fabrication sur silicium, micro-